MICROCOPY RESOLUTION TEST CHART
NATIONAL BUREAU OF STANDARDS-1963-A

Final Report
on

ANALYSIS OF CRACK ARREST TOUGHNESS
N00014-80-C-0521

Prepared for

Department of the Navy
Office of Naval Research
Arlington, Virginia

By

G.T. Hahn and C.A. Rubin
Department of Mechanical and Materials Engineering
Vanderbilt University
Nashville, TN 37235

January 15, 1988

88 3 01 093

Summary

The objective of the research was to provide theoretical and experimental backing for three concepts that will facilitate the design of structures capable of arresting cracks. The first concept is that the conventional static toughness measures, JIc or the JR curve, are bona fide measures of the fracture arrest capability of tough ductile steels. The second is that the J-values represent the crack driving force when a crack arrests in a tough material, <u>provided</u> the bulk of the propagation just prior to arrest occurs in a relatively brittle material.

The work includes:

(1) Verification of J-integral evaluation of arrest properties.
   (a) Analysis of the crack velocity dependence of toughness for the fibrous mode of crack extension.
   (b) A new test method for studying fast fracture and arrest in tough steels.
   (c) Measurements of fast fracture and crack arrest.
   (d) Fractographic studies.

(2) Application of J-resistance curve concept to crack arrest.
   (a) Development of a finite element model for analysis of a rapidly loaded stationary crack of a compact specimen of a tough, rate dependent steel.
   (b) Development of a general method for quantifying temperature and rate-sensitive constitutive relations for steel.
   (c) Development of crack extension capability using "local control" in the finite element program.
   (d) Finite element modeling of rapid crack extension in ductile viscoplastic materials.

DEFINITION OF CRACK ARREST PERFORMANCE OF TOUGH ALLOYS

V. Dantam and G.T. Hahn
Mechanical and Materials Engineering,
Vanderbilt University, Nashville, TN

1.   Introduction

Tough alloys are inserted into structures to arrest unstable fractures but the performance of such materials in terms of the size of cracks that will be stopped at different stress levels is not well defined. The conventional wedge-loaded compact specimen crack arrest test is difficult to perform on tough materials for which $0.25m^{1/2}$ $< KIa/\sigma_o < 0.5m^{1/2}$. The test calls for large stress intensity values at the onset of cracking, i.e. $K_I > 2K_{IC}$, and prohibitive specimen size requirements,[1] i.e., $W > 8(KIa/\sigma_o)^2 > 1m$. For this reason, the possibility of evaluating K_{Ja}--the J-equivalent of K_{Ia} expressed in stress intensity units--without recourse to a crack arrest test deserves attention. The basis for this idea is: (1) the fact that tough alloys normally display flat fibrous fractures with shear lips or the (fibrous) full shear mode, and (2) evidence that the resistance to penetration by a fibrous fracture normally _increases_ continuously with crack velocity (see Figure 1). In this case, K_{Ia} (the minimum of the K_{ID}-velocity curve) is found at zero velocity (see Figure 1b) and corresponds with K_{IC}.
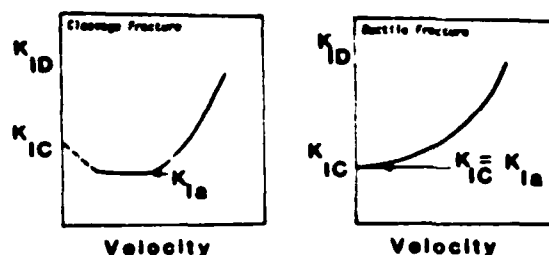

Figure 1.   Schematic representation of the dependence of the fast fracture toughness (K_{ID}) on crack velocity: (a) cleavage fracture, and (b) fibrous (ductile) fracture.

This paper briefly summarizes the evidence that the fibrous fracture resistance increases with crack velocity. It offers two "working"

definitions for K_{Ja} for tough alloys based on the $J_{IC}-$ and J_R ($\Delta a = 1.50$mm)-values obtained with conventional slow loading. Finally, it describes an experimental approach utilizing deep side grooves and preliminary results for a 7075-T651 Aluminum plate.

2. Previous Work

2.1 Experimental Measurements

Evidence that the resistance to fibrous fracture displays a positive crack velocity dependence is reviewed in Reference 2 and is drawn from a number of sources:

(i) CVN-energy values for the fibrous mode (on the ductile shelf) for ABS-C, A302B, HY-80, A 517F, HY-130 and a 10NiCr-Mo-Co steel are <u>higher</u> for standard impact rates of loading than for slow bending.

(ii) K_{IC}-values for the fibrous mode of crack extension in steels and high rates of loading <u>exceed</u> the values obtained with conventional slow rates of loading. The only exception is the results of Klepaczko[3,4] for PA6 and DTD 502A aluminum which reveal a 40% decrease in K_{IC} with increasing loading rate in the range $10^2 < K < 10^6$ MPam$^{1/2}$s^{-1}.

(iii) K_{Ia}-values for relatively high strength AISI 4140 and 4340 steel on the ductile shelf fall close to or slightly above the corresponding K_{IC}-values.

(iv) Actual measurements of K_{ID}, the resistance to fast fracture, for relatively high strength steels all show an increase in K_{ID} with crack velocity for the fibrous mode.

(v) The J-resistance curve of A533 B on the ductile shelf for high rates of loading that produce a crack velocity of $V \approx 0.25$ms^{-1} is elevated by 210KJm^{-2} (1200 lbin^{-1}) relative to conventional J-measurements ($V \sim 10^{-5}$ ms^{-1}).

2.2 Theoretical Calculations

Freund and Douglas[5,6] have estimated the crack velocity dependence of the ductile (fibrous) toughness on the basis of dynamic, elastic plastic, Mode III (antiplane shear analysis) which predicts a plastic zone contraction and steeper strain gradients directly in front of the crack with increasing crack velocities above $V/C_s > 0.2$ (C_s is the shear wave velocity). The present authors[2] have incorporated this result in a simplified model of the Mode I plastic strain gradient in an effort to evaluate:

(i) The plastic's strain rates generated by a fast propagating crack

and the resulting elevation of the yield stress,
(ii) The adiabatic heating[7] and corresponding reduction in the stress field intensity, and
(iii) The increase in applied stress intensity (fracture toughness) required to offset the net reduction of the size of the "process zone".

Figure 2 illustrates that the strain gradient of the model -- a stationary crack -- is similar to the near tip gradient accompanying steady state crack extension proposed by Hermann and Rice.[8] Figure 3 illustrates substantial increases of K_{ID} with crack velocity calculated for fibrous mode fracture in a number of materials. The calculations are based on assumed critical plastic zone strain - distance values which are independent of crack velocity. However, this assumption may not be valid when the number of voids nucleated ahead of the advancing crack tip is sensitive to the peak normal stress and increases with velocity (or loading rate) as a result of the strain rate induced elevation of the yield stress. This would have the effect of reducing the critical strain-distance value and the toughness at higher velocities (and loading rates) along the lines reported by Klepaczko.[3,4] Consequently, the calculations in Figure 3 need the support of the fractographic observations that confirm that the dimple population does not increase excessively with crack velocity.
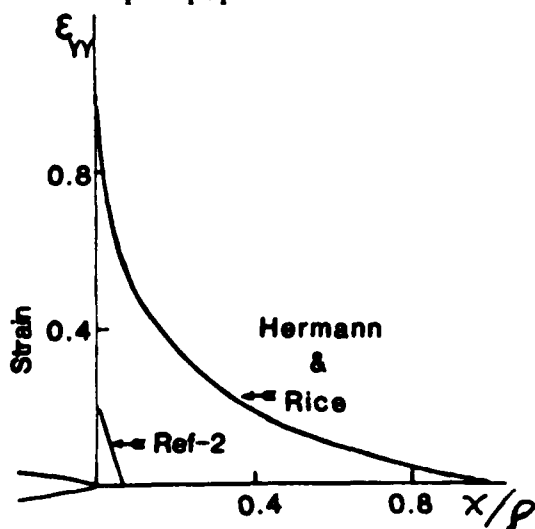

Figure 2. Strain gradient in advance of crack (ρ is extent of plastic zone).

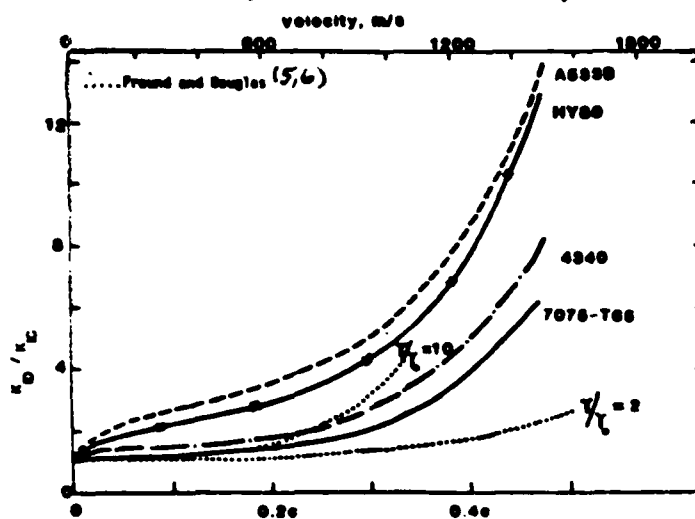Figure 3. Calculate variation of K_{ID}/K_{IC} with crack velocity.

3.   General Approach

In view of the foregoing, the value of K_{Ia} for fibrous fracture can be equated with K_{IC} or K_{JC} (the stress intensity equivalent of J_{IC}) or more correctly, with K_{JR}, the stress intensity equivalent of the point on the J-resistance curve coresponding with crack instability. For tough

materials the J-resistance curve itself comes closest to a geometry independent material property that reflects the crack penetration resistance. However, two points on the J-resistance curve, expressed as stress intensity parameters, can serve as convenient crack arrest design parameters:

$$K_{Ja}(1) \equiv K_J = [J_{IC} E/(1-v^2)]^{1/2} \tag{1}$$

$$K_{Ja}(2) \equiv K_{JR} = [J_R E/(1-v^2)]^{1/2} \tag{2}$$

where J_R corresponds with a $\Delta a = 1.50$mm offset from the blunting line, for a specimen with 10% to 20% deep side grooves. The quantity $K_{Ja}(1)$ is an appropriate measure of arrest toughness for relatively short cracks, i.e., a < 100mm, stopping near a free surface where large values of dJ/da are encountered. The quantity $K_{Ja}(2)$ is appropriate for the arrest of long cracks, i.e., a > 500mm, remote from a free surface, conditions for which unstable tearing* are not likely to be met in the first $\Delta a = 1.50$mm of penetration. The $\Delta a = 1.50$mm offset is selected, because this J_R-value is evaluated as part of the ASTM (tentative) standard J_{IC}-determination and, because the reliability of J_R-values for larger crack extensions is currently open to question. Values of $K_{Ja}(1)$ and $K_{Ja}(2)$ for a number of structural alloys based on measurements by the authors, Gudas and Co-workers[9], and Joyce and Hanson[10,11] and estimates of the crack arrest capabilities are summarized in Table 1.

4   Experimental Verification

Work is in progress to test the ideas introduced in the preceeding sections, specifically to:
(i)   Devise techniques for producing fast, unstable fracture in tough arrester grade materials,
(ii)   Measure the fibrous mode K_{ID}-velocity curve,
(iii) Examine fractographs for changes in the fracture appearance with crack velocity and
(iv)   Test the usefulness of $K_{Ja}(1)$ and $K_{Ja}(2)$ as structural design parameters.

As a first step, the possibility of employing deep face grooves to reduce the stored elastic energy requirement for fast fracture has been explored. Conventional J- curve measurements have been performed on 7075-Aluminum in different heat treated conditions and on HY-130 steel, with 45° face grooves occupying 0%, 25% and 80% of the cross section. The unloading compliance was used to evaluate the effective crack length, and the J-values were corrected for face-groove depth: J = J(measured) (B/B_N)**.   Some of the results of this study are summarized in Figure 4

---

*   dJ/da > dJ_R/da
** B is the ungrooved plate thickness and B_N, the net thickness after grooving.

TABLE 1. CRACK ARREST TOUGHNESS VALUES FOR SELECTED STEELS FOR SERVICE TEMPERATURES CORRESPONDING TO THE UPPER SHELF

MATERIAL	TEST TEMP, C	σ_o, MPA	CVN, J	ESTIMATED K_{Ia}, MPa m$^{1/2}$ $K_{Ja}(1)$	$K_{Ja}(2)$	CRACK ARREST CAPABILITY, 2a, mm*	REFERENCE
HY-130	RT	937	112, 116	182	231	155	9
HY-130	25°C	902	80	189	---		10
HY-130	RT	882	152	235	365	440	2
HY-80	RT	558		180	259	550	9
HY-80	RT	616	110	174	---		11
A533-B(02)	149	413	176	207	329	1620	9, 12
A533-B(03)	149	401	87	202	274	1190	9
A516-G70	149	303	137	180	259	1860	9
7075 Al	RT	280	---	78	85	235	Present Study
7075-Al	RT	552	---	35	56	26	Present Study

*Length of a centrally located crack 2a that can be stopped by long, nominally elastic arresters, σ = 0.5σ_o (σ_o is the yield stress), located on either side of the crack: 2a = 2/π[$K_{Ja}(2)$/σ]^2.

which compares the K_{JR}/K_{JR}(25% grooved)-ratios obtained at different
relative toughness levels. The results show that side grooves
occupying up to 80% of the cross section do not alter either the J_{IC}- or
J_R-values substantially. It appears that the use of deep face grooves to
reduce stored energy requirements for a fast fracture can be justified.

The effects of face grooves on fibrous mode crack arrest measurements
are being studied. So far, run-arrest events have been successfully
produced in 25mm-thick, 150mm by 150mm compact specimens of 7075-T651
with blunt, 2mm-radius starting slots. The relatively low toughness-to-
yield ratio of this heat treated condition: K_{JC}/ σ_o = 0.07 m$^{1/2}$ permits
an LEFM interpretation of the arrest event and the evaluation of K_{Ia}.
Results are summarized in Table 2 and show little influence of side
groove depth. In addition, the results seem to be consistant with the
proposed features of fibrous mode crack arrest:

(i) The K_{Ia}-values are close to and somewhat larger than $K_{Ja}(2)$,
(ii) The K_{ID}-values (the average values during run-arrest-event)
      are larger than K_{JR} reflecting a rising K_{ID}-crack velocity curve.

Propagation and arrest in the 7075-T651 test specimens (see Figure 5)
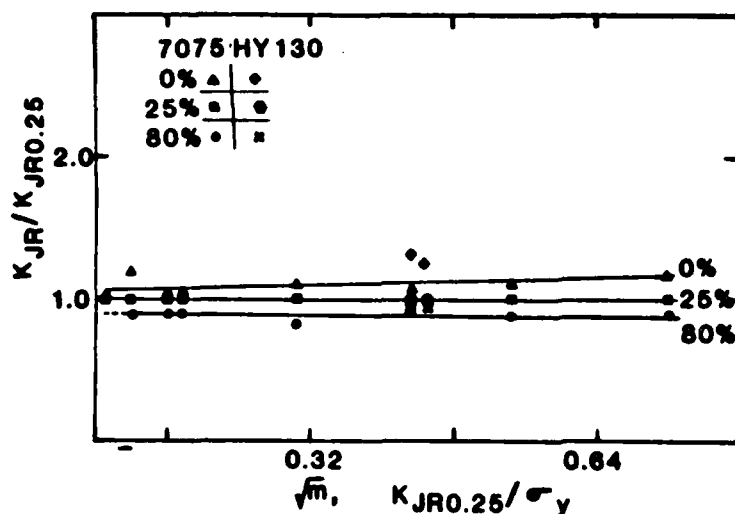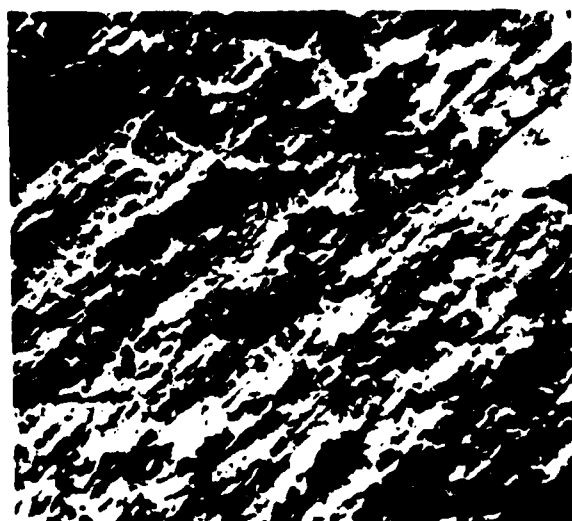is complicated by the relatively weak grain boundaries parallel to

Figure 4. Effect of face grooves on K_{JR} ($\Delta a=1.50mm$) values obtained from stable crack growth measurements.

Figure 5. Appearance of fractured 7075-T651 aluminum, compact crack arrest test specimens.
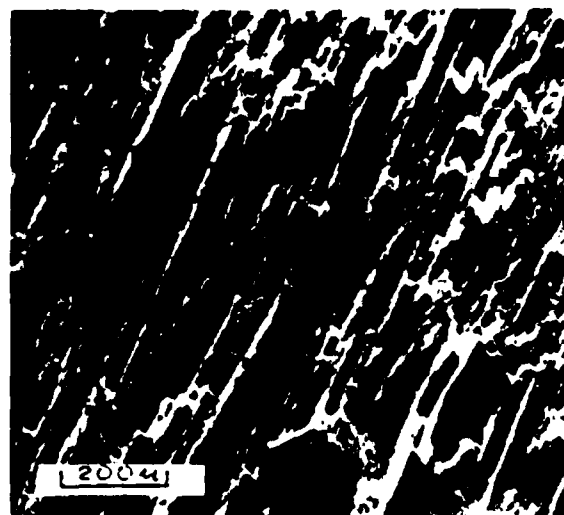
(a)   (b)

Figure 6. Appearance of fracture surfaces 7075-T651 Aluminum produced by (a): slow stable crack extension in a conventional J-test and (b) fast fracture in a compact crack arrest test.

TABLE 2. RESULTS OF STABLE CRACK GROWTH AND CRACK ARREST MEASUREMENTS IN 7075-T651[a] ALUMINUM COMPACT SPECIMENS WITH 0%, 25% AND 80% FACE GROOVES.

	STABLE GROWTH				CRACK ARREST	
FACE GROOVE[b] %	K_{JC}, MPa $m^{1/2}$	K_{JR}, MPa $m^{1/2}$ K_{Ja} (2)	K_Q, MPa $m^{1/2}$	Δa, mm	K_{Ia} MPa $m^{1/2}$	$\overline{K}_{ID}$, MPa $m^{1/2}$ [c]
0	38	50	139	58	56	88
0	38	50	118	53	54	79
25	39	49	139	51	64	94
25	39	49	139	52	57	89
25	39	49	174	>88	<84	<121
80	40	--	118	56	60	83

(a) 25mm-thick, 7075-T651 plate: σ_o =552 MPa, HRB = 91; with cracks extending $\perp$ to the LT-direction.

(b) Percent of cross section removed by face grooves.

(c) $\overline{K}_{ID} = [K_Q \cdot K_{Ia}]^{1/2}$

the rolling plane. Tensile stresses in the short transverse direction initiate cracks in these boundaries (delaminations) at the root of the face grooves and these permit the fracture path to deviate from the specimen symmetry plane. In addition, the high speed fracture surfaces become inclined to the tensile axis. Fractographs of these surfaces display a step-like appearance (Figure 6a and 6b) with the vertical segments of the steps corresponding with the delamination of the weak boundaries. Consequently, the fractographs contain evidence of changes in the details of the fibrous mode mechanism of 7075-T651 aluminum that could reduce the toughness values for high crack velocities in Figure 3.

Acknowledgements

REFERENCES

[1] Sanford, R.J., Fourney, W.L., Chona, R., and Irwin, G.R.,
     NUREG/CR-2179, ORNL/Sub-7778/2, Aug. 1981.

[2] Dantam, V., and Hahn, G.T., "Evaluation of the Crack Arrest
     Capabilities of Ductile Steels" Vanderbilt University Report to
     ONR (HO0014-80C-052) July 1981.

[3] Klepaczko, J., Conference on Mechanical Properties at High Rates of
     Strain, 1979, Proc. Inst. Phys., Ser. No. 47, Bristol, 1979, p. 201.

[4] Klepaczko, J., "Discussion of a New Experimental Method in Measuring
     Fracture Toughness Initiation at High Loading Rates by Stress Waves,"
     Technical Report for brown University, May 1981.

[5] Freund, L.B., and Douglas, A.S., "The Influence of Inertia on
     Elastic-Plastic Antiplane Shear Crack Growth," Brown University
     Report MRL E-126, Feb. 1981.

[6] Douglas, A.S., Freund, L.B., and Parks, D.M., "Dynamic Steady
     Airplane Shear Crack Growth in an Elastic Plastic Material," Proc.
     5th Int. Conference on Frac ture, Cannes, 1981.

[7] Lucas, R.A., "A Quasi-Static Thermo Elastic Analysis of A Propagating
     Crack," Int. J. Solid Structures, 1969, Vol. 5, p. 175.

[8] Hermann, L. and Rice, J.R., "Comparison of Theory and Experiment
     for Elastic Plastic Plane Strain Growth," Metal Science, 14, 1980,
     pp. 285-291.

[9] Gudas, J.P., Vassilaros, M.G., Joyce, J.A., Davis, D.A., and Anderson,
     D.R., "A Summary of Recent Investigations of Compact Specimen
     Geometry Effects on the J_I-R Curve of High-Strength Steels,"
     NUREG/CR-1813, Nov. 1980.

[10] Joyce, J.A. and Hasson, D.F., "Characterization of Transition
     Temperature Behavior of Hy-130 Steel by the J_{IC}-Fracture Toughness
     Parameter," Eng. Fract. Mech., Vol. 13, p. 417, 1980.

[11] Hasson, D.F., and Joyce, J.A., "The Effect of a Higher Loading Rate
     on The J_{IC}-Fracture Toughness Transition Temperature at HY-Steels,"
     J. Eng. Mats and Tech. 103, 1981, pp. 133-141.

[12] Wessel, E.T., "Linear Elastic Fracture Mechanics for Thick-Walled,
     Welded Steel Pressure Vessels, Material Property Considerations,"
     Practical Fracture Mechanics for Structural Steel, P.H. M.O. Dobson,
     ed., UKAEA 2 Chapman Hall, 1969.

R. Hoff[1]

L. M. Santi[2]

G. E. Johnson

C. A. Rubin

G. T. Hahn

Mechanical and Materials Engineering.
Vanderbilt University.
Nashville. TN 37235

Optimal Discretization of Power Stress-Strain Law Curves

A criterion for optimal discretization of power stress-strain law curves is proposed. The criterion is based on the assumption that it is desirable to have the fewest possible line segments without exceeding some predetermined bound on the error. The formulation produces a system of simultaneous nonlinear equations which are solved using an iterative search technique. Solutions are presented in both graphical and tabular form for a wide range of strain hardening exponents and acceptable error bounds. It is shown that stress and energy density can be accurately and efficiently modeled using the optimal discretization.

Introduction

The power stress-strain law is frequently used in the mathematical analysis of plasticity problems since it is a reasonable description of the behavior of many materials beyond first yield. One of the most common applications of the power-law is in elastic-plastic fracture mechanics since the stresses and strains at the tip of a stationary crack were determined by Hutchinson [1], and Rice and Rosengren [2] on the basis of a power-law material.

The finite element method (FEM) is widely applied in the study of elasto-plastic fracture mechanics. Whenever possible, the user should code the actual exact analytic representation of the constitutive relation into the FEM code as a part of a material library. Nevertheless, there may be occasions when this is impossible or impractical, notably when certain commercial FEM software is used. A common approach when this occurs is to approximate the stress-strain law with a series of discrete line segments. Until now, how to perform the discretization has been largely a matter of art and experience. Many strategies offer plausible solutions. Experience suggests that the greatest success can be obtained by using more segments on the portion of the curve with greatest curvature. In this note we suggest an objective criterion for the discretization based on the premise that it is desirable to have as few segments as possible without exceeding some predetermined bound on the error.

In order to accurately describe a smooth curve such as the power stress-strain law, a large number of line segments is typically required. However, a large number of line segments in the discretized stress-strain curve is computationally undesirable since this increases the CPU time required to sort and interpolate in order to find the stress corresponding to a
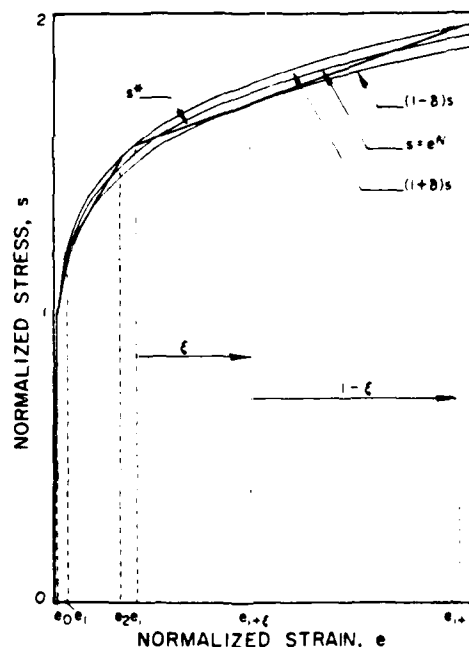

Fig. 1   Discretized power-law stress-strain curve

particular value of strain. This note describes a technique whereby the power-law stress-strain curve is discretized using the minimum number of line segments possible so that a predetermined error criterion is not violated. Results are presented for a large range of values of the strain hardening exponent, n, for cases where the stresses are held to within ± 0.1, ± 0.5 or ± 1.0 percent of the exact value.

Problem Formulation

Consider a power-law stress-strain curve of the form

$$\epsilon/\epsilon_i = \sigma/\sigma_i, \qquad \sigma \le \sigma_i \qquad (1a)$$

$$\epsilon/\epsilon_0 = (\sigma/\sigma_0)^n \qquad \sigma > \sigma_0, n > 1 \qquad (1b)$$

Let e and s be normalized quantities so that $e = \epsilon/\epsilon_0$ and $s = \sigma/\sigma_0$. Equations (1) can then be rewritten

$$e = s \qquad s \leq 1 \qquad (2a)$$

$$e = s^n \qquad s > 1 \qquad (2b)$$

These relations can be more conveniently addressed if we define $N = 1/n$ so that

$$s = e \qquad e \leq 1 \qquad (3a)$$

$$s = e^N \qquad e > 1, \ 0 < N \leq 1. \qquad (3b)$$

If the allowable relative error is denoted by δ, the line segments which approximate equation $(3b)$, s^*, must be within the limits

$$(1 - \delta)s \leq s^* \leq (1 + \delta)s. \qquad (4)$$

Clearly the longest line segment which will be bounded by equation (4), as shown in Fig. 1, will intersect the $(1 + \delta)s$ curve at points i, and $i + 1$, and be tangent to the $(1 - \delta)s$ curve at some intermediate point $i + \xi$. i.e.,

at point i: $\qquad s_i^* = (1 + \delta)e_i^N \qquad (5a)$

at point $i + 1$: $\quad s_{i+1}^* = (1 + \delta)e_{i+1}^N \qquad (5b)$

at point $i + \xi$: $\quad s_{i+\xi}^* = (1 - \delta)e_{i+\xi}^N \qquad (5c)$

$$= (1 - \delta)[(1 - \xi)e_i + \xi e_{i+1}]^N.$$

But since points i, $i + \xi$, and $i + 1$ all lie on a straight line,

$$s_{i+\xi}^* = (1 - \xi)s_i^* + \xi s_{i+1}^* \qquad (6a)$$

which, upon substitution for s_i^* and s_{i+1}^*, becomes

$$s_{i+\xi}^* = (1 + \delta)[(1 - \xi)e_i^N + \xi e_{i+1}^N]. \qquad (6b)$$

Since $i + \xi$ is a point of tangency, the value of $s_{i+\xi}^*$ as calculated from the $(1 - \delta)s$ curve $(5c)$ must equal the value calculated from the line segment $(6b)$:

$$(1 + \delta)[(1 - \xi)e_i^N + \xi e_{i+1}^N] - (1 - \delta)[(1 - \xi)e_i$$
$$+ \xi e_{i+1}]^N = 0. \qquad (7)$$

The slope of the $(1 - \delta)s$ curve, calculated at the point of tangency is

$$E_T = d[(1 - \delta)e^N]/de \,|_{i+\xi} \qquad (8)$$
$$= N(1 - \delta)[(1 - \xi)e_i + \xi e_{i+1}]^{N-1}.$$

Likewise, the slope of the line segment in this region is

$$E_T^* = (s_{i+1}^* - s_i^*)/(e_{i+1} - e_i). \qquad (9)$$

Since the slopes must be equal at the point of tangency,

$$(s_{i+1}^* - s_i^*)/(e_{i+1} - e_i) - N(1 - \delta)[(1 - \xi)e_i$$
$$+ \xi e_{i+1}]^{N-1} = 0, \qquad (10a)$$

or,

$$(1 + \delta)(e_{i+1}^N - e_i^N) - N(1 - \delta)(e_{i+1} - e_i)[(1 - \xi)e_i$$
$$+ \xi e_{i+1}]^{N-1} = 0. \qquad (10b)$$

In order for the discrete approximation to exhibit the same yield point as the power-law curve, and in order to mitigate errors for small plastic strains, we suggest that the first line segment should begin tangent to the power law curve. Therefore, the first line segment is defined by rules that differ from the approximation strategy used for other points.

The slope of the $s = e^N$ curve at the yield point is

$$E_T = d(e^N)/de \,|_{e=1} = N. \qquad (11)$$

The slope of the first line segment is

$$E_T^* = (s_1^* - 1)/(e_1 - 1). \qquad (12)$$

Since these slopes are equal,

$$(1 + \delta)e_1^N - 1 - N(e_1 - 1) = 0. \qquad (13)$$

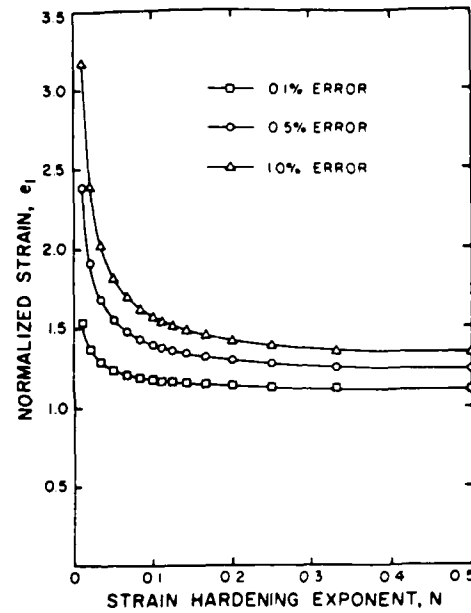Equations (7), $(10b)$, and (13) are three equations in the

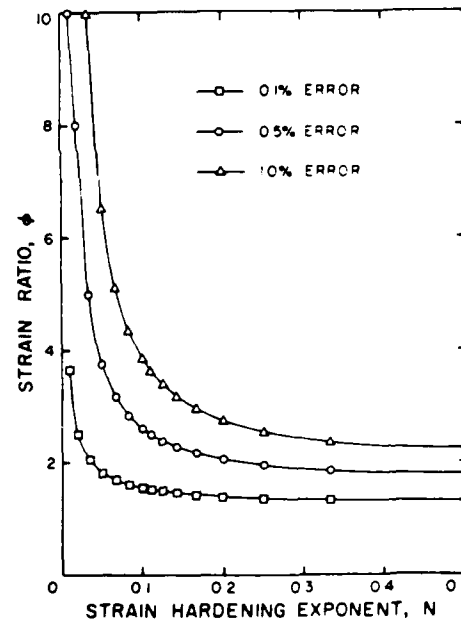Fig. 2 Values of strain at the end of the first line segment, e_1, for discretized power-law stress-strain curve

Fig. 3 Strain ratio, $\phi = e_{i+1}/e_i$, for discretized power-law stress-strain curve

three unknowns e_1, e_2 and ξ (if $i = 1$). Unfortunately, these equations are nonlinear and no closed form solution is apparent. These equations can nonetheless be solved using an iterative search strategy. An objective function is constructed by summing the squares of equations (7), $(10b)$, and (13):

$$f(e_1, e_2, \xi) = \{(1 + \delta)[(1 - \xi)e_1^N + \xi e_2^N]$$
$$- (1 - \delta)[(1 - \xi)e_1 + \xi e_2]^N\}^2 + \{(1 + \delta)(e_2^N$$
$$- e_1^N) - N(1 - \delta)(e_2 - e_1)[(1 - \xi)e_1 + \xi e_2]^{N-1}\}^2$$
$$+ \{(1 + \delta)e_1^N - 1 - N(e_1 - 1)\}^2. \qquad (14)$$

This function is equal to zero at the solution to equations (7), $(10b)$, and (13). The function, $f(e_1, e_2, \xi)$, was minimized for several values of N and δ using the BFGS-Armijo variable metric algorithm [3-7] as implemented by Santi et al. [8-9].
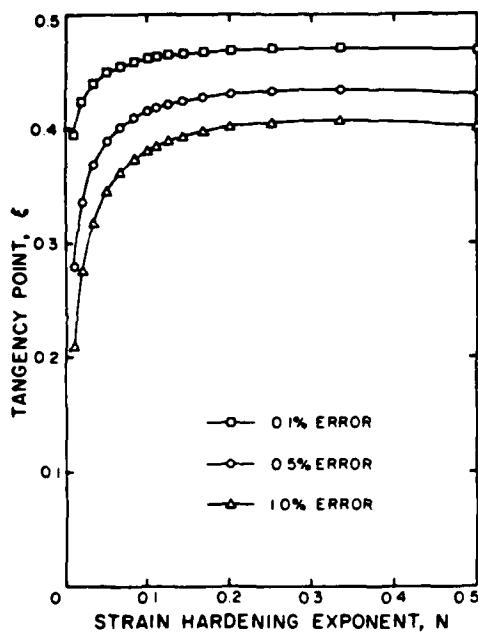
Fig. 4 Tangency point, ξ, for discretized power-law stress-strain curve
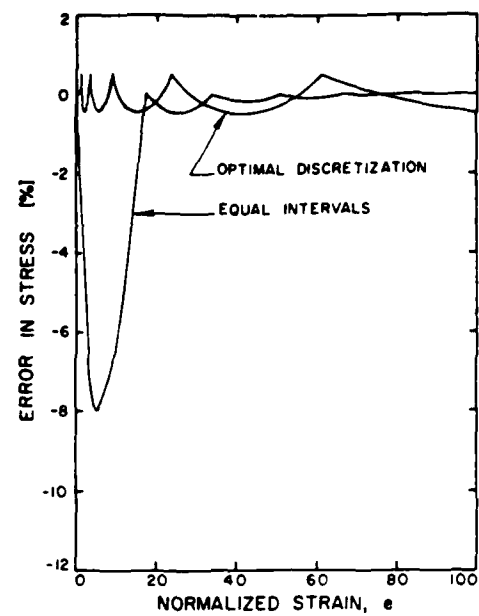

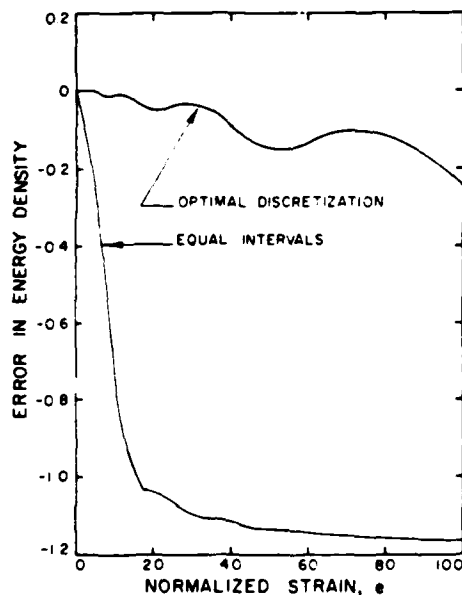Fig. 6 Errors in stress for $s = e^{0.1}$ with $\delta = 0.5$ percent

Fig. 5 Errors in energy density for $s = e^{0.1}$ with $\delta = 0.5$ percent

Convergence was assumed when the values for e_1, e_2, and ξ did not change in the eighth decimal place. Execution times were typically 5 seconds on a DEC-1099 computer.

It is a simple matter to reformulate equations (7) and (10b) into independent relations of the form $f(\phi, \xi) = 0$ where $\phi = e_{i+1}/e_i$. Since these relations admit but one solution for ϕ and ξ, once e_1 and e_2 are known, all other points on the discrete stress-strain curve can be determined using the recurrence relationship

$$e_2/e_1 = e_3/e_2 = \ldots = e_{i+1}/e_i = \ldots = \phi \qquad (15)$$

Other formulations of this problem are possible. The present approach is straightforward and computationally tractable.

Results

Equation (14) was minimized for 15 different values of N,

Table 1 Results of analyses

n	N	e_1	ϕ	ξ
			$\delta = 0.1\%$	
2	.500	1.0935565	1.2879691	.46840881
3	.333	1.0989588	1.3079128	.47021389
4	.250	1.1078153	1.3394505	.46960227
5	.200	1.1169015	1.3721958	.46841355
6	.167	1.1257073	1.4044492	.46704401
7	.143	1.1341422	1.4358636	.46562250
8	.125	1.1422117	1.4664131	.46419941
9	.111	1.1499450	1.4961580	.46279618
10	.100	1.1573751	1.5251778	.46142206
12	.083	1.1714466	1.5813474	.45877285
15	.067	1.1909432	1.6618679	.45504340
20	.050	1.2202481	1.7890327	.44938886
30	.033	1.2710279	2.0279355	.43961969
50	.020	1.3551207	2.4806927	.42381667
100	.010	1.5200229	3.6163146	.39467482
			$\xi = 0.5\%$	
2	.500	1.2213011	1.7623199	.42964112
3	.333	1.2331558	1.8242516	.43364654
4	.250	1.2541903	1.9247067	.43230698
5	.200	1.2760993	2.0323117	.42969350
6	.167	1.2975276	2.1416288	.42668437
7	.143	1.3182012	2.2513178	.42356504
8	.125	1.3381018	2.3610671	.42044697
9	.111	1.3572796	2.4708770	.41737749
10	.100	1.3758000	2.5808475	.41437680
12	.083	1.4111195	2.8017813	.40860684
15	.067	1.4605673	3.1374659	.40052053
20	.050	1.5359661	3.7146364	.38834941
30	.033	1.6695306	4.9634371	.36761045
50	.020	1.8983217	7.9794768	.33498484
100	.010	2.3719740	20.1519789	.27856478
			$\delta = 1.0\%$	
2	.500	1.3265844	2.2315196	.40099010
3	.333	1.3429212	2.3439699	.40660050
4	.250	1.3739640	2.5300273	.40475490
5	.200	1.4066679	2.7342585	.40113645
6	.167	1.4388638	2.9468586	.39697345
7	.143	1.4700809	3.1652695	.39266495
8	.125	1.5002578	3.3888095	.38836644
9	.111	1.5294477	3.6174035	.38414363
10	.100	1.5577331	3.8511970	.38002435
12	.083	1.6119230	4.3353257	.37212970
15	.067	1.6883053	5.1068099	.36112830
20	.050	1.8058489	6.5306078	.34472203
30	.033	2.0169563	10.0080919	.31725234
50	.020	2.3859947	20.4514398	.27554075
100	.010	3.1729754	87.8246897	.20905698

and for values of $\delta = 0.1$, 0.5, and 1.0 percent. Table 1 presents results for e_1, the ratio $o = e_{i+1}/e_i$, and ξ. All data have been verified as correct and none produce errors greater than 10^{-3} percent outside of the $(1 \pm \delta)s$ range. Values of e_1, o, and ξ are plotted in Figs. 2–4, respectively.

Attempts were made to determine if a linear relationship could be found between any of $\{e_1, e_2, o, \xi, \log e_1, \log e_2, \log o, \log \xi\}$ and any of $\{n, N, \sqrt{N}, \log N\}$, without success. If results are desired for values of N not listed in Table 1, then an appropriate interpolation scheme should give quite good values of e_1 and o. Stress-strain curves produced in this manner will still be optimal, but the error term, δ, may not be exactly the same as stated in Table 1.

Another frequently overlooked aspect of stress-strain curve discretization is that the energy density is poorly represented if a number of points *on* the stress strain curve are used to discretize the stress-strain curve. The energy density is the sum of the strain energy density and the plastic dissipation at a given material point:

$$W = \int_0^{\epsilon_{ij}} \sigma_{ij} \, d\epsilon_{ij}. \tag{16}$$

The optimal stress-strain discretization technique gives a much better representation of the energy density than would be obtained if a number of equal increments were used to discretize the stress-strain curve. Figure 5 depicts a rather extreme example of this. The curve $s = e^{0.1}$ is discretized using six line segments in the range $1 \le e \le 100$. In one case the optimal discretization technique is used with six intervals (i.e., $\delta = 0.5$ percent), and in the other case six equal intervals of e are used. The errors in energy density are plotted in Fig. 5. The optimal discretization technique produces errors in energy density of roughly -0.2 percent, whereas the equal interval technique produces errors of as high as -6.6 percent. Indeed, the equal interval technique also produces a very poor representation of the stress as a function of strain, where errors as large as -8.1 percent occur at small values of strain. This is depicted in Fig. 6.

Conclusions

An objective technique was described whereby the power-law stress-strain curve was represented by an optimal combination of line segments. Results were presented for a large variety of strain hardening exponent values, n, at each of three allowable deviation values, δ. A detailed investigation of one case revealed that stress and energy density are accurately modeled using the optimal discretization technique.

Acknowledgments

References

1 Hutchinson, J. W., "Singular Behavior at the End of a Tensile Crack in a Hardening Material," *Journal of the Mechanics and Physics of Solids*, Vol. 16, 1968, pp. 13–31.

2 Rice, J. R., and Rosengren, G. F., "Plane Strain Deformation Near a Crack Tip in a Power-Law Hardening Material," *Journal of the Mechanics and Physics of Solids*, Vol. 16, 1968, pp. 1–12.

3 Broyden, C. G., "The Convergence of a Class of Double-Rank Minimization Algorithms: 2. The New Algorithm," *Journal of the Institute of Mathematics and its Applications*, Vol. 6, 1970, pp. 223–231.

4 Fletcher, R., "A New Approach to Variable Metric Algorithms," *The Computer Journal*, Vol. 13, 1970, pp. 317–322.

5 Goldfarb, D., "A Family of Variable-Metric Methods Derived by Variational Means," *Mathematics of Computation*, Vol. 24, 1970, pp. 23–26.

6 Shanno, D. F., "Conditioning of Quasi-Newton Methods for Function Minimization," *Mathematics of Computation*, Vol. 24, 1970, pp. 647–656.

7 Armijo, L., "Minimization of Functions Having Lipschitz Continuous First Partial Derivatives," *Pacific Journal of Mathematics*, Vol. 16, 1966, pp. 1–3.

8 Santi, L. M., Townsend, M. A., and Johnson, G. E., "Effect of Algorithm Parameters on Numerical Performance of Variable Metric Acceptable Point Algorithms (As Represented by BFGS-Armijo)," *Engineering Optimization*, Vol. 6, 1982, pp. 1–11.

9 Santi, L. M., Townsend, M. A., and Johnson, G. E., "A Noniterative Penalty Function Technique for Constrained Optimization," *Engineering Optimization*, Vol. 6, 1982, pp. 63–76.

HIGH RATE DEFORMATION IN

THE FIELD OF A CRACK

R. Hoff, C. A. Rubin, and G. T. Hahn

Vanderbilt University
Department of Mechanical and Materials Engineering
Nashville, TN   37235

INTRODUCTION

As part of a study of the crack arrest capabilities of tough steels[1], efforts are underway to simulate rapid crack extension and arrest in elastic-plastic finite element models. As a first step, stationary cracks in compact tension specimens have been modelled and the effects of loading rate, strain rate sensitivity and inertia on J_I have been examined. The aim of this work is to examine those features of the plastic zone influential in determining the toughness, namely, the size of the process zone, and the crack tip opening displacement.

Plasticity associated with a stationary crack has been characterized as occurring in two separate zones, as shown in Fig. 1. The larger region, called the plastic zone, features small plastic strains in the range $0 < \epsilon_p < 0.1$. The size of the plastic zone (at $\theta = 0°$) is given by a characteristic dimension, r_o. Levy, et al.[2] have determined r_o for a nonhardening material with a semi-infinite crack in an infinite plate. In cases where the plastic zone is small compared to the specimen dimensions

$$r_o \approx 0.036 \; EJ_I/\sigma_o^2(1- \nu^2). \tag{1}$$

Even closer to the crack tip is the heavily-strained process zone, where plastic strains range roughly from 0.1 to 1.0. This intensely non-linear zone can be given a characteristic dimension, w, which can be related to the crack tip opening displacement, δ, by

$$w = \beta\delta. \tag{2}$$

Rice[3] suggests 1.9 as a possible value of β, and Paris[4] states it is of the order of 2. Since the process zone has no "obvious" boundary, the value of β depends on how the process zone is defined; for instance, a critical strain value may be chosen to define the process zone boundary. For convenience, $\beta = 1$ has been used in this analysis.

The crack tip opening displacement, δ, can be expressed as a function of the J-integral[5] by:

$$\delta = d_n J/\sigma_o, \tag{3}$$

for a nonlinear elastic, power law hardening material. The constant, d_n, is a function of material properties, α, σ_o, E and n (Ramberg-Osgood[6]), where

$$\varepsilon/\varepsilon_o = \alpha(\sigma/\sigma_o)^n. \tag{4}$$

For small values of strain, ε can be interpreted as the total strain; for large values of strain, ε can be interpreted as the plastic strain. Using values for a steel such as A533B, a value of d_n can be determined[5] as $d_n = 0.52$. Equation (3) can be substituted into (2) and then divided by (1) giving the relative size of the process and the plastic zones:

$$w/r_o = 13.14 \ \sigma_o/E. \tag{5}$$

If $E = 197$ GPa and $\sigma_o = 415$ MPa as in the case of A533B steel at 93°C, then

$$w/r_o \approx 0.03. \tag{6}$$

The plastic strain rates are related to the strain gradients and the extent of the plastic and process zones. If it is assumed that the equivalent plastic strain is 0.0 at $r = r_o$ (the plastic zone boundary), and varies linearly up to a value of 0.005 at $r = w$ (the process zone boundary), then the plastic strain can be expressed as:

$$\varepsilon_p = 0.005(r_o - r)/(r_o - w). \tag{7}$$

After making appropriate substitution from (6) and (1), and differentiating with respect to time:

$$\dot{\varepsilon}_p = 0.005(r/r_o)(\dot{J}_I/J_I). \tag{8}$$

An "average" value of plastic strain rate could be calculated at the middle of the plastic zone, i.e. where $r = 0.5r_o$.

This gives

$$\dot{\varepsilon}_p \approx 0.0025(\dot{J}_I/J_I) \approx 0.005(\dot{K}_I/K_I) \tag{9}$$

for the plastic zone, and is equivalent to the ε_p equation of Wilson[14].

Another expression for the strain rate in the plastic zone can be derived from the J-field solutions of Hutchison[7], Rice and Rosengren[8]. The equivalent plastic strain is

$$\varepsilon_p = (\sigma_o/E)[(EJ)/(\alpha\sigma_o^2 I_n r)]^{n/n+1} \ \tilde{\sigma}_e^n(n,\theta). \tag{10}$$

(Note that equation (10) assumes elastic strains to be negligible.) The constants I_n and $\tilde{\sigma}_e$ are given in Refs. [8,9], and the remaining values are defined by the Ramberg-Osgood model of eq. (4). Differentiating (10) with respect to time, and substituting the appropriate values for A533B ($\alpha = 1.12$, $n = 9.71$)[10] at $\theta = 0$, yields

$$\dot{\varepsilon}_p = 3.24 \times 10^{-11} \ r^{-0.9066}J^{-0.09337}\dot{J}. \tag{11}$$

Again, an "average" value of plastic strain can be calculated in the middle of plastic zone ($r = 0.5r_o$) giving

$$\dot{\varepsilon}_p \approx 0.00024(\dot{J}/J) \approx 0.00048 \ (\dot{K}_I/K_I). \tag{12}$$

The plastic strain rate predicted by (9) is 10 times larger than that predicted by (12). This is due to (i) the nature of the linear approximation used in (9), and (ii) the fact that the J-field is not a good approximation where plastic strains are small (such as in most of the plastic zone). It is not clear which model is better or more reliable.

A similar linear approximation could be used to determine the order of magnitude of plastic strains in the process zone. Here the assumptions, that $\varepsilon_p = 0.005$ at $r = w$ and $\varepsilon_p = 0.25$ at $r = 0$, are suggested by finite element results of McMeeking[11] for a material where $n = 10$. Typical strain rates in the center of the process zone for $\theta = 0$ are

$$\dot{\varepsilon}_p \approx 0.35(\dot{J}_I/J_I) \approx 0.7(\dot{K}_I/K_I). \tag{13}$$

The plastic strain rates can directly be calculated for $\theta = 0$ using the J-field solution of (11). The result given below is not reliable since $r = w/2$ [18].

$$\dot{\varepsilon}_p \approx 0.007(\dot{J}_I/J_I) \approx 0.014(\dot{K}_I/K_I). \tag{14}$$

In view of equations (9) and (13), plastic strain rate can be

determined at the onset of crack extension of ductile materials such as A533B. Table 1 gives typical values of plastic strain rates for "slow" and "fast" loading rates. Later, these shall be compared with finite element computations.

Ductile crack extension proceeds by void nucleation and growth in the process zone. Toughness is controlled by void spacing which determines w_c, the critical size of the process zone. From equations (2) and (3) one can deduce J_{Ic} in terms of the critical process zone size

$$J_{Ic} = w_c \sigma_o/\beta d_n \approx 2\sigma_o w_c. \tag{15}$$

Changes in the yield stress, for constant values of w_c, will alter J_{Ic} according to

$$[(J_{Icb})/(J_{Ica})] = [K^2_{Icb}/K^2_{Ica}] = \sigma_{ob}/\sigma_{oa}. \tag{16}$$

The subscripts a and b in (16) refer to two different loading rates.

Experimental data is available from a number of sources[12-16] which relate the variation in K_{Ic} to the loading rate $\dot{K}_I$. Some of these data are plotted in Figure 2. Using the strain rate expression (9), and the yield stress data given in Refs.[12-16], comparisons are made between the changes in yield stress and the changes in K_I, as a function of K_I-rate. These comparisons are given in Table 2. Equation (16) suggests that the last two columns in Table 2 should have equal values. In fact, good agreement is achieved only for AISI 1018. The lack of agreement may have 2 sources. The first one is connected with the relative contribution of the flow stress in the plastic and process zones. The yield stress ratios in Table 2 are based on the strain rates in the plastic zone. Since the strain rates in the process zone are 10^2 to 10^3 times the values for the plastic zone, the yield stress ratios appropriate for the process zone would be larger for materials whose rate sensitivity increases with strain rate (see Figure 4b). Consequently, a significant contribution by the resistance to flow in the process zone could account for the greater rate sensitivity of the K_{Ic}-values of A533B and AISI 1020. The second source is the rate sensitivity of w_c, which is neglected by Equation (16). The increases in the flow stresses and normal stresses associated with the higher strain rates can facilitate void nucleation and reduce the void spacing and w_c. A large reduction in w_c in the face of the increase in σ_o could account for the relatively low K_{Ic}-ratios displayed by AISI 1018 and the PA-6 aluminum alloy.

The existing analyses do not clearly distinguish the relative contributions of the changes in the plastic and process zones. The fact that the rate of strain hardening (the value of n) influences

both δ and $w[5,11]$, when the large strains and hardening are largely
confined to the process zone, is evidence that the rate sensitivity
of flow in the process zone cannot be ignored. The finite element
calculations described in the following sections were undertaken to
illuminate this issue.

FINITE ELEMENT MODELLING

A stationary crack in a compact tension specimen has been
modelled using finite elements. Figure 3 shows a plot of the mesh.
To limit the complexity of the model, the elements nearest the crack
tip were sized to 1 mm. The mesh was composed of 8-noded isopara-
metric elements. Numerical studies by deLorenzi, Shih[19], Hoff
and Byrne[20] have shown that these elements are suitable for use
in the fully plastic range.

The model shown in Fig. 3 has 3500 degrees-of-freedom, and con-
sequently the analysis times for the elastic-plastic problem are
very long. As a preliminary step, the same mesh configuration was
used in an analysis employing 4-noded isoparametric elements,
which resulted in execution times of about one-tenth of the 8-noded
analysis. The 4-noded isoparametric elements tend to be too stiff
in the fully plastic range, as discussed in Ref. [19], and this
will be borne out in the results.

The mesh was constructed so that the stationary crack analysis
could later be extended into the advancing crack regime. The method
of crack extension, as implemented by Kanninen et al.[17], involves
the release of constraints at the crack tip. This technique gives
no "obvious" crack tip opening displacement for the stationary
crack problem. The authors have selected the separation of the
crack faces 1 mm away from the crack tip to be the CTOD, as shown
in Figure 6. A more refined approach could be effected by imposing
displacements on the boundary of a region very close to the
crack tip, as has been done by Sorensen[22].

An important feature of the analysis is the incorporation of
the strain rate dependence of the flow stress. Considerable
experimental data is available for A533B steel[23] as a result of
testing for nuclear applications. The uniaxial stress-strain curve
is given in Figure 4a[17], and corresponds to a nominal strain
rate of 10^{-3}/s. The relationship between the instantaneous flow
stress, $\bar{\sigma}$, and the plastic strain rate, $\dot{\epsilon}_p$, is given by the
Malvern[24] equation

$$\bar{\sigma}/\sigma_o = [\dot{\epsilon}_p/D]^{1/p} + 1. \tag{17}$$

The parameters D and p must be determined experimentally, and σ_o
is the flow stress at zero strain rate. Using the data in Ref.
[23] at 93C, the rate dependence relationship is plotted in Fig. 4b.

RESULTS

The mesh configuration and material model, described in the previous section, were incorporated in 6 analyses; 3 different loading rates were employed with 4-noded and 8-noded elements. Table 3 summarizes the analyses which have been conducted.

Analysis 1 is static using σ-ϵ relations for A533B for an infinitesimally slow rate of loading. A displacement is applied to the load point in increments of 0.2 mm until a maximum displacement of 2.4 mm is reached. The maximum equivalent stress intensity factor, K_J, is calculated from

$$K_J = [JE/(1-\nu^2)]^{1/2}. \tag{18}$$

Analysis 2 is a dynamic analysis. A constant velocity of 0.008 m/s is applied to the load point, until a displacement of 2.4 mm is reached. This results in an almost constant K-rate, but not a constant J-rate.

Analysis 3 is also a dynamic analysis. A constant velocity of 0.8 m/s (100 times faster than Analysis 2) is applied to the load point. Previous studies using 8.0 m/s as a loading rate had been attempted, but the inertia of the model caused unwanted vibrations which made the interpretation of results very difficult.

Results for the static analysis are plotted in Figure 5. Fig. 5a shows a dimensionless J-integral as a function of a dimensionless load line displacement. A comparison with experimental results by Andrews and Shih[25] reveal that the numerically determined J-integral values are low. Figure 5b shows a dimensionless crack tip opening displacement as a function of a different dimensionless load line displacement. Results from the present study are again smaller than the experimental results of [25]. However, the finite element results of this study are in good agreement with the finite element results of Shih[18]. Equation (3) suggests that δ varies linearly with the J-integral. Fig. 7 plots this relationship and shows remarkable agreement with the static finite element results. The degree of agreement could be fortuitous since the definition of δ is somewhat arbitrary, but is does suggest that the definition of δ in Fig. 6 is reasonable.

The plastic strains in the crack tip vicinity are of interest since they essentially determine the plastic strain rates in a dynamic analysis. The magnitude of the plastic strain, as expressed by tensor product

$$\epsilon_p = [(3/2)\epsilon^P_{ij}:\epsilon^P_{ij}]^{1/2}, \tag{19}$$

is shown in Figure 8, as well as a comparison with the J-field

solution of equation (10) at an angle of 45°. Also shown in Figure 8 are results from the slip line solution of Rice and Johnson[26], which were later duplicated by McMeeking[11] using finite elements, for a blunt notch. A comparison shows that the present finite element results underpredict the plastic strains within a region of about 3δ from the crack tip. This is not surprising since the mesh is not sufficiently fine to capture this large strain gradient. It follows that the present finite element analysis only shows the effects of plastic strain rate in the plastic zone, and it is not refined enough to show the effects of plastic strain rate in the process zone.

The effect of loading rate is apparent in Fig. 9. If a critical value of crack tip opening displacement is chosen as a failure criterion, then higher values of J can be tolerated at higher loading rates. In fact, for the range of strain rates occurring in the plastic zone, as given in equation (9), the "average" increases in yield stress would be 11% and 21%, as given by the Malvern equation (17). In view of equation (16) one would expect equal increases in J-integral over this range. Fig. 9 shows that the J-integral values increase by 14% and 26% for a CTOD of 0.28 mm. Although the agreement between the two predictions of yield stress increase looks good, it is possible that, even at these relatively low loading rates the inertia of the specimen may have some effect on the CTOD. Therefore, it may be desirable, in future analysis, to attempt to separate the effects of inertia and strain rate sensitivity on the crack tip opening displacement.

The equivalent plastic strain rate is given in Fig. 10. Results are plotted for θ = 45°, since at this angle, the plastic strains are larger and comparisons are more obvious. Equation (10) can be differentiated with respect to time (at θ = 45°) in the same sense that equation (11) was derived. Values of the equivalent strain rate from the J-field, in Fig. 10, are in reasonable agreement with dynamic finite element results. Differences increase as the plastic strains become small, since the J-field is only valid where the elastic strains can be neglected. Here again, the J-field solution is only valid over a very small region.

CONCLUSIONS

1) The loading rate sensitivity of the fracture toughness for the ductile, fibrous mode, as expressed by J_{Ic}, should correspond with the rate sensitivity of the flow stress in the plastic and process zones, when the critical crack tip opening displacement is fixed.

2) The 1 mm, 8-noded finite element mesh used to model the region near the crack tip describes the plastic zone, but is not

sufficiently refined for an adequate representation of the process zone of A533B steel at the $J_I = 250$ KJ/m^2 level.

3) Numerical results obtained with the finite element model confirm that in the absence of a process zone, the increase of J_I with loading rate at constant CTOD corresponds closely with the increase in the flow stress in the plastic zone.

4) Experimental measurements reported in the literature, contain examples of J_{Ic}-values with a greater rate sensitivity, and values which are less rate sensitive than the flow stress in the plastic zone. These cases are associated with either the 10^2- to 10^3-fold higher strain rates generated in the process zone, or the possible negative rate depending on the void spacing.

5) Values of the equivalent (total) strain rate in the plastic zone derived from the J-field agree with equivalent plastic strain rate values from the finite element model in the range $36 < r < 0.5 \ r_o$.

ACKNOWLEDGEMENTS

TABLE 1: Estimates of Plastic Strain Rates

Loading Rate	$\dot{J}_I$ [kJ·m^{-2}·s^{-1}]	$\dot{K}_I$ [MPa·m$^{1/2}$·s^{-1}]	$\dot{\epsilon}_p$ [s^{-1}] Plastic Zone	$\dot{\epsilon}_p$ [s^{-1}] Process Zone
Slow	2	1	3×10^{-5}	4×10^{-3}
Fast	2×10^5	10^5	3	400

Tabulated values are for a ductile steel such as A533B.
$J_{Ic} = 180$kJ/m^2; $K_{Ic} = 200$ MPa·m$^{1/2}$

Alloy	Ref.	K_I-Range $[\text{MPa}\cdot\text{m}^{1/2}\cdot\text{s}^{-1}]$	$\dot{\epsilon}_p$-Range $[\text{s}^{-1}]$	$[\sigma_{ob}/\sigma_{oa}]^{1/2}$	K_{Icb}/K_{Ica}
A533B(@177C)	12,13	$2\text{-}2\times10^5$	$5\times10^{-5}\text{-}5$	1.09	1.60
AISI 1020(HR)	14	$1\text{-}2\times10^6$	$6\times10^{-5}\text{-}80$	1.36	1.65
AISI 1018(CR)	15	$1\text{-}2\times10^6$	$4\times10^{-5}\text{-}80$	1.14	1.08
PA6 Aluminum	16	$0.5\text{-}2\times10^6$	$6\times10^{-5}\text{-}350$	1.14	0.66

Subscript a refers to the lowest strain rate and b refers to the highest rate.

TABLE 3: Summary of Finite Element Analyses

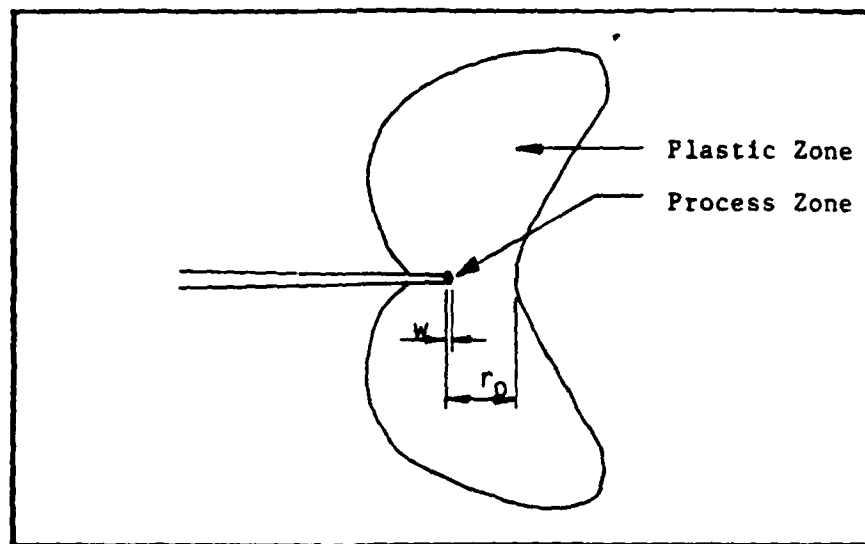| Analysis Number	Analysis Type	$\dot{v}_L$ [m/s]	v_{Lmax} [mm]	J_{Imax} [kJ/m^2]	K_{Jmax} [MPa·m$^{1/2}$]	$\dot{K}_J$ [MPa·m$^{1/2}$/s]
1	Static	0.0	2.4	245	230	0
2	Dynamic	0.008	2.4	254	235	689
3	Dynamic	0.8	2.4	260	238	71000

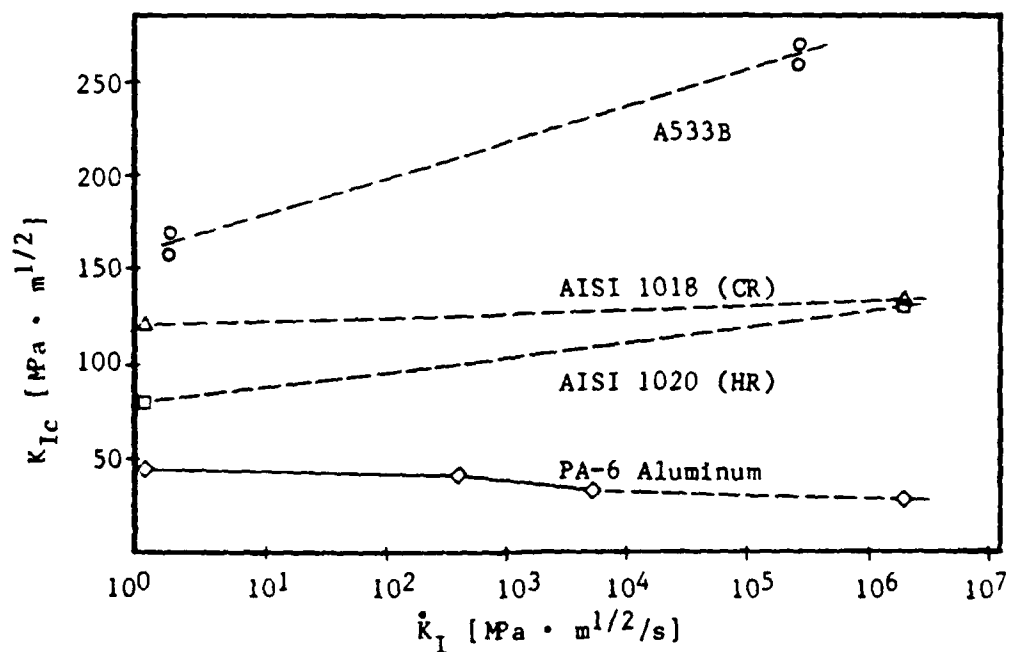Figure 1: Plastic and process zones in the vicinity of a crack.

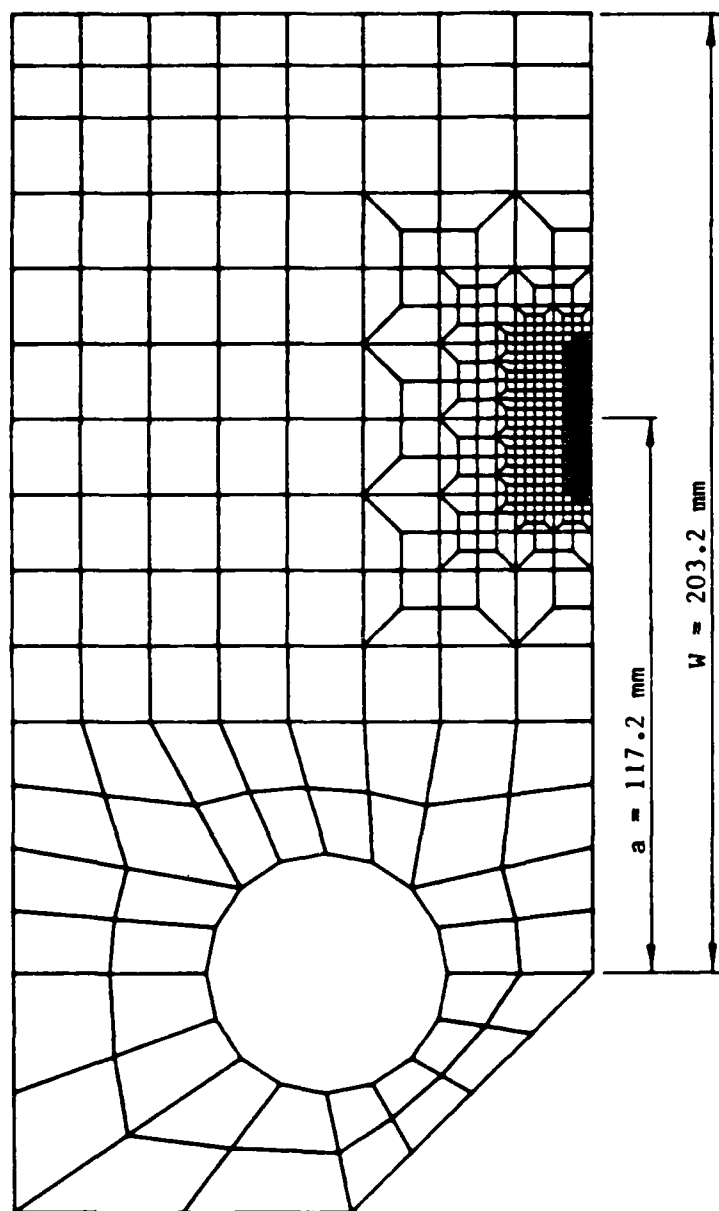Figure 2: Variation of K_{Ic} with K_I-rate for different materials for ductile, fibrous crack extension.

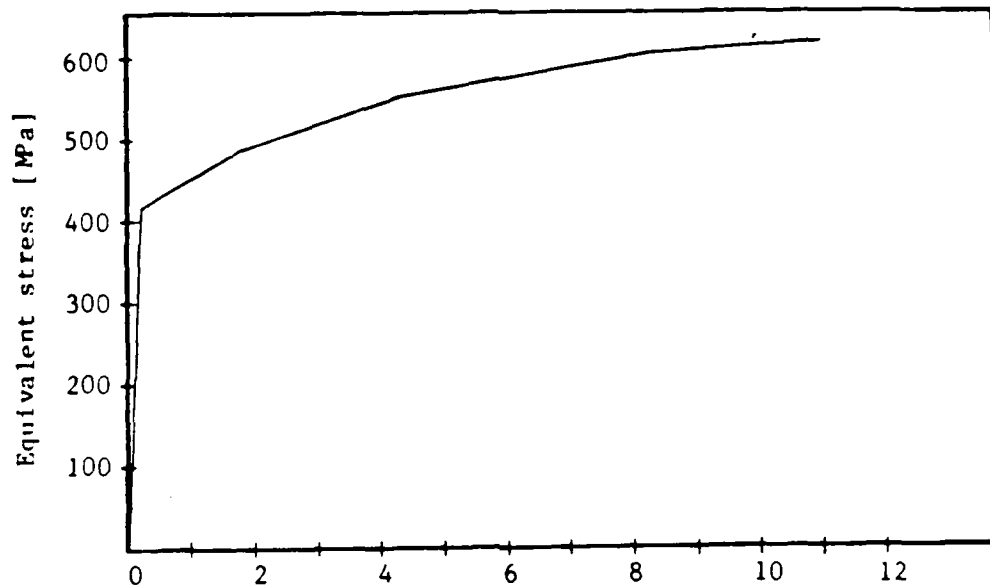Figure 3: Finite element model of compact tension specimen.

a = 117.2 mm

W = 203.2 mm

Figure 4a: Uniaxial stress-strain curve for A533B @ 93C.

$$\sigma_o = 386.57 \text{ MPa}$$
$$D = 66170.$$
$$p = 6.9$$

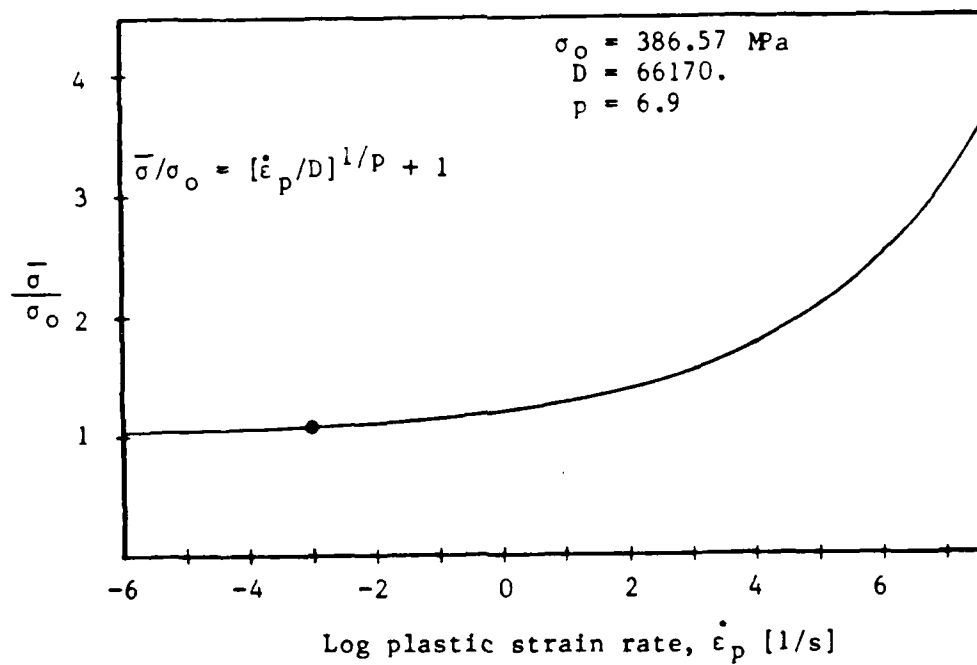$$\overline{\sigma}/\sigma_o = [\dot{\varepsilon}_p/D]^{1/p} + 1$$

Figure 4b: Variation of flow stress with plastic strain rate, for A533B @ 93C.
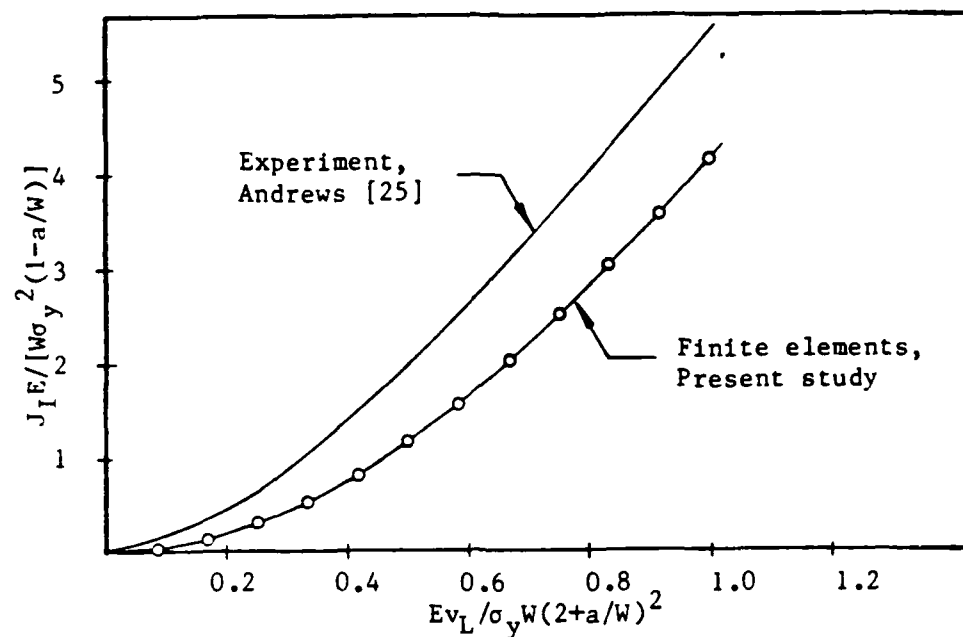
Figure 5a: Variation of the J-integral with
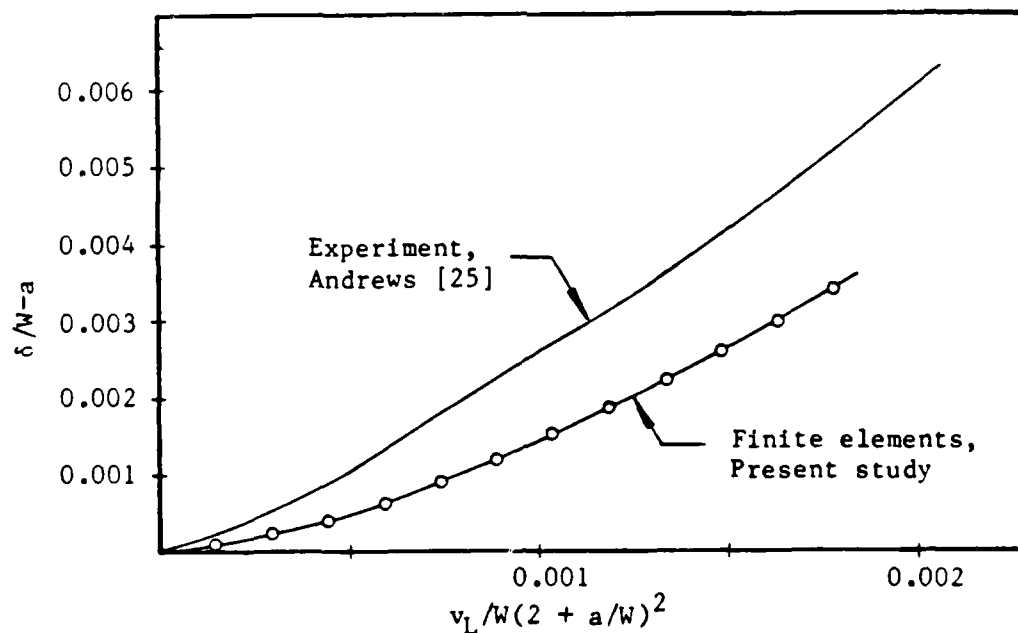load line displacement for the
static analysis.

Figure 5b: Variation of crack tip opening displacement
with load line displacement for the static
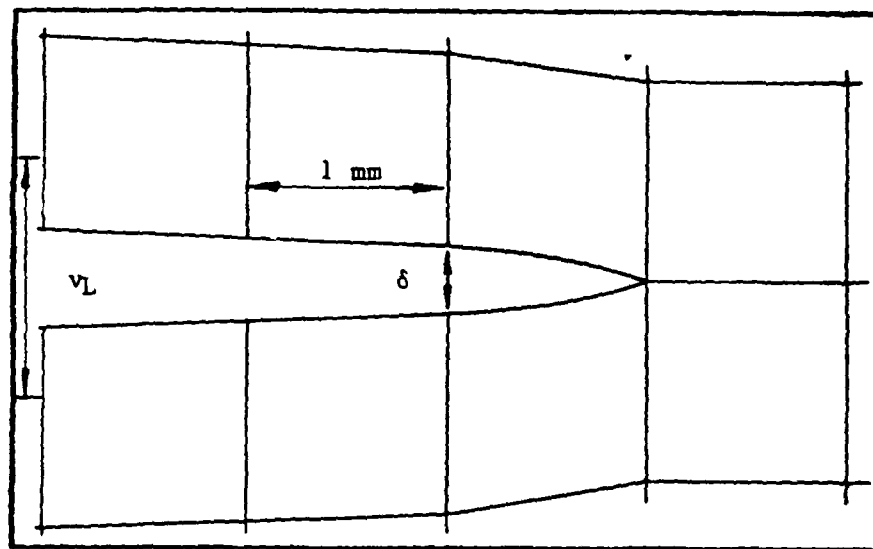analysis.

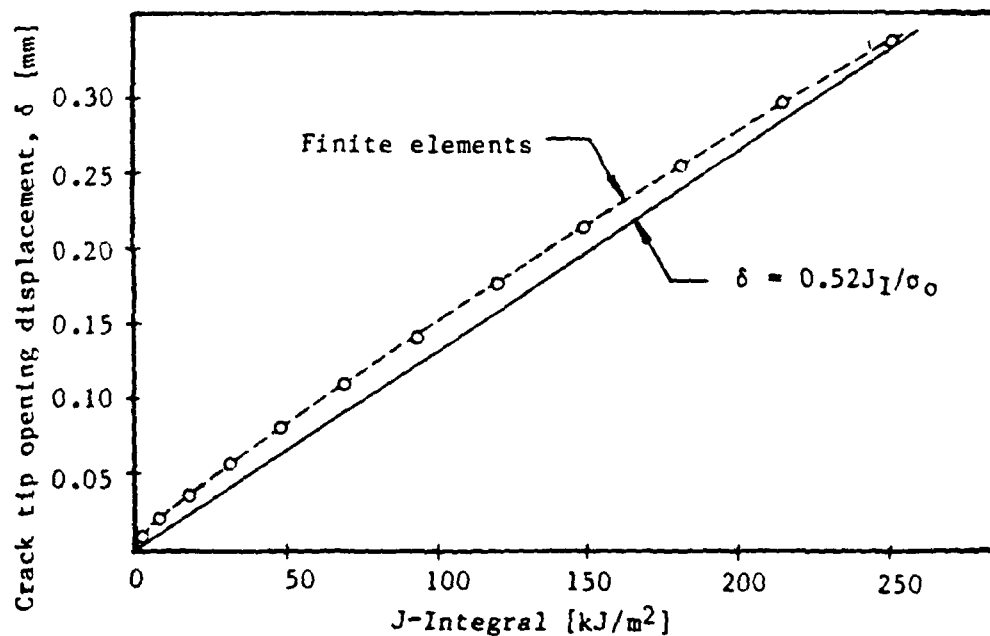Figure 6: Details of crack tip mesh, showing crack tip opening displacement, δ.

Figure 7: Relationship between crack tip opening displacement and J-integral for a static finite element analysis for A533B @ 93C.
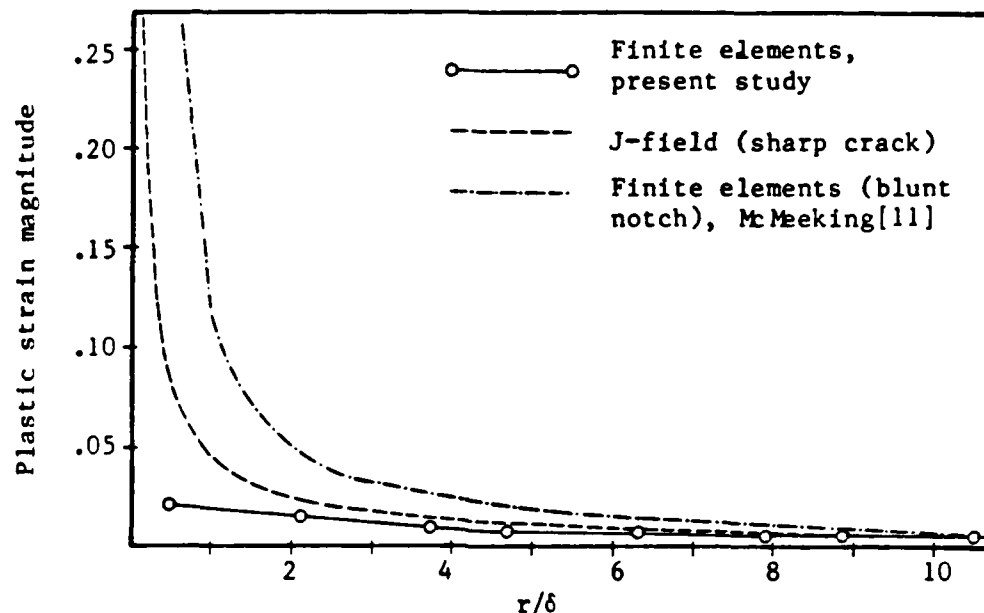
Figure 8: Variation of plastic strains with distance
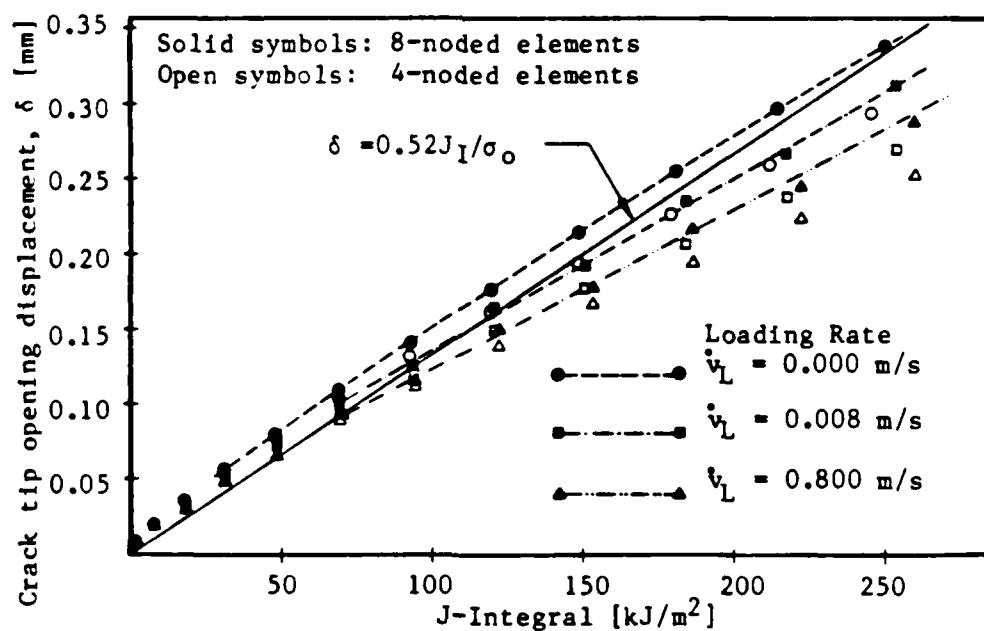from the crack tip @ θ = 45°.

Figure 9: Relationship between crack tip opening
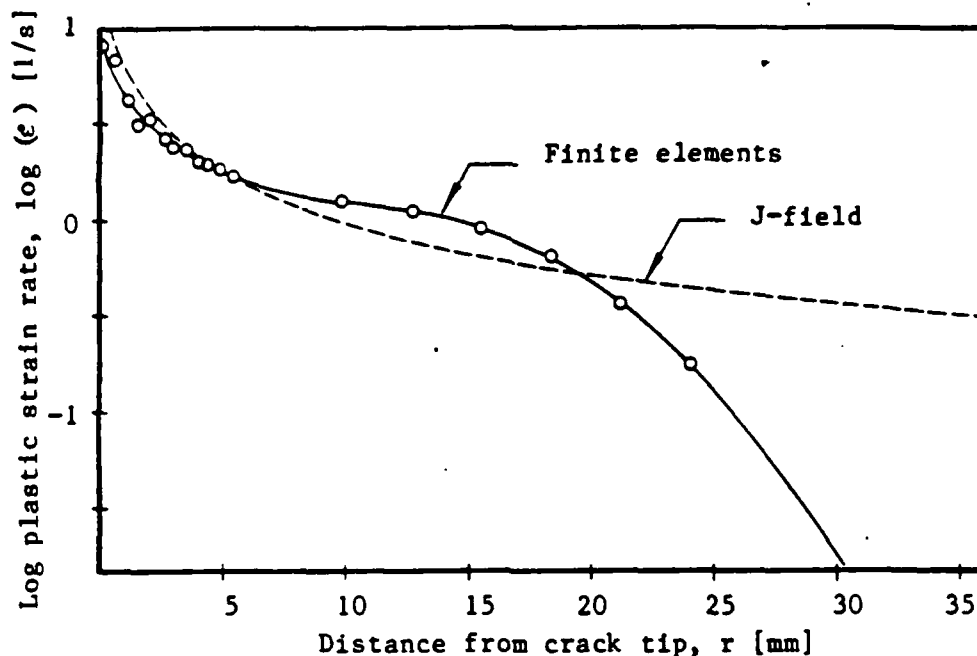displacement and J-integral for statically
and dynamically loaded analyses.

Figure 10: Relationship between plastic strain rate and distance from crack tip for $\theta = 45°$, $\dot{v}_L = 0.8$ m/s and $J_I = 245$ kJ/m^2.

1. G. T. Hahn, and C. A. Rubin, Analysis of Crack Arrest Toughness Measurement Procedures for Ship Hull Design, Vanderbilt University Proposal to Office of Naval Research, Nashville (1982).

2. N. Levy, P. V. Marcal, W. J. Ostergren, and J. R. Rice, Small Scale Yielding Near a Crack in Plane Strain: A Finite Element Analysis, Int. J. of Frac. Mech., 7:143 (1971).

3. J. R. Rice, A Path Independent Integral and the Approximate Analysis of Strain Concentration by Notches and Cracks, J. of Appl. Mech., 35:379 (1968).

4. P. C. Paris, Fracture Mechanics in the Elastic-Plastic Regimes in: "Flaw Growth and Fracture, ASTM STP 631", American Society for Testing and Materials, Philadelphia (1977).

5. C. F. Shih, W. R. Andrews, M. D. German, R. H. VanStone and J. P. D. Wilkinson, "Methodology for Plastic Fracture, EPRI Contract RP 601-2, Combined Seventh and Eighth Quarterly Report", General Electric, Schenectady, N.Y. (1978).

6. W. Ramberg and W. R. Osgood, NACA TN 902 (1943).

7. J. W. Hutchinson, Singular Behaviour at the End of a Tensile Crack in a Hardening Material, J. Mech. Phys. Solids, 16:13 (1968).

8. J. R. Rice and G. F. Rosengren, Plane Strain Deformation Near a Crack Tip in a Power-Law Hardening Material, J. Mech. Phys. Solids, 16:1 (1968).

9. C. F. Shih, "Elastic Plastic Analysis of Combined Mode Crack Problems", Ph.D. Thesis, Harvard University (1973).

10. V. Kumar, M. D. German, and C. F. Shih, "An Engineering Approach for Elastic-Plastic Fracture Analysis, EPRI NP-1931", Electric Power Research Institute, Palo Alto, Ca. (1981).

11. R. M. McMeeking, "Finite Deformation Analysis of Crack Tip Openings in Elastic-Plastic Materials and Implications for Fracture Initiation", Brown University Report COO-3084/44, Providence, R.I. (1976).

12. W. L. Server, Static and Dynamic Fibrous Initiation Toughness Results for Nine Pressure Vessel Materials, in: "Elastic-Plastic Fracture, ASTM STP 668", American Society for Testing and Materials, Philadelphia (1979).

13. W. L. Server, W. Oldfield, and R. A. Wullaert, "Experimental and Statistical Requirements for Developing a Well-Defined K_{IR} Curve", EPRI NP-372, Electric Power Research Institute (1977).

14. M. L. Wilson, R. H. Hawley, and J. Duffy, The Effect of Loading Rate and Temperature on Fracture Initiation in 1020 Hot-Rolled Steel, Eng. Frac. Mech., 13:371 (1980).

15. L. S. Costin, The Effect of Loading Rate and Temperature on the Initiation of Fracture in a Mild Rate-Sensitive Steel, J. Eng. Mat. Tech., 101: 258 (1979).

16. J. Klepaczko, Application of the Split Hopkinson Pressure Bar to Fracture Dynamics, Inst. Phys. Conf., 47:201 (1979).

17. M. F. Kanninen, E. F. Rybicki, R. B. Stonesifer, D. Broek, A. R. Rosenfield, C. W. Marschall, and G. T. Hahn, Elastic-Plastic Fracture Mechanics for Two-Dimensional Stable Crack Growth and Instability Problems, in: "Elastic-Plastic Fracture, ASTM STP 668", American Society for Testing And Materials, Philadelphia (1979).

18. C. F. Shih, H. G. deLorenzi, and W. R. Andrews, Studies on Crack Initiation and Stable Crack Growth, in: "Elastic-Plastic Fracture, ASTM STP 668", American Society for Testing and Materials, Philadelphia, (1979).

19. H. G. deLorenzi, and C. F. Shih, Int. J. of Frac. Mech., 13:507 (1977).

20. R. Hoff and T. P. Byrne, "Residual Stress Analysis - A Comparison of Finite Element Results with Closed-Form Solutions", Ontario Hydro Research Div. Report 81-232-K, Toronto, Ont. (1981).

21. R. S. Barsoum, Int. J. Num. Meth. Eng., 11:85 (1977).

22. E. P. Sorensen, A Numerical Investigation of Plane Strain Stable Crack Growth Under Small-Scale Yielding Conditions, in: "Elastic-Plastic Fracture, ASTM STP 668", American Society for Testing and Materials, Philadelphia, (1979).

23. R. O. Ritchie, W. L. Server, and R. A. Wullaert, Critical Fracture Stress and Fracture Strain Models for the Prediction of Lower and Upper Shelf Toughness in Nuclear Pressure Vessel Steels, Met. Trans. A, 10A:1557 (1979).

24. L. E. Malvern, Experimental Studies of Strain Rate Effects and Plastic Annealed Aluminum, in: "Proc. ASME Coll. on Behavior of Materials under Dynamic Loading", :81 (1965).

25. W. R. Andrews and C. F. Shih, Thickness and Side Groove Effects on J- and δ-Resistance Curves for A533-B Steel at 93°C, in: "Elastic-Plastic Fracture, ASTM STP 668", American Society for Testing and Materials, Philadelphia, (1979).

26. J. R. Rice and M. A. Johnson, in: "Inelastic Behavior of Solids", Ed. by M. F. Kanninen, W. F. Adler, A. R. Rosenfield, and R. I. Jaffee, McGraw-Hill, New York, :641 (1970).

The Influence of Microstructure on Brittle Fracture Toughness

G. T. HAHN

This lecture presents viewpoints of the role of microstructure in brittle fracture that have emerged in the past two decades. The fracture mechanics concept of crack arrest is inserted into the Griffith theory of microcracks to describe the resistance of microstructural boundaries. The implications of crack blunting are related to the essential role of carbide particles and other brittle phases in the steel. Dislocation pile-ups and the ferrite grain size are accorded a diminished role. The brittle fracture stress is related to the dimension of the largest "eligible" parent particle and the resistance experienced when the advancing microcrack crosses the boundary. "Eligibility" is connected with the probabilities of nucleating a crack and finding a boundary with minimal resistance. The boundaries of carbide particles, carbide films at the grain boundaries, brittle inclusion particles, ferrite grains, pearlite colonies, and bainite packets are possible barriers. The use of the growing data base of Griffith energy values — or equivalently, the local arrest toughness value — to identify controlling microstructural features is demonstrated. The lecture touches on the relation between the transition temperature and the brittle fracture stress and draws attention to the latter's dependence on the size of the stressed volume. Finally, the role of the stressed volume in analyses of the brittle fracture K_{Ic}-value and a statistical treatment that clarifies its origin are discussed. These analyses indicate that a small number of the largest particles may have disproportionate influence on K_{Ic}, and that the microstructural features that effect "eligibility" may have a modest effect on K_{Ic}.

G T HAHN, a native of Vienna. Austria. came to this country at the age of 8 He received his primary and secondary schooling in Manhattan and at the Brooklyn Technical High School He studied mechanical engineering at New York University (B M E , 1952) and metallurgy at Columbia University (M S , 1955) and the Massachussets Institute of Technology (Sc D , 1959).

In 1951 and 1952 he worked for short periods of time for the NYU Research Division and the Westinghouse Research Laboratories From 1953 to 1955 he served in the Titanium Section of the Air Force Material Laboratory In 1960, after graduate studies and a 1-year post doctorate at M I T , he assumed a research position at Battelle's Columbus Laboratories where he headed the Metal Science Group from 1966 to 1979 This period also included brief assignments with Battelle's Geneva Research Center (1963) and the Argentine Atomic Energy Commission (1970) In 1979 he moved to Vanderbilt University as Professor of Metallurgical Engineering

His research interests center on fracture At Battelle he pursued basic studies for sponsors concerned about the integrity of ships, line-pipe airframes, and nuclear pressure vessels His current research includes studies of rolling contact failure, crack arrest in tough steels, the mechanisms limiting sheet formability, and the strength of aluminum weldments He has edited several conference proceedings and is the author of over 120 papers and articles Professor Hahn is a Fellow of the ASM (1980), a member of Pi Tau Sigma, Tau Beta Pi, Alpha Sigma Mu, Sigma Xi and remains active in AIME, ASM, and ASTM

I. INTRODUCTION

I want to thank the ASM for the privilege of presenting the Edward DeMille Campbell Lecture. This lecture provides a few moments to dwell on a life that is conventional and inspiring.[1,2,3] Campbell was a professor of metallurgy, chemistry, and chemical engineering at the University of Michigan from 1890 to 1925. He was director of the University's Chemical Laboratory. He was a productive researcher — the author of 75 technical papers[3] — with pioneering work on the interpretation of the X-ray diffraction patterns of martensite to his credit. At the same time, he and his wife Jennie Ives raised and educated six children. In these respects, Campbell's life is not unlike that of many other distinguished members of the society.

What makes his life entirely unique is that Campbell was blind — blinded at the age of 28 in a laboratory accident. Campbell fathered children, taught metallurgy and chemistry, administered a laboratory, unraveled X-ray patterns, and published all but three of his papers *after* he became blind. Campbell's productive life reveals the enormous reserve of inner strength — the "toughness" of the human spirit — that resides in us. Fortified with that spirit we can overcome our share of tragedy, jettison our disappointments, and meet the challenges of our time.

Like the "toughness" of the human spirit, brittle fracture and the toughness of steel are fundamental issues that have engaged many people for a long time. Reports of brittle fracture in service appeared as early as 1879,[4] the Charpy test in 1905. Current explanations of brittle fracture and the ductile-to-brittle transition have their roots in papers published by Griffith[5] and Ludwik[6] in 1920 and 1921. The actual observations of Griffith cracks[7-12] led to the development of detailed mechanistic treatments[13-16] in the decade from about 1953 to 1963.

In the two decades that have followed, mechanistic studies have been extended to spherodized carbide,[17-20] pearlitic,[21-24] bainitic,[25-29] and martensitic[25,29,30] microstructures. McMahon and his collaborators[31,32] have shown that except for the crack path, the mechanisms of intergranular fracture of temper embrittled steels and transcrystalline (cleavage) fracture are nearly indistinguishable (Figure 2.3 and Figure 2.6). Knott and his collaborators[33] have linked the micromechanism and the statistics of particles[20] with the macroscopic fracture toughness. In addition, progress has been made in analyzing toughness on the atomic scale.[34,35,36]

Today, brittle fracture problems still exist and important questions remain unanswered. For example, ways of modifying the operation of existing nuclear plants are currently being sought to avoid brittle fracture. Toughness specifications for bridge steels are controversial.[37] The two common measures of toughness — the CVN-energy used in material specifications and the K_{Ic}-value used in design — resist correlation.[38] The microstructural features governing brittle fracture are not well defined for many steels. Even the inherent toughness of unalloyed ferrite in the absence of carbides and other particles is an open question.

I acquired an enduring interest in this subject in 1953 from Maxwell Gensamer[39] who faced ship plate fracture problems in World War II. Since that time, graduate studies at MIT and a succession of fracture prevention projects for gas pipes, rocket casings, and nuclear components have enabled me to view the field from time to time. The invitation to prepare this lecture was an opportunity for me to examine recent work and to reflect on how the views of microstructural involvement have changed since my introduction in 1953. What follows reflects my limited comprehension of the vast literature of this field — for example, Kotilaininen[4] alone cites over 400 references in a recent dissertation on brittle fracture of bainitic steels. I apologize to both readers and contributors for the omissions.

II. MECHANISMS OF BRITTLE FRACTURE

Metallographic observations of cleavage microcracks in mild steels were the key that led to detailed mechanistic treatments in the period 1953 to 1963. The work of Allen, Rees, Hopkins, and Tipler,[7] Low,[8,9] and the group at MIT[10,11,12] revealed Griffith-like cracks form after the onset of yielding[9,10] and span individual ferrite grains and carbide films at the grain boundaries (see Figure 1). The association with yielding made it possible to connect nucleation of the cracks with dislocation pile-ups as proposed by Zener in 1948[13] and elaborated on by Stroh[14] and Petch[15] (see Figure 2.1). All that was needed to make the Griffith theory[5] meaningful was to suppose that more fracture energy is spent disrupting the lattice when the microcrack crosses a grain boundary than in the grain interior. Consistent with this, estimates of the Griffith fracture energy term γ are $\sim 10\times$ larger than γ', the specific surface energy, which is a rough measure of γ in the interior of a crystal (see Table I). In fact, grain boundaries must offer a range of γ-values depending on the misorientation. Since fracture is associated with the first boundary crossed successfully, the weakest link and, consequently, a boundary with a relatively low γ-value will be controlling.

Subtleties of the problem and the application of the Griffith Theory are more easily discussed with the language of LEFM (Linear Elastic Fracture Mechanics). Since the grain boundary region is presented with an advancing (rather than a stationary) microcrack, fracture occurs when the microcrack fails to arrest. For this reason, I believe the Griffith energy term γ is properly viewed as an arrest toughness parameter[44] in this case. $G_c^B = 2\gamma$ and $K_c^B = [2E\gamma/(1 - \nu^2)]^{1/2}$, where E and ν are the elastic modulus and Poisson's ratio (see Table I). The superscript B is added to emphasize that G_c^B and K_c^B apply to a relatively smooth, microscopic crack crossing a boundary offering minimal resistance. As illustrated in Table I, K_c^B values are much lower than the conventional crack arrest toughness, $K_{Ia} \sim 50$ MPa$\sqrt{m}$, which applies to a rough macrocrack that is overcoming all the boundaries in its path as well as ductile ligaments.[46] The LEFM-form of the Griffith theory expresses σ_f, the brittle, cleavage, or transgranular-fracture stress in terms of $2a$, the (micro) crack size, β, a crack shape factor, and K_c^B:

$$\sigma_f = K_c^B / (\beta\sqrt{\pi a}) \tag{1a}$$

and more specifically,

$$\sigma_f = 1.25\, K_c^B\, d^{-1/2} \tag{1b}$$

$$\sigma_f = 0.798\, K_c^B\, c^{-1/2} \tag{1c}$$

where d is the diameter of a penny-shaped crack and c the total length of a crack whose depth is much greater than its length. Since the microcrack is generated after the
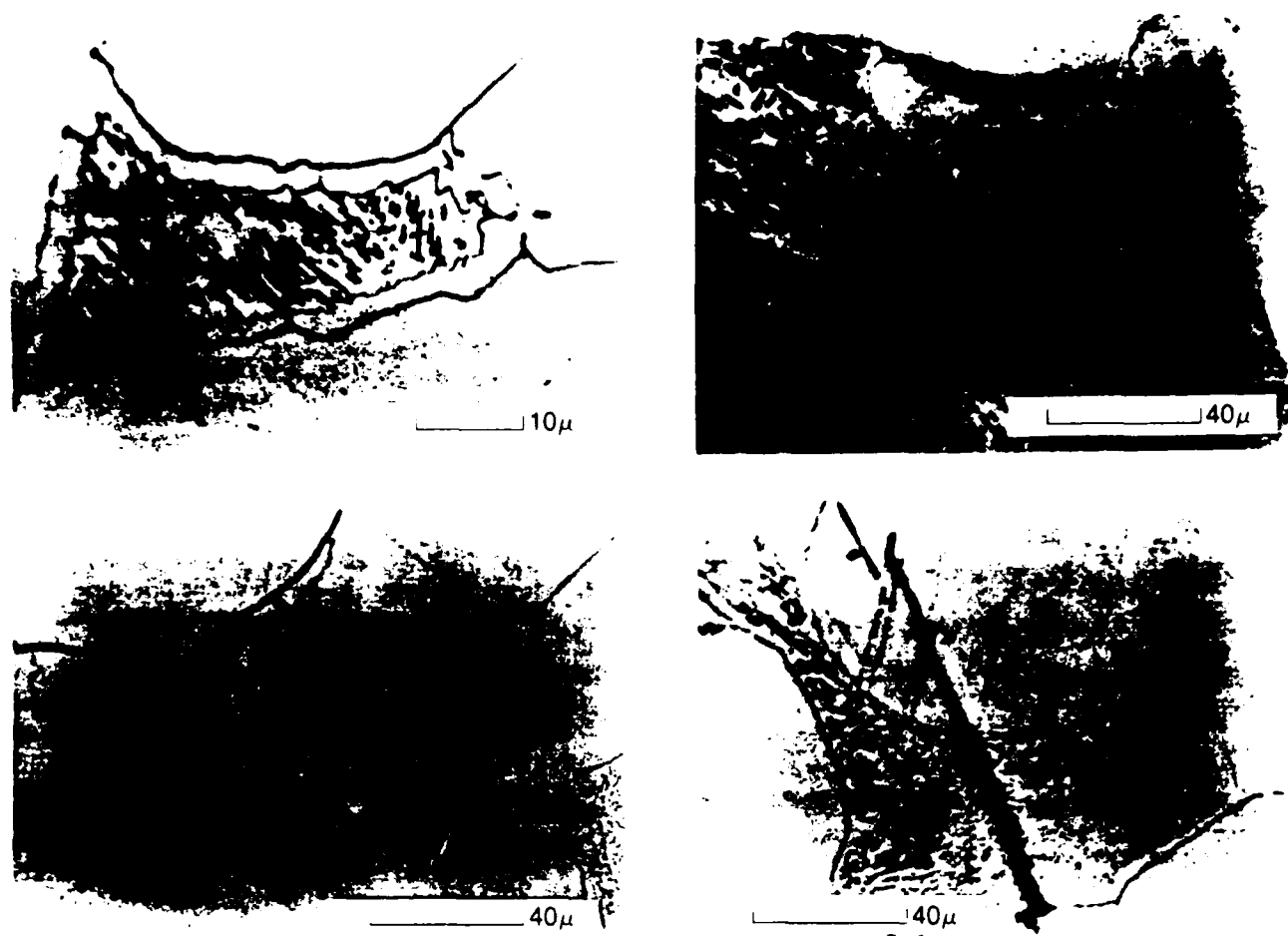
Fig. 1 — Examples of microcracks observed in a mild steel by Allen, Rees, Hopkins, and Tipler.

Table I. Summary of Microcrack and Macrocrack Resistance Values in Terms of γ, K^R_{1a}, K_{1a}, and K_{1c}

Materials (Reference)	γ Jm^{-2}	K^R_{1a} MPa $\sqrt{m}$	K_{1a} MPa $\sqrt{m}$	K_{1c} MPa $\sqrt{m}$
MgO — single crystal	1.5	—	—	0.9
Al$_2$O$_3$ — single crystal	6.0	—	—	2.3
Brittle Fe — single crystal	2.0*	—	0.9*	0.9*
MgO — bicrystal	15 to 100	—	—	2.9 to 7.4
Steel at a ferrite-ferrite grain boundary	56	5.0	—	—
Steel at a carbide-ferrite boundary	14	2.5	—	—
MgO — polycrystal	14	—	—	2.8
Al$_2$O$_3$ — polycrystal	10 to 40	—	—	2.9 to 5.9
Commercial grades of steel	—	—	~50	—

*Estimated assuming $\gamma = \gamma' = \mu b/10$ where γ is the specific surface energy, μ is the shear modulus, and b is the Burgers vector

onset of yielding, the probity of applying LEFM must be questioned. The use of Eq. [1] can be justified provided the nucleated crack advances rapidly and tests the condition for extension in a time duration too short for significant yielding of the ferrite. Dynamic contributions to Eq. [1] may also be negligible since little kinetic energy is reflected back to the microcrack from the far boundaries.

The theory connects fracture resistance with the microstructure because the critical microcrack dimensions correspond with either the carbide film thickness (c_0) or the ferrite grain diameter (d). This was demonstrated by Allen and coworkers and by Low. The 1953 Allen et al. paper shows that the refinement of carbide films by manganese additions is accompanied by a systematic lowering of the transition
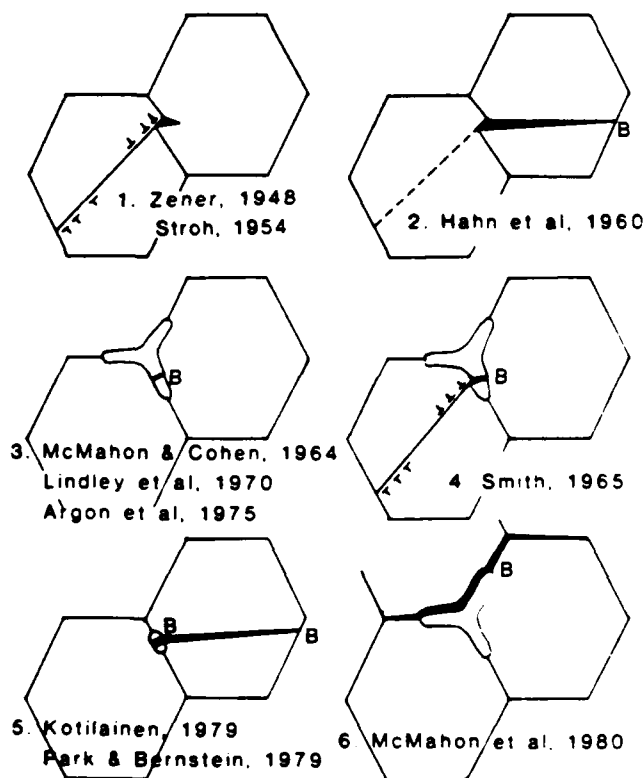
MECHANISMS OF BRITTLE FRACTURE

Fig. 2 — Schematic representations of the mechanisms of brittle fracture according to various authors.[11,14,16,24,33,40,62,63] The letter B identifies barriers to crack extension.

temperature; Low demonstrated that the brittle fracture stress varies linearly with $d^{-0.5}$.

At first, the dislocation pile-up was considered only in the nucleation stage and not in the analysis of the fracture condition, *i.e.*, microcrack extension across a boundary as in Figures 2.2 and 2.3. This was changed by the painstaking metallographic studies of McMahon and Cohen[12] which revealed that the large microcracks observed in the ferrite grains were invariably connected with a cleaved carbide particle located somewhere in the grain or on the surrounding boundary. Their findings imply that the rupture of the carbide is an essential, intermediate event between the formation of the pile-up and the cleavage of the ferrite. Accordingly, Smith[16] and Almond, Timbres and Embury[17] formulated models in which the pile-up continues to contribute to the crack driving force after the carbide crack nucleates (Figure 2.4). Accordingly, the expression for σ_f, the fracture stress for microcrack extension across the carbide ferrite boundary, contains a term arising from the carbide film and one from the pile-up:[16]

$$\sigma_f = \left\{\frac{2}{\pi}\frac{(K_{lc}^B)^2}{c_0} - \left[\tau_{eff}\left(\frac{d}{c_0}\right)^{0.5} - \frac{4\tau}{\pi}\right]^2\right\}^{1/2} \quad [2]$$

    carbide film   pile-up

The terms τ_{eff} and τ_f are the effective shear stress and the lattice friction stress, respectively. Equation [2] involves two microstructural dimensions: (i) the dislocation pile-up size which is equated with d, the ferrite grain diameter; and

(ii) the carbide film thickness, c_0. These analyses seem to ascribe a more central role to the carbide and reinforce the then prevalent view that the refinement of both the grain size and carbide dimensions enhance toughness. However, neither Smith nor Almond *et al.* really explain why the carbide is essential to the nucleation process.*

---

*The carbide particle is not an essential part of the fracture condition since c_0 is replaced by d when the grain-size ferrite microcracks are observed

---

III. CRACK BLUNTING AND THE ESSENTIAL ROLE OF HARD PARTICLES

The distinction between the static and dynamic aspects of the fracture mechanism also has a bearing on the transition temperature and the role of carbides. Rice and Thomson[34] have treated the origins of toughness in crystals and conclude that iron is brittle at temperatures close to 0 K and crack resistant at higher temperatures. The brittle behavior arises when bonds rupture before dislocations can form to blunt the crack; the tough response when the crack blunts before the bonds rupture. Results of a recent computer simulation of a crack tip in an atomistic iron lattice at 0 K and 400 K performed by Mullins and Dokainish[36] are in accord with this view. The temperature at which an iron crystal containing a stationary crack changes its behavior from brittle to tough — $TT(K_{lc})$, the K_{lc}-transition temperature — is not well-defined by these analyses and, to my knowledge, has not been measured experimentally. The $TT(K_{lc})$ for Fe-3 Si single crystals, about -100 °C, can be deduced from the work of Pilkington and Hull[46] (see Figure 3). Since Fe-3 Si is in many respects more brittle than unalloyed ferrite, the $TT(K_{lc})$ for ferrite crystals must fall below -100 °C and probably below -200 °C.

The response of a crystal to a rapidly advancing crack, characterized by K_{la}, differs from that for a stationary crack because there is less time for thermally assisted generation of dislocations near the crack tip. The time available for blunting a slowly loaded stationary crack is $t \sim 10$ seconds
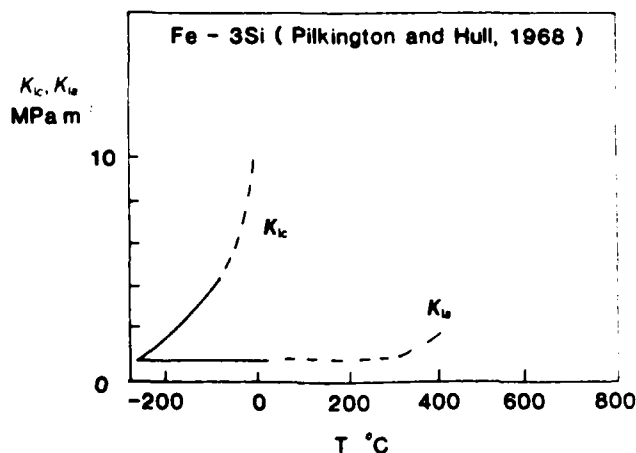

Fig. 3 — The K_{lc}-transition for Fe-3 Si single crystals with stationary cracks after Pilkington and Hull[46] and an estimate of the corresponding K_{la}-transition for cracks propagating with a velocity $a = 100$ m/s based on the theoretical model of Jokl, Vitek, and McMahon.[33] The dashed portions are based on the extrapolation of the measured K_{lc}-curve

In contrast, the time available to blunt a brittle crack advancing with a velocity of $a = 100$ ms^{-1} is $t \sim 10b/a = 2 \cdot 10^{-11}$ s ($10b$ represents the extent of the highly stressed tip region capable of generating dislocations and $b = 0.2$ nm is the Burgers vector). The approximate 10^{12}-fold reduction in the available time produces a $\sim 10^2$-fold reduction in the dislocation contribution to K_{1a} according to the theoretical model of Jokl, Vitek, and McMahon.[35] This means that K_{1a}-values for Fe-3 Si crystals remain at the 1 MPa$\sqrt{m}$ level displayed by K_1 below the transition for temperatures up to about 100 °C and possibly higher (see Figure 3). In other words, the $TT(K_{1a})$ for Fe-3 Si crystals occurs above 100 °C. The same reasoning applies to microcracks in the vicinity of grain boundaries although the relevant K_{1a}^B-values are likely to be higher than K_{1a} for the single crystal.

Several other observations support the view that K_{1a}^B-values for both Fe-3 Si and unalloyed ferrite reflect temperature independent brittle behavior to temperatures above ~ 100 °C. For example, the constancy of the brittle fracture stress of Fe-3 Si in the range -200 °C to at least $+50$ °C. reported by Griffith and Owen[48] (see Figure 4), taken together with Eq. [1] shows that K_{1a}^B must also be constant over this range since the microstructural dimension, d (or C_0), does not vary with test temperature. The photomicrograph of a fast propagating crack that arrested in Fe-3 Si at 22 °C. in Figure 5, shows that no dislocations are produced while
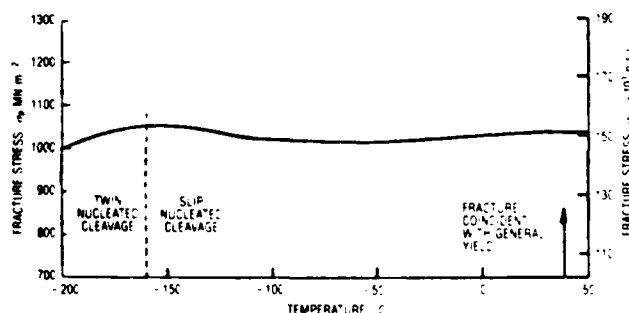

Fig 4 — The temperature dependence of the brittle fracture stress of Fe-3 Si steel measured with CVN-specimens after Griffith and Owen[48]

Fig. 5 — Micrograph of the tip of a fast propagating crack in Fe-3 Si steel that arrested at 22 °C after Hoagland, Rosenfield, and Hahn[44] The section has been etched to reveal dislocations. The dark etching region at the crack tip reflects dislocation generation and crack blunting which were absent while the crack is propagating

the crack is propagating, but that the crack does blunt after it arrests.[45] Another piece of evidence is that K_{1c}^f-values for steel correspond quite closely with K_{1c}-values for brittle ceramics bicrystals and polycrystals (see Table I). Lange[47] has identified processes responsible for fracture energy dissipation at the grain boundaries of the MgO bicrystals. They include the formation of multifaceted fracture surfaces with overlapping cracks with some plastic flow in the region of overlap. Similar processes are probably involved in steel. The $TT(K_{1a}^B)$ for ferrite is not established, but it seems likely that it corresponds closely with the $TT(K_{1c})$ for commercial grades of steel which occurs in the range 50 °C to 100 °C.[45,49] As noted by Rice and Thomson,[34] the transition temperature depends sensitively on the resistance to bond rupture. Thus, temper embrittled steels with weak bonds at the grain boundaries can display brittle behavior to temperatures above 400 °C.[32]

These circumstances provide possible explanations for the behavior of microcracks and the essential role of a carbide or other hard, brittle particles or inclusions in the brittle fracture of steel:

(i) Dislocation pile-ups against ferrite grains cannot ordinarily produce microcracks because the crack nucleus (in the ferrite) blunts when the temperature is above $TT(K_{1c})$: i.e., ≥ -200 °C.

(ii) Dislocation pile-ups can nucleate cracks in a carbide particle because the $TT(K_{1c})$ of Fe$_3$C is above 300 °C.[5] The same is true for other hard brittle particles below their $TT(K_{1c})$.

(iii) The fracture of a brittle carbide particle presents the adjacent ferrite with a rapidly advancing crack. This crack can penetrate the ferrite because K_{1c}^B-values remain at the brittle level in the temperature range $TT(K_{1c}^B) < T < TT(K_{1a}^B)$.

(iv) The microcrack will arrest at the grain boundary when the Griffith condition (Eq. [1]) is not satisfied. Ordinarily, such an arrested crack will blunt above $TT(K_{1c})$ and cannot reinitiate.

IV. THE DIMINISHED ROLE OF THE DISLOCATION PILE-UP AND THE ORIGINS OF GRAIN SIZE EFFECTS

Curry and Knott[19] have pointed out that the Smith pile-up theory of fracture (Eq. [2]) does not really predict a ferrite grain size dependence. They note that the value of τ_{eff} is limited by the operation of dislocation sources in neighboring grains and cannot exceed the value at yielding: $\tau_{eff} = d^{0.5} k_s'$ where $k_s' \approx 0.33$ MPa $\sqrt{m}$ is the Hall-Petch parameter.[15,51] When ($d^{0.5} k_s'$ is substituted for τ_{eff} in Eq. [2], the grain size dependence of σ is lost. Secondly, they note that the contribution of the pile-up term in Eq. [2] is negligible for reasonable values, i.e., $d = 20$ μm, $0.1 < c_0 < 1$ μ, $\tau_i = 100$ MPa, and $K_{1a}^B = 2.5$ MPa $\sqrt{m}$, and Eq. [2] reduces to Eq. [1c]. Curry and Knott propose that the strong carbide size dependence of Eq. [1c] has been incorrectly assigned to ferrite grain size because c_0 and d frequently go hand-in-hand as shown in Figure 6(a). To test this point, they formulate the apparent grain size dependence (replacing c_0 in Eq. [1c] with its dependence on d as specified in Figure 6(a)), and compare it with measurements in Figure 6(b) for different values of the fracture energy term. It can be seen that the curve for $\gamma = 14$ Jm^{-2}
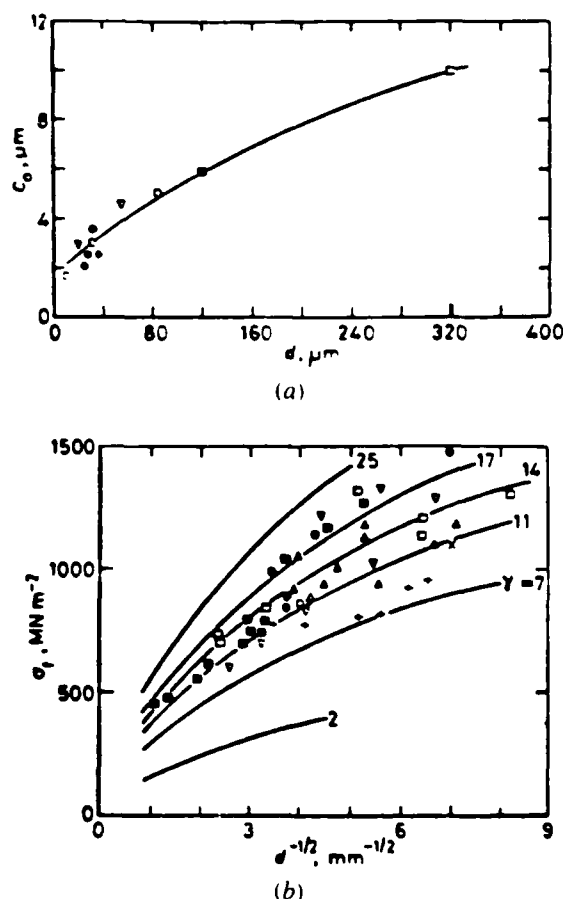
(a)

(b)

Fig 6—Relations among the brittle fracture stress, ferrite grain diameter, and the coarsest observed carbide film thickness, after Curry and Knott.[19] (a) Experimentally determined relation between c_0, the coarsest observed carbide film thickness, and d, the ferrite grain diameter $c_0 = f(d)$, and (b) the "apparent" $d^{-0.5}$ dependence of σ based on reported measurements The solid lines were obtained by replacing c_0 in the expression $\sigma_t = 0.798\, K_{Ia}^B\, c_0^{-0.5}$ with $f(d)$ for different values of K_{Ia}^B. The fact that the data are consistent with a linear dependence of σ on $c_0^{-0.5}$, but not on $d^{-0.5}$ supports the view that c_0 is the controlling variable. The value $K_{Ia}^B = 2.5$ MPa m$^{0.5}$ ($\gamma = 14$ Jm^{-2}) gives the best fit. The data in (b) are derived from Refs. 18, 52-61.

($K_{Ia}^B = 2.5$ MPa $\sqrt{m}$) agrees with the experiments. The scatter is not surprising since the relation between c_0 and d (Figure 6(a)) can hardly be precise. The fact that the dependence of σ on $d^{-0.5}$ is not linear also supports the view that c_0 is the controlling variable in these cases. A bonafide $d^{-0.5}$ ferrite grain-size dependence would still be displayed by steels with ferrite grain-size microcracks, as shown by Low.[9,10]

These findings do not alter the view that microcrack nucleation is assisted by slip and, possibly, even by pile-ups. This has been clarified by Argon, Im, and Safoglu[62] and by Lindley, Oates, and Richards[63] who show that σ^R, the peak tensile stress acting locally at the boundary of a non-yielding particle in a plastic matrix, $\sigma^R = (1/d)\,\sigma_0 + \sigma_m$, is the sum of terms involving $1/d$, the particle aspect ratio and yield stress and the mean stress. In other words, the tensile stress on the particle is amplified by the onset of yielding particularly in the presence of a larger hydrostatic component. Studies by Argon and Im[64] and Gurland[65] indicate that the local tensile stress needed to fracture cementite particles in

a ferrite matrix is $\sigma^R \sim 1500$ MPa. Since this value is well below the theoretical strength, the fracture of the carbide particle must be assisted by a local stress raiser such as a defect in the particle or a pile-up. Defects cannot be the answer for small carbide particles, d, $c_0 \leq 1$ μm, since the minimum Griffith crack diameter is $d = 0.7$ μm (for an assumed value $K_{Ic} = 1$ MPa μm). For this reason pile-ups cannot be ruled out.

V. THE EVALUATION OF K_{Ia}^B AND THE IDENTITY OF THE CONTROLLING MICROSTRUCTURAL FEATURES

The value of K_{Ia}^B is defined by measurements of the brittle fracture stress and the dimension of the particle whose boundary limits the microcrack size together with the appropriate form of the Griffith Equation (Eq. [1b] or [1c]). In addition to the carbide particle, film, or lamella, other hard particles or inclusions (Figure 7(a)), fracture may be controlled by one of the following features depending on the microstructure of the steel (Figure 7(b)):
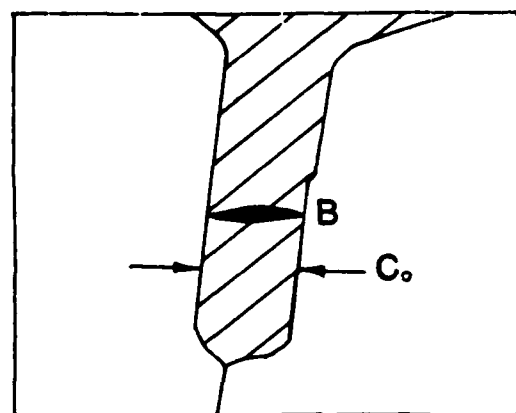
(i) ferrite grain[9,11]
(ii) pearlite colony[21-24]
(iii) bainite packet[25-28]
(iv) martensite packet.[25,29,30]

Particle-size microcracks have been observed in all of these microstructural features except in martensite packets. The microcracks in the pearlite nucleate in individual carbide lamellae in linear arrays. They are joined by the failure of the intervening ferrite and form colony- and prior austenite grain-size cracks[23,24] (see Figures 7(c) and 7(d)). It is not clear whether the critical dimension of the microcrack that determines σ^f is the colony or austenite grain diameter as assumed by Rosenfield, Votava, and Hahn[31] or the lamella thickness, as assumed by Park and Bernstein[32] although correlations with the TT (CVN) favor the former. The K_{Ia}^B-value consistent with lamella thickness, $K_{Ic}^B = 1.5$ MPa $\sqrt{m}$, is smaller than the other values in Figure 8.

The interpretation of brittle fracture stress values of different microstructures involves two complications. One is that the particle (or grain) generating the microcrack is represented by a distribution of sizes. The other is that not all particles are "eligible". "Eligibility" is here connected with the probability a given particle can produce a crack: (a) that it is associated with a suitable pile-up or stress raiser, (b) that it has an orientation favorable for nucleating a crack, and (c) that the misorientations at the particle boundary produce a low value of K_{Ia}^B. For example, if the probability of satisfying each of these requirements is $p = 0.1$, only 1 of 10^3 particles is "eligible". It is the dimension of the largest "eligible" particle within the stressed volume that enters into the expression for the brittle fracture stress (Eq. [1]). Knott and Curry[19] select the "largest observed" carbide thickness for the value of c_0 in Figure 6. They also select the 95th percentile diameter to analyze results for spheroidized carbides because this diameter leads to a K_{Ic}^B-value identical to the one derived from the "largest observed" film. Other workers have used the average particle diameter, and while this leads to an incorrect estimate of K_{Ia}^B, the $\sigma_f\text{-}d^{-1/2}$ relation serves as a useful signature.

Brittle fracture stress–particle size relations have been reported for a number of microstructural elements and are
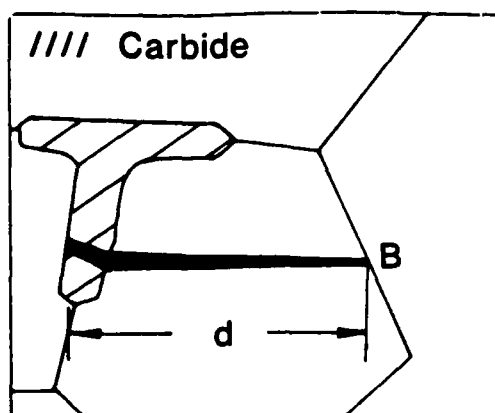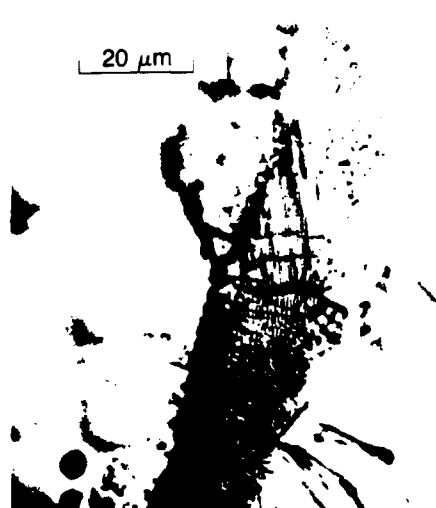
Fig. 7 — Barriers, (B), to microcrack extension and corresponding dimensions (a) grain boundary carbide and film thickness c, (b) ferrite grain boundary and grain diameter d, and (c) and (d) pearlite lamella or colony boundary (c) and (d) are photographs of the surfaces of tensile bars of mild steel (steel E) tested at −140 °C [11]

summarized in the convenient $\sigma\text{-}a^{-1/2}$ form of Eq. [1a] in Figure 8. The values of K_{Ia}^B can be deduced from the slopes of the lines, and these show that different boundaries have characteristic values of K_{Ia}^B. Fracture and the identity of the controlling microstructural feature are determined by the particle with the $(K_{Ia}^B \cdot d^{-1/2})$-combination that produces the largest value of fracture stress. The presentation in Figure 6 facilitates extrapolation and may be useful for identifying the controlling particle when the microstructural dimensions are known. For example, microcrack studies reported by Hahn et al.[11] included work on a coarse grained ferrite: $d = 40$ μm, with coarse carbide films: $c_0 = 15$ μm. Figure 8 shows that the fracture stress associated with microcracks in the ferrite grains of this size is somewhat larger than the value for microcracks in the carbide. This accounts for the observation of both ferrite and carbide microcracks in this steel. Ritchie, Server, and Wullaert[*] report a brittle fracture stress $\sigma = 1800$ MPa for a heat of grade A533B steel with bainite packets: $d = 10$ μm to 20 μm, cementite particles: $d = 0.5$ μm and oxide particle inclusions, $d = 5$ μm to 10 μm. Figure 8 indicates that the brittle fracture stress associated with spherical carbide particles of this size,

$\sigma \approx 4400$ MPa, is much larger than the reported fracture stress. It is therefore unlikely that carbide particles are participating in the nucleation process. On the other hand, microcracks nucleated in the oxide particles would extend at a stress that is lower than the reported σ-values,* and the

---

*Provided K_{Ia}^* for the oxide is close to the value for the carbide in Figure 8

---

fracture stress of the bainite packets is close to the value for the steel. The different fracture stress values are consistent with the view that the mechanism of brittle fracture of A533B involves nucleation of cracks in oxide inclusions but is controlled by the bainite packet size. The interpretation provides indirect evidence that hard particles other than the carbide can initiate cracks in steel.

VI. THE BRITTLE FRACTURE STRESS AND THE TRANSITION TEMPERATURE

The views expressed so far imply that σ, the brittle fracture stress, is a temperature-, loading rate-, and specimen
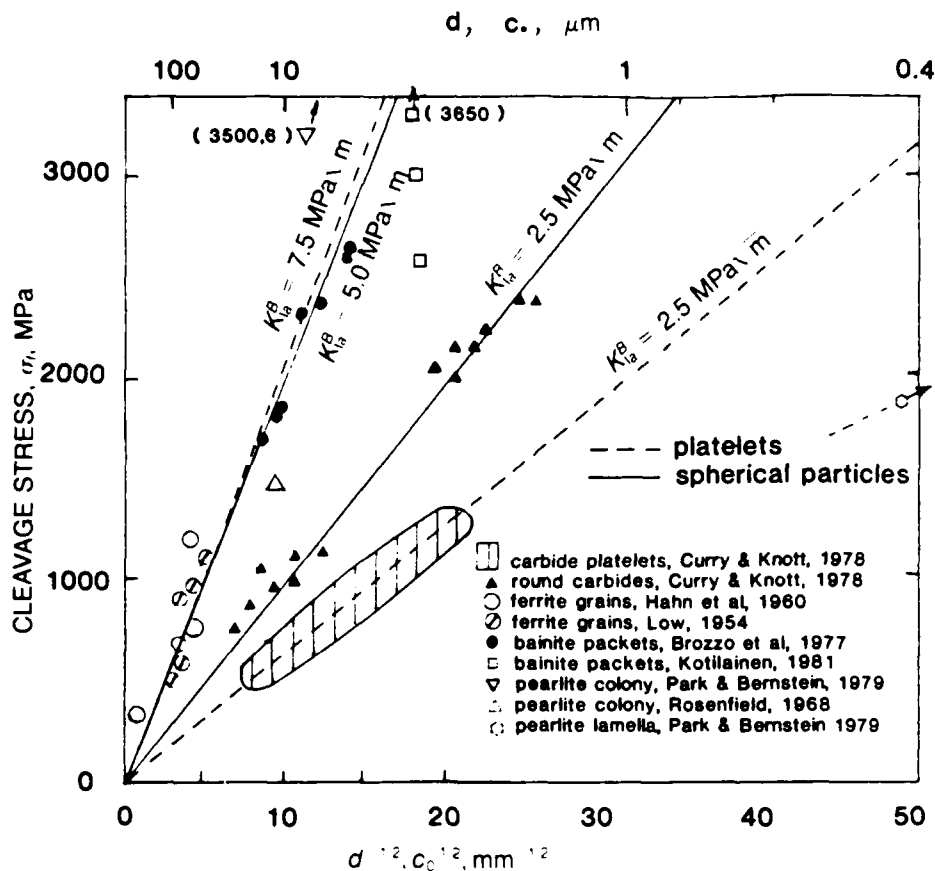
Fig 8—Summary of brittle fracture stress-particle dimension measurements for different microstructures, showing the characteristic values of K_L^c Refs 9-11, 19, 24, 26-28

geometry-independent material property because it is a function of two quantities, e.g., K_L^h and c_L that are both only functions of the microstructure. The transition temperature, TT, is the temperature below which the peak normal stress exceeds σ_f, and is defined by the condition:

$$\sigma_{1,\,max} = P\sigma_1 = \sigma \qquad [3]$$

where P is the plastic constraint factor* and σ_0 is the yield

---

*The quantity P depends on the mean stress and strain hardening. $P \approx 1.3$, ≈ 2.7, ≈ 3.5, for the tensile-, Charpy-, and K_1-specimen for typical strain hardening rates

---

strength. Accordingly, the various transition temperatures: TT (tensile bar), TT (CVN), TT (K_{1c}), and TT (K_{1d}), can be estimated when σ and σ_0 at the appropriate temperature and strain rates are known. This is illustrated in Figure 9, which shows effects of microstructure and the test method on the TT of a hypothetical medium strength steel that are qualitatively in accord with experiments.[7,67-69]

However, the construction in Figure 9(b) that assumes σ_f is independent of the test piece configuration is questionable. Estimates of σ_f derived from tensile-, CVN-, and K_{1c}-specimens of the same material, using Eq. [3] and the appropriate values of P and σ_0, just below the TT, summarized in Table II, increase substantially as the stressed volume of the test piece decreases. This is consistent with the view, developed in the preceding section, that the fracture stress is determined by the size of the largest "eligible"

particle in the stressed volume, and the fact that this size increases with the stressed volume for a material with the usual histogram of particle sizes. It seems likely that the distribution of particle sizes depends on composition and processing history, and it follows from this that the effects of changing the stressed volume vary from one material to another. Some evidence of this can be found in Table II

VII. THE RELATION BETWEEN FRACTURE TOUGHNESS AND THE PARTICLE SIZE DISTRIBUTION

The size of the stressed volume enters in the analysis of brittle crack extension and K_{1c} because it is the extent of

Table II. Influence of Test Specimen Geometry and the Relative Size of the Stressed Volume on the Brittle Fracture Stress

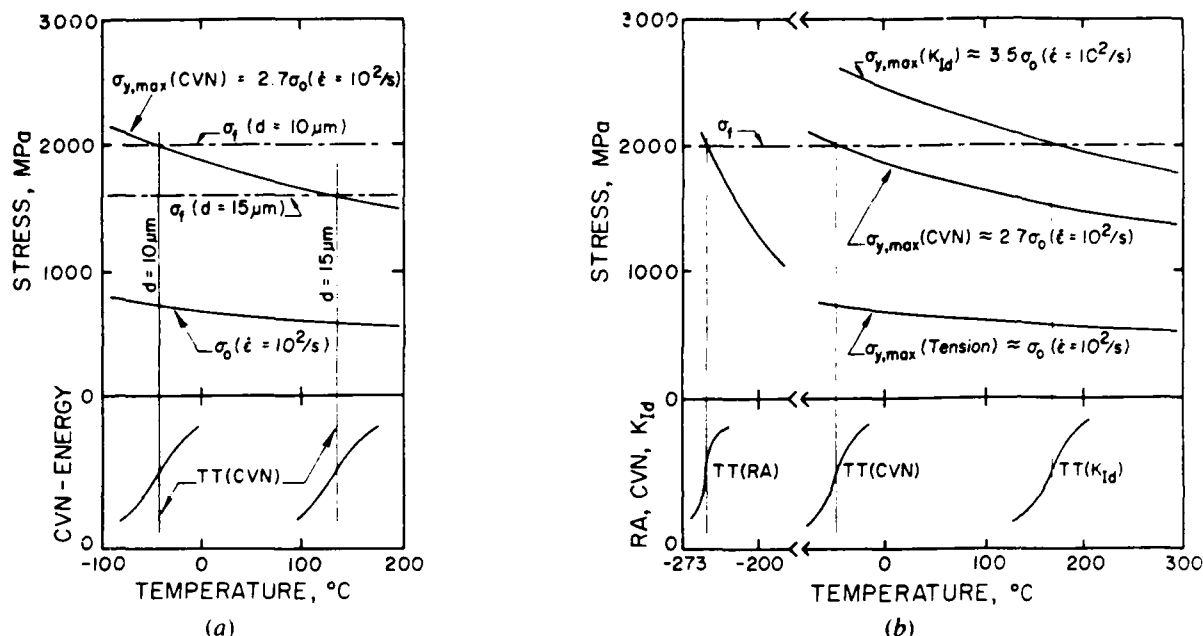| Relative Stressed Volume | σ_f, MPa | | |
	Tensile Bar ~400	CVN ~20	K_1 1
Steel K, Kotilainen[46]	995	—	2550
Steel M, Kotilainen[46]	1505	—	3650
Steel T, Kotilainen[46]	1230	2500	3015
Steel E, Hahn[70]	550	810	

Fig. 9—Schematic representation of transition temperatures of a hypothetical medium strength steel: (a) influence of the microstructural dimension d on the TT(CVN) and (b) influence of test piece geometry on the TT for a constant value of σ_f. Note: in practice σ_f varies with test piece geometry.

the highly stressed crack tip region, rather than the magnitude of the stresses, that is affected by K_1 and increases with the applied load. Ritchie, Knott, and Rice[33] therefore postulated the additional condition for cleavage crack extension, namely: Eq. [3] must be satisfied a characteristic distance X_0 in front of the crack (see Figure 10). A similar view of brittle intergranular crack extension has been presented by Jokl, Kameda, McMahon, and Vitek.[31] The value of K_{1c} below the TT (K_{1c}) is then fully determined by: (1) the character of the stress field, (2) the values of σ_0, the rate of strain hardening, and (3) σ_f and X_0. Figure 11(a) illustrates that a constant value of $X_0 = 3d$, where d is the average grain diameter, provides a rough description of the variation of K_{1c} for A533B steel below TT (K_{1c}).

At low temperature, the X_0-requirement reduces to the following expression for toughness:

$$K_{1c} = \sigma_0 \sqrt{25X_0} \qquad [4]$$

implying that the particle spacing rather than its size is the controlling dimension. The correlation between X_0 and λ_r, the mean free path between carbide particles, illustrated by Rawal and Gurland's[71] measurements in Table III, supports this concept. While K_{1c}-values below the $TT(K_{1c})$ are dominated by a particle spacing (Eq. [4]), CVN-values may be more strongly influenced by the largest eligible particle size (Eq. [1]). This notion and the fact that the spacing and size can vary independently account for the absence of a single, well-defined relation between the two standard measures of toughness valid for all steels.[3x] A classical example of non-correlation, reported by Ritchie, Francis, and Server,[72] is illustrated in Table IV.

The characteristic distance was initially connected with the need to accommodate a dislocation pile-up and an "eligible" carbide in the highly stressed region and estimated to be a small multiple of the average grain diameter, d (see Figure 11(a)). Subsequent studies that reveal X_0 is

independent of d (see Figure 11(b)) have led Curry and Knott[54] to the view that X_0 is connected with the volume of material needed to assure the presence of an "eligible" particle whose fracture condition is satisfied. Curry and Knott[5] have formulated this concept statistically and use it to analyze the fracture toughness of quenched and tempered microstructures with spheroidized carbides. Their analysis recognizes contributions from all the "eligible" particles, large and small (see Figure 10(d)). It involves three statistical quantities: (i) $P(r_i)$, the probability a particle has a radius r_i, (ii) $P(f, r_i)$, the probability a particle of radius r will initiate fracture, and (iii) θ, the probability a particle is "eligible", and the condition for crack extension:*

*$P(f, r_i) = \theta s X_i^2 n_s P(r_i)$, where X is the distance from the crack tip for which the fracture condtion (Eqs. [1] and [3]) is satisfied for r-particles. s is a factor of order unity describing the shape of the stressed region. sX_i^2 is area within which the fracture condition is satisfied, and n is the total number of particles per unit area Equation [5] defines $K_i = K$ where $\sum P(f, r_i) = 1$ since $X_i = f(r_i, K_i)$

$$\sum_{i}^{\Lambda} P(f, r_i) = 1 \qquad [5]$$

Results of the analysis, in Figure 12, reveal that the ~5 pct of the particle population with the largest radii are the most probable source of fracture in the crack tip region. This arises because the reduced stresses needed to fracture the largest particles are obtained in a volume ~30× larger than that corresponding to average-size particles. The analysis indicates that the contribution of the different particle sizes varies with the temperature, and that the fraction of the eligible particles $10^2 \leq \theta \leq 10^3$ is roughly independent of temperature. It should be noted that the value of θ depends on the nucleation process and enters the statistical fracture condition. For example, the Curry and Knott analysis indicates that a 15-fold decrease of θ leads to a 2-fold increase of K_{1c}. In other words, the microstructural
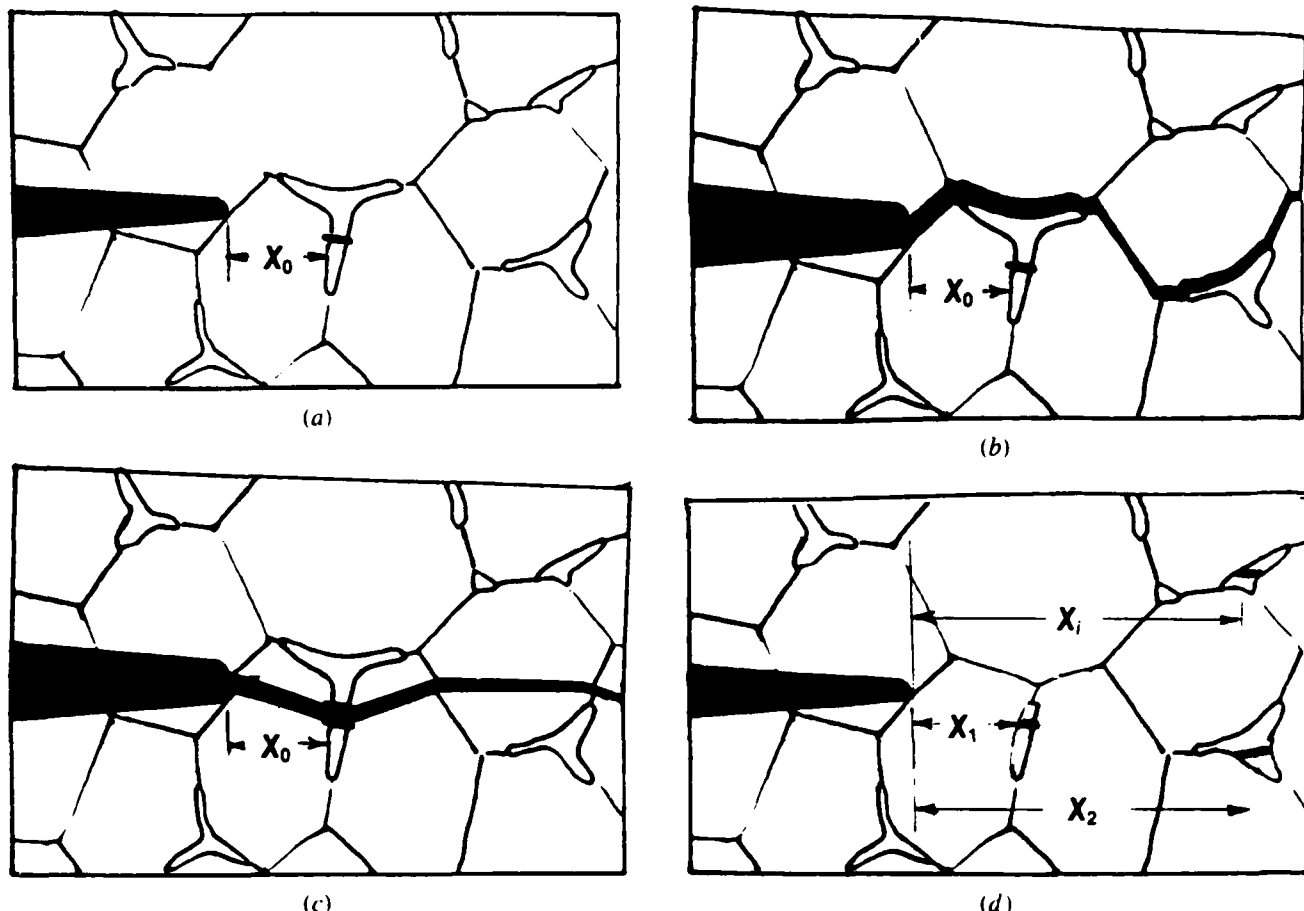
Fig. 10—Mechanisms of brittle crack extension: (a) and (b) transgranular crack extension after Ritchie, Knott, and Rice[?], (c) intergranular crack extension after Jokl, Kameda, McMahon, and Vitek,[?] and (d) statistical interpretation of Curry and Knott.[20]

Table III. Relation between the Characteristic Distance (X_0) and the Carbide Particle Mean Free Path (λ_p) in Spheroidized Carbon Steels Tested at $-196\,°C$ According to Measurements by Rawal and Gurland[?]

Steel	Carbon Weight. Pct	σ_u, MPa	K_{Ic}, MPa $\sqrt{m}$	a. X_0, μm	b. λ_p, μm
RC	0.13	766	18.0	22.1	39.3
YC	0.43	912	14.9	10.7	8.05
BC	0.83	841	13.7	10.6	7.8?
GC	1.46	813	11.3	7.7	5.2?
YF	0.43	997	15.6	9.8	4.32
BF	0.83	946	14.6	9.5	4.86

a. $X_0 = K_{Ic}^2/(25\,\sigma_u^2)$.

b. $\lambda_p = (1 - f)/N_{Lp}$, where f is the volume fraction calculated from the chemical analyses and N_{Lp} is the number of particles intercepted per unit length of random test lines.

features that control nucleation can make a modest contribution to K_{Ic}.

The Curry and Knott analysis is based on the questionable assumption that the fracture condition, Eq. [5], must be satisfied on every cross section because "the initiation of fracture has to be a more or less sympathetic event across a large proportion of the specimen thickness to allow sufficient elastic energy release."[54] In contrast, if the fracture condition must be satisfied only once in the stressed volume rather than on every cross section,* the relative contribution

*$P(f,r_i) = \theta B S x_i^? (na/2r_i) P(r_i)$ where B is the thickness

Table IV. Example of Non-Correlating CVN- and K_{Ic}-Toughness Measurements of AISI 4340 Steel after Ritchie, Francis, and Server[?]

Condition*	CVN-Energy, J	K_I, MPa $\sqrt{m}$	K_{Ic}, MPa $\sqrt{m}$
A	6.6	70	52
B	9.5	34	33

*A — 1 hour-1200 °C, salt quench to 870 °C, 1 hour-870 °C, oil quench to Rt. σ = 1592 MPa

B — 1 hour-870 °C, oil quench to RT σ = 1592 MPa
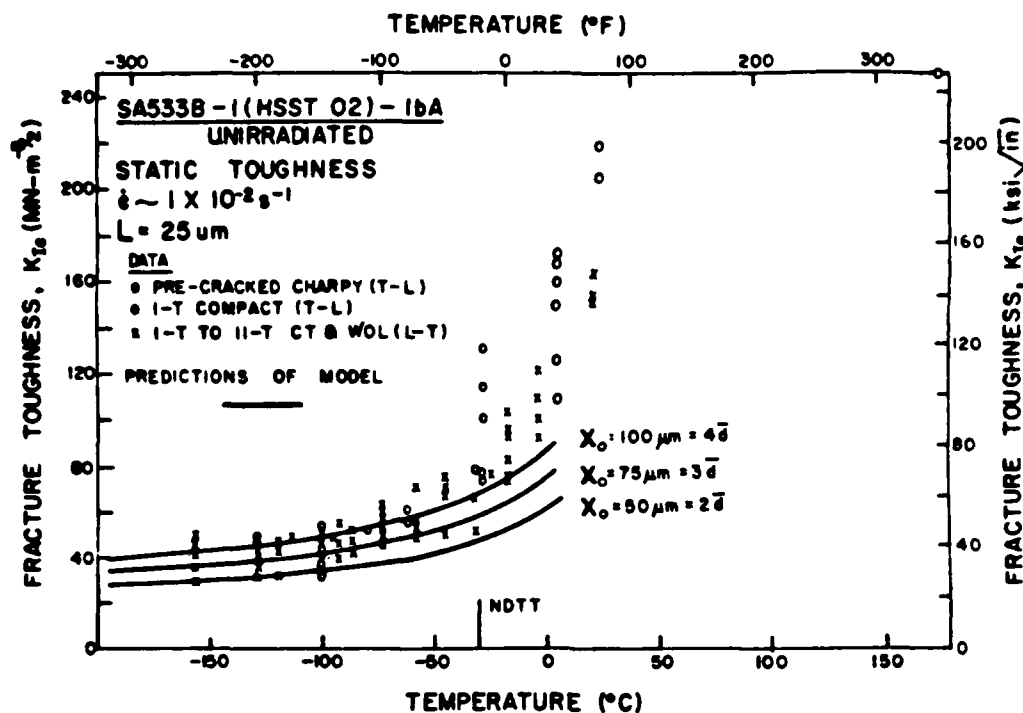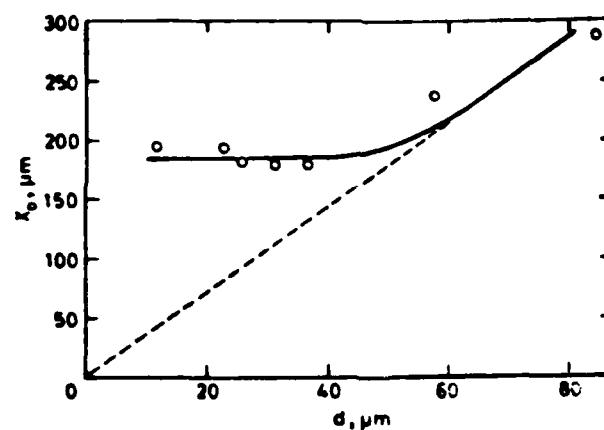
Fig. 11 — Estimates of the characteristic distance X_o (a) after Ritchie, Server, and Wullaert[64] and (b) after Curry and Knott[44]

Fig. 12 — Contribution of the carbide particle size distribution to the fracture toughness of a quenched and tempered steel with spheroidized carbide particles deduced by Curry and Knott[34] with an areal analysis, and the corresponding values for a volumetric analysis. The quantity $P(r_i)$ is the probability a particle has a radius r_i; $P(f,r_i)$ is the probability a particle of radius r_i will initiate fracture.

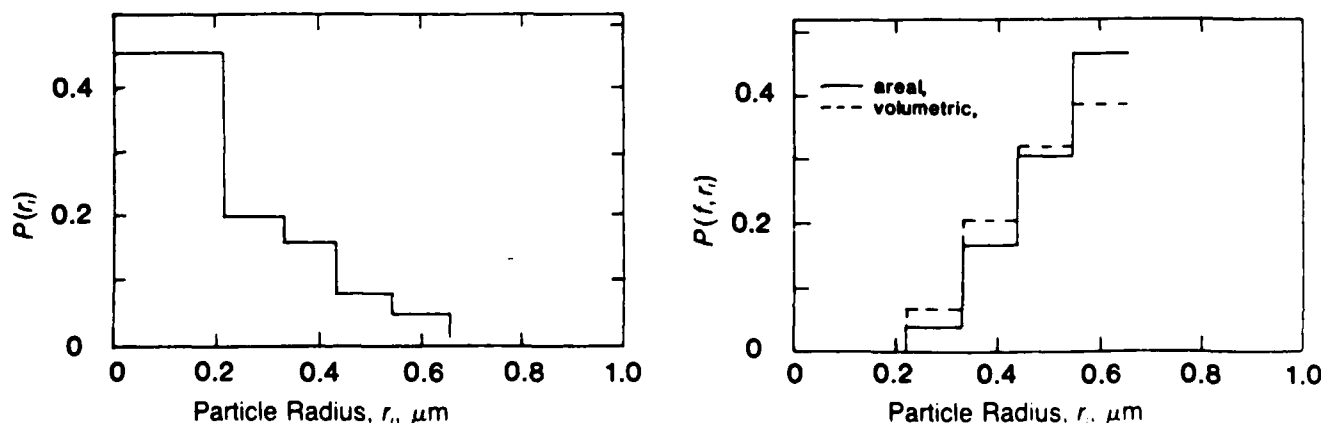of the different particle sizes is not altered very much (see Figure 12), but the estimated fraction of "eligible" particles is reduced to $\theta \approx 10^{-6}$. This fraction is consistent with the large number, $N = 1.1 \cdot 10^9$ mm^{-3}, of carbide particles in steel, but it is so small as to raise questions about the identity of the nucleating particle. The general conclusion to be drawn from either the areal or volumetric assumption is that the very small number of the largest particles has a disproportionate influence on both $TT(K_{Ic})$ and the value of K_{Ic} below the transition temperature.

VIII. CONCLUSIONS

1. The brittle fracture of steel is governed by the extension of fast propagating Griffith-type microcracks across microstructural boundaries.
2. The microcracks are not preexisting defects and must first nucleate. Carbides and possibly other brittle particles have an essential, intermediate role because, unlike the ferrite, they permit the crack nucleus to form without blunting it.
3. The brittle fracture stress depends on the values of two quantities: (i) the size of the microcracks; and (ii) the resistance it experiences, relevant when the microcrack attempts to cross the boundary. The resistance is expressed by the Griffith energy term: 15 Jm$^{-2} \leq \gamma \leq 100$ Jm^{-2}, or a corresponding LEFM crack arrest toughness value: 25 MPa $\sqrt{m} \leq K_{Ia}^B \leq 7$ MPa $\sqrt{m}$, that applies to a rapidly advancing microcrack. The size of the microcrack corresponds with the parent particle's dimension.
4. Since the parent particle or grain is represented in the microstructure by a distribution of sizes, the brittle fracture stress is determined by the largest "eligible" particle within the stressed volume. Particles are "eligible" when the conditions for nucleating a crack can be satisfied and when the resistance their boundaries offer to microcrack extension is not excessive.
5. The crack nucleation in hard particles is assisted by plastic deformation of the surrounding matrix but requires an additional stress raiser such as a dislocation pile-up or a defect in the particle. However, the pile-up dimensions do not influence the brittle fracture stress directly. The microstructural features that affect nucleation can alter the brittle fracture stress indirectly by changing the number of "eligible" particles and the largest "eligible" particle size.
6. The particles whose boundaries resist microcrack extension include: (i) carbide particles, (ii) carbide films at the grain boundaries, (iii) carbide lamellae in the pearlite, (iv) hard inclusions, (v) ferrite grains, (vi) pearlite colonies or grains, (vii) bainite packets, and (viii) martensite packets. The different boundaries display characteristic K_{Ia}^B-values.
7. The microstructural feature that controls the brittle fracture of a particular steel is the feature with the "eligible"-particle-size/K_{Ia}^B combination that produces the largest brittle fracture stress value. The existing K_{Ia}^B-measurements provide insights to the controlling microstructural features in different steels.
8. The differences in the size of the stressed volume in the tensile-, CVN-, and K_{Ic}-test complicate the analysis of the different transition temperatures and can make the K_{Ic}-CVN energy relation microstructure dependent.
9. Statistical analyses of the contribution of different particle sizes indicate that the small number of the very largest particles has a disproportionate influence on K_I below the transition temperature. Microstructural features that influence the fraction of the particles that is "eligible" have a modest effect on K_{Ic}.

REFERENCES

1. *History of the University of Michigan*. Ann Arbor, MI, 1966, p. 314
2. *The Michigan Alumnus*, October 10, 1925, vol. 31, p. 38
3. Z. Jeffries: *Trans. Am. Soc. Steel Treating*, 1928, vol. 13, p. 369
4. M. E. Shank: ASTM STP 158, 1954, p. 48
5. A. A. Griffith: *Phil. Trans. Roy. Soc.*, 1920, vol. A221, p. 163
6. P. Ludwik: *Stahl u. Eisen*, 1923, vol. 43, p. 1427
7. N. P. Allen, W. P. Rees, B. E. Hopkins, and H. R. Tipler: *J. Iron and Steel Inst.*, 1953, vol. 174, p. 103
8. J. R. Low: *Relation of Properties to Microstructure*, ASM, Cleveland, OH, 1954, p. 103
9. J. R. Low: *Deformation and Flow of Solids*, Springer Verlag, Berlin, 1956, p. 50
10. W. S. Owen, B. L. Averbach, and M. Cohen: *ASM Trans.*, 1958, vol. 50, p. 634
11. G. T. Hahn, B. L. Averbach, W. S. Owen, and M. Cohen: *Fracture*, B. L. Averbach et al., eds., John Wiley and Sons, New York, NY, 1959, p. 91
12. C. J. McMahon and M. Cohen: *Acta Metall.*, 1965, vol. 13, p. 591
13. C. Zener: *Fracturing of Metals*, ASM, Cleveland, OH, 1948, p. 3
14. A. N. Stroh: *Advances in Physics*, 1957, vol. 6, p. 418

15. N. J. Petch: *J. Iron and Steel Inst.*, 1953, vol. 174, p. 25.
16. E. Smith: *Proc. Conf. Physical Basis of Yield and Fracture*, Inst. of Physics and Physical Soc., Oxford, 1966, p. 36.
17. E. A. Almond, D. H. Timbres, and J. D. Embury: *Proc. 2nd Int. Conf. on Fracture*, P. L. Pratt, ed., London, Chapman and Hall, 1969, p. 253.
18. D. M. Hodgson and A. S. Tetelman: *Proc. 2nd Int. Conf. on Fracture*, P. L. Pratt, ed., London, Chapman and Hall, 1969, p. 266.
19. D. A. Curry and J. F. Knott: *Metal Science*, 1978, vol. 12, p. 511.
20. D. A. Curry and J. F. Knott: *Metal Science*, 1979, vol. 13, p. 341.
21. A. R. Rosenfield, E. Votava, and G. T. Hahn: *Trans. ASM*, 1968, vol. 61, p. 807.
22. D. A. Porter, K. E. Easterling, and G. D. W. Smith: *Acta Metall.*, 1978, vol. 26, p. 1405.
23. G. K. Bouse, I. M. Bernstein, and D. H. Stone: ASTM STP 644, 1978, p. 145.
24. Y. J. Park and I. M. Bernstein: *Metall. Trans. A*, 1979, vol. 10A, p. 1653.
25. A. Kamada, N. Koshizuka, and T. Funakoshi: *Trans. Iron and Steel Inst. of Japan*, 1976, vol. 16, p. 407.
26. P. Brozzo, G. Buzzichelli, A. Mascanzoni, and M. Mirabile: *Metal Science*, 1977, vol. 11, p. 123.
27. H. Kotilainen: *Fracture and Fatigue*, J. C. Radon, ed., Pergamon Press, 1980, p. 217.
28. H. Kotilainen, K. Torronen, and P. Neonen: *Advances in Fracture Research*, D. Francois, ed., Pergamon Press, 1982, vol. 2, p. 723.
29. H. Ohtani, F. Terasaki, and T. Kunitake: *Trans. Iron and Steel Inst. of Japan*, 1972, vol. 12, p. 118.
30. L. A. Norstrom and O. Vingsbo: *Metal Science*, 1979, vol. 13, p. 677.
31. M. L. Jokl, J. Kameda, C. J. McMahon, Jr., and V. Vitek: *Metal Science*, 1980, vol. 14, p. 375.
32. J. Kameda and C. J. McMahon, Jr.: *Metall. Trans. A*, 1980, vol. 11A, p. 91.
33. R. O. Ritchie, J. F. Knott, and J. R. Rice: *J. Mech. Phys. Solids*, 1973, vol. 21, p. 395.
34. J. R. Rice and R. Thomson: *Phil. Mag.*, 1975, vol. 29, p. 73.
35. M. L. Jokl, V. Vitek, and C. J. McMahon, Jr.: *Acta Metall.*, 1980, vol. 28, p. 1479.
36. M. Mullins and M. A. Dokainish: *Phil. Mag.*, 1982, vol. 46, p. 771.
37. C. E. Hartbower: Reliability of the AASHTO Temperature Shift in Material Toughness Testing, FHA Report, Structural Engineering Series, No. 7, 1979.
38. R. Roberts and C. Newton: Weld Res. Council Bulletin 265, 1981.
39. M. Gensamer: *ASM Trans.*, 1946, vol. 36, p. 301.
40. H. Kotilainen: Ph.D. Dissertation, Helsinki University of Technology, Otaniemi, 1980.
41. P. L. Pratt: *Metal Science*, 1980, vol. 14, p. 363.

42. F. F. Lange: *Phil. Mag.*, 1967, vol. 16, p. 761.
43. F. C. Frank and A. W. Stroh: *Proc. Phys. Soc.*, 1952, vol. 65B, p. 811.
44. R. G. Hoagland, A. R. Rosenfield, P. C. Gehlen, and G. T. Hahn: ASTM STP 627, 1977, p. 177.
45. G. T. Hahn, R. G. Hoagland, J. Lereim, A. J. Markworth, and A. R. Rosenfield: ASTM STP 711, 1980, p. 289.
46. R. G. Hoagland, A. R. Rosenfield, and G. T. Hahn: *Metall. Trans.*, 1972, vol. 3, p. 123.
47. R. Pilkington and D. Hull: *Conf. on Fracture Toughness*, Iron and Steel Inst., 1968, vol. 20, p. 5.
48. J. R. Griffiths and D. R. J. Owen: *J. Mech. Phys. Solids*, 1971, vol. 19, p. 419.
49. G. D. Whitman and R. H. Bryan: Oak Ridge Nat. Lab. Report TM-8369V3, 1983, p. 20.
50. A. Inoue, T. Ogura, and T. Masumoto: *Metall. Trans. A*, 1977, vol. 8A, p. 1689.
51. E. O. Hall: *Proc. Physical Soc.*, London, 1951, vol. B64, p. 747.
52. J. F. Knott: *J. Iron and Steel Inst.*, 1966, vol. 204, p. 104.
53. G. Oates: *J. Iron Steel Inst.*, 1969, vol. 207, p. 353.
54. D. A. Curry and J. F. Knott: *Metal Science*, 1976, vol. 10, p. 1.
55. J. F. Knott: *J. Mech. Phys. Solids*, 1967, vol. 15, p. 97.
56. T. R. Wilshaw: *J. Iron Steel Inst.*, 1966, vol. 204, p. 936.
57. T. R. Wilshaw, C. A. Ran, and A. S. Tetelman: *Eng. Fracture Mech.*, 1968, vol. 1, p. 191.
58. J. R. Low: Iron and Its Dilute Solid Solutions, Wiley, New York, NY, 1963, p. 255.
59. M. Holzman and J. Man: *J. Iron and Steel Inst.*, 1971, vol. 209, p. 836.
60. J. D. G. Groom and J. F. Knott: *Metal Science*, 1975, vol. 9, p. 390.
61. G. D. Fearnehough: M.Sc. Thesis, University of Manchester, 1964.
62. A. S. Argon, J. Im, and R. Safoglu: *Metall. Trans. A*, 1975, vol. 6A, p. 825.
63. T. C. Lindley, G. Oates, and C. E. Richards: *Acta Metall.*, 1970, vol. 18, p. 1127.
64. A. S. Argon and J. Im: *Metall. Trans. A*, 1975, vol. 6A, p. 839.
65. J. Gurland: *Acta Metall.*, 1972, vol. 20, p. 735.
66. R. O. Ritchie, W. L. Server, and R. A. Wullaert: *Metall. Trans. A*, 1979, vol. 10A, p. 1557.
67. J. M. Barson and S. T. Rolfe: ASTM STP 466, 1970, p. 281.
68. A. K. Shoemaker and S. T. Rolfe: *Eng. Fracture Mech.*, 1971, vol. 2, p. 319.
69. W. W. Gerberich and Y. T. Chen: *Metal Science*, 1978, vol. 12, p. 151.
70. G. T. Hahn: Sc.D. Dissertation, M.I.T., 1959.
71. S. P. Rawal and J. Gurland: *Metall. Trans. A*, 1977, vol. 8A, p. 691.
72. R. Ritchie, B. Francis, and W. L. Server: *Metall. Trans. A*, 1976, vol. 7A, p. 831.

FOREWORD

Establishment of Microstructural Spacing during Dendritic and Cooperative Growth

This symposium was organized under joint sponsorship by the ASM-MSD Phase Transformations Committee and the TMS-AIME Solidification Committee to provide a forum for discussion of micro-structural spacing in different morphologies during various transformations. The invited contributions were presented during the March 1983 meeting of TMS-AIME.

The size scale and phase spacing are among the most important characteristic features of regular microstructural morphologies. In practice a number of thermal and mechanical treatments have been developed to modify microstructural spacing during phase transformations. For some time there has been no generally established analysis to account for the selection of spacing under given conditions. However, recent advances in experiment have yielded accurate measurements in well-characterized systems which have stimulated new theoretical work on the analysis of the selection of spacing and scale.

Important theoretical progress has been made in applying the principle of marginal stability to the initial selection of dendrite spacing and with the description of dendrite coarsening to account for structural adjustment. Further progress in analysis and new results have been reported on spacings developed in cellular, eutectic, and monotectic structures. For solid state reactions recent experimental work on spacing selection has emphasized the importance of diffusional transport in the vicinity of the moving trans-formation interface. The written discussions in the papers that were available at the time of publication provide a valuable overview of recent work and point out a number of unresolved areas which should stimulate future work.

<div align="right">

J. H. Perepezko
University of Wisconsin-Madison
Madison, Wisconsin

G. J. Shiflet
University of Virginia
Charlottesville, Virginia

</div>

Rainer Hoff,[1] Carol A. Rubin,[1] and George T. Hahn[1]

Strain-Rate Dependence of the Deformation at the Tip of a Stationary Crack

ABSTRACT: A new analytical technique is presented whereby the Hutchinson-Rice-Rosengren singularity solutions can be used, in certain cases, to determine the stresses and strains near a crack tip for a dynamically loaded, strain rate–dependent material. This technique involves a simple modification of the constant, α, and the strain hardening exponent, n, in the power stress-strain law. Elastoplastic, dynamic finite element computations are in close agreement with this analytical technique.

Stresses and strains are generally higher in a dynamically loaded rate sensitive material than in a rate insensitive material. Also, J_{Ic} increases correspond to increases in the flow stress in rate-sensitive materials, provided that δ_c is rate-insensitive.

KEY WORDS: fracture, cracks, plastic fracture mechanics, dynamic, strain rate, J-integral, crack opening displacement, finite element models, compact tension specimen, steels, power-law hardening materials

Nomenclature

A_p Crack tip plastic zone area

d_n Constant in crack tip opening displacement relation (Eq 2). Value depends on the strain hardening exponent n

D Constant in Malvern equation (Eq 14)

E Young's modulus

I_n Constant in J-field equations (Eqs 5 and 6). Value depends on the strain hardening exponent, n

J, J_I Path-independent contour integral; energy release rate for quasi-statically loaded specimens

$\dot{J}, \dot{J}_I$ Time rate of change of the J-integral

[1] Graduate Assistant, Associate Professor, and Professor, respectively, Department of Mechanical and Materials Engineering, Vanderbilt University, Nashville, TN 37235. Dr. Hoff is currently Assistant Professor, Department of Mechanical Engineering, University of Waterloo, Waterloo, Ontario, Canada.

J, J_1 Path-independent integral; energy release rate for dynamically loaded specimens

J_{Ic} Critical value of J-integral when crack propagation initiates

J_{Ica}, J_{Icb} J_{Ic} at loading rates a and b, respectively

J_{Imax} Maximum value of J_1

$\dot{J}_{Imax}$ Maximum value of $\dot{J}_1$

J_0 Value of J-integral at time $= 0$

k Coordinate directions: $X_k = X_1, X_2$

K_I Mode I stress intensity factor (loosely defined as $\sqrt{EJ/1 - \nu^2}$)

$\dot{K}_I$ Time rate of change of the stress intensity factor

K_{Ica}, K_{Icb} K_{Ic} at loading rates a and b, respectively

n Strain hardening exponent in the power stress-strain law (Eq 3)

n' Strain hardening exponent in the modified power stress-strain law

n_k Direction cosines

N Reciprocal of the strain hardening exponent; $N = 1/n$

N' Reciprocal of the modified strain hardening exponent; $N' = 1/n'$

p Exponent in the Malvern equation (Eq 14)

r Radial distance from the crack tip (length units)

r_0 Plastic zone size at $\theta = 0$

R Dimensionless distance from crack tip; $R = r/(K_I/\sigma_0)^2$

s_{ij} Cauchy deviatoric stress tensor

S Arc length

t Time

t_i Traction vector; $t_i = \sigma_{ij}n_j$

T Kinetic energy density; $T = (1/2)\,\rho\dot{u}_i\dot{u}_i$

u_i Displacement vector

$\dot{u}_i$ Velocity vector

$\ddot{u}_i$ Acceleration vector

V Volume

W Strain energy density; $W = \int_0^\cdot \sigma_{ij}d\epsilon_{ij}$

α Constant in the power stress-strain law (Eq 3)

α' Constant in the modified power stress-strain law (Eq 18)

Γ Integration contour

δ Crack tip opening displacement

δ_c Critical crack tip opening displacement

ϵ_{ij} Strain tensor

$\dot{\epsilon}_{ij}$ Time rate of change of the strain tensor

$\tilde{\epsilon}_{ij}$ Known dimensionless functions of the circumferential position, θ, and the strain hardening exponent, n

ϵ_P Equivalent plastic strain

$\dot{\epsilon}_P$ Equivalent plastic strain rate

$\epsilon_{P(ave)}$ Average equivalent plastic strain

$\dot{\epsilon}_{P(ave)}$ Average equivalent plastic strain rate

ϵ_0 Yield strain under static tensile loading; $\epsilon_0 = \sigma_0/E$

θ Circumferential position measured counterclockwise from the crack plane

λ Loading rate parameter

ν Poisson's ratio

ρ Mass density

σ_d Instantaneous flow stress under dynamic loading

σ_e (von Mises) equivalent stress

σ_{ij} Cauchy stress tensor

$\tilde{\sigma}_{ij}$ Known dimensionless functions of the circumferential position, θ, and the strain hardening exponent, n

σ_0 Yield stress under static tensile loading

σ_{0a}, σ_{0b} Yield stress at loading rates a and b, respectively

σ_s Flow stress under static loading

As a first step in modelling rapidly advancing cracks in tough steels, this paper examines a stationary crack in a rapidly loaded compact tension specimen. The plastic strain rates and therefore the strain-rate sensitivity effects are smaller for a dynamically loaded stationary crack than for a rapidly propagating crack. However, strain-rate effects are by no means insignificant in the stationary crack case [1]. Yet, with the exception of the recent finite difference study of elasto-viscoplastic fracture by Aboudi and Achenbach [2] and creep studies by Little et al [3], virtually no analytical or numerical work has been reported incorporating strain-rate-dependent flow properties in the determination of the crack tip stress fields. The aim of this work is to examine the effects of loading rate and rate sensitivity on J_I and the crack tip opening displacement, features of the plastic and process zones that are influential in determining the toughness.

Plastic strains, in the region surrounding a stationary crack, can be characterized as occurring in two zones (Fig. 1). Small plastic strains in the range $0 \leq \epsilon_p \leq 0.1$ occur in the larger region called the plastic zone. The size of the plastic zone (at $\theta = 0$) is given by a characteristic dimension, r_0. In a nonhardening material where the plastic zone is small compared with the specimen dimensions [4]:

$$r_0 \simeq \frac{0.036 \, EJ}{\sigma_0^2 \, (1 - \nu^2)}. \tag{1}$$

In the immediate vicinity of the crack tip is the heavily strained fracture process zone, where plastic strains range roughly from 0.1 to 1.0 [1]. The size of this intensely nonlinear zone is on the order of the crack tip opening dis-
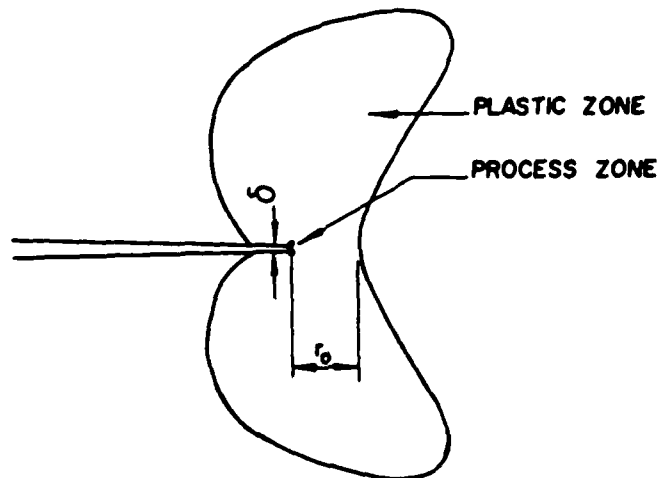
FIG. 1—*Plastic and process zones in the vicinity of a stationary crack.*

placement, δ. The crack tip opening displacement can be expressed as a function of Rice's [5] contour integral J by [6]

$$\delta = d_n \frac{J}{\sigma_0} \tag{2}$$

for a nonlinear elastic, power law hardening material. The constant, d_n, is a function of the material properties α, σ_0, E, and n (in the power stress-strain law), where

$$\frac{\epsilon}{\epsilon_0} = \alpha \left(\frac{\sigma}{\sigma_0} \right)^n \tag{3}$$

The relative *size* of the plastic and process zones is approximately

$$\frac{\delta}{r_0} \simeq 0.03 \tag{4}$$

for a material such as A533B [1]. Consequently the *volume* of the process zone is only 0.09% of the plastic zone volume, in two-dimensional, small-scale yielding, plane-strain situations.

Expressions for the stresses and strains in the plastic zone are given by the J-field solutions of Hutchinson [7] and Rice and Rosengren [8]:

$$\sigma_{ij} = \sigma_0 \left(\frac{EJ}{\alpha \sigma_0^2 I_n r} \right)^{(1/n+1)} \tilde{\sigma}_{ij}(\theta, n) \tag{5}$$

and

$$\epsilon_{ij} = \alpha \, \epsilon_0 \left(\frac{EJ}{\alpha \sigma_0^2 I_n r} \right)^{(n/n+1)} \tilde{\epsilon}_{ij}(\theta, \, n) \tag{6}$$

Also of interest are expressions for the equivalent stress and equivalent plastic strain:

$$\sigma_e = \sqrt{(3/2) \, s_{ij} s_{ij}} \tag{7}$$

and

$$\epsilon_P = \sqrt{(2/3) \, \epsilon_{ij} \epsilon_{ij}} \tag{8}$$

Since the power law relation (Eq 3) does not accurately represent the linear elastic portion of the stress-strain curve, Eqs 5 to 8 are most accurate where elastic strains are negligible.

Strain rates can be determined by differentiating Eq 6 with respect to time:

$$\dot{\epsilon}_{ij} = \alpha \, \epsilon_0 \left(\frac{EJ}{\alpha \sigma_0^2 I_n r} \right)^{(n/n+1)} \left(\frac{n}{n+1} \right) \quad J^{(-1/n+1)} \, \dot{J} \, \tilde{\epsilon}_{ij} \tag{9}$$

where the dot superscript denotes a time derivative. Observing the similarity between Eqs 6 and 9, the latter can be simplified to give

$$\dot{\epsilon}_{ij} = \left(\frac{n}{n+1} \right) \left(\frac{\dot{J}}{J} \right) \epsilon_{ij} \tag{10}$$

The strain rates given in Eqs 9 and 10 are not accurate in most situations. The angular distributions of strain rates, represented by $\tilde{\epsilon}_{ij}$ in Eq 9, were determined for static loading and therefore do not account for the effect of the inertial loads on the stresses. The amplitude of the strain rate singularity is a function of $\alpha, n, \sigma_0, I_n, J,$ and $\dot{J}$. Many materials exhibit strain-rate-dependent material properties, in which case the static $\sigma_0, \alpha,$ and n values do not represent the stress-strain relations under dynamic loading.

The application of Rice's J-integral to general dynamic situations is awkward, since it does not account for kinetic energy or inertia and is no longer path-independent. Recently, a number of path-independent integrals have been proposed [9–12] that are applicable to general dynamically loaded structures. The most promising of these is the J'-integral of Atluri et al [12], which corresponds physically to energy release rate for stationary and propagating dynamically loaded cracks. The J'-integral has some computational advantages over the others, since the integration is performed along a fixed contour in space and not along a contour that moves with a propagating

crack such as in Ref *10*. The J vector integral is given by

$$J_k = \int_\Gamma [(W + T)n_k - t_i u_{i,k}]dS + \int_v [\rho \ddot{u}_i u_{i,k} - \rho \dot{u}_i \dot{u}_{i,k}]dV \qquad (11)$$

whose first component, J_1, degenerates to Rice's J-integral for stationary, statically loaded cracks. The domain of the second integral in Eq 11 is the volume contained within the contour of the first integral in the equation.

Expressions such as Eqs 5 and 6 for stresses and strains near a crack tip are not available for most dynamically loaded structures. However, Eqs 5 and 6 can still be used for slowly loaded specimens and for rapidly loaded specimens with stationary cracks by using the "inertialess" modelling technique discussed in the next section.

Ductile crack extension proceeds by void nucleation, growth, and coalescence in the process zone. The critical crack tip opening displacement, δ_c, has been demonstrated to be a viable ductile fracture criterion [13,14]. From Eq 2 one can deduce J_{Ic} in terms of the critical crack opening displacement:

$$J_{Ic} = \frac{\sigma_0 \delta_c}{d_n} \qquad (12)$$

In rate-sensitive materials, the yield stress will generally increase with increasing strain rates. If δ_c is rate-insensitive, then changes in σ_0 will alter J_{Ic} according to

$$\frac{J_{Icb}}{J_{Ica}} = \left(\frac{K_{Icb}}{K_{Ica}}\right)^2 = \frac{\sigma_{0b}}{\sigma_{0a}} \qquad (13)$$

where the subscripts a and b in Eq 13 refer to two different loading rates. In other words, J_{Ic} will increase with loading rate, provided that δ_c is rate-insensitive.

The void nucleation and growth mechanism, which initiates the ductile fracture process, is enhanced by higher mean (or hydrostatic) stress. The mean stress scales with static yield stress (see, for instance, the slip-line file solution of Ref *5*); however, δ_c varies inversely with mean stress [15]. Therefore a higher yield stress will generally produce a lower critical crack tip opening displacement, which in turn would decrease J_{Ic}. Clearly, these two competing effects are occurring simultaneously, and it is not known which effect will dominate.

In the present study, we consider only the former case, where J_{Ic} increases because of the flow stress elevation in the dynamically loaded plastic zone. An analytical model is developed whereby the J-field solutions are modified to accommodate strain rate sensitivity. Finite element computations are also performed to verify the accuracy of this technique.

Experimental data from a number of sources [16–20] related J_{Ic} to the loading rate, $\dot{J}$. Materials that exhibit an increase in yield stress at high strain rates often show an increase in J_{Ic} at high strain rates corresponding to Eq 13, as was observed in a previous paper [1]. The relative contributions of the strain rates in the plastic and process zones are still unclear.

Estimation Technique for Strain-Rate Effects

The stresses and strains near the tip of a dynamically loaded crack in a ductile material are affected by the inertia of the structure and by the strain-rate sensitivity of the yield or flow stress. It is therefore desirable to isolate the strain-rate sensitivity effects in order to ascertain their significance. This section describes a technique whereby the parameters in the power stress-strain law are modified to account for strain-rate effects.

Suppose that a body were dynamically loaded, but that inertial effects could be ignored. Physical situations that would correspond to this are (1) a solid body with negligible density, or (2) a body loaded at constant velocity so that the accelerations are everywhere negligible (perhaps after an initial transient). Differences between the static behavior and the dynamic behavior, in such instances would be entirely due to the strain-rate effects.

Experimental results have shown that the flow stress typically increases with increasing strain rate [16–20]. Numerous models have been proposed to characterize this behavior, some of which are discussed in Ref 21. We have chosen a form of the equation used by Malvern [22] because of its computational simplicity, although any other stress-strain-rate relation could equally well have been used. Malvern suggested that the instantaneous flow stress under dynamic loading, σ_d, is a function of the equivalent plastic strain rate, $\dot{\epsilon}_p$, and the flow stress at zero strain rate, σ_s, according to

$$\sigma_d = \sigma_s \left[\left(\frac{\dot{\epsilon}_P}{D} \right)^{1/p} + 1 \right] \tag{14}$$

The constants σ_s, D, and p must be determined experimentally.

The power stress-strain law (Eq 3) can be inverted to obtain

$$\sigma_s = \sigma_0 \left(\frac{\epsilon}{\alpha \epsilon_0} \right)^N \tag{15}$$

where $N = 1/n$. Equation 15 can be substituted into Eq 14 to give

$$\sigma_d = \sigma_0 \left(\frac{\epsilon}{\alpha \epsilon_0} \right)^N \left[\left(\frac{\dot{\epsilon}_P}{D} \right)^{1/p} + 1 \right] \tag{16}$$

Substituting for the equivalent plastic strain rate from Eq 10 gives

$$\sigma_d = \sigma_0 \left(\frac{\epsilon}{\alpha \epsilon_0} \right)^N \left[\left(\frac{j_\epsilon}{(1 + N)DJ} \right)^{1/p} + 1 \right] \quad (17)$$

Equation 17 is too unwieldy to be used as a stress-strain relation. A more desirable dynamic stress-strain relation would be a power law of the form

$$\sigma_d' = \sigma_0 \left(\frac{\epsilon}{\alpha' \epsilon_0} \right)^{N'} \quad (18)$$

The parameters α' and N' cannot be found by equating Eq 18 to Eq 17 and solving for α' and N'. However, a very good approximation to Eq 17 can be found by selecting α' and N' to minimize the deviations (squared) between Eqs 17 and 18. That is, choose α' and N' to minimize

$$f(\alpha', N') = \int (\sigma_d - \sigma_d')^2 \, d\epsilon \quad (19)$$

Or, making substitutions from above, to minimize:

$$f(\alpha', N') = \int \left\{ \left(\frac{\epsilon}{\alpha' \epsilon_0} \right)^{N'} - \left(\frac{\epsilon}{\alpha \epsilon_0} \right)^N \left[\left(\frac{j_\epsilon}{(1 + N)DJ} \right)^{1/p} + 1 \right] \right\}^2 d\epsilon \quad (20)$$

(This minimization is best performed by using a nonlinear programming approach. Ref 23 discusses nonlinear programming in detail.) The limits of integration in Eq 20 should be chosen to reflect the strain range of interest, typically 0 to 0.25. Note that Eq 20 only applies to a particular instant in time, since $\dot{J}/J$ will, in general, not be constant ($\dot{J}/J$ is constant only in the special case where J varies with time according to $J = J_0 \exp\{\lambda t\}$).

Figure 2 illustrates the strain-rate-modified stress-strain curve obtained by using this approximation technique. The lower curve is the zero strain rate stress-strain curve for a material such as A533B ($\epsilon/\epsilon_0 = 2.12(\sigma/\sigma_0)^{8.46}$). The upper curve is the actual dynamic stress-strain curve produced according to Eq 17, with $\sigma_s = 383$ MPa, $D = 62\,920/s$, $p = 7.245$, $J = 188.0$ kJ/m^2, and $\dot{J} = 176.5$ MJ/m^{2}s. The curve reflects the variation of $\dot{\epsilon}_P$ with ϵ_P throughout the plastic zone. This curve can be contrasted with the conventional stress-strain curve, shown as a dashed line in Fig. 2, which assumes a constant average strain rate throughout the plastic zone. The high strain-rate estimation technique was applied to parameterize the upper curve. Values of $\alpha' = 0.533$ and $n' = 6.38$ correspond to the high strain rate curve so well that any deviations are not visible on the scale of Fig. 2.
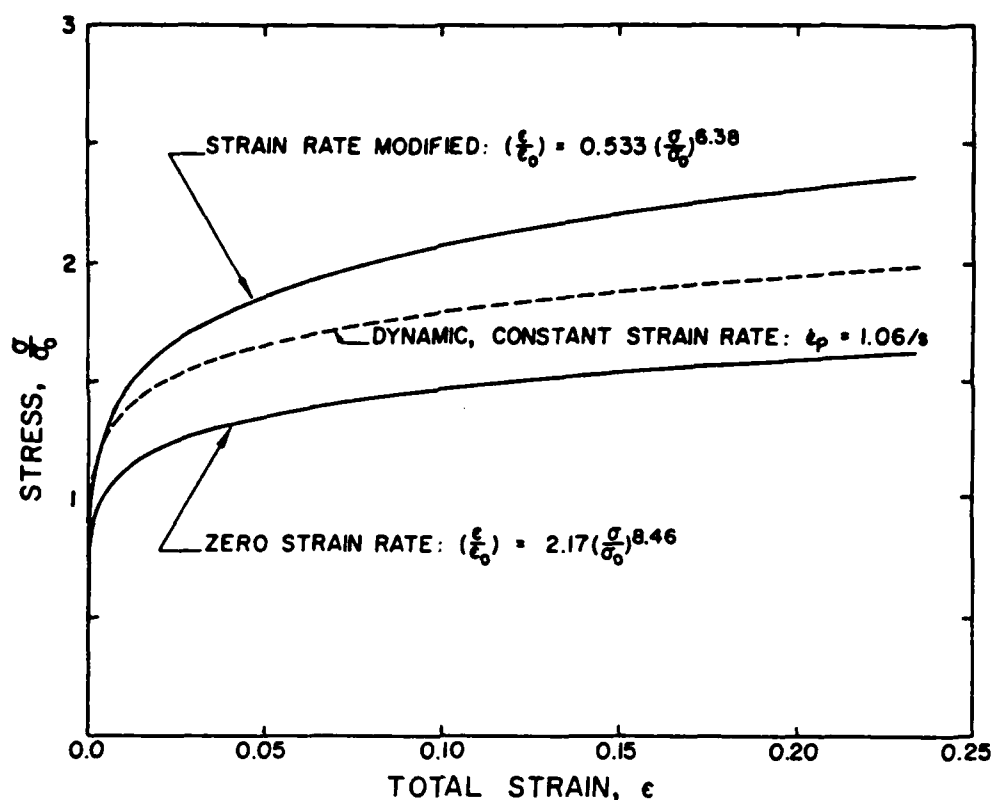
FIG. 2—*Power stress-strain law curves for A533B steel under static and dynamic loading.*

Finite Element Modelling

A stationary crack in a compact tension specimen was modelled using finite elements. Figure 3 is a plot of the mesh; an enlarged view of the crack tip region is shown below a view of the bulk of the model. The model is comprised of 646 nodal points joined by 190 eight-noded isoparametric finite elements. Numerical studies [24,25] have shown these elements to be suitable for use in the fully plastic range.

The crack is modelled with a sharp tip; the finite element analyses do not account for the continually changing tip geometry as progressive blunting takes place. This is, however, the same way in which the J-theory models the crack tip. Therefore the results of the finite element analyses ought to agree with the J-field equations (Eqs 5 to 8). Another study, currently under way, is focusing on the more realistic problem where the continually changing crack tip geometry is included in the analysis.

The material properties are given with an elastic strain-hardening plastic model, based on experimental data for A533B steel at 93°C [26,27]. The zero strain rate stress-strain curve is given in Fig. 4. Static and dynamic finite element analyses were performed using this material mode. Dynamic analyses were also performed using strain-rate-sensitive flow stress as modelled
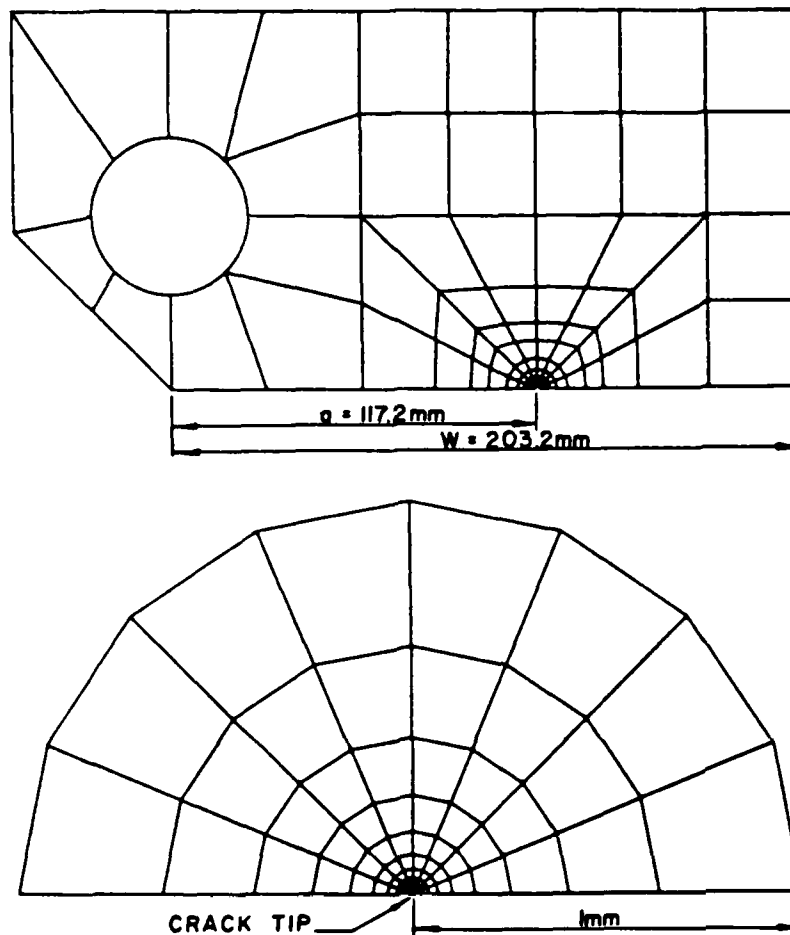
FIG. 3—*Finite element model of compact tension specimen.*

by Eq 14. The three parameters, $\sigma_s = 383$ MPa, $D = 62\,920/s$, and $p = 7.245$, were determined by Hoff et al [28] for A533B steel at 93°C.

The interaction of strain rate and inertial effects makes it difficult to isolate the contribution of either. A technique was devised to eliminate the inertial effect in order to quantitatively assess the importance of the strain rate effect. A linear elastic static analysis was first performed. All the resulting nodal displacements were scaled by a constant giving initial velocities at each node. The scaling constant was chosen so that the load point velocity produced by this scaling technique was equal to that load point velocity required to give the desired K_I-rate, $\dot{K}_I$. A dynamic analysis was then performed, starting with an unloaded model (all displacements zero) but with an initial velocity distribution. The nodal velocities did not change appreciably during the analysis. With almost constant nodal velocities, the nodal accelerations are very small and the model is essentially "inertialess". Further evidence of the inertialess character of this analysis is that the kinetic energy varied by only ±3.4% throughout the analysis.

Several finite element analyses were performed under static and inertialess dynamic loading. Table 1 summarizes the essential features of these analyses.
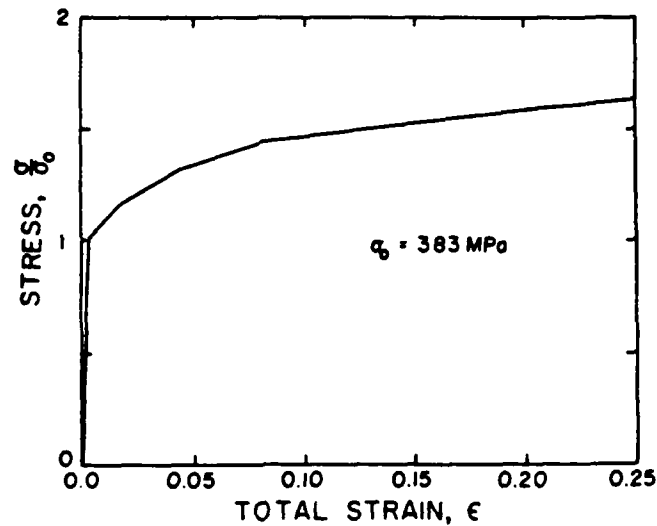
FIG. 4—*Zero strain rate stress-strain curve for A533B steel at 93°C.*

Results and Discussion

Results for the static analysis, S04, are given in Figs. 5 to 7 at a load level of $J_1 = 182$ kJ/m^2. Figure 5 shows contours of equivalent stress. Note that all distances are scaled by the similarity parameter, $(K_1/\sigma_0)^2$, so that

$$R = \frac{r}{(K_1/\sigma_0)^2} \tag{21}$$

Figure 6 shows contours of equivalent plastic strain in the same region as Fig. 5. A comparison of the equivalent plastic strain at $\theta = 45°$ from the finite element computation with the J-field solution of Eq 6 is shown in Fig. 7. Note the good agreement between these two approaches.

The average plastic strain can be determined from an area average of the plastic strains in the crack tip plastic zone according to

$$\epsilon_{P(ave)} = \frac{1}{A_P} \int \epsilon_P \, dA_P \tag{22}$$

In spite of the larger plastic strains near the crack tip, the average is $\epsilon_{P(ave)}$ = 0.0016 due to the large portion of the plastic zone that is lightly strained.

Analysis S16 features "fast" inertialess dynamic loading (see Table 1 for definition of fast and slow) without strain-rate-sensitive flow stress. The equivalent stress and equivalent plastic strain contours for this case are very similar to Figs. 5 and 6 and are not reproduced here. Plastic strain rate contours are plotted in Fig. 8 at a load level of $J_1 = 181$ kJ/m^2. Plastic strain rates along a line at $\theta = 45°$ plotted in Fig. 9 show the good agreement between the finite element results and the J-field solution of Eq 10. Some scat-

TABLE 1—Summary of finite element analyses.

Analysis Identification	Analysis Type	Load Line Velocity, m/s	$\dot{K}_1$, MPa$\sqrt{m}$/s	$J_{I(max)}$, kJ/m^2	$\dot{J}_{I(max)}$, kJ/m^{2}s	$\dot{\epsilon}_{P(ave)}$ at Maximum Load, 1/s	Rate Dependent?
S04	Static	0	0	362.	0	0	no
S12	dynamic-slow (inertialess)	10^{-5}	1.0	342.	2.00	1.33×10^{-5}	no
S16	dynamic-fast (inertialess)	1.0	10^5	362.	2.01×10^3	1.36	no
S20	dynamic-slow (inertialess)	10^{-5}	1.0	367.	2.04	1.31×10^{-5}	yes
S24	dynamic-fast (inertialess)	1.0	10^5	388.	2.18×10^5	1.21	yes
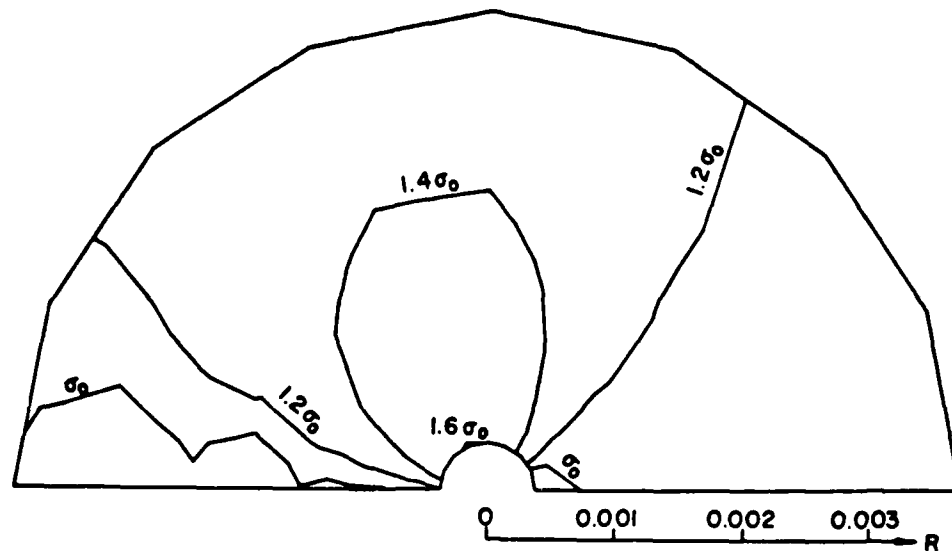
FIG. 5—*Contours of equivalent stress; static analysis S04.*

ter is present at very small values of R in Fig. 9 due to the difficulties in numerically modelling the very large strains at the crack tip.

The average plastic strain rate can also be determined from an area average according to

$$\dot{\epsilon}_{P(ave)} = \frac{1}{A_P} \int \dot{\epsilon}_P \, dA_P \tag{23}$$

Plastic strain rates as high as 10^3/s are observed near the crack tip, but the average strain rate is only 1.06/s. This is also due to the large portion of the plastic zone that is lightly strained and therefore strains at a lower rate. (The

FIG. 6—*Contours of equivalent plastic strain; static analysis S04.*
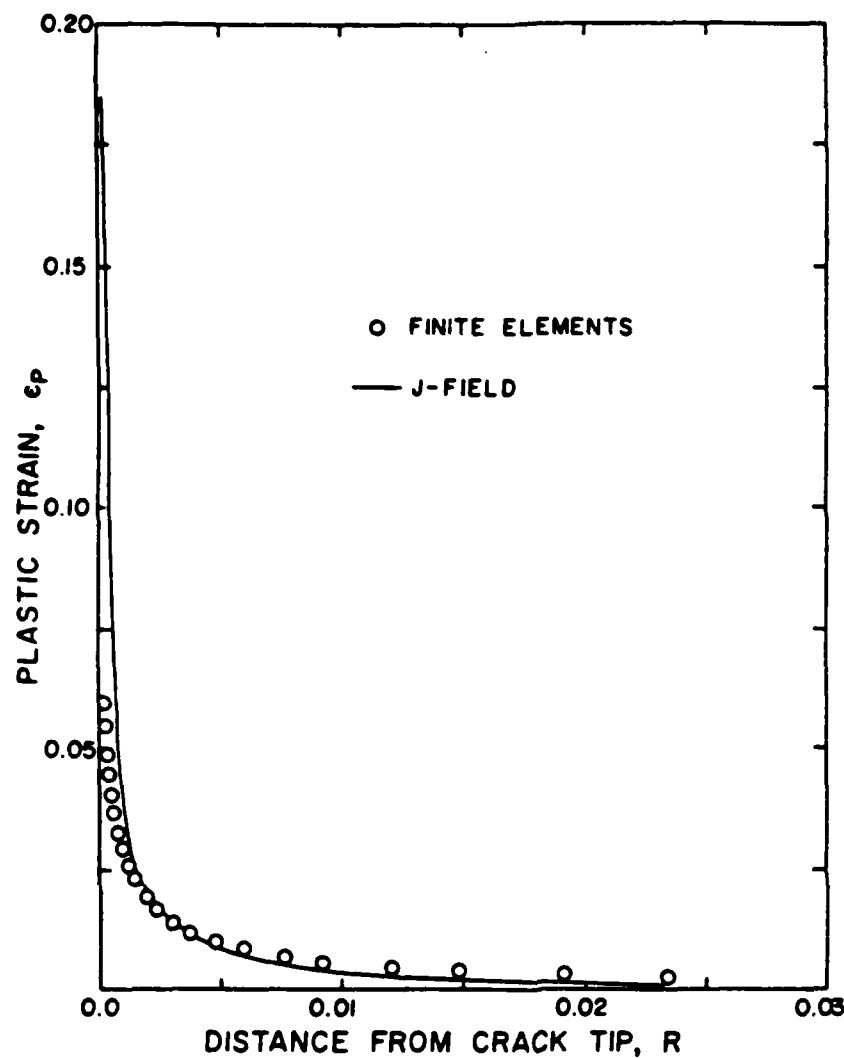
FIG. 7—*Plastic strain versus distance from crack tip at θ = 45°; static analysis S04.*

FIG. 8—*Contours of plastic strain rate; $J_1 = 181 \ kJ/m^2$, $\dot{J}_1 = 1.63 \times 10^5 \ kJ/m^2s$; rate-insensitive dynamic analysis S16.*
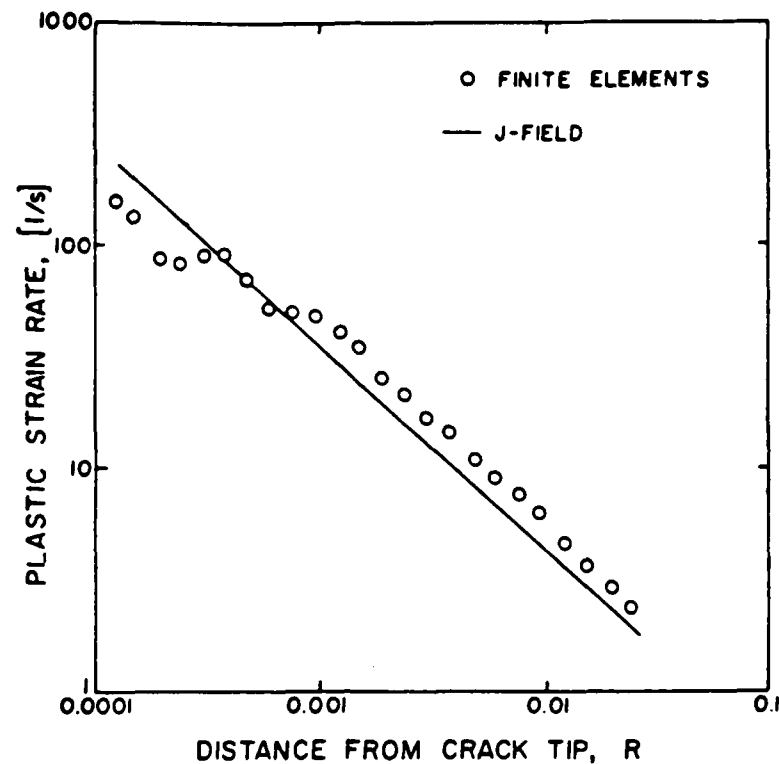
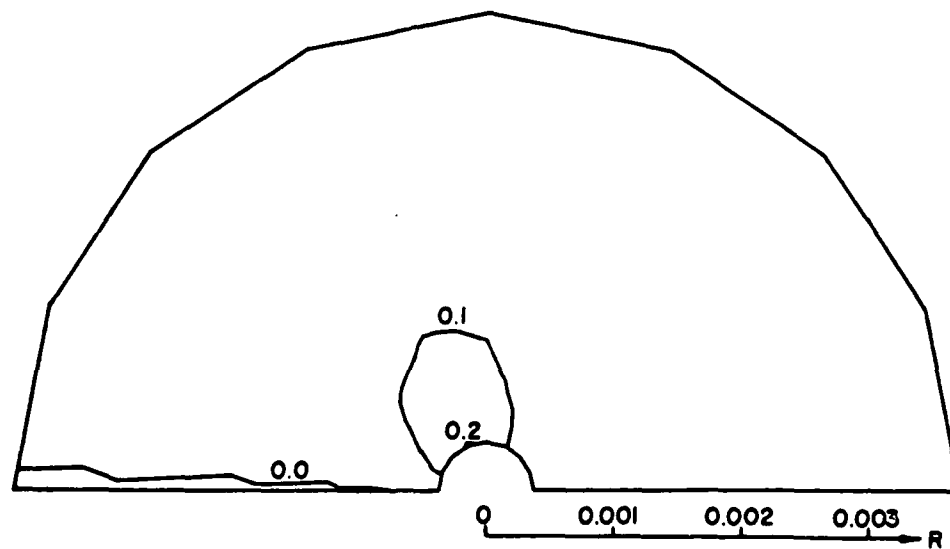FIG. 9—*Plastic strain rate versus distance from crack tip at* $\theta = 45°$; $J_1 = 181$ *kJ*/m^2, $\dot{J}_1 = 1.63 \times 10^5$ *kJ*/m^2s; *rate-insensitive dynamic analysis S16.*

analysis did not account for the possibility, and effects, of adiabatic heating in the very rapidly strained region at the crack tip.)

Analysis S24 is similar to S16, except that a strain-rate-dependent flow stress was used. The character of the equivalent stress, equivalent plastic strain, and plastic strain rate contours (Figs. 10 to 12) are similar in form to the static and the dynamic (rate-insensitive) case, but the magnitudes of these
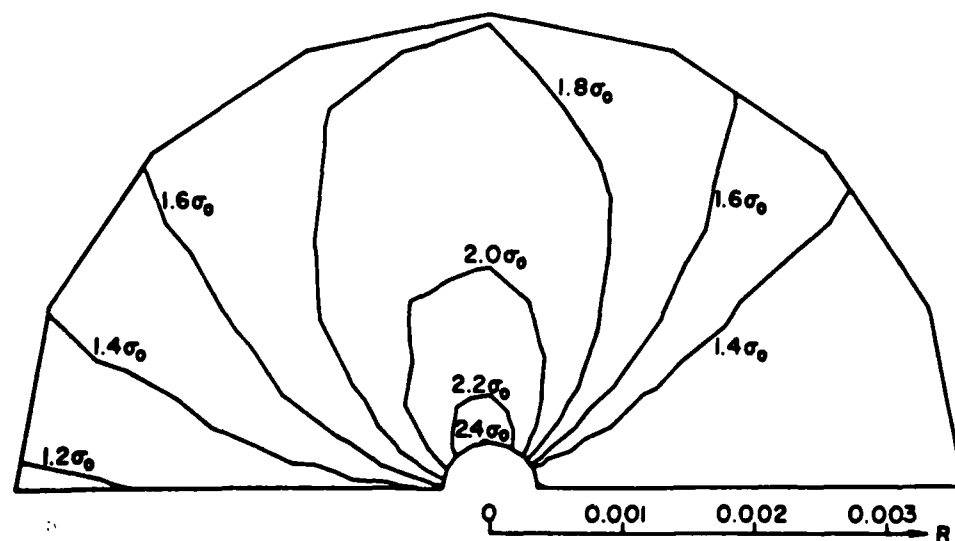
FIG. 10—*Contours of equivalent stress;* $J_1 = 188$ *kJ*/m^2, $\dot{J}_1 = 1.77 \times 10^5$ *kJ*/m^2s; *rate-sensitive analysis S24.*
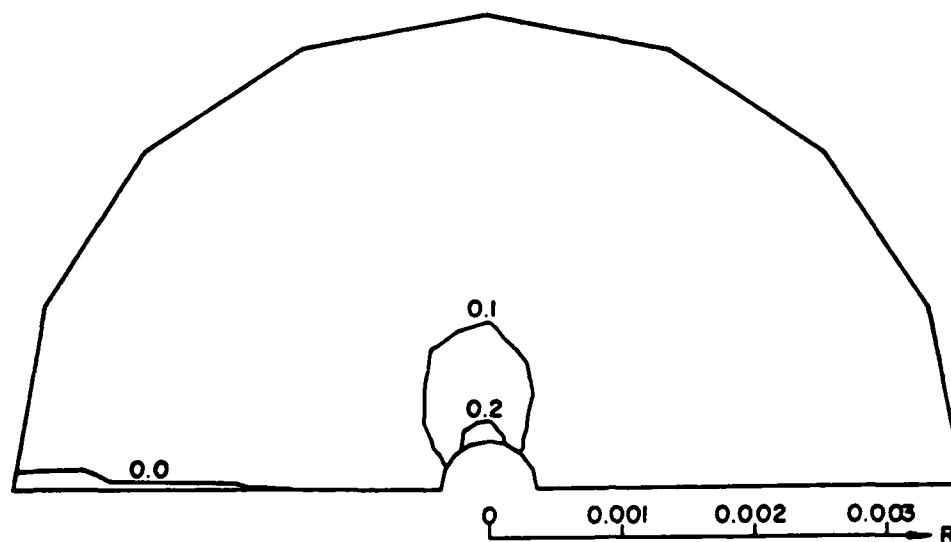
FIG. 11—*Contours of plastic strain;* $J_1 = 188 \ kJ/m^2$, $\dot{J}_1 = 1.77 \times 10^5 \ kJ/m^2 s$; *rate-sensitive dynamic analysis S24.*

quantities are quite different. It is interesting that the magnitudes of all these quantities are higher than for the static case at a comparable J_1-level. This is largely due to the change in the "effective" stress-strain curve resulting from the strain-rate effects (Fig. 2). Figure 13 compares the equivalent stresses and equivalent plastic strains from the dynamic rate-sensitive analysis (S24) with the dynamic rate-insensitive analysis (S16) along a line at $\theta = 45°$. The plotted points are from the finite element results, and the curves are from the J-field solution (the rate-sensitive curve was developed by using the modified α' and n' parameters). These results all show that the effect of strain-rate-sensitive
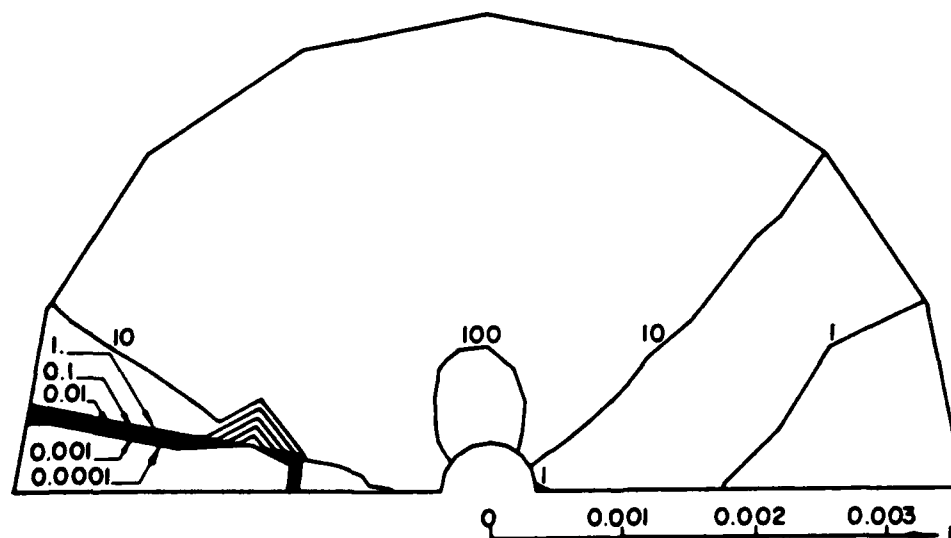
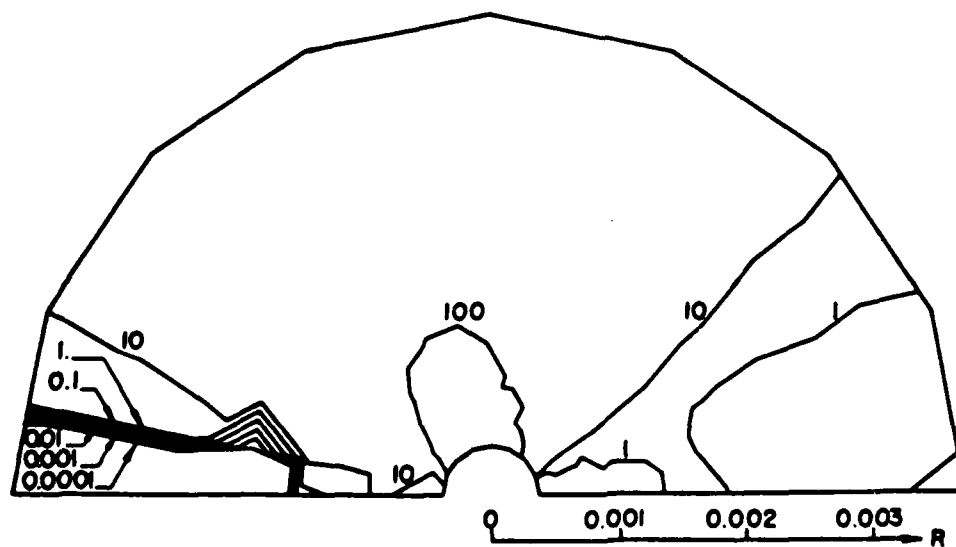FIG. 12—*Contours of plastic strain rate;* $J_1 = 188 \ kJ/m^2$, $\dot{J}_1 = 1.77 \times 10^5 \ kJ/m^2 s$; *rate-sensitive dynamic analysis S24.*
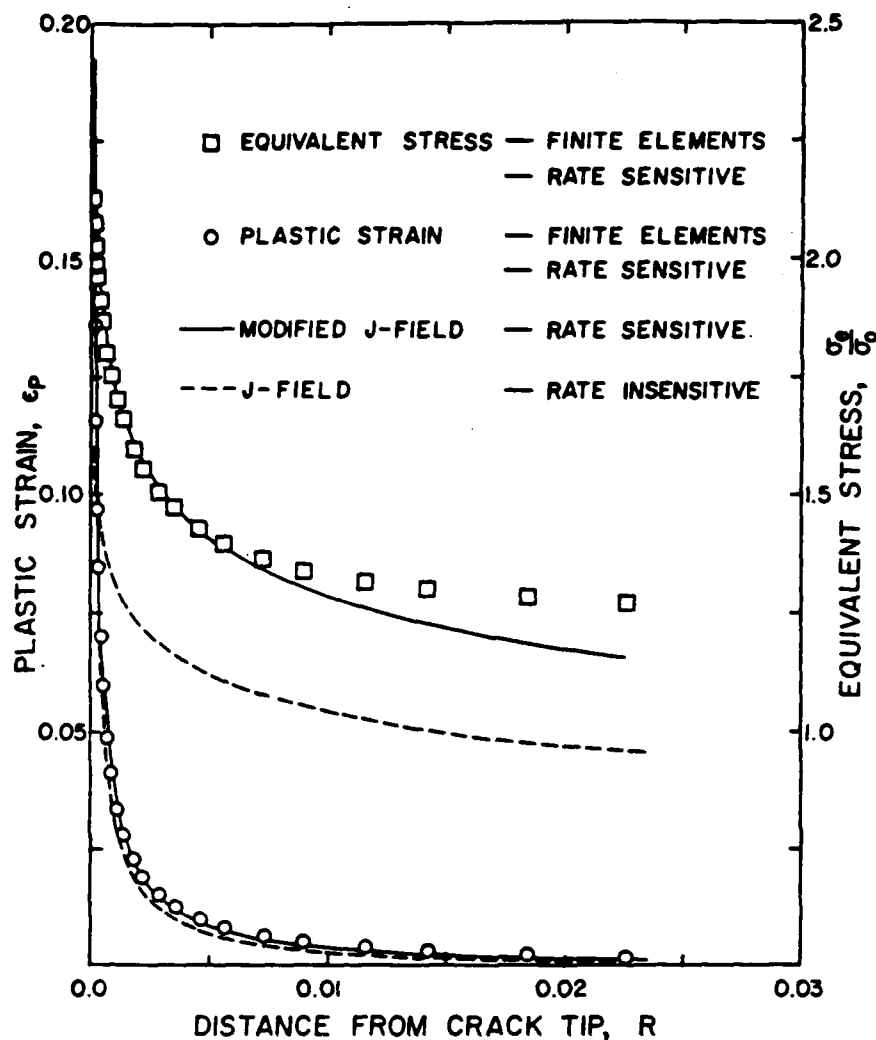
FIG. 13—*Comparison of equivalent stress and plastic strain from the fast dynamic rate-sensitive analysis, S24, with the fast dynamic rate-insensitive analysis, S16.*

flow stress is to significantly alter the magnitudes of the stresses and strains at the tip of a crack.

The constant-rate stress-strain curve, plotted as a dashed line in Fig. 2, does not map the finite element data in Fig. 13 when used in the J-field equations. The equivalent stress is underpredicted, particularly where the plastic strains are large.

Analyses S12 and S20 are much more slowly loaded dynamic, inertialess computations. The loading rate is $\dot{K}_1 = 1.0$ MPa$\sqrt{m}$/s, which is within the range of $0.55 \leq \dot{K}_1 \leq 2.75$ MPa$\sqrt{m}$/s used in ASTM Test for Plane-Strain Fracture Toughness of Metallic Materials (E 399). Even at this slow loading rate, there is a difference of roughly 10% in equivalent stress and 2% in equivalent plastic strain, as shown in Fig. 14 along a line at $\theta = 45°$.

The crack tip opening displacement has been used as a fracture initiation parameter. Figure 15 plots the crack tip opening displacement δ as a func-
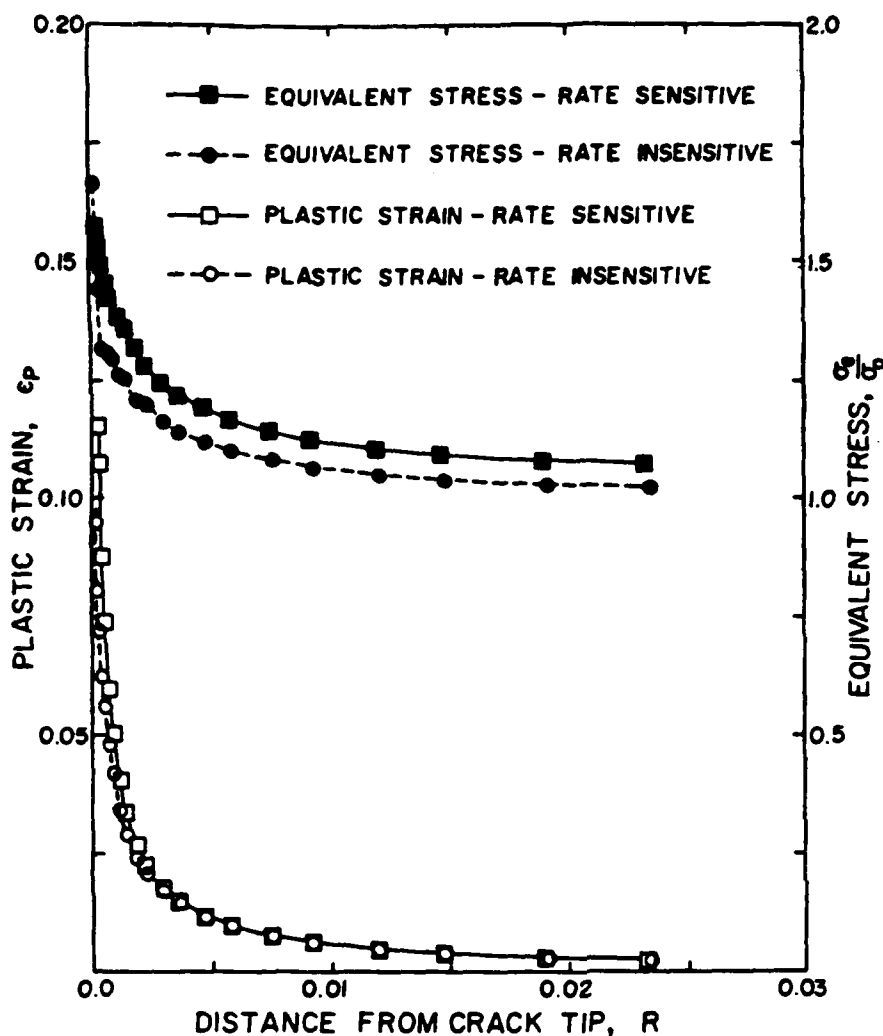
FIG. 14—*Comparison of equivalent stress and plastic strain from the slow dynamic rate-sensitive analysis, S20, with the slow dynamic rate-insensitive analysis, S12.*

tion of J_1. It is clear that the strain-rate-dependent flow stress has a significant effect on δ. Consider the rate-insensitive analysis, S16. At the point intersected by the dashed line, $J_1 = 182$ kJ/m^2 and $\delta = 237$ μm. The average plastic strain rate is 1.06/s. This strain rate would raise the flow stress by a factor of 1.22 according to the Malvern equation (Eq 14), with $D = 62\,920$/s and $p = 7.245$, and if the material were rate-sensitive. This increase in flow stress would correspond to a 22% larger J_1 value according to Eq 13, if δ were constant. Figure 15 shows that the J_1 value for the dynamic rate-sensitive analysis, S24, is in fact 25% larger than the rate-insensitive analysis. A less pronounced difference is found between the slowly loaded analyses, S12 and S20, where a 4% change in σ_0 and J_1 is predicted by Eq 13 but is not verified by finite elements, since this is within the noise level of the computation. This suggests that a rapidly loaded rate-sensitive ductile material could fail at a higher J_{1c} than a slowly loaded one, if a critical crack tip opening displace-
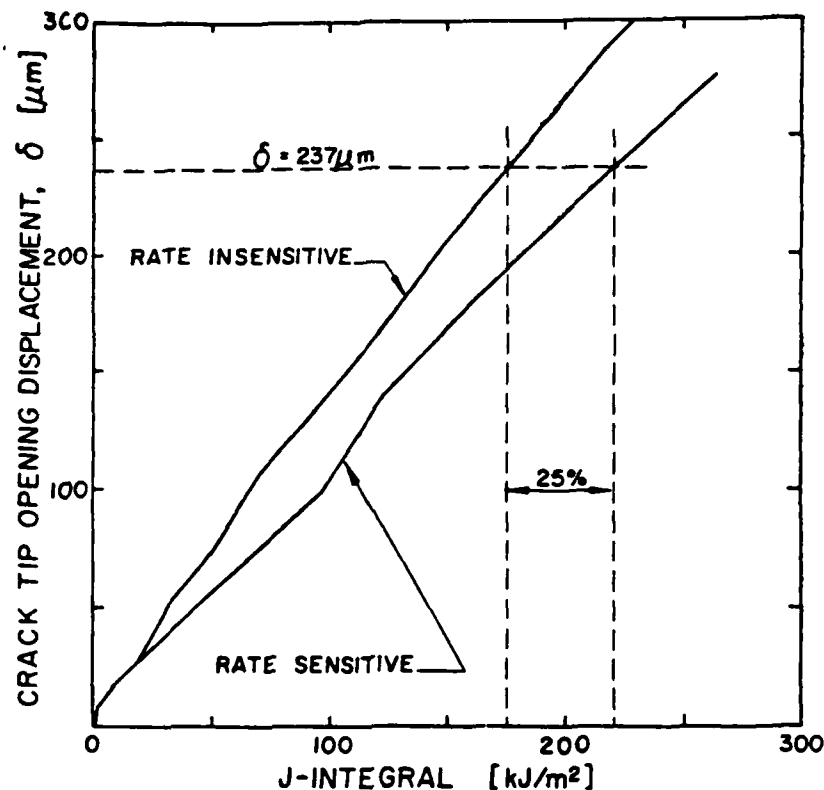
FIG. 15—*Crack tip opening displacement versus J-integral curves for the fast dynamic rate sensitive analysis, S24, and fast dynamic rate-insensitive analysis, S16.*

ment is the failure criterion. The work of Little et al [3] showed the same result, albeit that computations were performed in the $10^{-4} \leq \dot{K}_1 \leq 10^2$ MPa$\sqrt{m/s}$ range.

The J'-integral, discussed earlier in this paper, was also calculated for each dynamic analysis. The kinetic energy density term is very small along the integration contours close to the crack tip, and the inertia term is also very small due to the small accelerations produced by the inertialess loading techniques. As a result, the differences between Rice's J-integral and the J'-integral are less than 0.09% for the analyses considered in this study. Consequently, the treatment of these dynamic problems by using the (static) J-field solutions of Eqs 5 and 6 is justified in the case of inertialess loading.

The authors recognize that actual dynamically loaded structures and laboratory specimens do not exhibit the analytical tractability of inertialess numerical models. Determination of the stress and strain fields is complicated by vibrations that create localized unloading and even reverse plasticity. The J-field solutions are not applicable in these cases, and Rice's J-integral is no longer path-independent. As a first step in the dynamic analysis of cracked bodies where inertial effects are significant, the authors have performed preliminary elastic-plastic finite element analyses. The J'-integral *is* path-

independent in these cases and shows promise as an elastoplastic stress field characterizing parameter, since it has already been used to describe the stress state in elastodynamically propagating cracks [29]. The details are still unresolved of how the stress state can be described using J' in the elastoplastic dynamic case, providing a challenging topic for ongoing research.

Conclusions

A technique has been described in which finite element analyses were performed on dynamically loaded models without any inertial effects. This "inertialess loading technique" permitted quantitative determination of the effects of strain-rate-dependent flow stress.

Another technique was developed that enabled the stresses, strains, and crack opening displacement to be approximated by a simple modification of the α and n parameters in the power stress-strain law. Using the modified parameters, α' and n', in the J-field solution, stress and strains came to within 10% of a corresponding finite element computation, in regions where the J-field was applicable. This technique was only usable in conjunction with the inertialess loading technique.

Finite element computations revealed that stresses and strains in the crack tip plastic zone were higher in a rate-sensitive material than in a rate-insensitive material at corresponding J_1-values. Crack tip opening displacements, however, were lower in the rate-sensitive material. The same behavior was predicted using the α', n'-modified J-field solution.

Finite element computations also revealed that if a critical crack tip opening displacement were used as a failure criterion, then the strain-rate-dependent material could withstand a higher J-value before this δ_c was reached. Equation 13 showed that this increase in J_{Ic} could be predicted based on how the (area) average plastic strain rate would alter the flow stress.

The newly developed J'-integral was determined from the finite element results. In the case of a stationary crack under inertialess dynamic loading it is virtually identical to Rice's (static) J-integral. The J'-integral does appear promising in general dynamic loading situations with propagating cracks, since it remains path-independent, whereas Rice's J-integral does not.

References

[1] Hoff, R., Rubin, C. A., and Hahn, G. T. in *Proceedings, 29th Sagamore Army Research Conference*, J. Mescall and V. Weiss, Eds., Plenum Press, New York, 1983, p. 223.

[2] Aboudi, J. and Achenbach, J. D., *Engineering Fracture Mechanics*, Vol. 18, 1983, p. 109.

[3] Little, M. M., Krempl, E., and Shih, C. F., "On the Time and Loading Rate Dependence of Crack-Tip Fields at Room Temperature—A Viscoplastic Analysis of Small-Scale Yielding," in *Elastic-Plastic Fracture: Second Symposium, Volume 1—Inelastic Crack Analysis, ASTM STP 803*, American Society for Testing and Materials, Philadelphia, 1983, pp. 1-615-1-636.

[4] Levy, N., Marcal, P. V., Ostergren, W. J., and Rice, J. R., *International Journal of Fracture*, Vol. 7, 1971, p. 143.

[5] Rice, J. R., *Journal of Applied Mechanics*, Vol. 34, 1968, p. 379.

[6] Shih, C. F., *Journal of the Mechanics and Physics of Solids*, Vol. 29, 1981, p. 305.

[7] Hutchinson, J. W., *Journal of the Mechanics and Physics of Solids*, Vol. 16, 1968, p. 13.

[8] Rice, J. R. and Rosengren, G. F., *Journal of the Mechanics and Physics of Solids*, Vol. 16, 1968, p. 1.

[9] Bui, H. D. in *Fracture 3*, D. M. R. Taplin, Ed., University of Waterloo Press, Waterloo, Ontario, Canada, 1979, p. 91.

[10] Kishimoto, K., Aoki, S., and Sakata, M., *Engineering Fracture Mechanics*, Vol. 13, 1980, p. 841.

[11] Kishimoto, K., Aoki, S., and Sakata, M., *Engineering Fracture Mechanics*, Vol. 13, 1980, p. 387.

[12] Atluri, S. N., *Engineering Fracture Mechanics*, Vol. 16, 1982, p. 341.

[13] Green, G., and Knott, J. F., *Journal of the Mechanics and Physics of Solids*, Vol. 23, 1975, p. 167.

[14] Andrews, W. R. and Shih, C. F., "Thickness and Side-Groove Effects on J- and δ-Resistance Curves for A533-B Steel at 93°C, in *Elastic-Plastic Fracture, ASTM STP 668*, J. D. Landes, J. A. Begley, and G. A. Clarke, Eds., American Society for Testing and Materials, Philadelphia, 1979, pp. 426–450.

[15] Rice, J. R. and Johnson, M. A., in *Inelastic Behavior of Solids*, M. F. Kanninen et al, Eds., McGraw-Hill, New York, 1970, p. 641.

[16] Server, W. L., "Static and Dynamic Fibrous Initiation Toughness Results for Nine Pressure Vessel Materials," in *Elastic-Plastic Fracture, ASTM STP 668*, J. D. Landes, J. A. Begley, and G. A. Clarke, Eds., American Society for Testing and Materials, Philadelphia, 1979, pp. 493–514.

[17] Server, W. L., Oldfield, W., and Wullaert, R. A., "Experimental and Statistical Requirements for Developing a Well-Defined K_{IR} Curve," EPRI NP-372, Electric Power Research Institute, Palo Alto, CA, 1977.

[18] Wilson, M. L., Hawley, R. H., Duffy, J., *Engineering Fracture Mechanics*, Vol. 13, 1980, p. 371.

[19] Costin, L. S. and Duffy, J., *Journal of Engineering Materials and Technology*, Vol. 101, 1979, p. 258.

[20] Klepaczko, J., *Institute of Physics Conference Series*, Vol. 47, 1979, p. 201.

[21] Johnson, W. and Mellor, P. B., *Engineering Plasticity*, Van Nostrand, New York, 1973, p. 32.

[22] Malvern, L. E. in *Proceedings*, ASME Colloquium on Behavior of Materials under Dynamic Loading, American Society of Mechanical Engineers, New York, 1965, p. 81.

[23] Himmelblau, D. M., *Applied Nonlinear Programming*, McGraw-Hill, New York, 1972.

[24] DeLorenzi, H. G. and Shih, C. F., *International Journal of Fracture*, Vol. 13, 1977, p. 507.

[25] Hoff, R. and Byrne, T. P., "Residual Stress Analysis—A Comparison of Finite Element Results with Closed-Form Solutions," Research Division Report 81-232-K, Ontario Hydro, Toronto, Ontario, Canada, 1981.

[26] Kanninen, M. F., Rybicki, E. F., Stonesifer, R. B., Broek, D., Rosenfield, A. R., Marschall, C. W., and Hahn, G. T., "Elastic-Plastic Fracture Mechanics for Two-Dimensional Stable Crack Growth and Instability Problems," in *Elastic-Plastic Fracture, ASTM STP 668*, J. D. Landes, J. A. Begley, and G. A. Clarke, Eds., American Society for Testing and Materials, Philadelphia, 1979, pp. 121–150.

[27] Shih, C. F., deLorenzi, H. G., and Andrews, W. R., "Studies on Crack Initiation and Stable Crack Growth," in *Elastic-Plastic Fracture, ASTM STP 668*, J. D. Landes, J. A. Begley, and G. A. Clarke, Eds., American Society for Testing and Materials, Philadelphia, 1979, pp. 65–120.
[28] Hoff, R., Johnson, G. E., Rubin, C. A., and Hahn, G. T., *Journal of Pressure Vessel Technology*, Vol. 105, 1983, p. 316.
[29] Nishioka, T. and Atluri, S. N., *Engineering Fracture Mechanics*, Vol. 18, 1983, p. 1.

VISCOPLASTIC FINITE ELEMENT ANALYSIS OF RAPID FRACTURE

R. HOFF
Department of Mechanical Engineering, University of Waterloo, Ontario, Canada
N2L 3G1

and

C. A. RUBIN and G. T. HAHN
Mechanical and Materials Engineering, Vanderbilt University, Nashville, TN 37235, U.S.A.

Abstract—Rapid fracture in ductile viscoplastic materials is discussed in this paper. Following a review of previous studies of rapid fracture in ductile materials, a finite element model is developed for use with a crack extension algorithm discussed in a companion paper. Despite the lack of an established rapid ductile fracture criterion, computations which assumed that the δ–Δa history was the same for rapid fracture as it was for stable crack growth agree qualitatively with experimental data. It is shown that viscoplastic materials absorb considerably more energy during rapid fracture than rate insensitive materials and are therefore "tougher". A detailed examination of the stresses in the immediate vicinity of the crack tip reveals a constantly changing stress field that does not reach a "steady-state" as the crack tip translates.

NOMENCLATURE

A_p	crack tip plastic zone area
a	crack length
$\dot{a}$	crack velocity
Δa	crack growth
C_s	shear wave speed of the material; $C_s = (\mu/\rho)^{1/2}$
D	constant in viscoplastic constitutive relation (3)
E	Young's modulus
E_{ij}	undetermined function of θ and sometimes v, m or $\dot{a}/C_s$
J_1	Rice's path independent contour integral; energy release rate under quasistatic loading
J_{1c}	critical value of J-integral; when crack propagation initiates
J'_1	Atluri's path independent contour integral; energy release rate under dynamic loading
K	amplitude of stress or strain singularity
K_1	mode I stress intensity factor
m	ratio of tangent modulus to elastic modulus for a linear hardening material
n	strain hardening exponent
n_i	direction cosines
p	exponent in viscoplastic constitutive relation (3)
r, θ	polar coordinates
s	arc length
s	strength (exponent) of the stress and strain singularity for rapidly propagating crack; given in equation (1.2)
T	kinetic energy density; $T = \dot{u}_i \dot{u}_i / 2$
t	traction vector; $t_i = \sigma_{ij} n_j$
$\tilde{u}$	dimensionless function of θ and $\dot{a}$
$\mathbf{u}$	displacement vector
$\dot{\mathbf{u}}$	velocity vector
$\ddot{\mathbf{u}}$	acceleration vector
V	volume
v_L	load point displacement
$\dot{v}_L$	load point velocity
W	strain energy density; $W = \int_0^t \sigma_{ij} \, d\varepsilon_{ij}$
α	crack tip opening angle
α_c	critical crack tip opening angle
Γ	integration contour
δ	crack tip opening displacement
ε_{ij}	strain tensor
$\dot{\varepsilon}_{ij}^P$	dimensionless functions of θ and a

ε_0	yield strain: $\varepsilon_0 = \sigma_0/E$
$\dot{\varepsilon}_p$	equivalent plastic strain rate
$\dot{\varepsilon}_{p_{ave}}$	average plastic strain rate
μ	shear modulus
Σ_{ij}	undetermined function of θ and sometimes v, m or $\dot{a}/C_s$
σ_{ij}	Cauchy stress tensor
σ_{ij}	dimensionless functions of θ and $\dot{a}$
σ_m	mean or hydrostatic stress: $\sigma_m = (\sigma_x + \sigma_y + \sigma_z)/3$
σ_0	yield stress under static tensile loading
$\sigma_x, \sigma_y, \sigma_z$	normal stresses in the x, y and z-directions

INTRODUCTION

RAPIDLY propagating cracks in rate sensitive (viscoplastic) ductile materials are examined in this paper. Despite the practical importance of this class of fracture problem, particularly in relation to crack arrest phenomena, relatively little analytical or numerical work has been done in this field. After a brief review of previous work, the fracture criteria and finite element model will be described. The results of rapid crack growth simulation with crack velocities up to 100 m/s reveal that viscoplastic materials are significantly more resistant to crack propagation than rate insensitive materials.

The analysis of dynamic fracture in rate sensitive ductile materials is complicated by at least three nonlinearities: the material is ductile so fracture is accompanied by large amounts of plastic flow, load rates and crack speeds are sufficiently large to necessitate the inclusion of inertia effects in the analysis, and, many ductile materials of industrial interest have strain rate dependent flow properties. Other nonlinearities such as finite deformation effects and adiabatic heating at the tip of a rapidly propagating crack could be investigated, but these will not be included in this study.

The stress and strain fields at the tip of a rapidly propagating crack in a ductile rate insensitive material were characterized by Achenbach and Kanninen [1] for the Mode III case, and later by Achenbach *et al.* [2] for the Mode I case. For an elastic–linear strain hardening material:

$$\sigma_{ij} = K \sigma_0 r^s \Sigma_{ij} (\theta, v, m, \dot{a}/C_s) \tag{1}$$

$$\varepsilon_{ij} = K \sigma_0 r^s E_{ij} (\theta, v, m, \dot{a}/C_s) . \tag{2}$$

The order of stress and strain singularity is in the range $-0.5 < s < 0$. The asymptotic approach used to determine eqs (1) and (2) is unable to give values for the magnitude factor, K, which must be determined by other means.

Finite element modelling of rapid ductile fracture was performed by Ahmad *et al.* [3] and later by Barnes *et al.* [4] at Battelle Columbus Laboratories. Motivated by previous discoveries of Kanninen *et al.* [5] that quasistatic analyses or elastodynamic analyses grossly underestimate the resistance of AISI 4340 steel to crack growth under impact loading, the Battelle group performed dynamic finite element simulations of 3-point bend specimens using experimentally determined elastic–strain-hardening–plastic material properties. A critical crack tip opening angle was used as the fracture criterion, and crack extension was modelled using the "node release" technique described by various researchers [6–10]. Their numerical results for macroscopic parameters such as crack position as a function of time, and dynamic stress intensity factor agreed very well with the corresponding experiments. However, due to the coarseness of the computational grid, no results for near tip stresses or strain rates were obtained.

Lo [11] recently presented solutions to the problem of rapid crack extension in ductile materials with rate sensitivity. A semi-infinite crack propagating in the x-direction under small scale yielding conditions was modelled. An asymptotic analysis, in the sense of Amazigo and Hutchinson [12] and Achenbach *et al.* [2], was performed on the basis of crack velocities less than the shear wave velocity of the material. The analysis uses one of the elastic–viscoplastic constitutive relations described by Perzyna [13] which does not include strain hardening but models associated viscoplastic flow. The Perzyna relations are stated in a general three-dimensional form, of which the one-dimensional case specializes to

$$\dot{\varepsilon}_P = D\left[\frac{\sigma}{\sigma_0} - 1\right]^p. \tag{3}$$

The parameters σ_0, D and p must be determined experimentally [14].

The near tip stresses, strains and displacements were determined based on the assumption that they would be singular in r:

$$\sigma_{ij} = \left[\frac{\dot{a}}{BE}\right]^{1/p-1} r^{1/p-1} \tilde{\sigma}_{ij}(\theta, \dot{a}) \tag{4}$$

$$\varepsilon_{ij}^P = r^{1/p-1} \tilde{\varepsilon}_{ij}^P(\theta, \dot{a}) \tag{5}$$

$$u_i = \frac{1}{E}\left[\frac{\dot{a}}{BE}\right]^{1/p-1} r^{p-2/p-1} \tilde{u}_i(\theta, \dot{a}), \tag{6}$$

where $\dot{a}$ is the crack velocity, $B = D/\sigma_0^p$, D and p are defined by eq. (3), E is Young's modulus, r and θ are coordinates centered on the moving crack tip, and $\tilde{\sigma}_{ij}$, and $\tilde{\varepsilon}^P_{ij}$ and $\tilde{u}_i$ are dimensionless functions of θ and $\dot{a}$.

The possibility of using the J-integral, or any dynamic variation of the J-integral idea, as a near tip characterizing parameter is completely ruled out by eqs (4–6). The J-integral is path independent for stationary cracks since it is comprised of energy density terms, order r^{-1}, integrated around a closed path, order r^1, which result in the order r^0 integral J. (Energy density terms are of the form $\sigma_{ij} \varepsilon_{ij}$ and are given by the HRR singularity solution as being singular in r to the order -1). In the rate sensitive rapid ductile crack extension case, eq (4–6) would result in the energy density, order $r^{-2/p-1}$, being integrated around a path, order r, giving a quantity of order $r^{p-3/p-1}$. Therefore as $r \to 0$, (for $p > 3$) this contour integral also tends to zero, not a desirable property for a path independent integral. Some form of J may still be used as a (relatively) far field characterizing parameter, providing it is calculated along a contour where no unloading takes place. That is not unlike the justification for using J_1 to predict tearing instability [15] or using J_1 in the presence of crack tip blunting [16, 17].

The Lo results also reveal that the hydrostatic or mean normal stresses, $\sigma_m = (\sigma_{xx} + \sigma_{yy} + \sigma_{zz})3$, ahead of the propagating crack tip, decreases with increasing crack velocity. As $\dot{a}$, C, increases from 0 to 0.61, decreases in σ_m of 40% and 28% are reported for $p = 4$ and $p = 6$, respectively. It was shown by McClintock [18] and Rice and Tracey [19] that void and hole growth is enhanced by high hydrostatic tensile stresses (neglecting the issue of whether sufficient time is available for this to occur in dynamic situations). Since ductile fracture is the end result of a hole growth process, any phenomenon which affects hole growth will affect ductile fracture. However, it is difficult to predict what affects the interrelation between hydrostatic stresses, critical strain to fracture, and crack velocity, will have on a fracture parameter such as the critical crack tip opening angle.

The only reported finite element study of rapid crack propagation in rate sensitive ductile materials was performed by Brickstad [20]. The Brickstad analysis makes use of the Perzyna [13] elastic-viscoplastic constitutive model with linear strain hardening, for a high strength carbon steel ($\sigma_0 = 1485$ MPa). The "energy flow into the crack tip region" was used as the fracture criterion, and crack extension was modelled using the "node release" technique [6–10]. The energy flow into the crack tip region is a mesh size dependent parameter, but previous finite element calculations of this parameter by Rydholm et al. [21] had agreed well with theoretical predictions in elastodynamic problems.

Brickstad [20] used a rather coarse mesh, and could not comment on the near tip stress and strain distributions. However he noted strain rates of the order 10^3/s at the Gauss points nearest the crack tip propagating at 250–750 m s.

The analytical work of Lo [11] and the finite element analyses of Brickstad [20] suggest that the fracture resistance of viscoplastic materials is enhanced at high crack velocities. The finite element analyses undertaken in this study quantitatively assess the increased fracture resistance of a viscoplastic material: A533B steel at 93 C, and elucidate details of the crack tip stress field during rapid crack propagation.

FINITE ELEMENT MODELLING

The finite element model used in the analysis of rapid crack growth is depicted in Fig. 1. The material is modelled as linear elastic up to the yield point, and then with power law hardening beyond first yield:

$$\frac{\varepsilon}{\varepsilon_0} = \frac{\sigma}{\sigma_0}, \quad \sigma \leqslant \sigma_0 \tag{7}$$

$$\frac{\varepsilon}{\varepsilon_0} = \left(\frac{\sigma}{\sigma_0}\right)^n, \quad \sigma \geqslant \sigma_0. \tag{8}$$

with $\sigma_0 = 382.866\,\text{MPa}$, $E = 197.62\,\text{GPa}$, $\varepsilon_0 = \sigma_0/E$, and $n = 10$. The rate dependent analyses employed the rate sensitivity model stated by Perzyna in ref. [13].

$$\dot{\varepsilon}_P = D\left[\frac{\sigma}{\sigma_0} - 1\right]^p, \tag{9}$$

with $D = 62919.55$ and $p = 7.24545$. Close correspondence of the analytical model with measurements of the flow properties of A533B steel at 93°C is demonstrated in a separate paper [14]. While it is still debatable whether eq. (9) is the "correct" representation of the constitutive behaviour of A533B steel at very high strain rates, it does give good agreement with experimental results in the range $\dot{\varepsilon}_P < 10^4$/s.

Any crack growth simulation must incorporate a method for continuously changing the boundary conditions. A companion paper [22] presents a detailed discussion about how spring and gap elements may be used, in the general purpose program ABAQUS, to simulate crack extension.

An initial velocity field was imposed on the specimen at the beginning of the analysis. This was to prevent the occurrance of large load impulses at the beginning of the analysis. Impulsive loads induce large amplitude vibrations in the model which overwhelm the inertial and viscoplastic effects at the crack tip. The same technique was used successfully in the analysis of rapidly loaded stationary cracks [23].
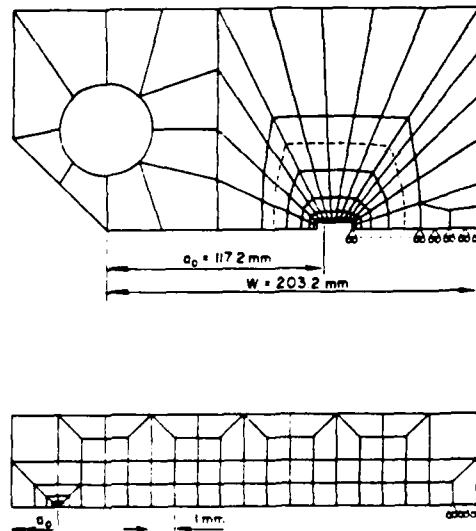

Fig. 1. Finite element model of compact tension specimen used in the investigation of propagating cracks.

Four analyses were performed: a rate insensitive one and a viscoplastic one at a moderate loading rate of $\dot{v}_L = 1$ m/s, as well as a rate insensitive analysis and a viscoplastic analysis at a higher loading rate of $\dot{v}_L = 100$ m/s. These analyses are summarized in Table 1. The computation time required for these simulations was typically 12–16 CPU hr. Although these computations were performed on a Decsystem-10 computer with a Tops-10 operating system, it was later shown that very similar times could be expected on a VAX 11/750 running the VMS operating system.

Table 1. Summary of finite element analyses for propagating cracks

Analysis identification	Analysis type	Load line velocity (m/s)	K_i at start (MPa$\sqrt{m}$/s)	Rate dependent?
P26	Static	0	0	No
P32	Dynamic	1.0	1.1×10^5	No
P42	Dynamic	1.0	1.1×10^5	Yes
P52	Dynamic	100.0	1.1×10^7	No
P62	Dynamic	100.0	1.1×10^7	Yes

IMPLEMENTATION OF FRACTURE CRITERIA

The necessity of using a particular fracture criterion in a finite element crack growth simulation forces one to make some *a priori* assumptions about the characterization of the ductile fracture process under rapid loading. Whereas stable crack growth can be characterized by an experimentally obtained J_r–Δa relationship just after initiation [7, 24], very few J_r–Δa results are available for rapid crack growth. In the absence of such experimental data, some other fracture criterion must be used at initiation and immediately following initiation.

The crack tip opening displacement, δ, shows promise as a near tip characterizing parameter since it can be interpreted as the integral of strains around the crack tip [25]. The δ–Δa history, used as the fracture criterion for the first 4 mm of growth in the dynamic analysis, was obtained from the results of the stable crack growth analysis [22]. Figure 2 illustrates that

$$\delta = -33.58\,(\Delta a)^2 + 0.47082\,\Delta a + 2.5332 \times 10^{-4} \tag{10}$$
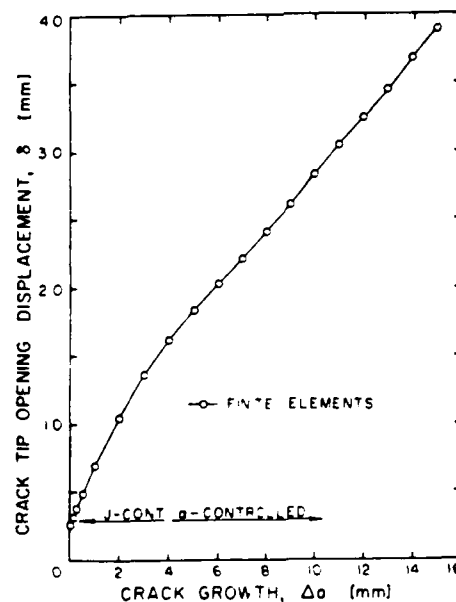

Fig. 2 Crack tip opening displacement vs crack growth.

(where δ and Δa are in meters), for $\Delta a \leqslant 4$ mm. A critical crack tip opening angle was used as the fracture criterion for $\Delta a > 4$ mm. The stable crack growth value of $\alpha_c = 0.24$ radians was used as the fracture criterion. The use of rate invariant values of δ (Δa) and α_c is equivalent to assuming that the local ductile fracture mechanism is rate insensitive. This assumption cannot be defended at this time. It is made so that its consequences can be tested against experiments.

The computational algorithms which performed the rapidly growing crack simulations were almost identical to those used for stable crack growth. However, the first 4 mm of crack growth were δ-controlled rather than J-controlled, as discussed in the preceding paragraphs.

RESULTS AND DISCUSSION

The results of the rapid crack growth simulations are presented in this section. Experimental results [24] and numerical results [22], pertaining to slow stable crack growth, are also presented where possible and appropriate.

Figure 3 is a plot of J_1 as a function of crack growth. It is known [24] that J_{1c} for the slow stable crack growth analysis is 200 kJ/m^2. Yet, fracture initiated in the rate insensitive dynamic analysis at $(J_1^i =)$ 205 kJ/m^2 and 223 kJ/m^2 for $\dot{v}_L = 1.0$ m/s and $\dot{v}_L = 100.0$ m/s, respectively; and fracture initiated in the viscoplastic analyses at 257 kJ/m^2 and 330 kJ/m^2 for $\dot{v}_L = 1.0$ m/s and $\dot{v}_L = 100.0$ m/s, respectively. Therefore, the effect of the local material inertia is not very significant at initiation, whereas the viscoplastic effects are quite large.

The rate insensitive dynamic results for $\dot{v}_L = 1.0$ m/s are virtually identical to the slow stable crack growth results. However, values of J_1^i from the viscoplastic analysis are always about 17% larger than the stable crack growth values. The same trend is evident in the $\dot{v}_L = 100.0$ m/s results: the rate insensitive results average out to about the same as the stable crack growth values, yet the viscoplastic results are about 30% larger.

The observation that rapid crack propagation in ductile materials must overcome more resistance than slow crack propagation was also observed by Kanninen *et al.* [5]. Although the Kanninen *et al.* study is inconclusive as to the source of the difference in toughness between slow and rapid loading, the finite element results of this paper do suggest that viscoplasticity could account for the difference.

The first 2.5 mm of crack growth are replotted in Fig. 4 and compared with experimentally determined J-resistance curves obtained by Joyce [26]. Joyce loaded 1/2T compact tension specimens ($W = 25.4$ mm) of A533B steel at a rate of 600 in/s whereby K_1 at the start of the test
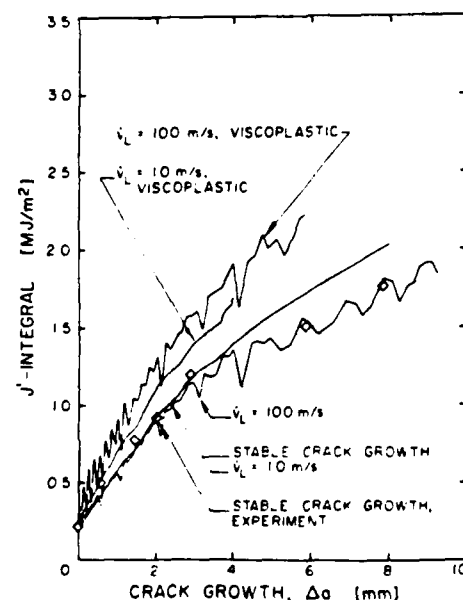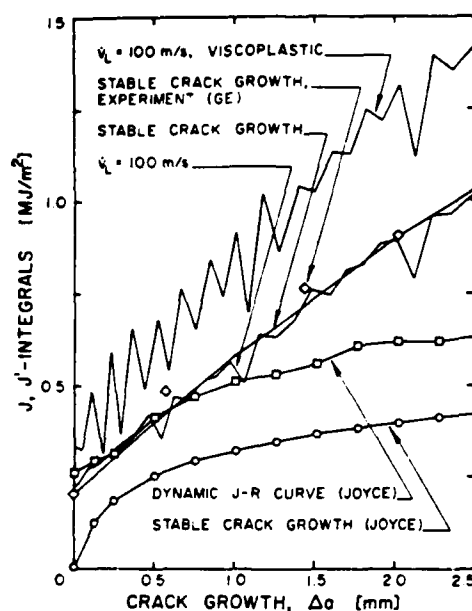

Fig. 3. J'-integral vs crack growth.

Fig 4. Static and dynamic J-resistance curves.

is about 22% higher than for the $\dot{v}_L = 100$ m/s cases studied here. Joyce's experimental results show more of a rate sensitive effect and this may be due to (i) Joyce tested at 150°C, whereas the finite element solutions assumed a temperature of 93°C, (ii) Joyce tested 1/2" thick specimens, whereas the finite element solution is based on a plane strain model, (iii) crack tip blunting is counted as crack growth in the slow stable crack growth results of Joyce, and, (iv) the inertia of the specimen appears as increased resistance to crack extension in the experimental results.

The $\dot{v}_L = 100.0$ m/s results have a high frequency oscillation superimposed on an otherwise monotonically increasing response. This is likely caused by the crack extension procedure which, by incrementally relaxing the boundary conditions at the crack tip nodes, puts small impulses into the crack tip region at each time increment. Evidence that the crack extension procedure is the source of these oscillations is, that during the first millimeter of crack growth, the oscillations are of a higher "frequency" than later on. Secondly. the "wavelength" of oscillations is about 1 mm (for $\Delta a > 1$ mm) where the element size is 1 mm. This crack extension technique may, therefore, be limited to load point velocities below, say, 500 m/s. This comment also applies to the node release technique mentioned in refs [6–8, 10]. However, the moving singularity element of Atluri and Nishioka [27–29] does show promise in this area, if a correct viscoplastic formulation can be found.

If the value of J_1 as stated by Rice,

$$J_1 = \int_\Gamma (Wn_1 - t_iu_{i,1})\, ds, \tag{11}$$

decreases as a function of time for the case of a stationary crack, then the specimen *must* be unloading and the use of J_1 is invalid. In contrast, the value of J_1 as stated by Atluri [30],

$$J_1' = \int_\Gamma [(W + T)n_1 - t_iu_{i,1}]\, ds + \int_V \rho[\ddot{u}_iu_{i,1} - \dot{u}_i\dot{u}_{i,1}]\, dV. \tag{12}$$

may decrease during the load history without the specimen necessarily unloading. At high loading rates, the inertia term ($\int_V \rho[\ddot{u}_i \ldots]\, dV$) of eq. (12) is comparable in magnitude to the strain energy

and traction terms. Small changes in the material point velocities will make the inertia term negative, and reduce J_1', even though the bulk of the specimen is still loading. This is the situation observed in the $\dot{v}_L = 100.0$ m/s analyses, and is the source of the oscillations in these results. The J'-integral values quoted in this paper are calculated along the contour shown by the dashed line in Fig. 1. Values of J' calculated at contours interior to this one are path independent (to within $\pm 10\%$) until the points at which the integration is performed experience unloading due to the effects of the growing crack.

Figure 5 is a plot of the crack tip opening angle as a function of crack growth. The crack tip opening angle is poorly defined during the first millimeter of crack growth, as in the case of stable crack growth. Between 1 and 4 mm of crack growth, the crack tip opening angle is very similar for the quasistatic and dynamic computations. This is likely due to the fact that the δ–Δa relationship from the stable crack growth analysis was used as the fracture criterion for the first 4 mm of crack growth in the dynamic analyses. After 4 mm of crack growth, all of the analyses use the same value of $a = 0.24$ radians as the fracture criterion. The viscoplastic $\dot{v}_L = 1.0$ m/s analysis has two anomalous points at $\Delta a = 0.125$ and 2.0 mm. After verifying that these data points are indeed correct, we can still offer no explanation for them.

Figures 6 and 7 are plots of load point displacement and load as a function of crack growth, respectively. The rate insensitive $\dot{v}_L = 1.0$ m/s results are virtually the same as the slow stable crack growth results. Since the load point displacement and load are higher in the viscoplastic $\dot{v}_L = 1.0$ m/s analysis (2% and 20%, respectively), an analysis which does not address viscoplastic effects for this case would seriously underestimate the energy dissipated during rapid crack growth. The $\dot{v}_L = 100.0$ m/s results have a different character than the slower loading rate results. The general form of the load vs Δa curves in Fig. 7 is that of a sine wave with a period of 190 μs (i.e. twice the time for about 6 mm of crack growth). This implies that the natural frequency of the overall specimen is about 5.3 kHz, which agrees very well with a handbook value for an cantilever beam with the same length as the arms of the compact tension specimen. This illustrates, not surprisingly, that the bulk motion of the specimen is greatly affected by the dynamic response of the specimen. The viscoplastic $\dot{v}_L = 100.0$ m/s analysis shows again that considerably more energy is dissipated due to viscoplasticity than could be accounted for in a rate insensitive elastoplastic dynamic analysis.

The normalized crack velocity, $\dot{a}/\dot{v}_L$, is plotted as a function of crack growth in Fig. 8. For the four cases here it appears that

$$\dot{a} \simeq (\alpha + \beta \, \Delta a) \, \dot{v}_L \qquad (13)$$
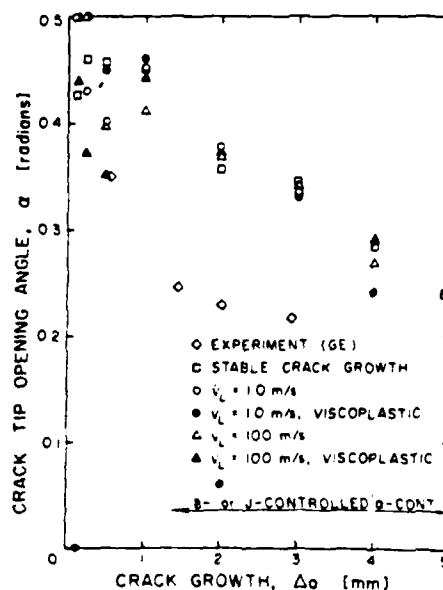$$= (0.4 + 1.40 \, \Delta a) \, \dot{v}_L$$
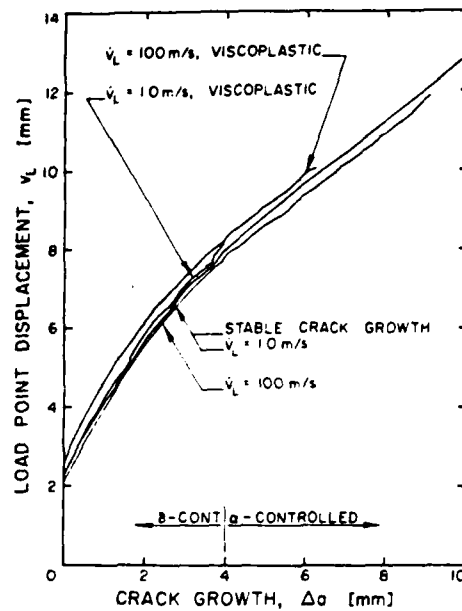

Fig. 5 Crack tip opening angle vs crack growth.

Fig. 6. Load point displacement vs crack growth.

(Δa is in meters). The constants α and β are geometry dependent: indeed, α and β reflect the fact that a compact tension specimen is kinematically equivalent to two cantilever beams. It appears that α and β are insensitive to inertia, load rate and strain rate.

Stresses ahead of the propagating crack tip are shown in Fig. 9–11. Unless otherwise stated in this discussion the word "stress" shall refer to equivalent stress, σ_e; "strain" shall refer to equivalent plastic strain, ε_P; and "strain rate" shall refer to equivalent plastic strain rate, $\dot{\varepsilon}_P$. At initiation, the stresses ahead of the crack tip are not a function of the material inertia so the
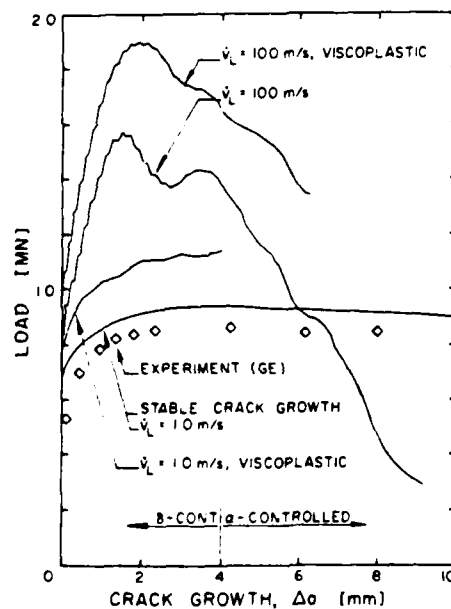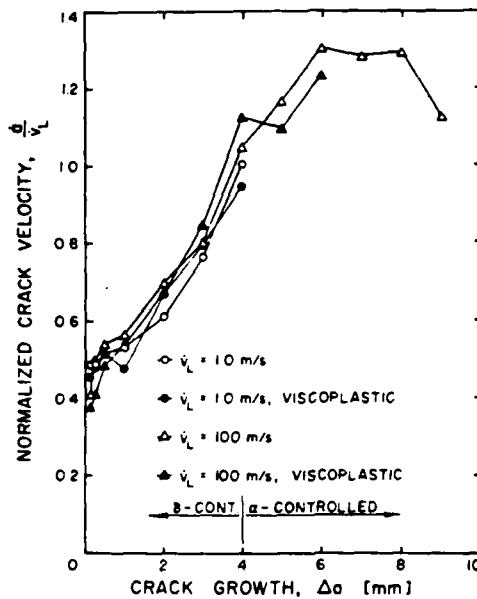

Fig 7. Load vs crack growth

Fig. 8. Normalized crack velocity vs crack growth.

$\dot{v}_L = 1.0$ m/s results are the same as the $\dot{v}_L = 100.0$ m/s results in Fig. 9. This idea was proved by Achenbach et al. [31] as $r \to 0$, and introduced into the finite element computation using the inertialess loading technique discussed in ref. [23]. Figure 9 shows that the stress is elevated by about 21% for the $\dot{v}_L = 100.0$ m/s analysis due to viscoplastic effects.

Figure 10 is a plot of the stresses for the four dynamic analyses after 4 mm of crack growth. The results are not nearly as smooth as the initiation results. The oscillations in stress could be due to noise in the computation, but are more likely due to the dynamic response of the material near the crack tip. The stress oscillations are very similar for the two $\dot{v}_L = 100.0$ m/s analyses, and for the two $\dot{v}_L = 1.0$ m/s analyses, and are therefore not due to random noise. The viscoplastic effects again raise the magnitude of the stresses appreciably. The notion of Lo [11] that
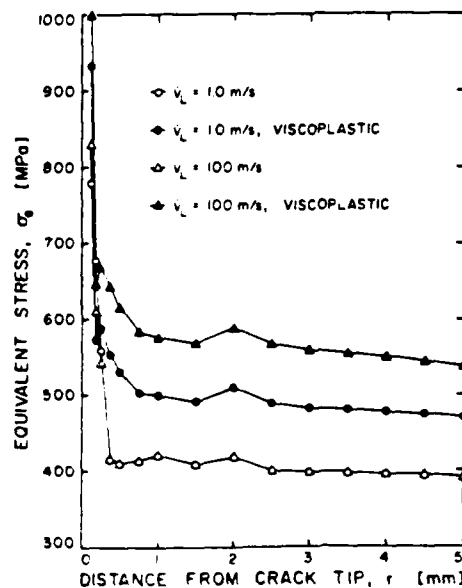
Fig 9 Equivalent stress vs distance from crack tip at fracture initiation.
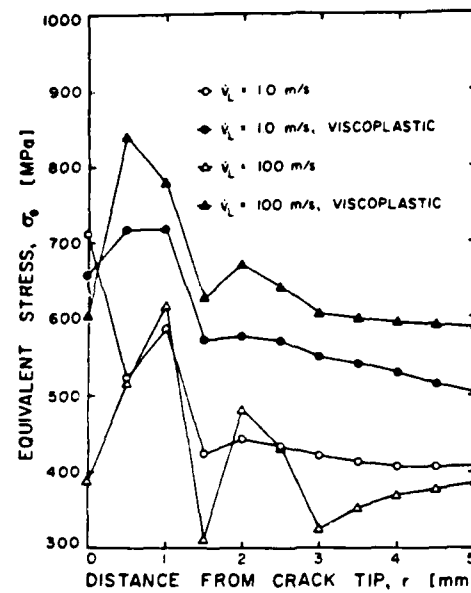
Fig. 10. Equivalent stress vs distance from crack tip after 4 mm of crack growth.

viscoplasticity makes the near tip stress fields more singular cannot be addressed on the bases of Fig. 9–11 since this would require a crack tip mesh at least an order of magnitude finer than the one used here.

Figures 11 is a plot of the stresses after 8 mm of crack growth. Results were only available for the $\dot{v}_L$ = 100.0 m/s case. Again significant elevation in stress is apparent due to viscoplastic effects.

Figures 12–14 are plots of the strain ahead of the propagating crack tip and correspond to the stress plots in Figs. 9–11. The inertia of the material near the crack tip does not appear to influence the strain. However, the rate sensitivity increases the strain, a small amount at initiation, a little more after 4 mm of crack growth, and more still after 8 mm of crack growth, as shown in

Fig 11. Equivalent stress vs distance from crack tip after 8 mm of crack growth

R. HOFF *et al.*
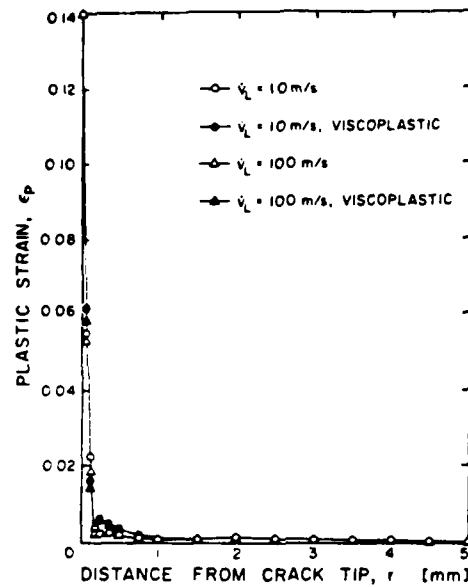
Fig. 12. Plastic strain vs distance from crack tip at fracture initiation.

Figs 12–14. This is contrary to the results of creep studies by Little *et al.* [32] which indicated smaller plastic strains due to increasing strain rate.

The results presented in Figs 9–14 do not represent the crack tip stress or strain fields on a sufficiently fine size scale to permit conclusions to be drawn about what effects inertia and rate sensitivity have on the critical strain to fracture in the fracture process zone. The results do give a good representation of stress and strain in the region around the crack tip where the *J*-field solutions would be applicable if the cracks were stationary.

The plastic strain rates are plotted as a function of distance from the crack tip in Figs 15–17. In general, the $\dot{v}_L = 100.0$ m s strain rates are 2 orders of magnitude higher than the $\dot{v}_L = 1.0$ m s strain rates. The strain rates at initiation are well-behaved, whereas, the strain rates after 4 or
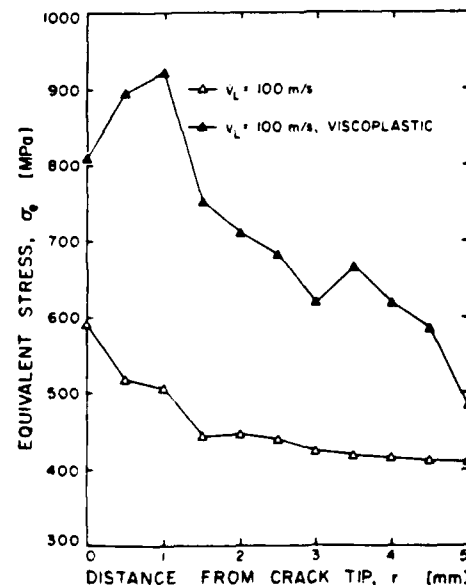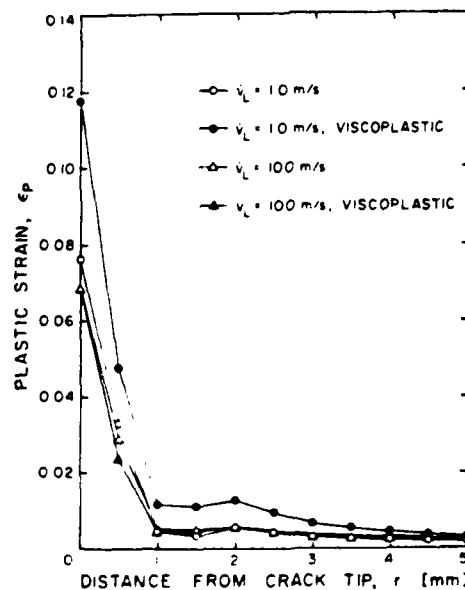

Fig 13. Plastic strain vs distance from crack tip after 4 mm of crack growth.
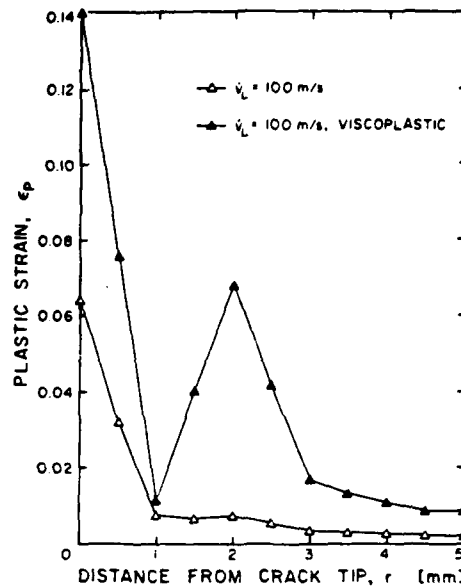
Fig. 14. Plastic strain vs distance from crack tip after 8 mm of crack growth.

8 mm of crack growth vary dramatically. Small errors in strain tend to be magnified when calculating strain rates; this is partly the cause of the large strain rate fluctuation. It is therefore difficult to generalize these results. (Note that data points which would fall below the axes shown in these figures have been omitted. Their omission is indicated by joining the adjacent data points with dotted lines.)

Figure 18 is a plot of the average plastic strain rate, defined by

$$\dot{\varepsilon}_{Pave} = \frac{1}{A_p} \int \dot{\varepsilon}_P \, dA_P, \tag{14}$$
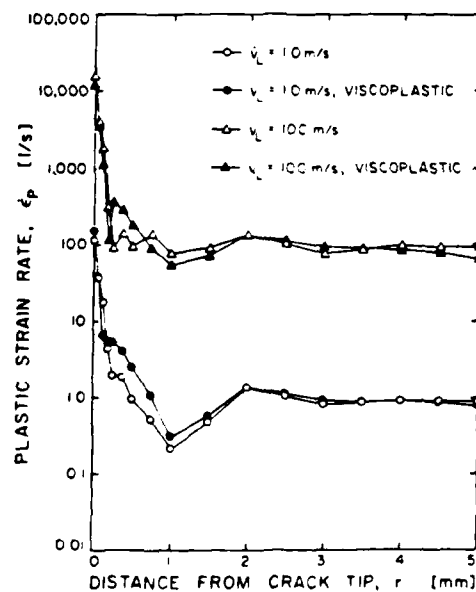
Fig. 15. Plastic strain rate vs distance from crack tip at fracture initiation.
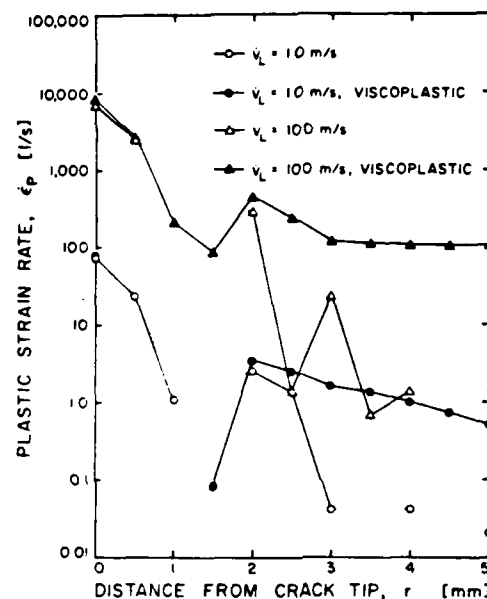
Fig. 16. Plastic strain rate vs distance from crack tip after 4 mm of crack growth.

as a function of crack growth. The average plastic strain rates are about 1/s and 100/s for the $\dot{v}_L = 1.0$ m s analysis and the $\dot{v}_L = 100.0$ m/s analysis respectively. Substituting these values into the Perzyna equation (3) implies that the stresses increase by 22% and 41%, respectively, due to viscoplastic effects. This is substantiated by Fig. 9 at initiation, and to a lesser degree by Figs 10 and 11 after 4 or 8 mm of crack growth. This supports the observation made previously [23] that rate effects in the bulk of the specimen can be estimated based on the knowledge of an average strain rate.

The deformed crack profiles are shown in Fig. 19 for the $\dot{v}_L = 100.0$ m s viscoplastic analysis. A startling feature is the large peak located at $x = 0$, which develops after crack initiation. This must be due to viscoplastic effects, since it was not observed in the rate insensitive analyses or
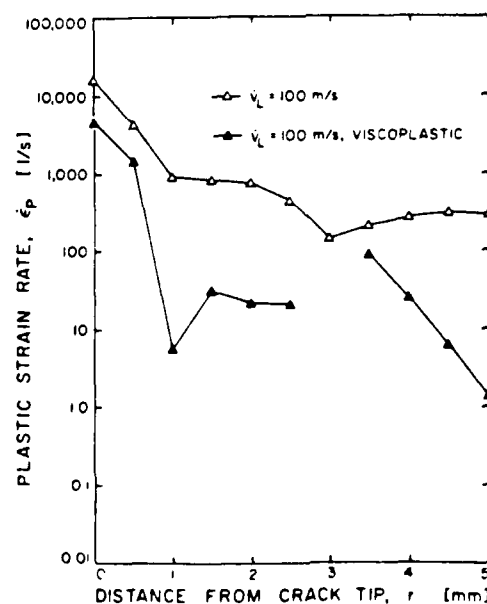
Fig. 17. Plastic strain rate vs distance from crack tip after 8 mm of crack growth.
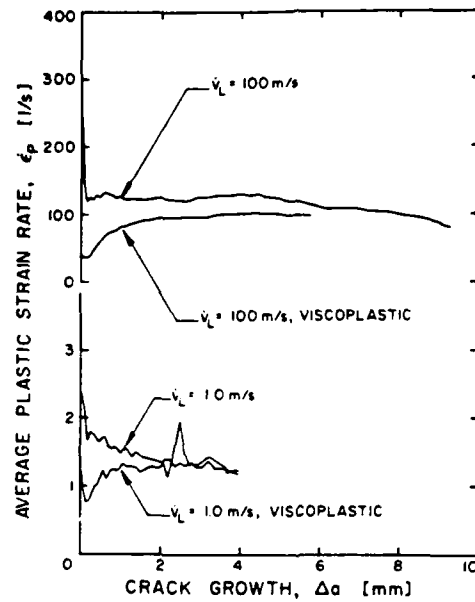
Fig. 18. Average plastic strain rate vs crack growth.

the stable crack growth analysis [22]. Due to the very large strain rates at initiation ($\dot{\varepsilon}_p \simeq 12,000/s$), the stress is elevated about 80% over the rate insensitive value, and therefore considerably more unloading takes place at the initial crack tip than at the surrounding material.

CONCLUSIONS

The technique for modelling crack propagation using spring and gap elements, described in a companion paper [22], was successfully applied to rapid crack propagation in viscoplastic materials.
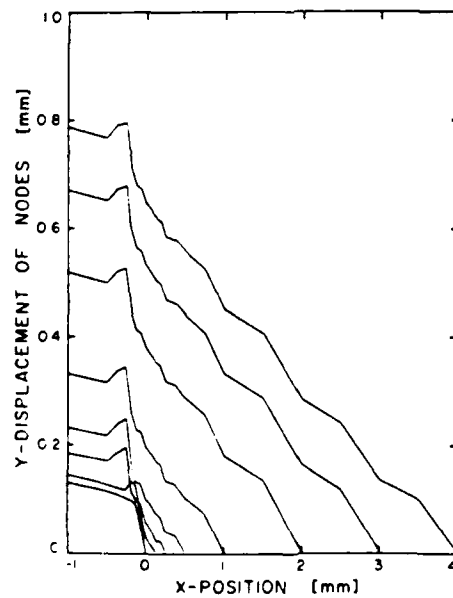
Fig 19. Deformed crack profiles for 100 m s load point velocity, viscoplastic analysis

Due to the lack of an established fracture criterion for rapid ductile fracture, the δ–Δa history from a stable crack growth and analysis [22] was employed for the first 4 mm of crack growth, whereafter the crack tip opening angle was used as the fracture criterion. This assumption implies that the initial strain to fracture, as represented in an integral sense by δ, is insensitive to strain rate and inertia. The effect of loading rate as the calculated resistance curves agree qualitatively with experimental results by Joyce [26] (who tested at a different temperature). However, the fact that the measurements seem to show a greater rate sensitivity than the calculations may assign that δ–Δa and a_c display a positive rate sensitivity.

Computations for crack velocities around 1.0 m/s and 100 m/s reveal that the viscoplastic materials absorb considerably more energy during fracture than rate insensitive materials. This difference increases at higher crack velocities. This is evidenced by the higher J–Δa curve at higher loading rates.

For the four cases studies, the crack velocity normalized with respect to the load point velocity, $\dot{a}/\dot{v}_L$, is a linear function of crack growth and insensitive to inertia or strain rate. However, the normalized crack velocity is likely geometry and load history dependent.

A detailed examination of the stresses in the 5 mm region ahead of the crack tip revealed that stresses were increased due to strain rate effects. Contrary to slow stable crack growth case, where a fixed stress distribution appears to translate with the crack tip after an initial transient, it was not observed that the stresses reached a "steady state" distribution after 4 or 8 mm or crack growth. The dynamic response of the material near the crack tip seems to preclude the determination of such a solution.

REFERENCES

[1] J. D. Achenbach and M. F. Kanninen. Crack tip plasticity in dynamic fracture mechanics. *Fracture Mechanics*. University Press of Virginia, Charlottesville (Edited by N. Perrone *et al.*) pp. 649–670 (1978).

[2] J. D. Achenbach, M. F. Kanninen and C. H. Popelar. Crack tip fields for fast fracture of an elastic–plastic material. *J. Mech. Phys. Solids* 29, 211–225 (1981).

[3] J. Ahmad *et al.*. Elastic–plastic finite element analysis of dynamic fracture. *Engng Fracture Mech* 17, 235–246 (1983).

[4] C. R. Barnes, J. Ahmad and M. F. Kanninen. Dynamic crack propagation through welded HY80 plates under blast loading, presented at the Sixteenth National Symposium on Fracture Mechanics, Columbus, Ohio, August 15–17 (1983). To appear in symposium proceedings.

[5] M. F. Kanninen *et al.*. Dynamic crack propagation under impact loading. *Nonlinear and Dynamic Fracture Mechanics* (Edited by N. Perrone and S. N. Atluri). ASME-AMD Vol. 35, pp. 185–200 (1979).

[6] H. Andersson. The steadily growing elastic–plastic crack tip in a finite element treatment. *Int. J. Fracture* 9, 221–233 (1973).

[7] M. F. Kanninen *et al.*. Elastic–plastic fracture mechanics for two-dimensional stable crack growth and instability problems. *Elastic–Plastic Fracture, ASTM STP 668*, (Edited by J. D. Landes, J. A. Begley and G. A. Clarke). pp. 121–150 (1979).

[8] M. F. Light, A. R. Luxmoore and W. T. Evans. Prediction of slow crack growth by a finite element method. *Int. J. Fracture* 11, 1045–1046 (1975).

[9] J. R. Rice, W. J. Drugan and T. -L. Sham. Elastic–plastic analysis of growing cracks. *Fracture Mechanics: Twelfth Conference, ASTM STP 700*, 189–221 (1980).

[10] E. P. Sorensen. A numerical investigation of plane strain stable crack growth under small-scale yielding conditions. *Elastic–Plastic Fracture ASTM STP 668*, (Edited by J. D. Landes, J. A. Begley and G. A. Clarke). pp. 151–174 (1979).

[11] K. K. Lo. Dynamic crack-tip fields in rate-sensitive solids. *J. Mech. Phys. Solids* 31, 287–305 (1983).

[12] J. C. Amazigo and J. W. Hutchinson. Crack-tip fields in steady crack growth with linear strain hardening. *J. Mech. Phys. Solids* 25, 81–97 (1977).

[13] P. Perzyna. The constitutive equations for rate sensitive plastic materials. *Appl Math* 20, 321–332 (1963).

[14] R. Hoff *et al.*. Parametric representation of the yield strength strain rate behavior of A533B steel. *J. Press. Vess. Technol* 105, 316–319 (1983).

[15] P. C. Paris *et al.*. The theory of instability of the tearing mode of elastic–plastic crack growth. *Elastic–Plastic Fracture ASTM STP 668*. (Edited by J. D. Landes, J. A. Begley and G. A. Clarke). pp. 5–36 (1979).

[16] R. M. McMeeking. Path dependence of the *J*-integral and the role of *J* as a parameter characterizing the near-tip field. *Flaw Growth and Fracture, ASTM STP 631*, 28–41 (1977).

[17] R. M. McMeeking. Finite deformation analysis of crack tip opening in elastic–plastic materials and implications for fracture. *J. Mech. Phys. Solids* 25, 357–381 (1977).

[18] F. A. McClintock. A criterion for ductile fracture by growth of holes. *J. appl. Mech.* 35, 363–371 (1968).

[19] J. R. Rice and D. M. Tracey, On the ductile enlargement of voids in triaxial stress fields. *J. Mech. Phys. Solids* **17**, 201–217 (1969).

[20] B. Brickstad, A viscoplastic analysis of rapid crack propagation experiments in steel. *J. Mech. Phys. Solids* **31**, 307–327 (1983).

[21] G. Rydholm, B. Fredriksson and F. Nilsson, Numerical investigations of rapid crack propagation. *Numerical Methods in Fracture Mechanics* (Edited by A. R. Luxmoore and D. R. J. Owen), pp. 660–673. University of Swansea Press (1978).

[22] R. Hoff, C. A. Rubin and G. T. Hahn, A new finite element technique for modelling stable crack growth. *Engng Fracture Mech.* **23**, 105–118 (1986).

[23] R. Hoff, C. A. Rubin and G. T. Hahn, Strain rate dependence of the deformation at the tip of a stationary crack. *Fracture Mechanics: Sixteenth Symposium, ASTM STP 86B*, (Edited by M. F. Kanninen and A. T. Hopper), pp. 409–430 (1985).

[24] C. F. Shih, H. G. DeLorenzi and W. R. Andrews, Studies on crack initiation and stable crack growth. *Elastic–Plastic Fracture, ASTM STP 668*, (Edited by J. D. Landes, J. A. Begley and G. A. Clarke), pp. 65–120 (1979).

[25] J. R. Rice and M. A. Johnson, The role of large crack tip geometry changes in plane strain fracture. *Inelastic Behavior of Solids* (Edited by M. F. Kanninen, et al.), pp. 641–672. McGraw-Hill, New York (1970).

[26] J. A. Joyce, Static and dynamic *J–R* Curve testing of A533B steel using the key curve and analysis technique. Nuclear Regulatory Commission Report No. NUREG CR-2274, Washington (1981).

[27] M. Nakagaki, W. H. Chen and S. N. Atluri, A finite element analysis of stable crack growth-I. *Elastic–Plastic Fracture, ASTM STP 668*, (Edited by J. D. Landes, J. A. Begley and G. A. Clarke), pp. 195–213 (1979).

[28] S. N. Atluri, T. Nishioka and M. Nakagaki, Numerical modelling of dynamic and nonlinear crack propagation in finite bodies, by moving singular-elements. *Nonlinear and Dynamic Fracture Mechanics* (Edited by N. Perrone and S. N. Atluri) ASME-AMD Vol. 35, pp. 185–200 (1979).

[29] S. N. Atluri, M. Nakagaki and K. Kathiresan, Hybrid finite element analysis of some nonlinear and 3-dimensional problems of engineering fracture mechanics. *Comput Structures* **12**, 511–520 (1980).

[30] S. N. Atluri, Path-independent integrals in finite elasticity and inelasticity, with body forces, inertia, and arbitrary crack face conditions. *Engng Fracture Mech.* **16**, 341–364 (1982).

[31] J. D. Achenbach, P. Burgers and V. Dunayevsky, Near tip plastic deformations in dynamic fracture problems. *Nonlinear and Dynamic Fracture Mechanics* (Edited by N. Perrone and S. N. Atluri), ASME-AMD Vol. 35, pp. 105–124 (1979).

[32] M. M. Little, E. Krempl and C. F. Shih, On the time and loading rate dependence of crack tip fields at room temperature. A viscoplastic analysis of small-scale yielding, presented at the Second International Symposium on Elastic–Plastic Fracture Mechanics, Philadelphia, (October 1981) (to appear in proceedings).
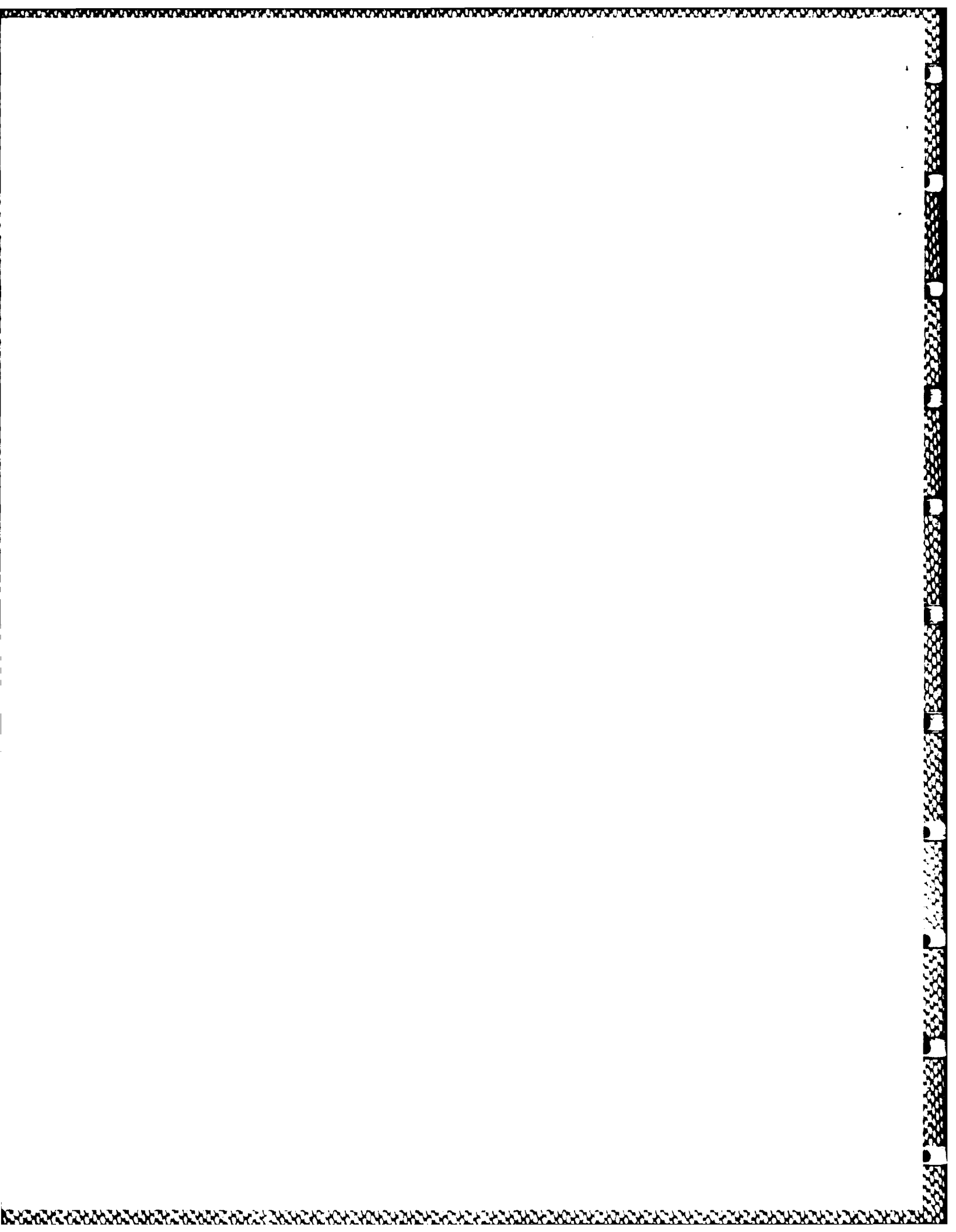
A NEW FINITE-ELEMENT TECHNIQUE FOR MODELLING STABLE CRACK GROWTH

R. HOFF
Department of Mechanical Engineering, University of Waterloo, Waterloo, Ontario
N2L 3G1, Canada

and

C. A. RUBIN and G. T. HAHN
Mechanical and Materials Engineering, Vanderbilt University, Nashville, TN 37235, U.S.A.

Abstract—This paper presents a new technique for simulating crack extension in conjunction with the finite-element method. The technique uses spring and gap elements to control the motion of nodes on the crack plane. These elements are available in many proprietary finite-element codes, thereby obviating the need for a user-written finite-element code. Numerical results for stable crack growth are in excellent agreement with corresponding experiments. The technique is also applied to rapid fracture in ductile materials, as discussed in a companion paper.

NOMENCLATURE

a crack length
$\dot{a}$ crack velocity
Δa crack growth
E Young's modulus
h element size
J_1 Rice's contour integral
n strain-hardening exponent
u, v, w displacements in the X, Y and Z directions, respectively
x, y, z coordinate directions
α crack-tip opening angle
δ crack-tip opening displacement
ϵ strain
ϵ_0 yield strain
σ stress
σ_0 yield stress

INTRODUCTION

THE ANALYSIS of stable crack growth in ductile materials using finite elements is a necessary precursor to the finite-element analysis of rapid crack growth in these same materials. Not only is stable crack growth a special case of rapid crack propagation (i.e. as $\dot{a} \rightarrow 0$), but many of the techniques developed for modelling stable crack growth can be extended to the rapid-propagation case. After a review of previous work in this field, a new technique for modelling stable crack growth will be described in this paper. Finally, stable-crack-growth results will be presented based on an analysis using this new technique. A companion paper[1] describes the application of this technique to rapid viscoplastic fracture.

Other investigators have taken basically two approaches to modelling stable crack growth with finite elements; we shall call them the microscopic approach and the macroscopic approach. The microscopic approach models a region in the immediate vicinity of the crack tip. The elements at the crack tip are much smaller than the crack-tip opening displacement at initiation and the entire mesh is usually much smaller than the crack length. With this fine-mesh gradation, it is possible to model the large strains in the fracture process zone (especially if a large-strain finite-element formulation is used). It is also feasible to use microstructurally significant fracture criteria such as the "critical plastic strain at a critical distance" criterion of McClintock and Irwin[2] (also discussed in Rice[3]). The microscopic approach can give accurate representations of the near-tip stress and strain singularities for limited amounts of crack growth. Examples of research involving the microscopic-crack-growth approach are An-

derson[4], Rice *et al.*[5], Rice and Sorensen[6], and Sorensen[7, 8]. Unfortunately, the near-tip stress fields elucidated using this approach are often difficult to relate to experimentally measureable quantities such as load, load-point displacement, or even the *J* integral (where applicable).

The macroscopic approach to modelling stable crack growth provides data which are easily related to experimentally measured parameters. The finite-element mesh typically models an entire laboratory-sized specimen or a relatively large portion of a structural component. The size of the elements near the crack tip is of the order of the crack-tip opening displacement at initiation, or larger. Since all dimensions of the model are very large compared to microstructurally significant distances, the fracture criterion must also be meaningful and calculable on that size scale. Currently the most frequently used are the *J* integral, the crack-tip opening angle α, and a combination of the two. Since the critical values of *J* and α are initially determined experimentally, it is therefore not surprising that crack-growth simulations using the macroscopic approach and these fracture criteria correspond well with experimental measurements. The macroscopic-crack-growth approach has received far more attention than the microscopic approach and representative studies include work by Andersson[9], Du and Lee[10,11], Hellan and Lotsberg[12], Kanninen *et al.*[13], and Shih *et al.*[14].

A finite-element crack-growth simulation must employ some mechanism for altering the boundary conditions (once the fracture criteron is satisfied) to simulate crack extension. By far the most commonly used method is the "node-release" technique. Conceptually speaking, when the fracture criterion is satisfied the displacement constraint at the crack-tip node is replaced by an equivalent force. This nodal force is then gradually reduced to zero in subsequent increments of the analysis, allowing the node in question to displace, thereby making the next node the new crack tip. This procedure is repeated for as many subsequent nodes as required for the desired amount of crack growth. Andersson[4, 9, 15], Du and Lee[10, 11], Hellan and Lotsberg[12], Kanninen *et al.*[13], Light *et al.*[16, 17], Rice *et al.*[5], Rice and Sorensen[6], and Sorensen[7, 8] have all used variations of this technique.

An alternative technique, used successfully by Shih *et al.*[14, 18], is to shift the crack-tip node in the direction of crack growth, thereby modelling the lengthening crack. However, this technique is still unproven in a dynamic context so it is not used in this study. Atluri, Nishioka and coworkers[19–21] have developed special crack-tip elements which contain embedded singularities, and translate with the moving crack tip. Although this technique proved very successful in elastodynamic problems[20, 22–28], it has some theoretical shortcomings in stable-crack-growth problems, since the order of the crack-tip strain singularity must be known *a priori* in order to formulate the element. Since the order of the strain singularity is velocity dependent in rapid crack propagation (see Achenbach *et al.*[29]), the application of the moving-singularity element to elastoplastic dynamic problems is even less accurate.

The finite-element model and methodology discussed in this paper were developed in view of two constraints: (i) the methodology developed for modelling stable crack growth must be useable for elastoplastic dynamic crack growth, and (ii) these computations must be performed using a commercially available finite-element program. Stable crack growth is the zero-velocity special case of rapid crack propagation in ductile materials. Since the computations are more easily performed in the absence of inertia effects, stable crack growth was chosen as the starting point for the finite-element analysis of rapid crack growth in ductile materials. Most of the finite-element work performed in a production environment is done with commercially available finite-element codes. However, no results of crack-growth simulations have been reported which were obtained using any of these commercially available programs (Shih *et al.*[14] used ADINA[30]; however, the program was specially modified for this purpose). It was felt that the development of crack-growth methodology, which could be used with a proprietary finite-element program, would be of more utility than a methodology which also required a user-developed finite-element code. The proprietary code ABAQUS[31] was chosen for this work because of its proven capabilities in the solution of nonlinear problems. The installation at Vanderbilt University featured ABAQUS version 3-12-78, running on a DEC-1099 computer, with the TOPS-10 operating system. The technique described in this paper should also work equally well with other proprietary finite-element programs.

FINITE-ELEMENT MODELLING

A finite-element model was developed to permit the investigation of stable and rapid crack growth in ductile steels. Figure 1 is a plot of the undeformed mesh. The cutout in the top figure is shown enlarged below. In both cases the initial crack tip is indicated by an arrow. The dimensions of the model are identical to specimen T52, from a recent study by Shih *et al.*[14], at General Electric. The dashed lines show the contours where the J integral will later be calculated.

The material is modelled as linear elastic up to the yield point, with power-law hardening beyond first yield:

$$\frac{\epsilon}{\epsilon_0} = \frac{\sigma}{\sigma_0}, \qquad \sigma \leq \sigma_0, \tag{1}$$

$$\frac{\epsilon}{\epsilon_0} = \left(\frac{\sigma}{\sigma_0}\right)^n, \qquad \sigma > \sigma_0. \tag{2}$$

Values for the material constants were chosen appropriate for A533B steel at 93°C: $\sigma_0 = 382.866$ MPa, $E = 197.62$ GPa, $\epsilon_0 = \sigma_0/E$, and $n = 10$. Since ABAQUS requires a multilinear stress–strain curve, the power-law portion was discretized. The stress–strain curve was discretized in an optimal sense so that deviations were held to within $\pm 0.5\%$ (see Hoff *et al.*[32]).

A series of 38 springs is defined from points in space to ground. The purpose of these springs is to associate a stiffness with degree-of-freedom number 2 (i.e. y displacement) for nodes 60005 to 60042 inclusive (see Fig. 2). In fact, the y coordinate of nodes 60005 to 60042 is initially zero, so that those nodes begin on the crack plane. Nodes 60005 to 60042 are shown elevated from the crack plane in Fig. 2 for clarity. Gap elements are defined between nodes 60005 and 50005, 60006 and 50006, etc. up to 60042 and 50042. The gap elements are formulated so that they can transmit only compressive loads, i.e. no tensile or shear loads. Since the tendency of nodes 50005–50042 is to move upwards, due to tensile loading of the specimen, all of the gaps will close. A displacement boundary condition is applied to nodes 60005–60042, constraining these nodes from moving in the y direction. With all of the gaps closed, nodes
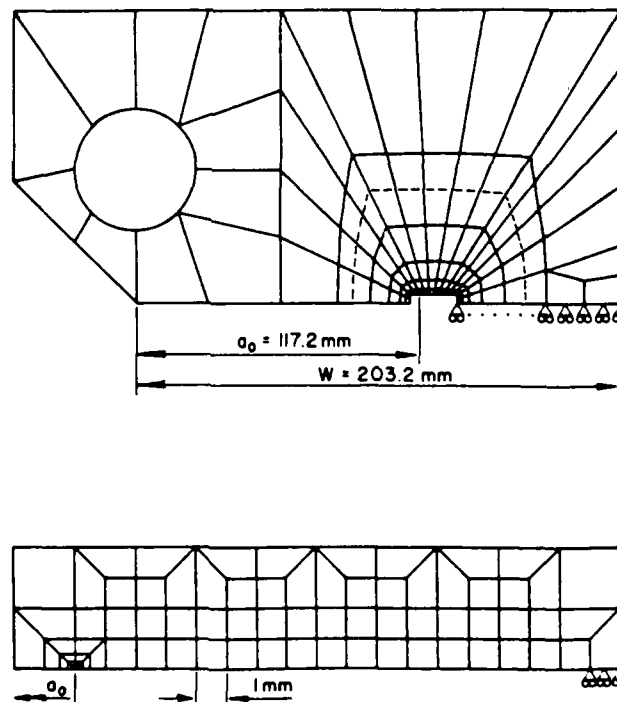

Fig. 1. Finite-element model of compact tension specimen used in the investigation of propagating cracks.
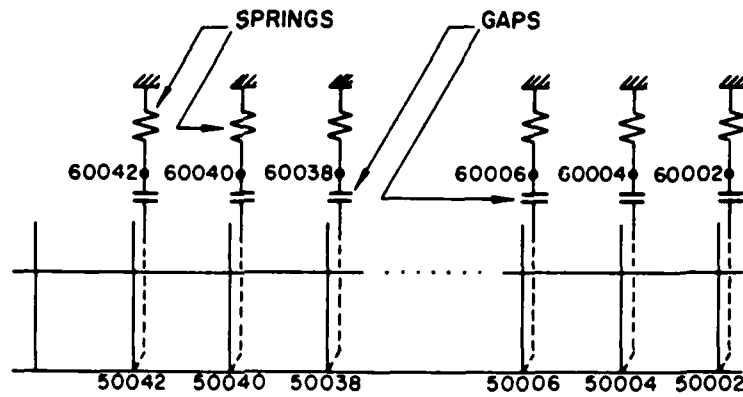
Fig. 2. Schematic details of springs and gaps at the crack tip.

50005–50042 are also constrained to the crack plane. thereby locating the crack tip at node 50042. It would not be possible to grow the crack with displacement boundary conditions applied to nodes 50005–50042. since the motion of these nodes after crack growth cannot be determined *a priori*.

A static elastic analysis was performed to verify the adequacy of the spring-and-gap method of specifying the boundary conditions. The y displacements of the nodes constrained by the gaps were all of order 10^{-20}. Since the displacements of the remainder of the nodes in the mesh were of order 10^{-11}. one can conclude that the gaps only allow negligible displacements. By opening and closing the appropriate gaps. the crack length was varied from 117.2 to 129.2 mm. For each different crack length. values of the stress-intensity factor K_1 were determined from the finite-element results using two different methods and compared with the polynomial equation of Srawley[33]:

$$K_1 = \frac{P}{BW^{1/2}} f\left(\frac{a}{w}\right) ,$$

$$f\left(\frac{a}{w}\right) = \frac{(2 + a/w)[0.866 + 4.64a/w - 13.32(a/w)^2 + 14.72(a/W)^3 - 5.6(a/W)^4]}{(1 - a/W)^{3/2}} . \quad (3)$$

Equation (3) is accurate to +0.5% in the range $0.2 \le a/W < 1$. The values of K_1 determined using the stiffness-derivative method of Parks[34] agree with eqn (3) to within 0.2%. This result verifies that the spring-and-gap method is capable of modelling displacement constraints accurately. Unfortunately the stiffness-derivative method has not been generalized to elastoplastic dynamic problems and will not be used henceforth. The J integral of Rice[35] is. of course. suitable to elastoplastic problems, and variations such as J_i' [36, 37] are appropriate for dynamic problems. Values of K_1 were also determined by performing the contour integration for $J_1[38]$. but agree less well with the polynomial equation (+5.2%). This is, however. sufficient accuracy for the crack-growth simulations to be performed in this study.

Values of J_1 or K_1 could have been determined more accurately using contour integration if singular elements were used at the crack tip. However. the presence of singular elements caused convergence difficulties with the gaps when this was attempted. Moreover. the standard singular element, created by collapsing one side of an eight-noded isoparametric finite element and shifting the adjacent nodes to the quarter points[39, 40]. did not offer any advantage in crack-growth studies.

Numerical experimentation revealed that the choice of spring constant affected the conditioning of the stiffness matrix[4]. It was determined that if the spring constant was *numerically* equal to Young's modulus then the best performance was obtained. For instance. if $E = 200 \times 10^9$ Pa. then the spring constant should be set to 200×10^9 N/m. Very stiff springs (i.e. 12–18 orders of magnitude stiffer than the recommended value) did not cause any detectable degradation in solution accuracy. whereas very soft springs (i.e. the stiffness is 12 or more orders of magnitude less than the recommended value) significantly degraded the results. It is

difficult to determine exact limits on acceptable spring stiffnesses since the conditioning of a stiffness matrix depends on the number of degrees of freedom in the analysis and the number of springs. For the problems worked in this paper, spring stiffnesses within 6 orders of magnitude of the recommended value were employed and produced no deleterious effect on the results.

IMPLEMENTATION OF THE FRACTURE CRITERION

Several studies[13, 14] have focused attention on which fracture parameters are suitable for describing stable crack growth. Candidate parameters such as J_1, α, δ, dJ/da, average crack-opening angle, generalized energy release rate, etc. were assessed on the basis of a large number of requirements: not only must the ideal parameter be physically significant, but it must also be readily determinable using finite elements. It was found[13, 14] that, for a given material and small amounts of crack growth, the J integral has a unique relationship to the amount of crack growth, Δa. This relationship is only mildly specimen dependent. The crack-tip opening angle α initially has a very high value, but after a small amount of crack growth reduces to a constant value. In this study the J_1-Δa relationship determined from experiment[14] was used for the first 4 mm of crack growth, whereafter a constant crack-tip opening angle was used for the remaining crack growth. This two parameter fracture criterion is depicted in Fig. 3, where the first regime is termed J-controlled and the second regime is termed α-controlled.

The major difficulty encountered in modelling J-controlled crack growth centers on this paradox: the boundary conditions, which are a function of Δa which in turn is only a function of J_1, must be specified at the beginning of an increment in the solution *but* J_1 can only be determined at the end of that particular increment. This would not constitute a major problem if boundary conditions could be handled *implicitly* at each increment in a finite-element analysis (i.e. the boundary conditions are determined as part of the solution process). However, boundary conditions must always be stated *explicitly* in a finite-element analysis. This necessitates the use of a rather sophisticated extrapolation scheme to predict what the value of J_1 will be at the end of a particular increment. The following paragraphs will describe the evolution of the J_1 extrapolation technique.
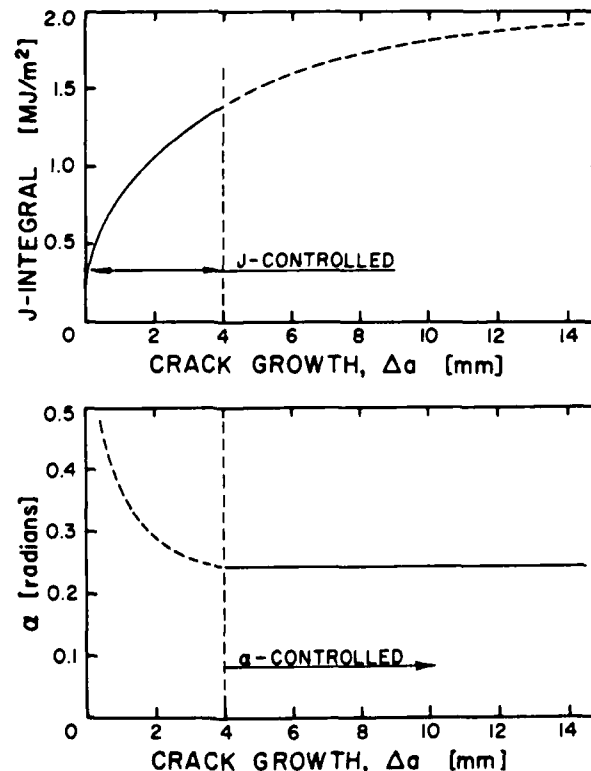

Fig. 3. Comparison of regimes of crack growth where J_1 and α are appropriate characterizing parameters.

The specimen was loaded so that the load-point displacement varied linearly with a non-dimensional "time." Since K_1 varies linearly with load-point displacement in the elastic case, and J_1 varies quadratically with K_1, therefore J_1 should vary quadratically with time. Referring to Fig. 4(a), if the solution increment just completed is at t_i, then a parabola was fit through the values of J_1 at times t_{i-2}, t_{i-1}, and t_i. The upcoming increment would end at t_{i-1}, and J_1 could be predicted by extending the parabola to t_{i+1}. This technique proved to be very unstable. Generally the predicted value of J_1 tended to be much too great (Fig. 4(a)) or much too small (Fig. 4(b)). The latter case was more serious since the desired crack length is determined from the predicted J_1 value, and if the predicted J_1 value was less than the previous J_1 value then the crack would become shorter instead of longer.

It turns out that in an elastic–plastic analysis J_1 varies almost linearly with load-point displacement (with some perturbation due to the changing stiffness of the model as the crack grows), so the assumed quadratic behaviour was not a good model. A linear-extrapolation scheme was therefore attempted, whereby J_1 at t_{i+1} was determined based on data taken at t_{i-1} and t_i. As shown in Fig. 4(c), linear extrapolation was more stable than quadratic extrapolation but minor perturbations in J_1 were still amplified in time.

The technique finally implemented was a modification of the linear-extrapolation method. Instead of using data at t_{i-1} and t_i, the predicted value of J_1 was determined by extrapolating data at t_{i-2} and t_i. In addition, the slope of the J_1 vs t curve was not allowed to change by more than 20% between successive increments. This produced the most stable results of all and is depicted in Fig. 4(d). The J_1-t history is shown in Fig. 5 for J-controlled crack growth. and it is evident that this is a very stable technique.

Once the value at J_1 was predicted, the value of Δa was determined from a parabolic fit to experimental data from a General Electric study[14]. Δa was the smaller root of

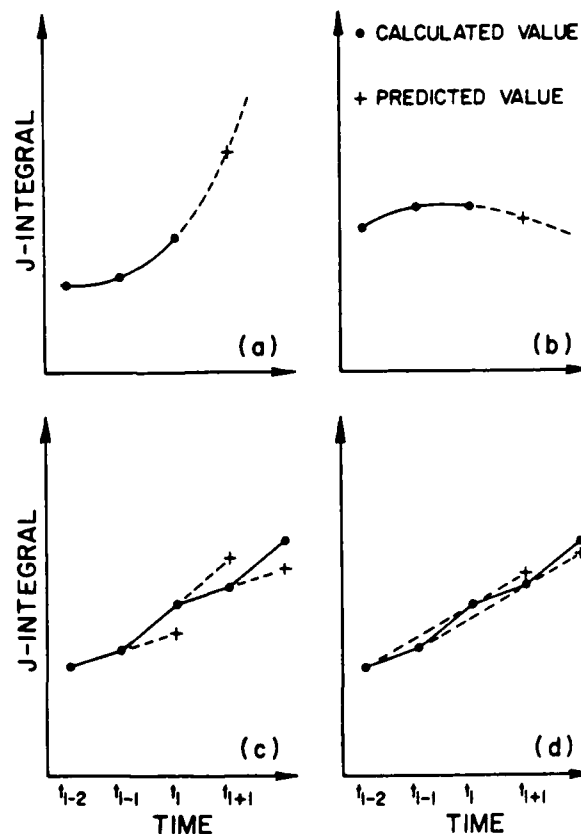$$J_1 = -2.562 \times 10^{10}(\Delta a)^2 + 3.985 \times 10^8 \Delta a + 2.000 \times 10^5, \qquad (4)$$

Fig. 4. Comparison of J_1 prediction schemes: (a) Parabolic extrapolation overestimating J_{i+1}.
(b) parabolic extrapolation underestimating J_{i+1}, (c) linear extrapolation from points at t_{i-1} and
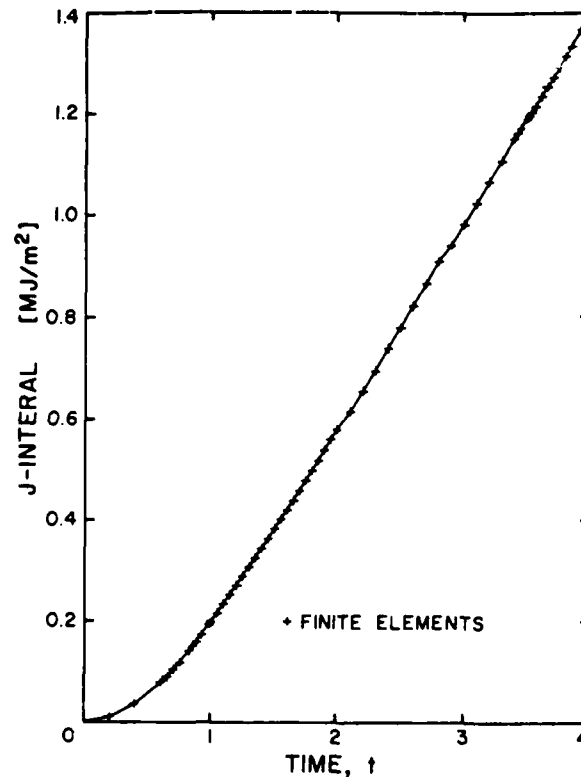t_i, and (d) linear extrapolation from points at t_{i-2} and t_i.

Fig. 5. J_1 history for the J-controlled portion of stable crack growth.

where Δa is in units of meters and J_1 is in units of J/m^2. The value of Δa, determined from eqn (4), was never equal to an integer multiple of the element length.

This raises the question of how to model these crack lengths which do not coincide with element boundaries. Suppose that the "effective" crack length Δa would put the crack tip at a position as shown in Fig. 6. Clearly nodes $n, n - 1, n - 2$, etc. must be constrained in the y direction. This is done by leaving nodes $m, m - 1, m - 2$, etc. on the crack plane as they have been since the beginning of the analysis. The gaps between n and $m, n - 1$ and $m - 1$, etc. will remain closed, thereby constraining nodes $n, n - 1, n - 2$, etc. to remain on the crack plane. Nodes $n + 3, n + 4, n + 5$, etc., which previously were used to constrain $n + 3, n + 4$. etc., are now displaced upwards so that the gaps are open. Spring node $m + 2$ is displaced upwards in proportion to how far the effective crack tip has advanced through element i: e.g. if the crack tip has advanced 25% of the way between nodes $n + 2$ and n, then node $m + 2$ is raised 25% of its maximum value. The maximum displacement of $m + 2$ is almost twice what the final displacement of node $n + 2$ will be. Therefore, about halfway through the incremental gap-opening procedure, the node $n + 2$ will separate from the gap (i.e. the gap opens) and node $n + 2$ will find its own equilibrium position. In general, the gaps were closed
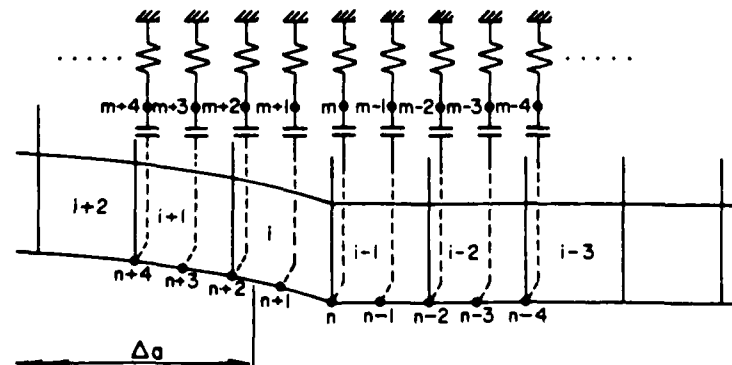

Fig. 6. Details of crack-extension procedure.

for three increments and then open for another two increments during the incremental opening procedure.

When the crack tip moved past node n, then nodes $m - 1$ and m were moved upwards incrementally. This procedure repeated itself until 4 mm of crack growth had occurred. At that time the critical value of the crack-tip opening angle, 0.24 rad, was used as the fracture criterion for further crack growth. Opening of the crack-tip element was handled using springs and gaps, as just described, except that the determination of the effective crack length was slightly different. The motion of the spring nodes, . . . $m - 1, m, m + 1$ . . . , are specified in a user-developed subroutine which is attached to the ABAQUS program at link time. A listing of the subroutines used in this study appears in Ref. [38].

RESULTS AND DISCUSSION

The results of a simulation of stable crack growth are presented in this section. An exhaustive presentation is not made; however, sufficient evidence is given to demonstrate that the spring-and-gap technique is appropriate for modelling crack extension. In addition, the stresses and strains ahead of the stably growing crack are contrasted with those ahead of a stationary crack.

The variation of J_1 with crack growth is plotted in Fig. 7. The values of J_1 are determined by integration along the contour shown in Fig. 1. Contours much closer to the crack tip were generally unacceptable for J_1 evaluation since material unloading took place behind the crack tip as crack extension progressed. Unloading violates one of the conditions of using J_2 flow theory in the finite-element analysis to evaluate the J integral, which is based on the deformation theory of plasticity. Besides, as pointed out by McMeeking[42] on the basis of finite-strain studies, the J integral is not path independent when calculated along contours closer than about 5δ from the crack tip.

The variation of J_1 with Δa corresponds very well with the experimental results of Shih *et al.*[14]. *Since the crack growth is determined during the analysis from eqn (4), it is not* surprising that there is almost an exact correspondence to experiment during the first 4 mm of
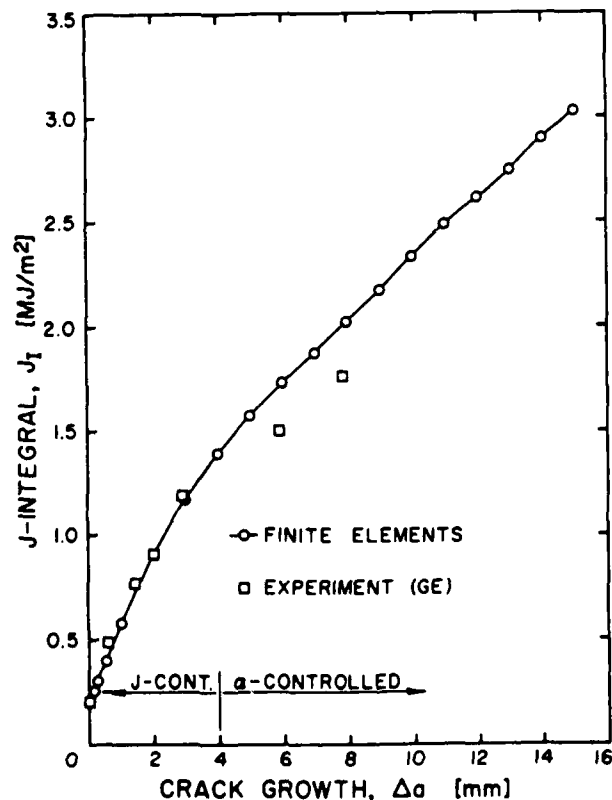
Fig. 7. J integral *vs* crack growth.
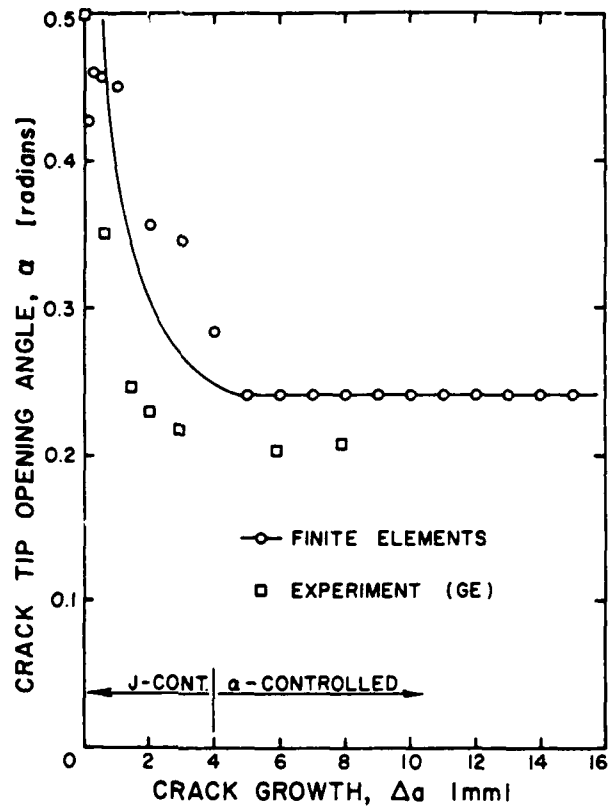
Fig. 8. Crack-tip opening angle vs crack growth.

g. wth. At 4 mm of crack growth, the crack extension is no longer considered to be J-controlled and the fracture criterion switches to a critical value of α.

The variation of α with crack growth is plotted in Fig. 8. The trend in α is that it starts at a large value, about 0.5 rad, and decreases to its steady-state value of 0.24 rad. There is
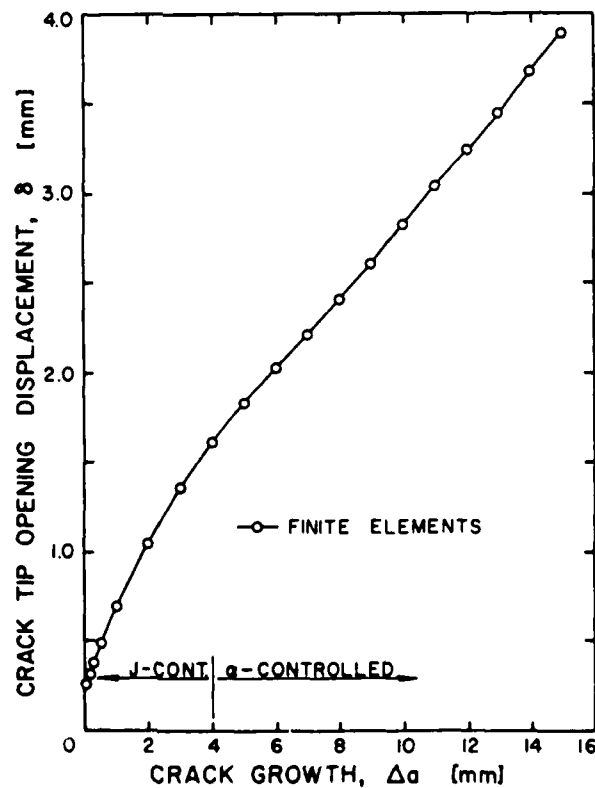
Fig. 9. Crack-tip opening displacement vs crack growth.

considerable noise in α at the start, however, and this may be due to a number of factors. First, it can be shown that at initiation the J-field solution predicts π rad as the tip opening angle. Since α is determined according to

$$\alpha = \tan^{-1} \frac{2v_{n-2}}{h},$$ (5)

it is not uniquely defined at initiation. The element size h and the y displacement of node $n - 2$, v_{n-2}, are illustrated in Fig. 6. Second, due to the mesh refinement near the initiation site, the element size h keeps changing for the first 5 elements of crack growth.

The steady-state value of the crack-tip opening angle, 0.24 rad, was obtained graphically by determining the asymptote of the α vs t variation during the first 4 mm of crack growth (although this plot is not shown). This value is slightly higher than the experimental steady-state value of 0.21 rad, which is not unexpected since the numerical values of α are almost all higher than the experimental values at less than 4 mm of crack growth.

The variation of δ with Δa is plotted in Fig. 9. In this instance, δ is twice the y displacement of the node 1 mm behind the original crack tip. In the J-controlled region, the calculated values deviate by less than 2.2% from a curve defined by

$$\delta = -33.58(\Delta a)^2 + 0.47082\Delta a + 2.5332 \times 10^{-4},$$ (6)

where δ and Δa are in units of meters. In the α-controlled region, the calculated values deviate by less than 1.3% from a line defined by

$$\delta = 0.23673\Delta a + 7.6159 \times 10^{-4}.$$ (7)

Although the J_1-Δa relationship in Fig. 7 is similar to this, J_1 vs δ does not plot as a straight line over the entire range of crack growth.
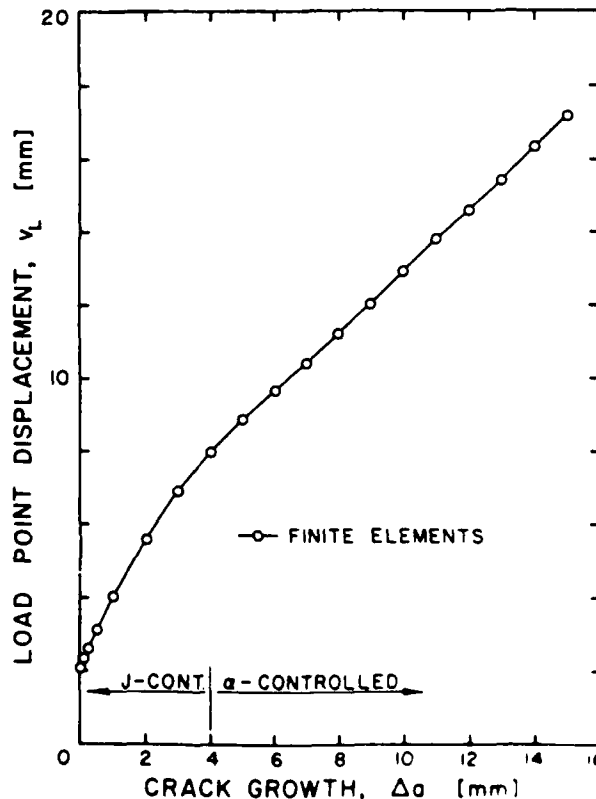

Fig. 10. Load-point displacement vs crack growth.

END
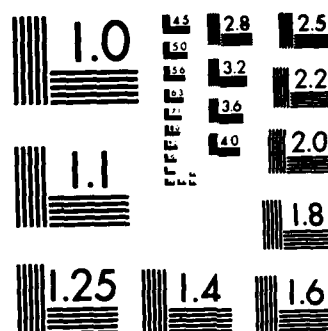DATE
FILMED
6 1988
DTIC

1.0

45
50
55

2.8
3.2
3.6
4.0

2.5

2.2

2.0

1.1

1.8

1.25 1.4 1.6

MICROCOPY RESOLUTION TEST CHART
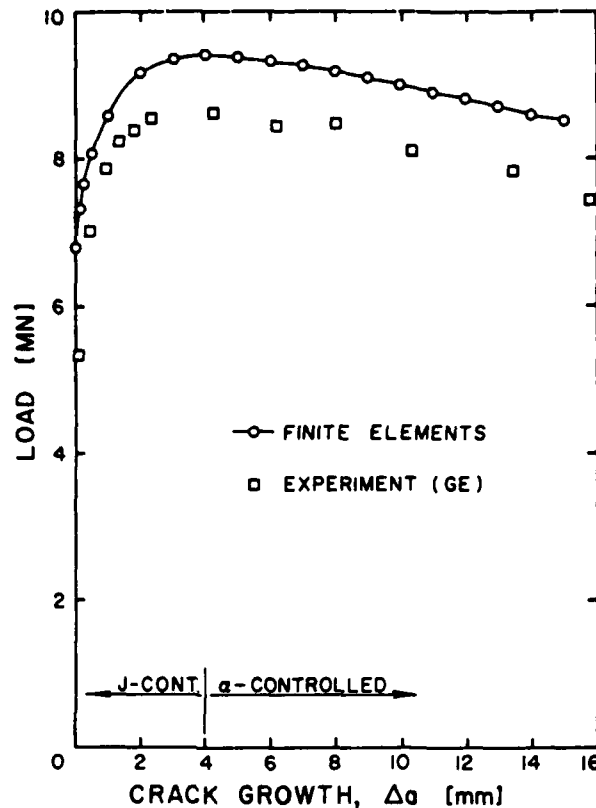NATIONAL BUREAU OF STANDARDS-1963-A

Fig. 11. Load vs crack growth.

The plot of load-point displacement v_L vs Δa shown in Fig. 10, exhibits a similar bimodal (parabolic/linear) characteristic. The load-point displacement is defined as twice the y displacement of the node at the top of the load hole. Since the finite-element model is only of the top half of the specimen, this factor of 2 is necessary for correspondence with experiment where v_L is defined as the relative displacement of the top loading pin with respect to the bottom one. The slope of the linear portion in Fig. 10 is significant because its value, 0.834, can be used to estimate the crack velocity in α-controlled rapid crack extension. That is, if $\partial(\Delta a)/\partial v_L = 1/0.834$ for stable growth, then the crack velocity $\dot{a}$ can be estimated from the load-point velocity $\dot{v}_L$ according to

$$\dot{a} = \frac{\dot{v}_L}{0.834} = 1.20 \, \dot{v}_L. \tag{8}$$

Departures from the behaviour predicted by eqn (8) would be due to inertia and strain-rate effects.

The variation of load with Δa is plotted in Fig. 11. The finite-element results were determined by assuming a 1-m-thick plane-strain specimen with 25% side grooves. The experimental results were therefore multiplied by a suitable constant to allow comparison with the numerical results. The two results unquestionably show the same trends. Any quantitative differences are due to the computational model being (intentionally) slightly different from the experimental specimen in terms of material properties, fracture criteria, etc.

The deformed-crack profiles are shown in Fig. 12 for the first 4 mm of crack growth. Note that the scales are different on the abscissa and ordinate so that the crack opening is exaggerated in the figure. Several features of this plot are noteworthy. The character of deformation changes abruptly since the strain fields are quite different at initiation from what they are after finite amounts of growth. Sorensen[7] and Miller and Kfouri[43] noted similar behaviour in the deformed-crack profiles. A more puzzling phenomenon is the jagged nature of the deformed profiles. This is perhaps due to the nature of the gap-release mechanism.
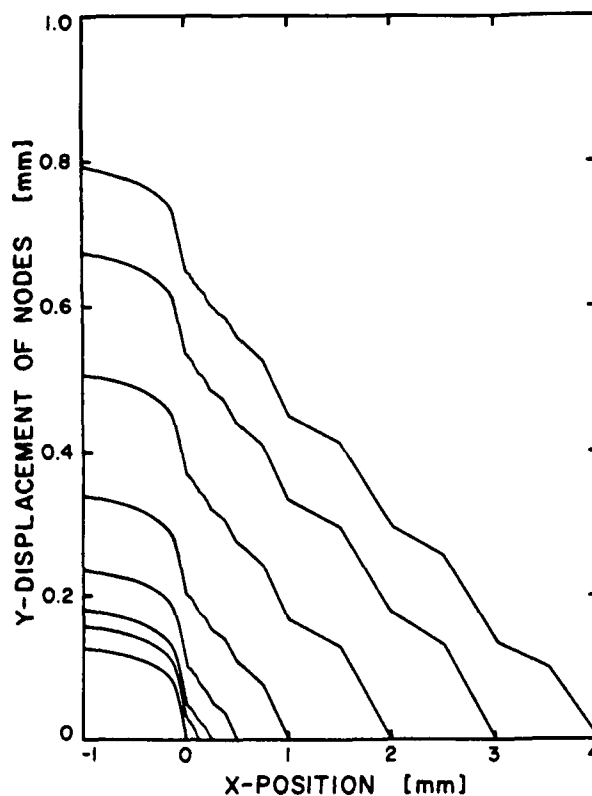
Fig. 12. Deformed-crack profiles.

The equivalent stresses and plastic strains at 45° to the tip of the growing crack are plotted in Figs. 13 and 14. The stresses and strains are virtually the same after 4 mm of crack growth as they are after 10 mm of crack growth, indicating that the 4 mm point gives indicative results for stable crack growth. The stresses and strains are generally higher after stable growth than
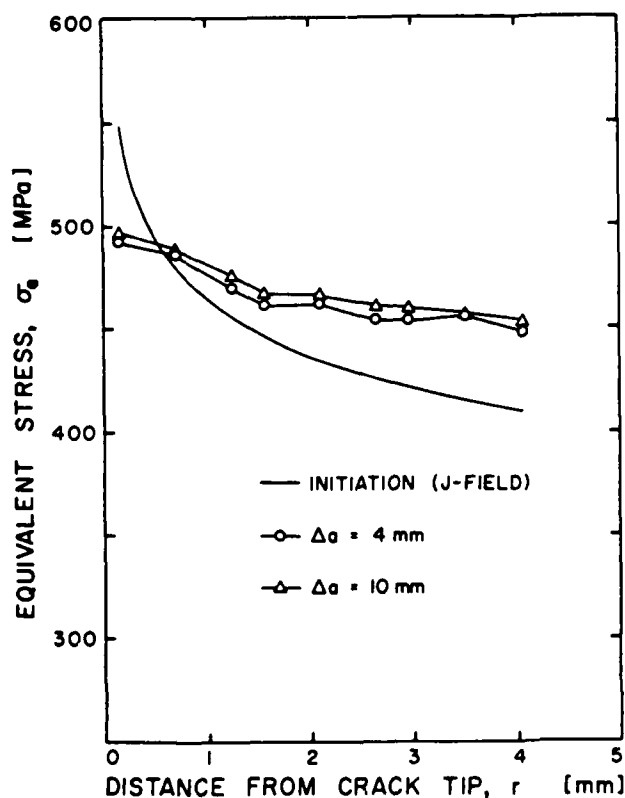
Fig. 13. Equivalent stress along a line at 45° to the propagating crack tip.
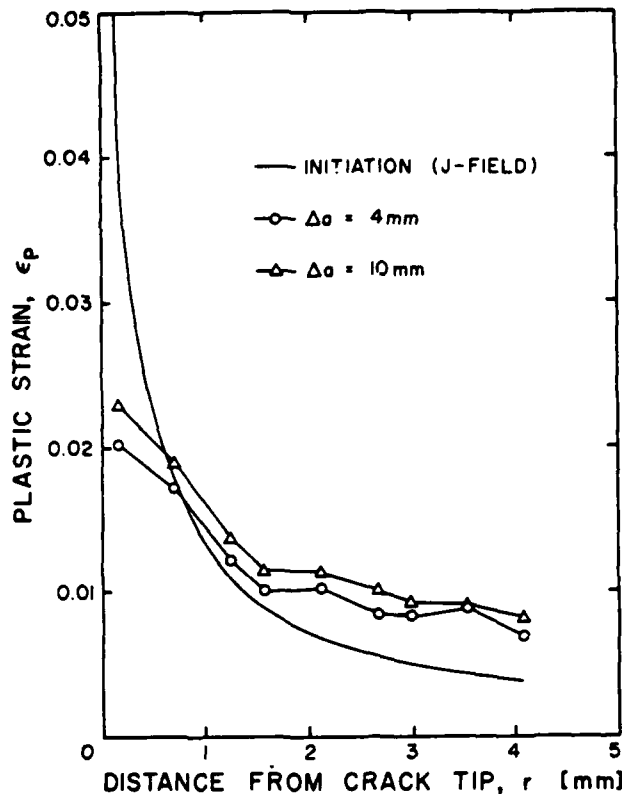
Fig. 14. Plastic strain along a line at 45° to the propagation crack tip.

they are at initiation, but are much less singular. These smaller stress and strain singularities for stable growth were anticipated on the basis work by Amazigo and Hutchinson[44]. Although the data in Figs. 13 and 14 do not prove the existence of a weaker crack-tip singularity, they do indicate the anticipated trend.

CONCLUSIONS

A new technique was described, employing spring and gap finite elements, which can be used to simulate crack growth. An advantage of this technique is that it does not require a user-developed finite-element code; rather, it can be used with commercially available codes such as ABAQUS.

This technique was applied to the modelling of stable crack growth in a compact tension specimen of A533B steel. The J integral and the crack-tip opening angle were used as a two-parameter fracture criterion. Numerical results agree well with corresponding experiments previously performed by Shih *et al.*

REFERENCES

[1] R. Hoff, C. A. Rubin and G. T. Hahn. Vicoplastic finite element analysis of rapid fracture. *J. Appl. Mech.* (to be published).
[2] F. A. McClintock and G. R. Irwin. Plasticity aspects of fracture mechanics. in *Fracture Toughness Testing and its Applications. ASTM STP* **381**, 84–113 (1965).
[3] J. R. Rice. Mathematical analysis in the mechanics of fracture. in *Fracture* (H. Liebowitz, ed.). Vol. 2, pp. 191–311. Academic Press, New York (1968).
[4] H. Andersson. The steadily growing, elastic–plastic crack tip in a finite element treatment. *Int. J. Fracture* **9**, 231–233 (1973).
[5] J. R. Rice, W. J. Drugan and T.-L. Sham. Elastic–plastic analysis of growing cracks. in *Fracture Mechanics: Twelfth Conference. ASTM STP* **700**, 189–221 (1980).

[6] J. R. Rice and E. P. Sorensen, Continuing crack-tip deformation and fracture for plane-strain crack growth in elastic–plastic solids. *J. Mech. Phys. Solids* **26**, 163–186 (1978).

[7] E. P. Sorensen, A numerical investigation of plane strain stable crack growth under small scale yielding conditions, in *Elastic–Plastic Fracture*, (J. D. Landes, J. A. Begley and G. A. Clarke, eds.), pp. 151–174. *ASTM STP* **668** (1979).

[8] E. P. Sorensen, A finite element investigation of stable crack growth in anti-plane shear. *Int. J. Fracture* **14**, 485–500 (1978).

[9] H. Andersson, A finite element representation of stable crack growth. *J. Mech. Phys. Solids* **21**, 337–356 (1973).

[10] S. Du and J. D. Lee. Finite element analysis of slow crack growth. *Engng Fracture Mech.* **16**, 229–245 (1982).

[11] S. Du and J. D. Lee. Variations of various fracture parameters during the process of subcritical crack growth. *Engng Fracture Mech.* **17**, 173–183 (1983).

[12] K. Hellan and I. Lotsberg, On absolute convergence of the separation work as calculated by release of nodes in a finite element model. *Int. J. Fracture* **13**, 539–543 (1977).

[13] M. F. Kanninen *et al.*. Elastic–plastic fracture mechanics for two-dimensional stable crack growth and instability problems. in *Elastic–Plastic Fracture* (J. D. Landes, J. A. Begley and G. A. Clarke, eds.), pp. 121–150. *ASTM STP* (1979).

[14] C. F. Shih, H. G. deLorenzi and H. R. Andrews, Studies on crack initiation and stable crack growth. in *Elastic–Plastic Fracturing* (J. D. Landes, J. A. Begley and G. A. Clarke, eds.), pp. 65–120. *ASTM STP* **668** (1979).

[15] H. Andersson. Finite element treatment of a uniformly moving elastic–plastic crack tip. *J. Mech. Phys. Solids* **22**, 285–308 (1974).

[16] M. F. Light. A. Luxmoore and W. T. Evans, Prediction of slow crack growth by a finite element method *Int. J. Fracture* **11**, 1045–1046 (1975).

[17] M. F. Light, A. R. Luxmoore and W. T. Evans, Some further results on slow crack growth prediction by a finite element method. *Int. J. Fracture* **12**, 503–506 (1976).

[18] C. F. Shih, H. G. deLorenzi and M. D. German, Crack extension modelling with singular quadratic isoparametric elements. *Int. J. Fracture* **12**, 647–651 (1976).

[19] M. Nakagaki, W. H. Chen and S. N. Atluri, A finite-element analysis of stabel crack growth—I. in *Elastic–Plastic Fracture* (J. D. Landes, J. A. Begley and G. A. clarke, eds.), pp. 195–213. *ASTM STP* **668** (1979).

[20] S. N. Atluri, T. Nishioka and M. Nakagaki. Numerical modelling of dynamic and nonlinear crack propagation in finite bodies by moving singular elements. in *Nonlinear and Dynamic Fracture Mechanics* (N. Perrone and S. N. Atluri, eds.), Vol. 35, pp. 37–66. *ASME-AMD* (1979).

[21] S. N. Atluri, M. Nakagaki and K. Kathiresan, Hybrid finite element analysis of some nonlinear and 3-dimensional problems of engineering fracture mechanics. *Computers and Structures* **12**, 511–520 (1980).

[22] T. Nishioka and S. N. Atluri. Numerical modelling of dynamic crack propagation in finite bodies, by moving singular elements, Part 1: Formulation. *J. Appl. Mech.* **47**, 570–576 (1980).

[23] T. Nishioka and S. N. Atluri. Numerical modelling of dynamic crack propagation in finite bodies, by moving singular elements, Part 2: Results. *J. Appl. Mech.* **47**, 577–582 (1980).

[24] T. Nishioka, R. B. Stonesifer and S. N. Atluri. An evaluation of several moving singularity finite element models for fast fracture analysis. *Engng. Fracture Mech.* **15**, 205–218 (1981).

[25] T. Nishioka and S. N. Atluri. Finite element simulation of fast fracture in steel DCB specimen. *Engng Fracture Mech.* **16**, 157–175 (1982).

[26] T. Nishioka and S. N. Atluri. Numerical analysis of dynamic crack propagation: Generation and prediction studies. *Engng Fracture Mech.* **16**, 302–332 (1982).

[27] T. Nishioka and S. N. Atluri, A method for determining dynamic stress intensity factors from COD measurement at the notch mouth in dynamic tear testing. *Engng Fracture Mech.* **16**, 333–339 (1982).

[28] T. Nishioka and S. N. Atluri, A numerical study of the use of path independent integrals in elasto-dynamic crack propagation. *Engng Fracture Mech.* **18**, 23–33 (1983).

[29] J. D. Achenbach, M. F. Kanninen and C. H. Popelar, Crack tip fields for fast fracture of an elastic–plastic material. *J. Mech. Phys. Solids* **29**, 211–225 (1981).

[30] K.-J. Bathe, *ADINA-Reference/User Manual*. Control Data Corporation Publ. No. 76071900, Mineapolis (1980).

[31] Hibbitt and Karlsson, Inc., *ABAQUS-User's Manual, Version 3*. Providence RI (Sept. 1980).

[32] R. Hoff *et al.*, Optimal discretization of power stress–strain law curves. *J. Eng. Mat. Tech.* **107**, 115–118 (1985).

[33] J. E. Srawley. Wide range stress intensity for factor expressions for ASTM E-399 standard fracture toughness specimens. *Int. J. Fracture* **12**, 475–502 (1976).

[34] D. M. Parks, A stiffness derivative finite element technique for determination of crack tip stress intensity factors. *Int. J. Fracture* **10**, 487–502 (1976).

[35] J. R. Rice, A path independent integral and the approximate analysis of strain concentration by notches and cracks. *J. Appl. Mech.* **34**, 379–386 (1968).

[36] T. Nishioka and S. N. Atluri, Path-independent integrals, energy release rates, and general solutions of near tip fields in mixed-mode dynamic fracture mechanics. *Engng Fracture Mech.* **18**, 1–22 (1983).

[37] S. N. Atluri, Path-independent integrals in finite elasticity and inelasticity, with body forces, inertia, and arbitrary crack-face conditions. *Engng Fracture Mech.* **16**, 341–364 (1982).

[38] R. Hoff. Viscoplastic finite element analysis of rapid fracture. Ph.D. dissertation, Vanderbilt University (1984).

[39] H. D. Hibbitt, Some properties of singular isoparametric elements. *Int. J. Num. Meth. Engng.* **11**, 180–184 (1977).

[40] R. S. Barsoum. Triangular quarter-point elements as elastic and perfectly-plastic crack tip elements. *Int. J. Num. Meth. Engng.* **11**, 85–98 (1977).

[41] J. M. Ortega and W. G. Poole. Jr., *An Introduction to Numerical Methods for Differential Equations*. Pitman, Marshfield, MA (1981).

[42] R. M. McMeeking, Path dependence of the *J*-integral and the role of *J* as a parameter characterizing the near tip field. in *Flaw Growth and Fracture*. pp. 28–41. *ASTM STP* **631** (1977).

[43] K. J. Miller and A. P. Kfouri, A comparison of elastic–plastic fracture parameters in biaxial stress states. in *Elastic–Plastic Fracture* (J. D. Landes, J. A. Begley and G. A. Clarke, eds.), pp. 214–228. *ASTM STP* **668** (1979).

[44] J. C. Amazigo and J. W. Hutchinson, Crack tip fields in steady crack-growth with linear strain-hardening. *J. Mech. Phys. Solids* **25**, 81–97 (1977).

R. Hoff

G. E. Johnson

C. A. Rubin

G. T. Hahn

Mechanical and Materials Engineering
Vanderbilt University.
Nashville. Tenn 37235

Parametric Representation of the Yield Strength-Strain Rate Behavior of A533B Steel

A nonlinear programming technique to estimate the parameters for a temperature normalized version of the Malvern equation is presented. The general conjugate gradient algorithm is used to minimize a least-squares function formulated from data for A533B steel. A constrained solution (which provides preferential treatment for a particular data point) is also given. The results satisfactorily represent experimental data over a temperature range from − 73C to 260C. The approach is well suited to design applications where data at a specific temperature of interest are limited or nonexistent.

Introduction

The yield strength of a metal is a function of a number of variables, notably temperature and strain rate. For body-centered-cubic metals, such as steel above the ductile to brittle transition temperature, the yield strength typically increases with increasing strain rate. Large increases in yield strength are observed at high strain rates, which may occur in applications involving rapidly propagating cracks, or projectiles impacting on a surface. In order to take advantage of the enhanced material properties at high strain rates, the strain rate dependence of yield strength must be characterized quantitatively. With recent advances in computational stress analysis techniques (such as the finite element method), analyses employing strain rate dependent yield strength have become tractable, thereby emphasizing the need for an accurate yield strength/strain rate relationship.

A number of stress strain strain rate temperature relationships have been proposed [1]. One of these is the Malvern relationship [1, 2] given in equation (1).

$$\epsilon_{TOT} = \dot{\sigma}/E + D[(\sigma/\sigma_o) - 1]^p \qquad (1)$$

If the elastic component is eliminated from (1), we obtain

$$\dot{\epsilon} = D[(\sigma/\sigma_o) - 1]^p \qquad (2)$$

where
- $\dot{\epsilon}$ = the plastic strain rate
- σ = the instantaneous yield strength
- σ_o = the "static" yield strength (at $\dot{\epsilon}$ = 0)
- D, p = temperature-dependent parameters.

It is common to estimate σ_o, D, and p by writing equation (2) for three selected data points and solving the resulting system of nonlinear equations. Such approaches are often adequate; however, which three data points to choose is a subjective decision and the quality of the outcome is dependent on the experience and insight of the engineer.

In this paper we present an alternative method for the

estimation of these parameters based on the well-known principle of least squares. A nonlinear programming strategy is used to accommodate the nonlinear nature of the Malvern equation. Results are given for a temperature normalized version of equation (2) based on data for A533B steel. These are now being used in FEM analyses of dynamic crack-tip stress fields at Vanderbilt University.

Our purpose here is to present an objective approach to this curve-fitting problem. The method reported could be used in conjunction with functional relations different from equation (1). The Malvern model was chosen for illustration of the technique because it is often included in commercially available FEM codes and it appears to be widely used. It is important to note that the use of a least-squares approach for the estimation of the model parameters assures that the model will fully utilize the available experimental data. Presumably, this will result in the best possible curve fit within the limitations of the mathematical form. Since there is virtually always scatter in experimental data, any mathematical description of the physical phenomenon should benefit by such treatment.

There are several solution techniques for the nonlinear least-squares problem, among them the well-known Marquardt algorithm [3] and the Gauss least-squares method [4]. These require the formulation and inversion of a large Jacobian matrix. The general conjugate gradient method utilized in this note involves only vector operations. Since no matrices or inversion processes are required, stability problems are avoided and round off is less significant. These benefits are usually gained at the expense of additional iterations for convergence; however, since each iteration is less complex, computation times are small (typically a few seconds or less on a main frame computer).

Material Data

A considerable amount of yield strength strain rate data is available for A533B steel (a pressure vessel quality steel used extensively in the nuclear power industry). Experimental data
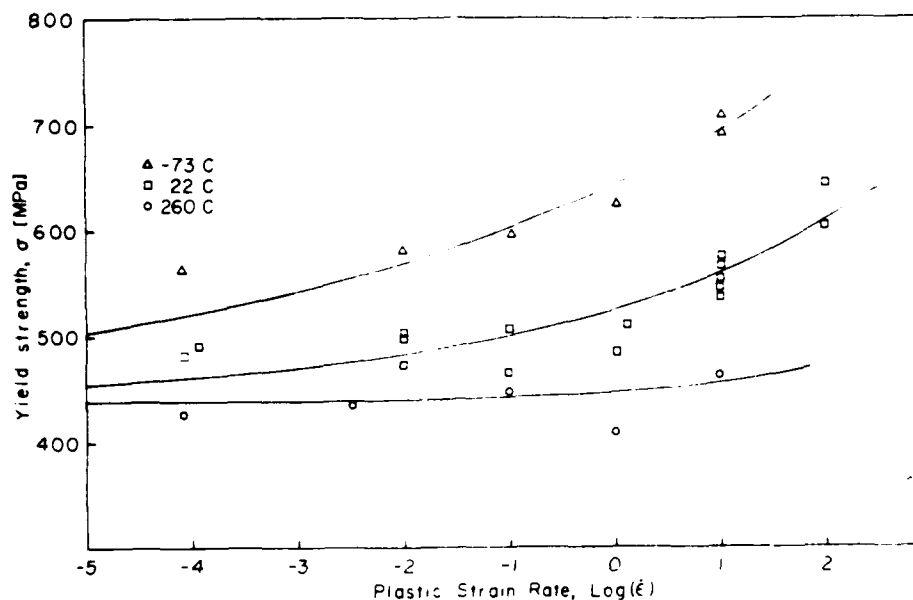
Fig. 1 Yield strength/strain rate relationship for A533B at various temperatures. Strain rate is in s^{-1}.

have been given by Steichen and Williams [5] and by Oldfield, et al. [6]. Their results (obtained from high-speed tensile tests) are plotted in Fig. 1. Server [7] has obtained similar data using precracked Charpy specimens.

Figure 1 shows that the yield strength of A533B is temperature dependent. An exponential dependence of strain rate on temperature is predicted by chemical rate theory. Statistical mechanics has been used to formalize this relationship, as discussed in [8]. The relationship, based on the Arrhenius rate equation is

$$\dot{\epsilon} \propto A \exp[-H/T] \qquad (3)$$

where

A = "frequency" factor
H = stress-dependent activation energy term
T = absolute temperature.

The activation energy term has been shown to be a function of the yield stress by Christian [9]; hence

$$\sigma = f(T \ln[A/\dot{\epsilon}]) \qquad (4)$$

The value of A has been experimentally determined by Bennett and Sinclair [10] as 10^8 s^{-1}, and is reportedly quite insensitive to stress, microstructure, temperature and strain rate. Combining (3) and (4) gives

$$\dot{\epsilon}_R = A(\dot{\epsilon}_i/A)^{\,T_i/T_R} \qquad (5)$$

which converts strain rates, $\dot{\epsilon}_i$, at temperature, T_i, to comparable strain rates, $\dot{\epsilon}_R$, at the reference temperature, T_R. Accordingly, data at any temperature can be converted to data at any desired (reference) temperature.

The data of Fig. 1 were obtained at three different temperatures. Equation (5) was used to transform these data to equivalent points at $T_R = 366.15$ K (93C). Of course, it would be possible to consider the behavior at each temperature separately. The principal disadvantage of this approach is that it requires experimental data at any temperature of interest. Such data are not always readily available or easily obtained. The approach we present here is well suited to design applications where data at the specific temperature of interest are limited or nonexistant. Within the range of temperatures and strain rates considered in Fig. 1, reasonable results could be expected. Extrapolation to obtain information about behavior outside the range of the experimental data would be difficult to defend and is not recommended.

Estimation of the Parameters

The general curve-fitting problem requires that we find a functional relation, $z(y)$, to represent n data points, (y_i, z_i). The least-squares curve minimizes the sum of the deviations squared, i.e.,

$$\text{minimize } \Sigma [z(y_i) - z_i]^2 \qquad (6)$$

If $z(y)$ is posed as a polynomial or some other simple function, then a solution can be found by solving a set of simultaneous linear equations. This technique is discussed in numerous textbooks on statistics and numerical methods [11, 12]. If a more complex relationship exists between z and y, then some other approach is necessary. Special purpose [3] and general purpose algorithms [13] have been reported in the literature.

Development of the Objective Function. A relationship for the yield strength as a function of the plastic strain rate can be derived from (2) as

$$\sigma = \sigma_o[(\dot{\epsilon}/D)^{1/m} + 1] \qquad (7)$$

The least-squares formulation is then

$$\text{minimize } f(\sigma_o, D, p) = \Sigma\{\sigma_o[(\dot{\epsilon}_i/D)^{1/m} + 1] - \sigma_i\}^2 \qquad (8)$$

where the function f is the objective function. Values of σ_o, D, and p which minimize f will be obtained by the iterative search strategy outlined in the forthcoming.

Algorithm and Implementation. The objective function was minimized by the General Conjugate Gradient (GCG) algorithm with an acceptable point line search, as outlined in [14]. The variables σ_o, D, and p were scaled by 10^3, 5×10^4, and 5.0, respectively. Analytical derivatives were used. Reset was employed every ten multivariate iterations. Computations were done in double precision Fortran on the DEC-1099 computer at Vanderbilt University. Convergence was assumed when the magnitude of the gradient was reduced to 10^{-6} or less.

The computer program was used to minimize a wide range of functions with known minima (including least-squares objectives in the form of equation (8)) prior to conducting this investigation. The expected minimizers were correctly identified by the algorithm in every case.
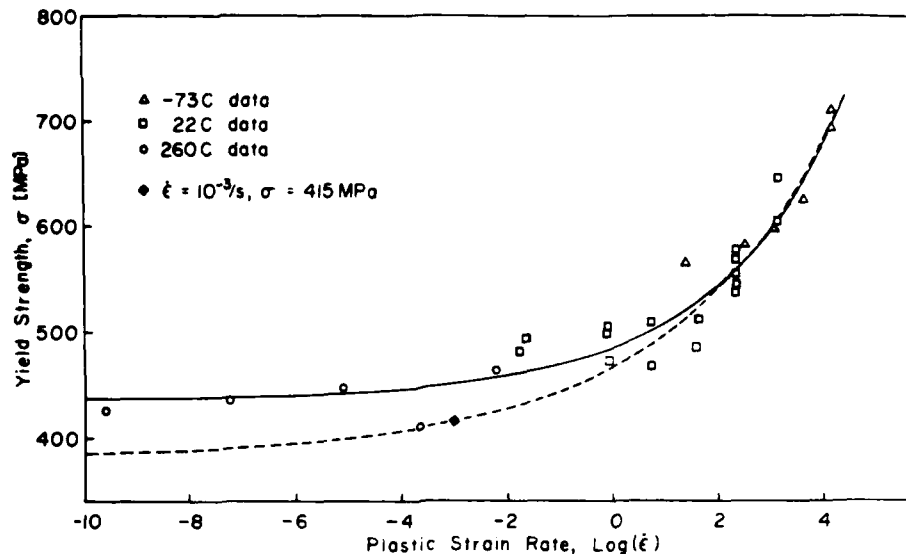
Fig. 2 Yield strength/strain rate data for A533B normalized to 93C. Strain rate is in s⁻¹.

Results

The data normalized to 93C by equation (5) (see Fig. 2) were used to formulate the objective function. Initial estimates of the parameters were

$$\begin{bmatrix} \sigma_o \\ D \\ p \end{bmatrix} = \begin{bmatrix} 100 \text{ MPa} \\ 50000 \\ 5.0 \end{bmatrix}$$

The final solution obtained by the minimization algorithm was

$$\begin{bmatrix} \sigma_o \\ D \\ p \end{bmatrix} = \begin{bmatrix} 437.40 \text{ MPa} \\ 297930 \\ 5.6338 \end{bmatrix}$$

The resulting curve is given by the solid line of Fig. 2 where we see that equation (7) maps the data with maximum yield strength error of less than ± 9 percent and an average error of less than 4 percent. The solid line of Fig. 2 can be transformed to other temperatures by manipulating equations (5) and (7) to obtain

$$\sigma = \sigma_o[(\dot{\epsilon}_j/D')^{(1/p')} + 1] \qquad (10)$$

where $D' = A(D/A)^{T_R/T_j}$ and $p' = T_R p/T_j$. Since A, D, p, T_j and T_R are all known, the yield strength can be determined at any strain rate $\dot{\epsilon}_j$, corresponding to T_j. The curves presented in Fig. 1 were obtained in this manner. Even though these curves are not formally "optimal" in the least-squares sense, there is excellent qualitative agreement at each temperature and deviations are acceptably small. Again, extrapolation outside the range of existing data is not recommended.

Forcing the Curve to Contain a Particular Point

The strategy outlined in the foregoing will be satisfactory for many applications; however, there may be occasions when it is desirable to give preferential treatment to a particular point. For example, facilities may be available to conduct tensile tests at the single strain rate of $10^{-3} s^{-1}$. It may be desirable to take advantage of published data at higher strain

rates in the development of the model. One approach would be to include the locally obtained data in the least-squares formulation of equation (8). This would essentially give equal consideration to all of the available data in the estimation of the model parameters. A second approach, which favors the local data point over the others, would be to force the mathematical function to contain the preferred point. This would be done by taking one variable out of equation (7) with considerable algebraic manipulation. Alternatively an equality constraint can be introduced in the minimization to enforce the preferred relation. This procedure is illustrated in the forthcoming.

Consider the case where the yield strength for a particular specimen has been found to be 415 MPa at a plastic strain rate of $10^{-3} s^{-1}$ and a temperature of 93C. The required equality constraint for the minimization would be

$$\sigma_o[(0.001/D)^{(1/p)} + 1] - 415 \times 10^6 = 0 \qquad (11)$$

The constrained nonlinear programming problem is given by equation (8) such that equation (11) is satisfied and this problem can be addressed in numerous ways (e.g., reduced gradient, Lagrange multiplier based penalty function, etc., see [13] for a survey of methods). For simplicity we chose to use a sequential unconstrained minimization technique as outlined by Fiacco and McCormick [15]. The initial constraint weighting factor was .1 and this was multiplied by 0.08 for each successive minimization. The solution obtained was

$$\begin{bmatrix} \sigma_o \\ D \\ p \end{bmatrix} = \begin{bmatrix} 382.84 \text{ MPa} \\ 62920 \\ 7.2455 \end{bmatrix}$$

Convergence was based on step length reduction to 10^{-6} rather than the gradient test.

The constrained relation is given by the dashed line of Fig. 2. This curve minimizes the objective function of equation (8) subject to the requirement that equation (11) be satisfied. Although not formally least-squares optimal because it gives preferential treatment to a single data point, there are occasions when such an approach may be considered appropriate. The nonlinear programming method outlined here can readily accommodate the situation.

Conclusions

In this note we have presented an objective technique (based on the principle of least squares) to estimate the parameters of the Malvern equation. The nonlinear programming approach provides values for σ_o, D, and p which exhibit excellent agreement with experimental data for A533B steel over a wide range of temperatures.

Acknowledgments

This work has been supported by the Office of Naval Research, Structural Mechanics Division under Contract No. N00014-80C-0521. The authors would like to thank Dr. Y. Rajapakse of ONR for his support and assistance. The support of the National Science Foundation under Grant No. MEA-8119130 is also gratefully acknowledged.

References

1 Johnson, W., and Mellor, P. B., *Engineering Plasticity*, Van Nostrand Reinhold Company, Toronto, 1973.

2 Malvern, L. E., "Experimental Studies of Strain Rate Effects and Plastic Wave Propagation in Annealed Aluminum," *Proceedings of the ASME Colloquium on Behavior of Material under Dynamic Loading*, 1965, p. 81.

3 Marquardt, D. W., "An Algorithm for Least Squares Estimation of Nonlinear Parameters," *SIAM Journal*, Vol. 11, 1963, p. 431.

4 Himmelblau, D. M., *Applied Nonlinear Programming*, McGraw-Hill Book Co., New York, 1972, pp. 213-217.

5 Steichen, J. M., and Williams, J. A., "High Strain Rate Tensile Properties of Irradiated ASTM Grade B Class 1 Pressure Vessel Steel," *HSST Technical Report No. 32*, July 1973.

6 Oldfield, W., Wullaert, R. A., Server, W. L., and Wilshaw, T. R., "Fracture Toughness Data for Ferritic Nuclear Pressure Vessel Materials," Task A—Program Office, Control Material Round Robin Program, *Effects Technology, INC. TR75-34R*, July 1975.

7 Server, W. L., "General Yielding of Charpy V-Notch and Precracked Charpy Specimens," ASME *Journal of Engineering Materials and Technology*, Vol. 102, 1973, p. 183.

8 Fowler, R. H., *Statistical Mechanics*, The MacMillan Company, New York, 1936.

9 Christian, J. W., "The Stress Dependence of Dislocation Velocity and its Relation to the Strain Rate Sensitivity," *Acta Metallurgica*, Vol. 12, 1964, p. 99.

10 Bennett, P. E., and Sinclair, G. M., "Parameter Representation of Low-Temperature Yield Behavior of Body-Centered Cubic Transition Metals," ASME *Journal of Basic Engineering*, Vol. 88, 1966, p. 518.

11 Neville, A. M., and Kennedy, J. B., *Basic Statistical Methods for Engineers and Scientists*, International Textbook Co., Scranton, Pa., 1964.

12 Hornbeck, R. W., *Numerical Methods*, Quantum Publishers, New York, 1975.

13 Himmelblau, D. M., *Applied Nonlinear Programming*, McGraw-Hill Book Co., New York, 1972.

14 Johnson, G. E., and Townsend, M. A., "A Generalized Direct Search Acceptable Point Technique for Use with Descent-Type Multivariate Algorithms," *Journal of Franklin Institute*, Vol. 309, 1980, p. 163.

15 Fiacco, A. V., and McCormick, G. P., *Management Science*, Vol. 10, 1964, pp. 363, 601.

ANALYSIS OF CRACK ARREST UNDER ELASTIC-PLASTIC CONDITIONS

by

G. T. Hahn*, P. Bastias**, A. Kumar**, and C. A. Rubin***

ABSTRACT

Elastic-plastic finite element analyses of quasistatic crack propagation and
arrest in a compact test specimen are described. The analyses evaluate the
effect of the prior plastic deformation history of the propagation event on
the shape of the J-resistance curve of the arrestor. In addition, experiments
employing a special device are used to simulate fast fracture and arrest in
small laboratory test specimens of ductile HY-80 steel and tough 7075 aluminum.
The results show that large dynamic elevations of the J-curve are encountered
during arrest. A relatively simple procedure for assessing or designing welded-
in, steel crack arrestors, based on these findings is proposed.

Key Words: Fracture, crack arrest, J-resistance curve, HY-80 steel,
7075 aluminum, crack arrestors, design, history, rate, dynamic
J-curve.

INTRODUCTION

There is long-standing interest in designs that will stop a rapidly
advancing crack before structural integrity is compromised[1-4]. Methods are
available for determining the NDT-temperature[3] or the arrest toughness
values[5-8] of steel plates that will arrest a short crack, i.e., ~ 10 mm-
long, emerging from a locally embrittled region. Existing toughness

*Professor, **Graduate Student, and ***Associate Professor, Department of
Mechanical and Materials Engineering, Vanderbilt University, Nashville, TN
37235

specifications have thus controlled the kind of "pop-in" crack that originated from an arc strike and severed the hull of the U.S.S. Ponaganset in 1947.[8] However, there is no general and rational method for designing welded-in crack arrestors that can stop a long fracture, i.e., $0.1m \leq \alpha \leq 2m$ in large structures such as ship hulls, pressure vessels, line pipe, etc.[9] This remains a difficult problem because very high toughness levels: 200 MPa$\sqrt{m}$ < K_{Ia} < 600 MPa$\sqrt{m}$ (200 KJ/m^2 < J_{Ia} < 2 MJ/m^2) are needed to arrest long fractures in a fully loaded structure. Figure 1 describes a practical example: a fracture initiated by a short defect in a 100 mm-wide, brittle weld. The adjacent steel plates probably must possess an arrest toughness, $K_{Ia} \approx 200$ MPa$\sqrt{m}$ to stop the unstable crack from penetrating with a reasonable margin of safety.* If the plates fail to stop the fracture, a tough welded-in arrestor of the same weakness located in the path of the crack 1 m from the weld may produce arrest if it possesses a toughness $K_{Ia} \approx 600$ MPa.** Arrestors located farther from the weld would have to be proportionately thicker or tougher.

The LEFM-based toughness estimates given above are not reliable because the LEFM requirements are difficult to satisfy at the high K_I-levels.***

---

*The statically evaluated K_I-value for the 2a = 100 mm-long crack emerging from the weld zone is K_I = 149 MPa$\sqrt{m}$. This assumes a total stress of σ = 375 MPa ($\sigma_{applied}$ = 250 MPa plus $\sigma_{residual}$ = 125 MPa), and that the other dimensions are much larger than 2a. This calls for an arrest toughness of at least K_{Ia} = 200 MPa$\sqrt{m}$ to arrest the crack with a margin of safety.

**The statically evaluated K_I-value for the 2a = 2m-long crack entering a welded in arrestor of the same thickness is K_I = 443 MPa. This assumes that the weld residual stresses can now be neglected and that the other dimensions of the structure are still much larger than 2a. An arrest toughness of at least K_{Ia} = 600 MPa$\sqrt{m}$ is required to stop the crack with a margin of safety.

***For example, to satisfy the requirement that the crack length is less than 1/10 of the plastic zone extent: $a > 10 \, r_o \approx 2 \, (K_I/\sigma_o)^2$. When K_I = 200 MPa$\sqrt{m}$ and σ_o = 500 MPa, this means that 2a > 0.6m at arrest which is 6x the value involved in the preceding example.

Figure 1. Example of a practical crack arrest problem. A 100 mm-wide weld: fusion plus HAZ, with a low toughness: K_{IC} = 40 MPa (J_{IC} = 7.7 KJ/m^2) contains a 2a = 4mm long crack. The crack becomes unstable when the total stress ($\sigma_{applied}$ = 250 MPa plus $\sigma_{residual}$ = 250 MPa) reaches σ = 500 MPa. The crack begins to extend and becomes a 2a = 100 mm-long rapidly propagating fracture when it emerges from the weld zone and begins to penetrate the adjacent steel plates. Question: How tough do the plates have to be to assure that the crack will be arrested? How tough does a welded-in arrestor plate located in the path of the fracture 1 m from the weld have to be to assure arrest?

They are also unreliable because the estimates given do not take account of the increase in toughness obtained when the ductile crack begins to penetrate the arrestor as described by its R-curve. The J-integral concept together with the J-resistance curve are therefore better suited for characterizing the response of relatively tough materials. With this in mind, Hahn and Dantam[10] proposed that the J_R-value evaluated at $\Delta a = 1.5$ mm can serve as a measure of the crack arrest toughness: $Ja(2) = J_R$.* This measure is valid for long cracks and arrestors that display the ductile fibrous mode of fracture during the arrest process.**

However, the use of J-curves in arrest analyses involves several unresolved complications illustrated in Figure 2:

(i) Deformation History Effects. Figures 2a, b and c illustrate that the shape of the J-resistance curve depends on the prior plastic deformation history. The conventional J-curve (Figure 1a), produced by ductile crack extension with a prior history of completely brittle extension, is different from the J-curve (Figure 1b) for ductile crack extension with a prior history of ductile crack extension. The J-curve for a propagation-arrest event (in Figure 1c) is intermediate. This raises questions whether the conventional J_R-curve has the right shape for a crack arrest analysis.

(ii) Geometry Dependence. The shape of the J-curve for a tough material is geometry dependent for anything but small amounts of ductile crack extension,

---

*Hahn and Dantam identify two measures of arrest toughness: $Ja(i) \equiv J_{IC}$, and $Ja(2) \equiv J_R(\Delta a = 1.5$ mm$)$. The quantity $Ja(1)$ is appropriate when the crack extension is a small fraction of the initial crack length; $Ja(2)$ when the extension is a large multiple of the initial length. The K_I-equivalents of these 2 values are: $K_{Ja}(1) \equiv K_{JC} = \sqrt{J_{IC}E}$, and $K_{Ja}(2) \equiv K_{JR} = \sqrt{J_R E}$.

**The transition temperature of a steel arrestor must be well below the service temperature to assure that it will display high toughness fibrous fracture under dynamic conditions rather than low toughness cleavage.
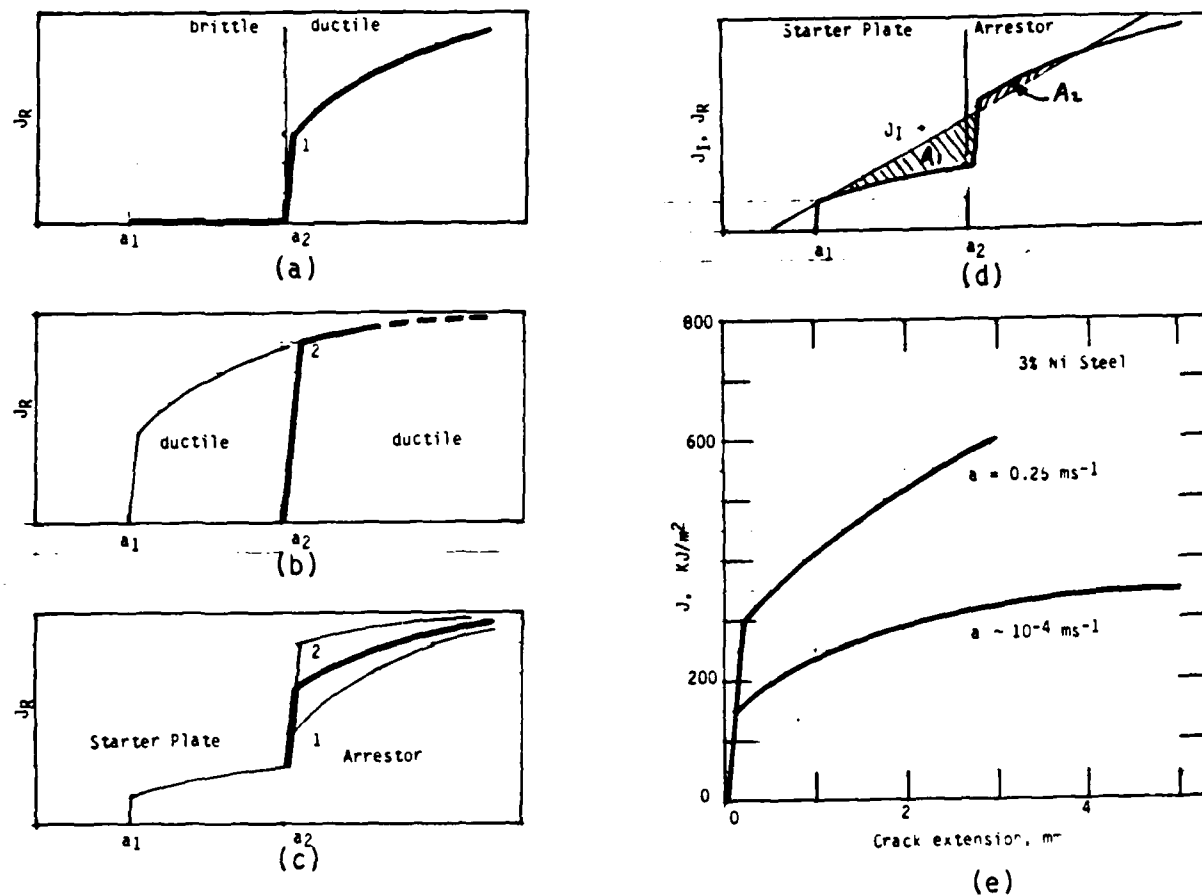
Figure 2. Complications attending the use of J-resistance curves in the analysis of crack arrest: (a), (b) and (c) compare the shape of the J-curve for ductile crack extension from a pre-existing crack of length a_2 with different prior deformation histories in the interval from a_1 to a_2, (d) schematic drawing illustrating the excess strain energy (shaded area A_1) part of which may be returned to make up the energy deficit (shaded area A_2) and permit the crack to split the arrestor, and (e) example of dynamic elevation of the J-curve.[17,18]

typically no more than $0.05 < \Delta a/(w-a) < 0.1$ where w is the uncracked ligament.[11]
Consequently, it is again not clear that the conventional J-curve is appropriate
when arrest is preceded by large amounts of extension, as in the examples
cited earlier.

(iii) <u>Kinetic Energy Release.</u> A part of the excess strain energy (defined by
the difference between the static J-driving force and J-resistance curves at
instability in Figure 2d) is converted into kinetic energy, and part of this may
be returned adding to the crack driving force during arrest (see Figure 2).[6,12]
The kinetic energy return is difficult to evaluate without a dynamic analysis
and this complicates the task of defining the arrest condition.

(iv) <u>Dynamic Elevation of the J-Curve.</u> There is evidence from several sources
that the J-curve ductile crack extension, normally measured for very low rates
of crack extension, i.e., a $\sim 10^{-4}$ ms^{-1} is elevated by increasing the crack
speed.[13-15] This does not fundamentally alter the ultimate crack stopping
ability of the material because the crack velocity must be reduced to zero even-
tually to produce arrest. However, the transient elevation of the J-curve
produced by the high velocities of unstable cracks 10^2ms$^{-1} < a < 10^3$ms^{-1}, could
provide a mechanism for dissipating the returned kinetic energy.

This paper presents finite element calculations of the effect of the prior
deformation history on the shape of the J-curve. It also presents measurements
of the arrest of fully brittle fractures in tough, ductile aluminum and HY-80
steel. The results show that prior history can frequently be neglected and
that the J-curve retains its geometry independence when arrest is preceded by
relatively brittle fracture. There are indications the elevation of the
J-curve with crack velocity can compensate for kinetic energy return. Simplified,
guidelines for designing crack arrestors are proposed on this basis.

ANALYSES AND PROCEDURES

Finite Element Analysis

Finite element calculations were performed to examine the effects of the deformation history - - the plastic deformation produced by an advancing fracture before it reaches the arrestor - - on the J-resistance curve subsequently displayed by the arrestor. To simplify the problem, quasi-static, stable crack growth and arrest were simulated in the elastic-plastic finite element model of a 4T Compact Test Specimen shown in Figure 3. The model is composed of 172 quadrilateral and 8 noded elements with a total of 38 nodes forming the path of the crack. The simulations were performed with the finite element code ABAQUS on VAX 11/780 and 11/785 machines.

The initial position of the crack tip is within the region labeled Material A, which is endowed with a relatively low toughness. The model is subjected to a continuously increasing load-point displacement and the nodes ahead of the crack are released at the appropriate time to simulate crack extension on the symmetry plane. Details of the procedure are given elsewhere.[16] The crack eventually reaches the region labeled Material B after a crack extension of either Δa = 6mm (shown in Figure 3) or Δa = 2mm (configuration not shown). The crack then arrests for a time since Material B is tougher than Material A, and then continues to grow as the conditions for extension in Material B are satisfied as a result of the increasing load point displacement.

The deformation behavior of the 2 materials is the same. It is given by the piecewise-linear representation of the stress-strain curve of A533B pressure vessel steel at 93°C (see Figure 4a), and approximates power law hardening after the initial yield: E = 198 GPa, σ_0 = 383 MPa, n = 10.[13,17] The crack extension in Material A was controlled to proceed according to a predetermined J-resistance curve. The effects of several J-curves appropriate
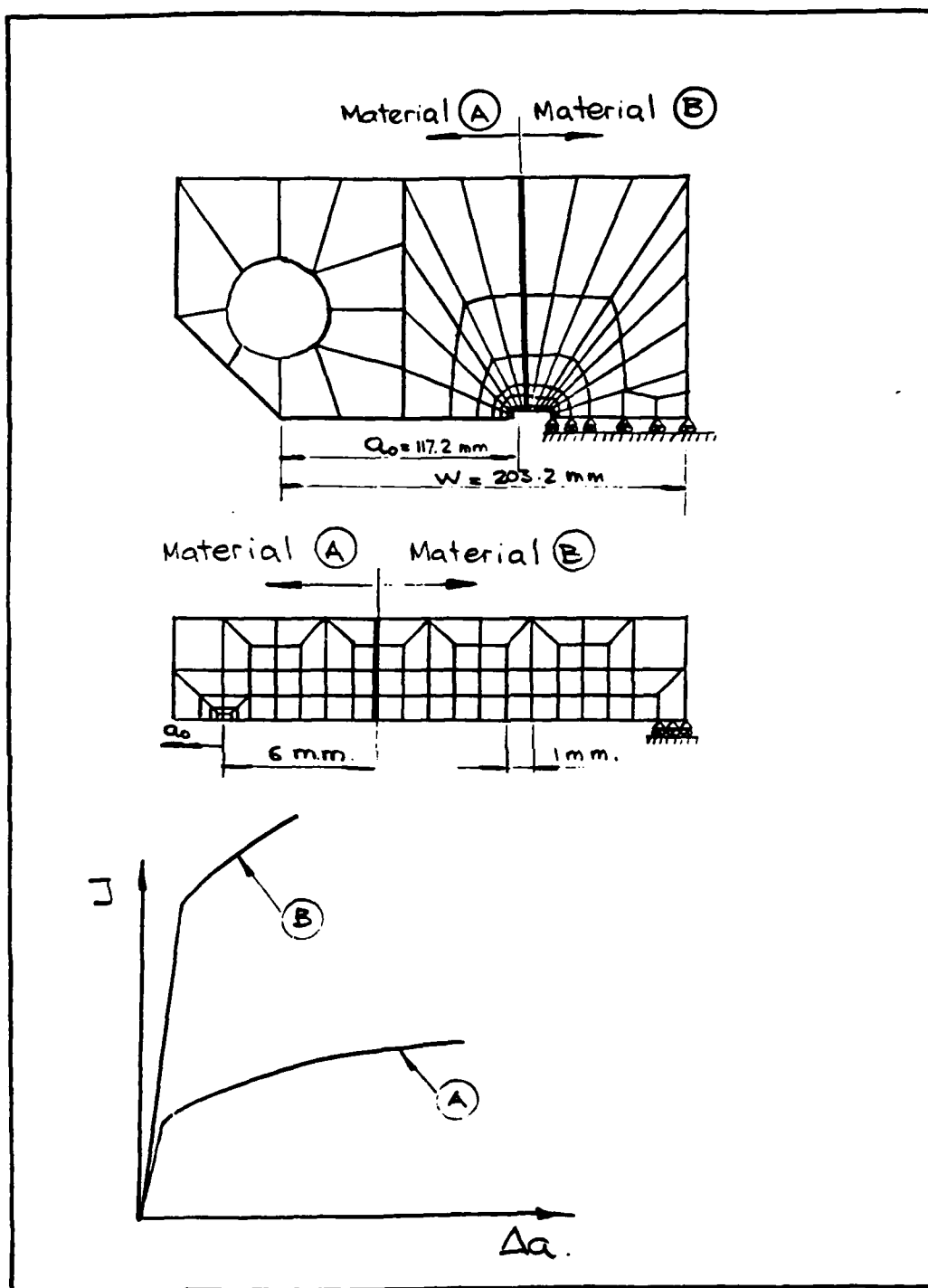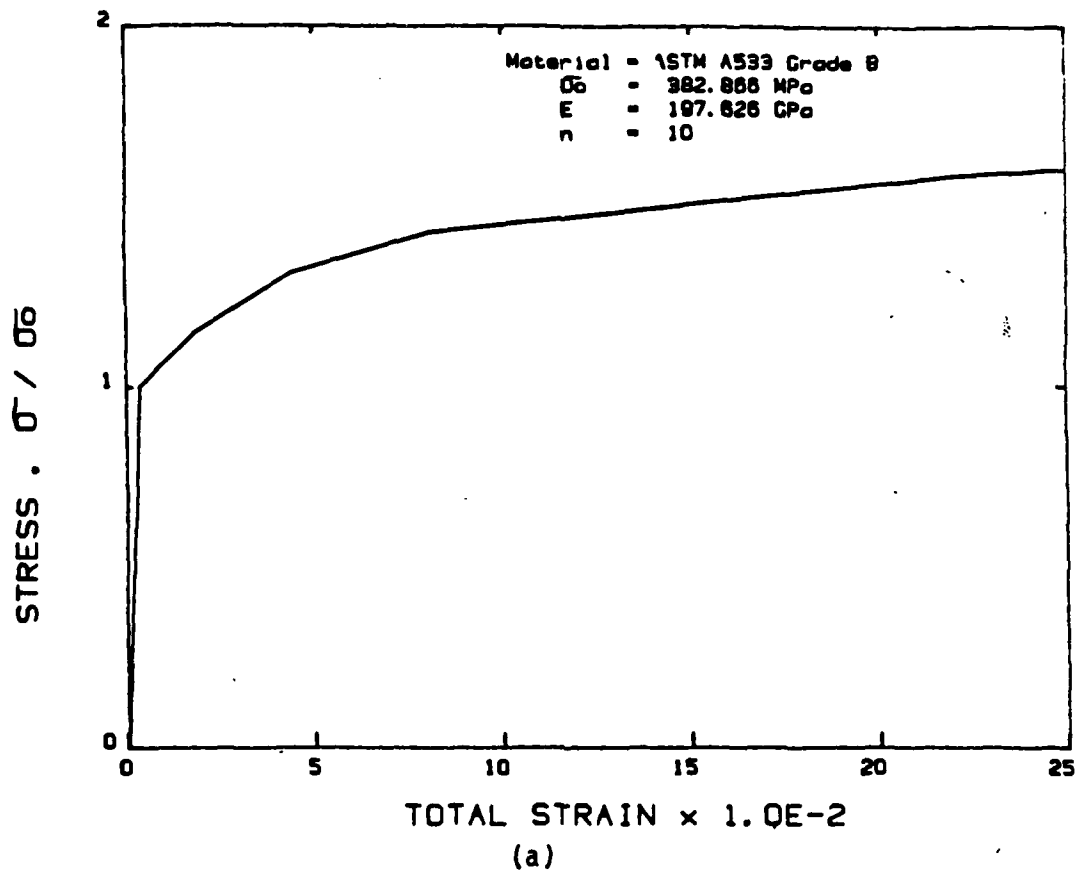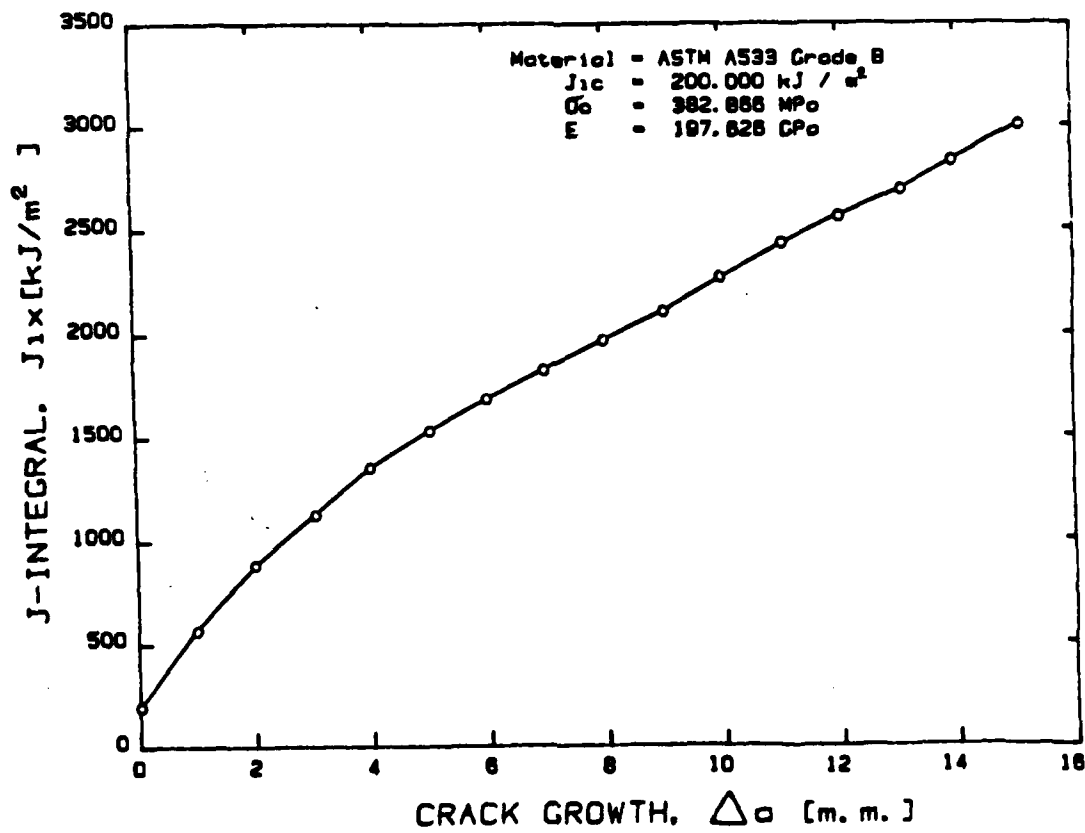
Figure 3. Finite element model of 4T compact test specimen.

Figure 4. Stress-strain characteristics and J-resistance curve of model materials: (a) piecewise-linear stress strain curve of A533B pressure vessel steel employed for Material A and Material B, and (b) conventional J-resistance curve of Material B.[17,18]

for toughness levels in the range: $50\ MPa\sqrt{m} < J_c < 120\ MPa\sqrt{m}$ were examined.
Crack extension in Material B was controlled by the crack opening displacement-
resistance curve previously derived for A533B at 93°C[13,18]: $COD = 2.5332 \cdot 10^{-4}$
$+ 0.47082\ \Delta a - 33.58\ (\Delta a)^2$. This resistance curve is viewed as a local criterion
that is insensitive to the prior deformation history. For ductile crack exten-
sion, it produced a toughness of: $J_{Ic} = 200\ KJ/m^2$ ($K_{Jc} = 203\ MPa\sqrt{m}$), and the
conventional J-curve shown in Figure 4b, when the extension proceeds from a
pre-existing, perfectly brittle crack. In the present calculations, the
different deformation histories prior to arrest produced different $J-\Delta a$
relations for the arrestor. These J-curves were evaluated with the finite
element model as the crack penetrated into Material B.

Crack Arrest Measurements

Measurements of crack arrest in a ductile steel and aluminum alloy were
carried out to evaluate the dynamic elevation of the J-curve by large crack
velocities. These measurements employed a non-standard, 6 in x 6 in (152.4 mm
x 152.4 mm) pre-cracked, compact-type test specimen whose measuring capacity
is increased by attaching reusable, hardened steel arms. The operation of the
system, referred to here as a "fast fracture device" is shown schematically in
Figures 5a and 5b. The test specimen and other components are described in
Figures 5c and 5d. To facilitate the analysis of the experiments, the variation
of compliance of the system with crack length was evaluated with the aid of a
finite element model. Details of these calculations are presented elsewhere.[19]

After the bolt breaks, the system behaves as if split by a zero toughness
crack which runs to the precrack and is arrested by the compact specimen, i.e.,
ductile arrest with a history of completely brittle crack propagation. The
displacement of the arms at the bolt and wedge at the onset of fracture were
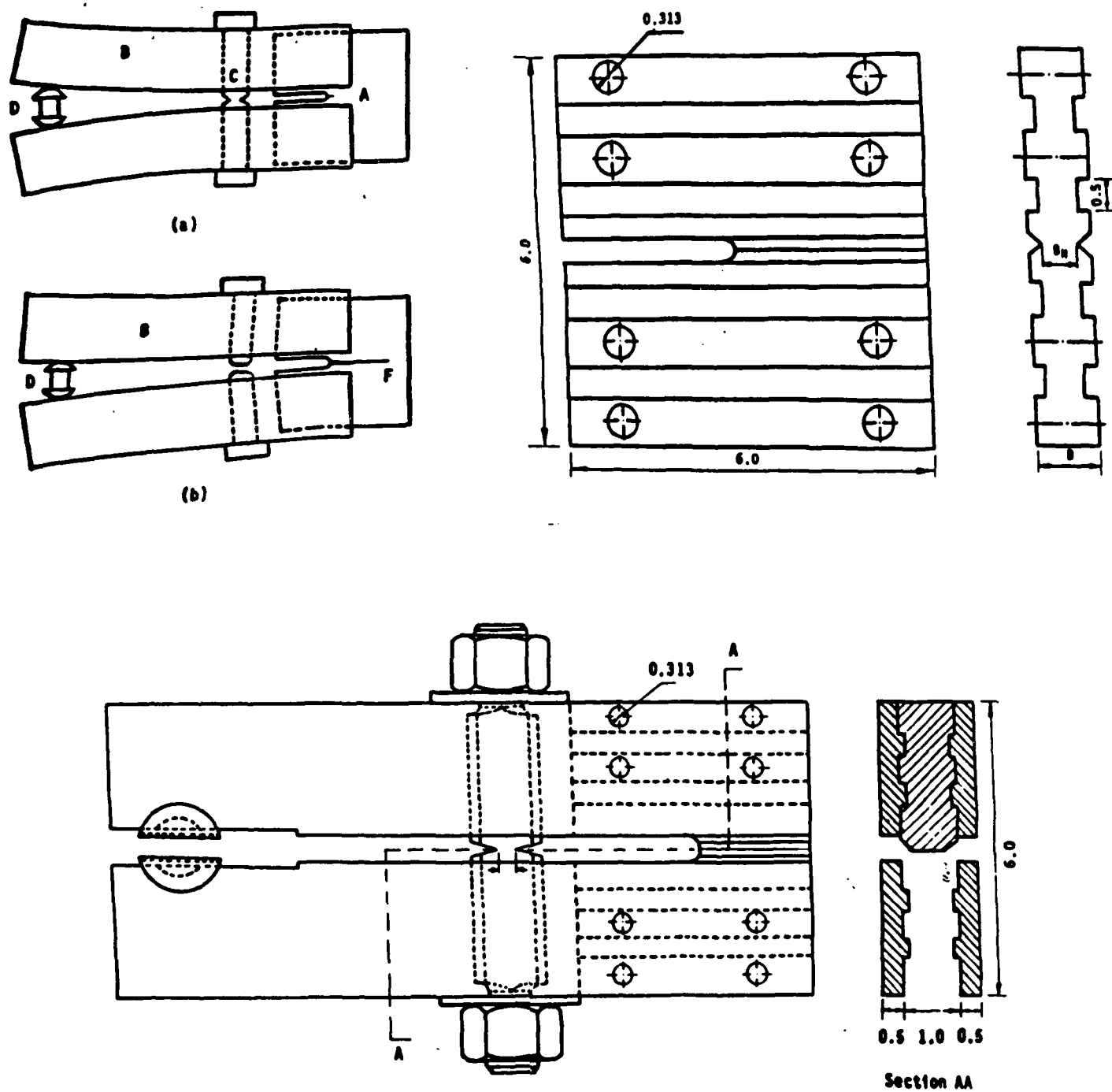
Figure 5. Fast fracture device: (a) and (b) schematic drawing of operation,
(c) test specimen, and (d) details of assembly.

measured with standard displacement gages. These displacements and the static compliance values for the system before and after arrest were used to estimate the elastic energy released during the arrest event. The average value of the propagating crack toughness, G_D, was then determined by dividing the released energy by the total fracture area, assuming that all of the released energy is consumed as fracture energy. The quantity G_D can be viewed as a measure of the elevation of the J-resistance curve as a result of crack extension and crack velocity.

Measurements were carried out on HY-80 steel and the 7075-Aluminum alloy, which was solution treated at 470°C for 1/2 hr. and aged at 120°C at different time intervals to achieve HRB = 45, 78, and 92. The toughness values J_{IC} and $J_a(2) = J_R$ are listed in Table 1.

RESULTS

Finite Element Analyses

The results of the finite element computations are presented in Figure 6. These show the different J-curves which were prescribed for Material A and controlled the "start" of the relatively brittle propagation, and the corresponding, calculated J-curves for Material B which served as the arrestor. The results illustrate the J-curve for the arrestor is influenced by the deformation history, and is unaffected by the deformation history when the starter toughness, i.e., the J_{IC}-values for the material in which the crack starts propagating, are much lower than the arrest toughness:

$$\frac{J_{IC} \text{ (starter)}}{J_{IC} \text{ (arrestor)}} < 0.1 \text{ or} \tag{1a}$$

$$\frac{K_{Jc} \text{ (starter)}}{K_{Jc} \text{ (arrestor)}} < 0.3 \tag{1b}$$

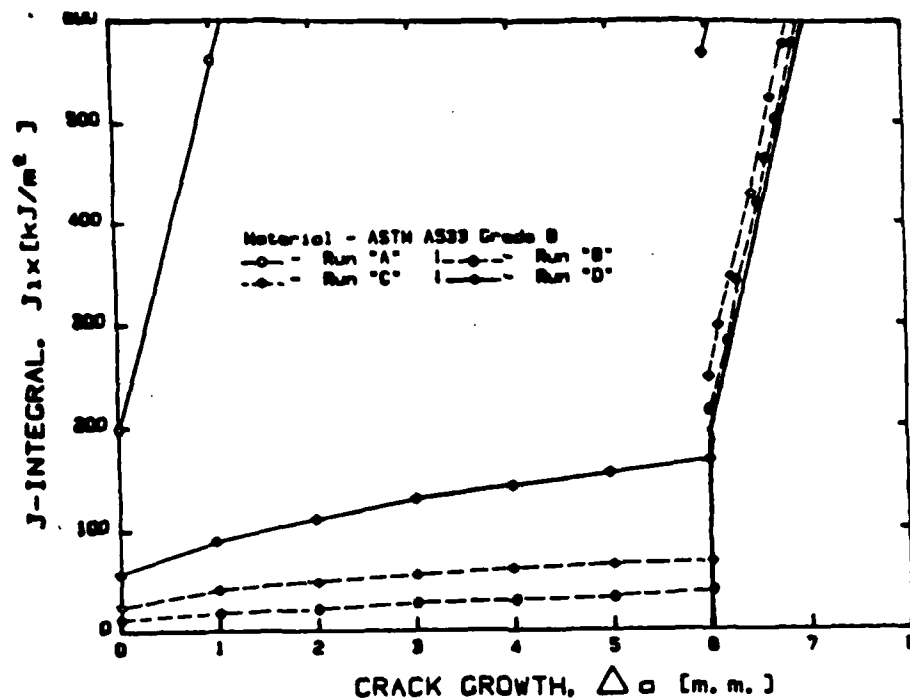Figure 6. Results of finite element calculations showing the effects of the prior plastic deformation history on the shape of the J-resistance curve of the arrestor.
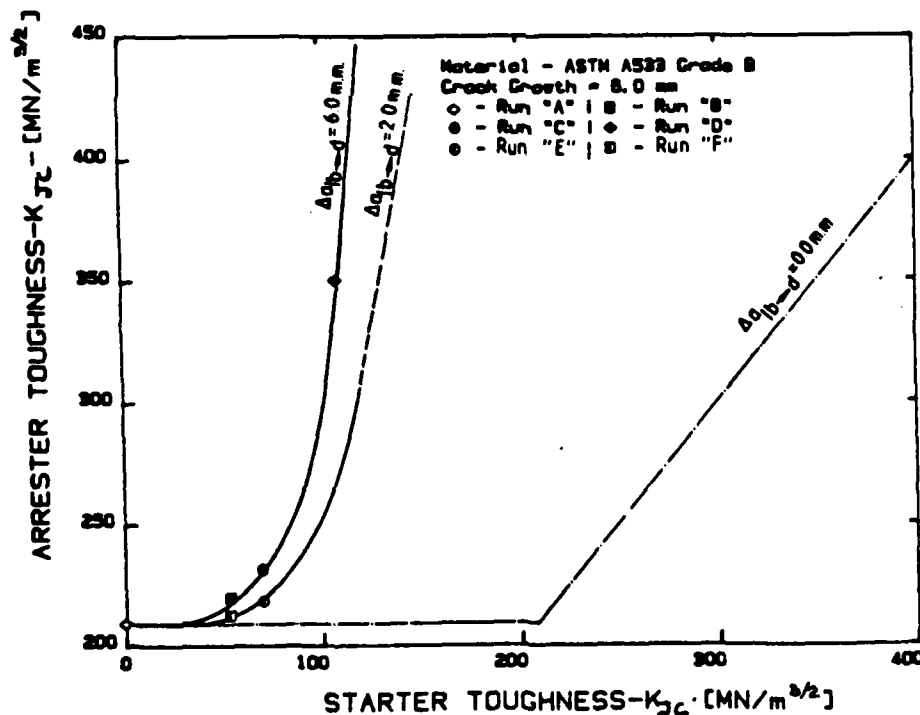

Figure 7. Summary of finite element calculations showing the effects of the toughness of Material A (starter toughness) on the calculated toughness of Material B (arrestor toughness) for crack extension increments of Δa = 2mm and Δa = 6mm.

These results are summarized in Figure 7, which also shows that these conclusions are relatively insensitive to the extent of propagation prior to arrest. In other words, it appears that the arrestor's response to a relatively brittle, prior propagation history is the same as its response to a pre-existing crack. It follows that the rules for the geometry independence of the J-curve for extension, from a pre-existing (brittle) crack, will also apply. This means that the conventional J-curve for the arrestor material will describe resistance to penetration even when arrest is preceded by large crack extensions and for relatively small remaining ligaments.

Crack Arrest Measurements

The results in Table 1 show that the tough steel and aluminum alloy suffer relatively small crack penetrations prior to arrest. When the relatively large energy releases, e.g. ~ 400 J, produced by the fast fracture device are combined with small penetrations and deep face grooves, large values of G_D, the fast propagating crack toughness, result. The G_D value is 18X and 3.6X larger than $J_a(2)$ for the HY-80 steel and the tough, HRB = 45, aluminum alloy, respectively. These increases are qualitatively consistent with the measurements of Joyce[14,15] in Figure 2e which reveal a ~ 2X increase in J-values for an increase in crack velocity from a $\sim 10^{-4}$ ms^{-1} to a ~ 0.25 ms^{-1}. These increases in toughness are related to the rate sensitivity of the plastic flow stress[13] and to changes in the fracture process[19].*

The interpretation of the present measurements involves uncertainties because other sources of energy dissipation have been neglected. However, even allowing for a factor of 2 error in the energy consumed by fracture,

---

*The fracture surfaces of the HY-80 steel and HRB 45, 7075 aluminum are ~ 5X and ~ 3X rougher, respectively, than the surfaces produced by a slow tearing test.

Table 1. Summary of Crack Arrest Measurements

Material	B_N/B	Δa mm	J_{IC} KJ/m^2	$J_a(2)$ KJ/m^2	G_D KJ/m^2
HY-80	0.80	9	221	324	5830
7075 Al					
HRB 45	0.25	8.5	192	740	2680
HRB 78	0.25	50.8	52	292	670
HRB 90	0.25	>88	22	148	<490

B_N/B is the fraction of the specimen thickness remaining at the face grooves.

it appears that the dynamic elevation of the J-curve for arrest of fast propagating cracks by ductile steel could be ~ 10X. Such a high transient toughness would consume the kinetic energy return which is not accessible to the static analysis.

DISCUSSION

The results of this study suggest that a relatively simple J-integral based procedure may be adequate when assessing or designing tough, welded-in, steel crack arrestors for long crack extensions, i.e., $\Delta a > 10 a_0$. The main features of such a procedure and a tentative requirement for the arrestor width are proposed below:

(i) Crack Driving Force. The crack driving force produced when the crack reaches the arrestor interface is evaluated in terms of J_I using a static analysis usch as the one developed by Kumar, German and Shih[20] and Kumar, et al.[21]. When appropriate, an LEFM analysis can be used.

(ii) Crack Arrest Toughness. The plane strain, crack arrest toughness: $Ja(2) \equiv J_R$ ($\Delta a = 1.5$ mm), is derived from information provided by a conventional J_{Ic}-determination (ASTM E-813) or a Resistance Curve measurement (ASTM E-561). To assure ductile, fibrous crack extension in the arrestor material, DT tests of the arrestor must show 100% fibrous fractures at temperatures from 25°C to 50°C below the lowest service temperature. Effects of prior history are neglected. Plane strain conditions are assumed since these are more easily obtained with a rapidly propagating crack, and effects of the deformation history on the J-curve of the arrestor are neglected.

(iii) Arrest Criterion. The criterion for arrest is $J_I < J_a(2)$. Complications attending kinetic energy return are neglected for steel arrestors.

(iv) Arrestor Thickness. The arrestor thickness determines the level of tensile stress and the value of J_I. Increasing the thickness will reduce J_I and improve the crack stopping capability.

(v) Arrestor Width. The arrest criterion employed insures that in the absence of kinetic energy return, the maximum crack penetration into the arrestor Δa < 1.5 mm. With kinetic energy return (i.e., total crack extensions prior to arrest that are large compared to the overall dimensions of the structure), arrestor penetrations are likely to be Δa < 50 mm. To assure that the arrestor can both survive such a penetration and contain the plastic zone of the crack to reduce the risk of weld-failure, an arrestor width dimension, w, related to the plastic zone size at arrest and the J_I-value of par 1 is proposed.

$$W = 0.05m + \frac{0.4\, J_I E}{\sigma_0^2} \qquad (2)$$

where E and σ_0 are the elastic modulus and yield strength of the arrestor.

A similar procedure for aluminum arrestors may require an added provision for kinetic energy return since the dynamic elevation of the J-curve may be too small to accommodate it. The proposed procedure is intended to serve as a starting point for further discussion. Clearly, as a design approach, it requires careful scrutiny and should be critically tested before adoption. Values of $J_a(2)$ and corresponding estimates of the crack stopping capabilities of several steels derived from the proposed procedure are listed in Table 2.

CONCLUSIONS

1. Effects of the prior plastic deformation history on the shape of the J-resistance curve have been examined with a finite element model. The calculations reveal that history effects can be neglected when the toughness ratio: J_{IC} (starter)/J_{IC} (arrestor) < 0.1 or K_{IC} (starter)/K_{IC} (arrestor) < 0.3

Table 2. Compilation of Crack Arrest Toughness Values of Selected Steel and an Aluminum Alloy for Temperature Producing Fibrous Crack Extension in the Arrestor

Material	Test Temp, C	σ_o, MPA	CVN, J	J_{Ic}, KJ/m²	$J_a(2)$, KJ/m²	Crack Arrest Capability, 2a, mm*	Reference
HY-130	RT	937	112,116	160	258	155	22
HY-130	25°C	902	80	172	--		23
HY-130	RT	882	152	268	643	440	24
HY-80	RT	558		156	324	550	22
HY-80	RT	616	110	146	--		14
A533-B(02)	149	413	176	207	523	1620	22,25
A533-B(03)	149	401	87	197	363	1190	22
A516-G70	149	303	137	156	324	1860	22
A106	RT	345		166	550	2420	14
7075-Al	RT	280	--	88	105	235	10
7075-Al	RT	552	--	45	45	26	10

*Length of a centrally located crack 2a that can be stopped by long, nominally elastic arrestors, $\sigma = 0.5\sigma_o$ (σ_o is the yield stress), located on either side of the crack: $2a = 2/\pi[K_{Ja}(2)/\sigma]^2$.

2. Experiments employing a special fast fracture device show that very large dynamic elevations of the J-resistance curve are encountered during the arrest of fast propagating cracks in tough, ductile arrestors. The measurements point to an 18-fold and 3.6-fold increase in the level of the J-curve for steel and an aluminum alloy, respectively.

3. The dynamic elevation of the J-curve for fibrous crack extension in a tough steel may be large enough to consume any kinetic energy which is returned to the crack during arrest.

4. The findings suggest that a relatively simple J-based procedure may be adequate for assessing or designing tough, welded-in steel crack arrestors.

ACKNOWLEDGEMENTS

REFERENCES

1. Williams, M. L. in Symposium on Effect of Temperature on the Brittle Behavior of Metals with Particular Reference to Low Temperatures, ASTM STP 158, American Society for Testing Materials, 1954, p. 11-41.

2. Robertson, T. S., J. Iron and Steel Inst., Vol. 175, 1953, p. 361.

3. Pellini, W. S., Principles of Structural Integrity Technology, Office of Naval Research, Arlington, VA, 1976.

4. Rolfe, S. T., Rhea, D. M., and Kuzmanovic, B. O., Fracture-Control Guidelines for Welded Steel Ship Hulls. Ship Structure Committee Report SSC-244, National Academy of Sciences, Washington, DC, 1974.

5. Krafft, J. M. and Irwin, G. R. in Applied Fracture Mechanics, ASTM STP-381 American Society for Testing Materials, 1965, p. 114-129.

6. Hahn, G. T., Rosenfield, A. R., Marshall, C. W., Hoagland, R. G., Gehlen, P. C., and Kanninen, M. F., in Fracture Mechanics, p. 205-227, N. Perrone et al. Eds., University Press of Virginia, Charlottesville, VA, 1978.

7. Fast Fracture and Crack Arrest, ASTM STP-627, G. T. Hahn and M. F. Kanninen, Eds., American Society for Testing Materials, 1972.

8. Pellini, W. S. and Puzak, P. P., "Fracture Analysis Diagram Procedures for the Fracture-Safe Engineering Design of Steel Structures", U. S. Naval Research Laboratory Report 5920, Washington, DC 1963.

9. Kanninen, M., Mills, E., Hahn, G., Marschall, C., Broek, D., Coyle, A., Masabushi, K., and Ituga, K., "A Study of Ship Hull Crack Arrestor Systems", Ship Structure Committee Report, SSC-265, National Academy of Sciences, 1976.

10. Dantam, V. and Hahn, G. T., in Proceedings of U.S.-Japan Cooperative Seminar, p. 213-220, T. Kanazawa, et al. Eds., Toyoprint Co., Japan, 1981.

11. Hutchinson, J. W. and Paris, P. C. in Elastic-Plastic Fracture, ASTM STP-668, American Society for Testing Materials, Philadelphia, PA, 1979, p. 37-64.

12. Kalthoff, J. F., Beinert, J., and Winkler, S. in Fast Fracture and Crack Arrest, ASTM STP 627, American Society for Testing Materials, Philadelphia, PA, 1977, p. 161-176.

13. Hoff, R., Viscoplastic Finite Element Analysis of Rapid Fracture, Ph.D. Dissertation, Vanderbilt University, 1984.

14. Joyce, J. A., "Static and Dynamic J-R Curve Testing of A533B Steel Using the Key Curve Analysis Technique", Nuclear Regulatory Commission, Report NUREG (CR-2274, Washington, 1981).

15. Joyce, J. A. and Hackett, E. M., The Application of the Key Curve and Multi-Specimen Techniques to Dynamic J-R Curve Testing of Alloy Steel. Nuclear Regulatory Commission, Report NUREG/CR-4579, Washington, 1986.

16. Bastias, P., "Finite Element Analysis of Crack Growth and Arrest", M.S. Dissertation, Vanderbilt University, 1986.

17. Hoff, R., Rubin, C. A. and Hahn, G. T., in Fracture Mechanics: Sixteenth Symposium, ASTM STP-868, American Society for Testing Materials, 1985, p. 409-430.

18. Hoff, R., Rubin, C. A., and Hahn, G. T., Eng. Fracture Mech., Vol. 23, 1986, p. 105-118.

19. A. Kumar, "Analysis of Crack Arrest Toughness Measurement for Design of Tough Materials", M.S. Dissertation, Vanderbilt University, 1985.

20. Kumar, V., German, M. D., and Shih, C. F., "An Engineering Approach for Elastic-Plastic Fracture Analysis", Electric Power Research Inst. Report NP-1931, Electric Power Research Institute, CA, 1981.

21. Kumar, V, German, M. D., Wilkening, W. W., Andrews, W. R., deLorenzi, H. G., and Mowbray, D. F., "Advances in Elsatic-Plastic Fracture Mechanics", Electric Power Research Institute Report NP-3607, Electric Power Research Institute, CA 1984.

22. Gudas, J. P., Vassilaros, M. G., Joyce, J. A., Davis, D. A. and Anderson, D. R., "A Summary of Recent Investigations of Compact Specimen Geometry Effects on the J_I-R Curve of High-Strength Steels", Nuclear Regulatory Commission Report NUREG/CR-1813, Washington, DC, 1980.

23. Joyce, J. A. and Hasson, D. F., "Characterization of Transition Temperature Behavior of HY-130 Steel by the J_{IC}-Fracture Toughness Parameter", Eng. Frac. Mech., Vol. 13, 1980, p. 417.

24. Hasson, D. F. and Joyce, J. A., "The Effect of a Higher Loading Rate on the J_{IC}-Fracture Toughness Transition Temperature at HY-Steels", J. Eng. Mats. and Tech., Vol. 103, 1981, p. 133-141.

25. Wessel, E. T., "Linear Elastic Fracture Mechanics for Thick-Walled, Welded Steel Pressure Vessels, Material Property Considerations", Practical Fracture Mechanics for Structural Steel, P.H. M.O. Dobson, ed., UKAEA 2 Chapman Hall, 1969.

Figure 1. Example of a practical crack arrest problem. A 100 mm-wide weld: fusion plus HAZ, with a low toughness: K_{IC} = 40 MPa (J_{IC} = 7.7 KJ/m^2) contains a 2a = 4mm long crack. The crack becomes unstable when the total stress ($\sigma_{applied}$ = 250 MPa plus $\sigma_{residual}$ = 250 MPa) reaches σ = 500 MPa. The crack begins to extend and becomes a 2a = 100 mm-long rapidly propagating fracture when it emerges from the weld zone and begins to penetrate the adjacent steel plates. Question: How tough do the plates have to be to assure that the crack will be arrested? How tough does a welded-in arrestor plate located in the path of the fracture 1 m from the weld have to be to assure arrest?

Figure 2. Complications attending the use of J-resistance curves in the analysis of crack arrest: (a), (b) and (c) compare the shape of the J-curve for ductile crack extension from a pre-existing crack of length a_2 with different prior deformation histories in the interval from a_1 to a_2, (d) schematic drawing illustrating the excess strain energy (shaded area A_1) part of which may be returned to make up the energy deficit (shaded area A_2) and permit the crack to split the arrestor, and (e) example of dynamic elevation of the J-curve.[17,18]

Figure 3. Finite element model of 4T compact test specimen.

Figure 4. Stress-strain characteristics and J-resistance curve of model materials: (a) piecewise-linear stress strain curve of A533B pressure vessel steel employed for Material A and Material B, and (b) conventional J-resistance curve of Material B.[17,18]

Figure 5. Fast fracture device: (a) and (b) schematic drawing of operation, (c) test specimen, and (d) details of assembly.

Figure 6. Results of finite element calculations showing the effects of the prior plastic deformation history on the shape of the J-resistance curve of the arrestor.

Figure 7. Summary of finite element calculations showing the effects of the toughness of Material A (starter toughness) on the calculated toughness of Material B (arrestor toughness) for crack extension increments of Δa = 2mm and Δa = 6mm.

ANALYSIS OF CRACK ARREST TOUGHNESS MEASUREMENT
FOR DESIGN OF TOUGH MATERIALS

A. M. Kumar*, G. T. Hahn**, C. A. Rubin** and N. Xu*

CENTER FOR MATERIALS TRIBOLOGY
Vanderbilt University
Nashville, TN 37235

ABSTRACT

This paper reports a preliminary study of a new laboratory test method designed to measure crack arrest toughness for tough, arrester grade steels The design is basically focused on producing large enough driving force to produce fast fracture and arrest in a small test piece of a very tough, ductile material. Tests conducted on HY-80 steel and 7075 aluminum specimens are reported. The analysis of arrest measurements presented assumes that all the energy released is conserved or converted into fracture energy. A static, lower-bound arrest toughness is evaluated from compliance analysis using an elastic-static finite element simulation of the loading device. A photogrammetric aspect of the fracture surface is performed to quantify and relate the microstructural features with fracture toughness. The results are consistent with the view that arrest toughness value derived from the J-Resistance curve is a valid measure of arrest capabilities of a tough material. It also indicates that rapid crack extension in a tough, ductile material can consume large amounts of kinetic energy released from the process of fracture.

*Graduate Student, **Professor, Department of Mechanical and Materials Engineering

INTRODUCTION

Initial attempts to measure crack arrest capabilities of steel by Robertson[1], were followed by the development of the Esso test[2], and the double tension test described by Yoshiki, et al.[3]. These tests provided measures of applied stress, crack length and temperature for which arrest is possible. Crosley and Ripling applied fracture mechanics concepts to measure the arrest toughness, K_{Ia}, with a double cantilever beam (DCB) specimen[4]. This was followed by the developed ot a wedge loaded 'duplex' specimen with a hardened steel starter section by Hahn, et al.[5], and a similarly loaded specimen with a hard weld starter by Crosley and Ripling[6]. Several methods have been proposed tor analyzing measurements of crack arrest in stift, wedge loaded specimens, whose static elastic energy release rate parameter, G, decreases continuously with crack growth. Kraft and Irwin[7], and Crosley and ripling[8] proposed a static, nonconservative interpretation of the crack arrest process in which they assumed that all the kinematic energy of the running crack is dissipated before arrest. Hoagland, Hahn and Rosenfield[9] proposed an alternative static analysis in which the kineatic energy was assumed to be completely conserved. In this case the same experiment is interpreted differently. Accordingly, in the latter stages of the propagation event, the stored kinetic energy supplied part of the fracture energy requirements. The same authors proposed a dynamic analysis assuming the conservation of kinetic energy and accounting for the dependence of the propagating crack's material toughness, G_D on crack velocity[10]. The latter theory was confirmed by experiments conducted by Kalthoff, Beinert and Winkler[11].

The above concepts provide a reasonable estimate of the crack arrest behavior of relatively brittle materials. However, with very tough materials,

neither the apparent critical energy release rate, G_c, nor J_c remain constant but increase with crack length. Recent work by Hoff, Hahn and Rubin[12] on strain rate effects using finite element analysis revealed that the J-resistance curve is elevated when a crack extends rapidly in a material with rate sensitive yield and flow properties. This result agrees with the experimental evidence of Joyce[13]. In real structures, crack extention is also likely to proceed very rapidly, producing large plastic strain rates (10^3/s to 10^6/s). As a consequence, there will be large elevations in the yield stress, resulting in higher toughness values while the crack is propagating. With this in mind, Dantam and Hahn[14] have proposed two points on the J-resistance curve (or their corresponding K equivalents) as lower bound measures of crack arrest toughness that can be used to design arresters:

$$J_a(1) \simeq J_{Ic}, \qquad\qquad K_{Ja}(1) = [J_{Ic}E/(1-\nu^2)]^{1/2} \qquad\qquad (1)$$

$$J_a(2) \equiv J_R(a = 1.5 \text{ mm}), \quad K_{Ja}(2) = [J_R E/(1-\nu^2)]^{1/2} \qquad\qquad (2)$$

The quantities $J_a(1)$ and $K_{Ja}(1)$ are appropriate for short arrester cracks, i.e., a < 100 mm, where the instability condition is determined by the initial part of the J_R-curve; $J_a(2)$ and $K_{Ja}(2)$ are indicated for longer arrested cracks, i.e., a > 500 mm, where the instability condition is determined by the latter part of the J_R-curve. While these quantities are relatively easy to obtain for tough materials from J_R-meaurements, their use as arrest toughness parameters has not been critically tested.

The proposed ASTM crack arrest method relies on the non-conservative, LEFM analysis that places lower limits on the size of the test piece. The maximum allowable initiation stress intensity, K_Q, for a .200 m x .200 m x 050 m specimen is about 120 MPa m$^{1/2}$. Therefore a test specimen of the design ~4x to ~16x larger would be required to evaluate very tough materials like ship hull steels with arrest toughness values in the range 200 MPa m$^{1/2}$

to 500 MPa m$^{1/2}$.[15] In other words, the ASTM specimen size required becomes prohibitive.

There are several ways of increasing the capacity of crack arrest tests. One is to insert deeper face grooves on the specimens, thus reducing the energy consumed by the crack, proportionately. Although questions are raised about the 3-dimensionality of the crack tip stress field introduced by the face grooves, experimental evidence[16,17] shows that face grooves occupying 80% of the cross section do not interfere with static measurements. Another way of increasing the capacity is to attach reusable hardened steel arms. Initiation can be facilitated by an external mechanical restraint which is suddenly removed. The concept that evolved in the present work utilizes a combination of the above techniques to increase capacity.

Figure 1 schematically illustrates the operation of the modified test. Load is applied at point D by means of a wedge and split pin, which offers a stiff loading. The hardened steel arms (B) attached to the pre-cracked specimen (A) are wedged open against the restraint of the notched bolt (C). As the wedge load is increased, the notched bolt breaks and releases the elastic energy stored in the arms, causing the crack to grow under a high strain rate condition. Since stiff loading produces a decreasing stress intensity, K, with crack length, the crack arrests at a point F when the stress intensity factor drops below the fracture resistance of the material at arrest.

As part of the present study, an elastic-static finite element analysis. has been performed to evaluate the compliance of the fast fracture loading device with the bolt intact and after it fractures, using the general purpose fintie element code, ABAQUS[18,19]. Measurements of fast fracture and arrest were also carried out with the device on 7075 aluminum alloys and HY-80 steel.

Estimates of the propagating crack toughness, K_{ID}, and the arrest toughness, K_{Ia}, are derived from the compliance values assuming that all of the kinetic energy is conserved and is converted into fracture energy.

EXPERIMENTAL PROCEDURE AND ANALYSIS

Materials

Experimental materials include HY-80 steel and 7075-T651 aluminum alloys. The aluminum alloys are solution treated at 470°C for 1/2 hr., quenched in water and aged at 120°C for different time intervals to achieve different hardness levels After the heat treatment, the hardness values measured were 45, 78, and 92 on Rockwell B Scale for the three aluminum specimens, respectively. Variation of the toughness parameters J_{Ic} and $J_a(2)$, as functions of hardness is shown in Figure 2. The specimen geometry, shown in Figure 3, is a simple compact type specimen measuring .150 m x .150 m x .025 m Sharp 45° face grooves are used on the specimen occupying 25% and 80% of the thickness for the aluminum and steel specimens, respectively. A fatigue crack is introduced in the specimens, following the procedures listed in the standard K_{Ic} test[20], in order to reduce the initial stress intensity, K_Q.

Loading Device

The fast fracture device consists of reusable, hardened steel arms which are attached to the specimen by means of a key-like coupling and a set of bolts (refer to Figure 4). The loading device, designed by Xu[21], also consists of a wedge and split pin arrangement located towards one end of the steel arms. The wedge, the split pins, and the arms are made of hardened 4140 steel (HRC 50). Mechanical restraint is provided by a notched bolt made of 4340 steel, quenched and tempered to a hardness of HRC 38. The bolt in this condition is capable of withstanding about 275 kN before fracture.

Loading and Instrumentation

The tests are conducted using a Tinius-Olsen closed loop servohydraulic testing machine. The load applied on the wedge is measured by means of a load cell and is input directly into an XY-recorder. Displacements are measured by means of clip gages, one attached to the edge of steel arms (near the wedge) and the other located near the notched bolt. This enables simultaneous recording of the end and the bolt displacements. After lubricating the contact surfaces in the wedge and split pin assembly, the wedge is inserted at a rate of 0.05 meters per minute. Loading is continued till the bolt fractures and pre-existing crack in the specimen extends and gets arrested. The wedge is then extracted from the device, which is held down by means of stoppers.

Analysis of Arrest Measurements

At the instant when the pin breaks, the elastic energy stored in the arms is released and the crack extends with the aid of this energy. In terms of compliance, this energy can be expressed as

$$U_{a_0} = \frac{(v_{end})^2}{2C_{p,a_0}} \tag{3}$$

Here, U_{a_0} stands for the energy stored in the arms before the pin breaks, C_{p,a_0} denotes the compliance of the device that is pinned by the bolt, and v_{end} is the displacement measured at the load point. After the pin breaks and the crack extends from a_0 to a_a, the compliance of the device increases to a value, C_{u,a_1}. The elastic energy stored drops down to a value, U_{a_1}, given by

$$U_{a_1} = \frac{(v_{end})^2}{2C_{u,a_1}} \tag{4}$$

Here, it is assumed that the crack propagates under a constant displacement condition. The difference between the two energies is the total energy available for fracture, and should give an estimate of the elastic energy release rate, G_R as follows:

$$G_R = \frac{U_{a_0} - U_{a_1}}{B(a_1 - a_0)} \tag{5}$$

where B is the effective specimen thickness. Known G_R, fracture resistance, can be evaluated using the equation

$$(K_{IR})^2 = \frac{EG_R}{(1 - \nu^2)} = (\bar{K}_{ID})^2 \tag{6}$$

Finite Element Analysis

A linear, elastic-static finite element simulation of the loading device was performed using eight noded, quadrilateral, isoparametric elements. The mesh shown in Figure 5 contains 228 plane strain elements, with 649 nodes and 1947 degrees of freedom. The region labeled Zone 1 represents two half inch thick arms enclosing air gap an inch thick. The specimen sandwiched between these arms is represented by Zone 2. Since a difference in elastic stiffness arises due to this arrangement, a weighted average of the elastic modulus value was used for each of the two zones. A concentrated load was applied at D to simulate the wedge opening force and a distributed load was applied at C to simulate the constraint due to the notch bolt. Points A and B represent the positions of the two clip gages used in the test to measure the displacements. The location of the fatigue crack before the test is represented by the point E. After the bolt fractures, load applied at C is removed and the nodes are released one by one starting from E to simulate static crack growth.

Compliance values obtained from the finite element computations agreed reasonably well with those from the experiment (refer to Figure 6). For constant displacement, the change in stress intensity with crack length can be calculated knowing the change in compliance values using the equation

$$K^2 = EG = \frac{E(v_{end})^2}{2BC^2} \frac{dC}{da} = K^2_{Ia,LB} \tag{7}$$

The quantity $K_{Ia,LB}$ gives a static, lower-bound estimate of arrest toughness. Since the above function in compliance is very sensitive to small variations in the compliance values, the following polynomial fit (with a maximum error of 5%) is used, to smooth out any scatter:

$$C_{u,a_1} = ma^3 \tag{8}$$

where, the value of m is calculated to be $3.4596 \times 10^{-6} \ N^{-1}m^{-2}$. Using equations (7) and (8), the stress intensity change as a function of crack length is calculated (refer to Table 1).

Fractographic Analysis

Since the fracture appearance in the case of fast fracture is significantly different from that of slow fracture, an attempt is made to quantify the differences. A photogrammetric technique[22] is modified to measure the (x,y,z) coordinates of various points on the fractograph with reference to an imaginary reference coordinate systme. Assuming that the difference between the adjacent peaks and valleys on the fracture surface gives a measure of the surface roughness, the average difference between the z-coordinates is measured using the above technique. This difference between the z-coordinates of adjacent peaks and valleys can be taken as a measure of surface roughness only if the tilt axis, the imaginary x-axis, and the edge of the SEM specimen coincide with each other. These measurements are done on both slow and fast fracture surfaces and are summarized in Table 2.

EXPERIMENTAL RESULTS

Figure 7 shows the load-displacement record for the specimens of steel and aluminum. The displacement shown is recorded by the clip gage attached to the device near the notched bar and the load measured by the load cell is the vertical load applied on the wedge. Displacement measured at the end of the device close to the wedge is recorded versus time and is shown in Figure 8.

The load-displacement values are listed in Table 3 with those obtained from finite element calculations for the difference specimens tested. These values represent the load-displacement situation at an instant just before the fracture of the notched bolt. After the bolt fractured, the crack extensions measured are listed in the last column of Table 3.

Results of Fractographic Observations

Some of the micrographs of fracture surfaces produced by the fast fracture loading device are shown here. For purposes of comparison, fractographs of the corresponding slowly fractured surfaces are also shown. Figures 9 and 10 depict the typical fast and slow fracture surfaces, respectively, for steel (50X magnification). Similarly, Figures 11 and 12 show the typical fractographs of aluminum surfaces (at the same magnification). On comparing the corresponding pairs of surfaces, it is apparent that the appearance of fast fracture surface is significantly coarser than that of slow fracture. Microstructural features, such as the aspect ratio (defined as the ratio of average "height" of a dimple on its average width or diameter) seem to be higher in the former case.

DISCUSSION

The analysis of the arrest measurements described earlier yields estimates of G_D and $K_{ID} = [EG_D/(1-\nu^2)]^{1/2}$, the average value of the energy consumed by the propagating crack and the corresponding toughness. The values of G_Q and

G_a (and K_Q and K_{Ia}) the statically evaluated elastic energy release rates at the onset of crack extension and arrest (and the corresponding stress intensity values) can also be derived from the compliance calculations. These values are identified in Figure 13, which also shows schematically the variation of G^{dyn} and G^{stat} with crack length.

At the instant the bolt breaks, elastic energy is conveyed down the arms of the device and test piece to the pre-existing crack tip at wave speeds. The changes in the strain energy distribution are similar to those produced by a very brittle crack propagating from the bolt to the test material. The dynamic energy release rate G^{dyn}, at the location of the pre-existing crack tip, increases rapidly, consistent with a very high loading rate and rises well above $G^{stat} = G_Q$, because of the kinetic energy inserted in the test piece by the fracture of the bolt.

The crack begins to extend when

$$G^{dyn} = G_D(\dot{a} = 0) \simeq J_{IC}(\dot{J}) \qquad (7)$$

where $J_{IC}(J)$ signifies the J-value at the onset of crack extension for the high loading rate. The requirement:

$$G^{dyn} = G_D(\dot{a}) \qquad (8)$$

where $G_D(a)$ represents the crack velocity dependence of the fracture energy, is satisfied while the crack is propagating and determines its speed. The crack velocity diminishes after the bulk of the kinetic energy in the system is consumed as fracture energy. The crack arrests when $a = a_a$ and:

$$G^{dyn} \leq G_A = G_D(\dot{a} = 0) \simeq J_a(2) \qquad (9)$$

It should be noted that the value of G^{dyn} at the onset of crack extension, Equation [7], and at arrest, Equation [8], are not necessarily the same in view of differences in the character of crack tip strain field (the rising nature of the J_R-curve) existing at these locations. The average values of

value of $\bar{K}_{ID}$. However, it should be noted that even if 30% of the released energy were dissipated in this way, remote from the crack tip, this would only reduce K_{ID} by $\sim 15\%$.

(ii)   Rate dependence of the yield strength. The calculations of Hoff, Hahn and Rubin[12] show that the rate dependence of the yield strength of steel can elevate the J_R-curve by an amount comparable to J_{IC}, independent of the local resistance to fracture.

(iii)   Rate dependence of the resistance to fracture. The changes in the fracture appearance described in the previous section reflect an increase in the local resistance to fracture. This is discussed more fully in the next paragraph.

As pointed out earlier, the fracture appearance of fast fracture surface is much coarser, and is accompanied by larger plastic deformation, than the slow fracture surface. Recently, there have been several attempts to relate the elastic energy release rate (or the corresponding stress intensity) with the microstructural features in the case of very tough and ductile materials. One of the important contributions is from Stuwe[23], whose work indicates that fracture resistance increases as the magnitude of the microroughness or the depth of an average dimple increases. In more specific terms, doubling the roughness will approximately increase the stress intensity by a factor of 1.3. Similar observations of Thompson and Ashby[24] also verify the results of Stuwe. While these analyses are based on empirical formulations, it is reasonable to state that a fracture surface revealing enormous plastic work and large microstructural features resulting in a coarse structure, indicates an increase in the resistance to fracture.

In summary, the above effects add up in such a way as to enhance the static values of energy release rate (or the corresponding values of stress

intensity). From the energy viewpoint, the factors due to the 3 effects are
~1.3, ~2.0 and ~1.7, for energy losses, rate dependence of yield strength and
rate dependence of resistance to fracture, respectively. These add up to a
factor of ~5. Experimentally measured values (Tables 4 and 5) indicate a
factor ~4x to ~16x larger than the static, rate insensitive values of the
energy release rate. While the net effect of the above explanations falls
somewhat short, more sensitive instrumentation and a device of higher capacity
are required to assess the dynamic effects in a thorough way.

CONCLUSIONS

1. The "fast fracture device" is able to simulate crack extension and arrest
   in a very tough material. However, the energy and toughness measuring
   capacity of the present design is marginal for tough, arrester grade steels.

2. The relatively small crack extensions produced with relatively large
   expenditures of energy indicate that the average toughness values for
   fast propagating fractures are ~2x to ~4x larger than the values for
   slow crack extension in a tough aluminum alloy and steel.

3. The large values of the toughness K_{ID}, derived from the measurements may
   have 3 sources (i) the rate dependence of the resistance to plastic flow,
   (ii) the rate dependence of the resistance to fracture and (iii) unaccounted
   for energy losses in the device.

4. Fracture surfaces produced by fast fracture are substantially rougher than
   those produced by slow crack extension. This change is consistent with an
   increase in the resistance to fracture.

5. Rapid crack extension in a tough, ductile material can consume substantial
   amounts of kinetic energy released in the process of fracture.

6. The $K_{Ja}(2)$ toughness values are intermediate with $\overline{K}_{ID}$ and K_{Ia}. While this

is consistent with the view that $K_{Ja}(2)$ is a valid measure of the arrest

capabilities of a tough material, more direct evidence of a close relation

between $K_{Ja}(2)$ and K_{IA} is called for to support the use of $K_{Ja}(2)$ in design.

7. Measured values of $\overline{G_D}$ indicate a factor 4x to 16x the energy of slowly

extending fractures and the net factor due to various effects accompanying

fast fracture adds up to ~5x.

REFERENCES

1. Robertson, T. S., J. Iron Steel Inst., 1953 Vol. 175, p. 361.

2. Akita, Y. and Ikeda, K., Transporational Tech. Rest. Inst., Report
    56, Tokyo, December, 1962.

3. Yoshiki, M., Kanazawa, T., and Machida, S., Proc. Seventh Japanese Cong.
    Test Materials, 1964, p. 71.

4. Crosley, P. B., and Ripling, E. J., "Towards Development of a Standard
    Test for Measuring K_{Ia}," ASTM STP 627, Philadelphia, 1979.

5. Hahn, G. T., Hoagland, R. G., Rosenfield, A. R., and Barnes, C. R.,
    "A Cooperative Program for Evaluating Crack Arrest Testing Methods,"
    ASTM STP 711, Philadelphia, 1980.

6. Crosley, P. B., and Ripling, E. J., "Significance of Crack Arrest
    Toughness (K_{Ia}) Testing," ASTM STP 711, Philadelphia, 1980.

7. Krafft, J. M. and Irwin, G. R., "Crack Velocity Considerations,"
    ASTM STP 581, Philadelphia, 1965.

8. Crosley, P. B., and Ripling, E J., "Crack Arrest Studies," Second Annual
    Report for EPRI, Project RP303-1, September, 1976.

9. Hahn, G. T., Hoagland, R. G., and Rosenfield, A. R., Met. Trans.,
    Vol. 7A, 1976, pp. 49-54.

10. Hahn, g. T., Hoagland, R. G., Rosenfield, A. R., and Kanninen, M. F.,
    "Dynamic Crack Propagation," G. C. Shi, editor, Noordhoff Int. Publishing,
    Leyden, The Netherlands, 1973.

11. Kalthoff, J. F., Beinert, J., Winkler, S., and Klemm, W., "Experimental
    Analysis of Dynamic Effects in Different Crack Arrest Test Specimens,"
    ASTM STP 711, Phil., 1980.

12. Hahn, G. T., Hoff, R., and Rubin, C. A., "Strain Rate Dependence of the
    Deformation at the Tip of a Stationary Crack," Sixteenth National Symposium
    on Fracture Mech., Columbus, August, 1983.

13. Joyce, J. A., "Static and Dynamic J-R Curve Testing of A533 B Steel Using the Key Curve Analysis Technique," No. NUREG/CR-2274, Washington, 1981.

14. Dantam, V. K., and Hahn, G. T. "Definition of Crack Arrest Performance of Tough Alloys," Proc. of U.S.-Japan Coop. Seminar, Fracture Tolerance Evaluation, Honolulu, December, 1971.

15. Broek, D., "Elementary Engineering Fracture Mechanics," 3rd Rev. Edition, Martinus Nijhoff, Boston, 1982.

16. Dantam, V. K., M.S. Thesis, Vanderbilt University, 1982.

17. Mejias, H. D., and L. A. Devidia, "Influence of Side Grooving on Crack Arrest Toughness of C-Mn Steels," submitted for publication to Engr. Fracutre Mechanics, April, 1985.

18. Hibbitt, Karlsson and Sorensen, Inc., "ABAQUS - User's Manual," Providence, RI, 1982.

19. Hibbitt, Karlsson and Sorensen, Inc., "ABAQUS - Theory Manual," Providence, RI, 1982.

20. ASTM Standard E399-78A, "Standard Test Method for Plane Strain Fracture Toughness of Metallic Materials," Annual Book of ASTM Standards, Part 10, Philadelphia, PA 1979.

21. Xu, N., "Towards Development of Fast Fracture Loading Device," Vanderbilt University, Private Communication, 1983.

22. Nelson, J. L., and Beavers, J. A., "Application of a Photogrammetric Technique to the Determination of the Orientation of Stress Corrosion Fractures," Met. Trans., May 1979, pp. 658-662.

23. Stuwe, H. P., "The Work Necessary to Form a Ductile Fracture Surface," Eng. Frac. Mech., Vol. 13, 1980, pp. 231-236.

24. Thompson, A. W., and Ashby, M. F., "Fracture Surface Microroughness," Script Met., Vol. 18, 1984, pp. 127-130.
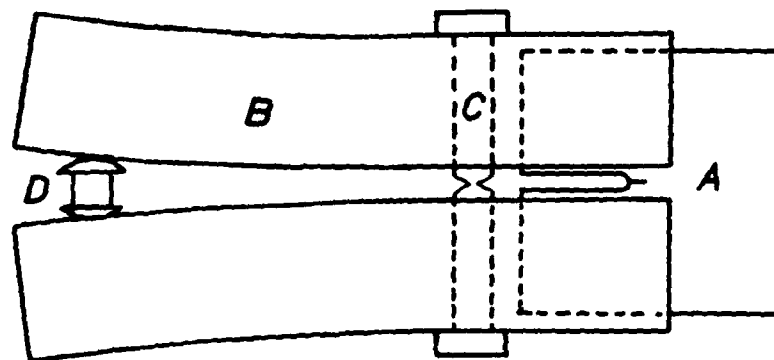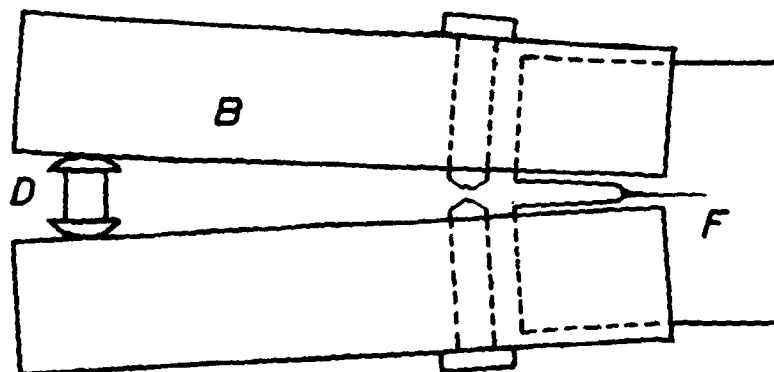
FIGURE 1. Schematic operation of fast fracture device: (A) Wedge load
is applied, storing elastic energy in the arms; and (B) the bolt fractures
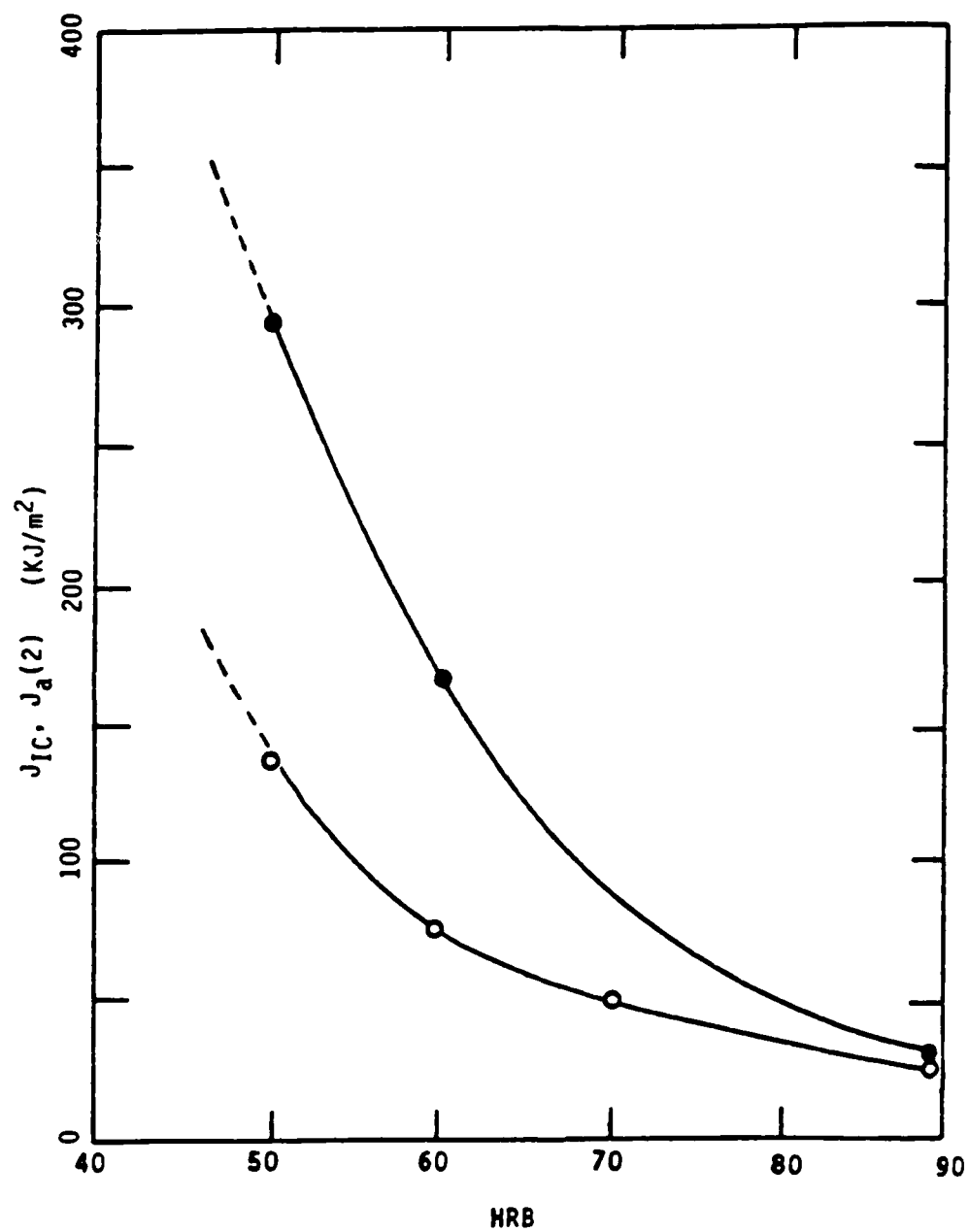causing the crack to extend.

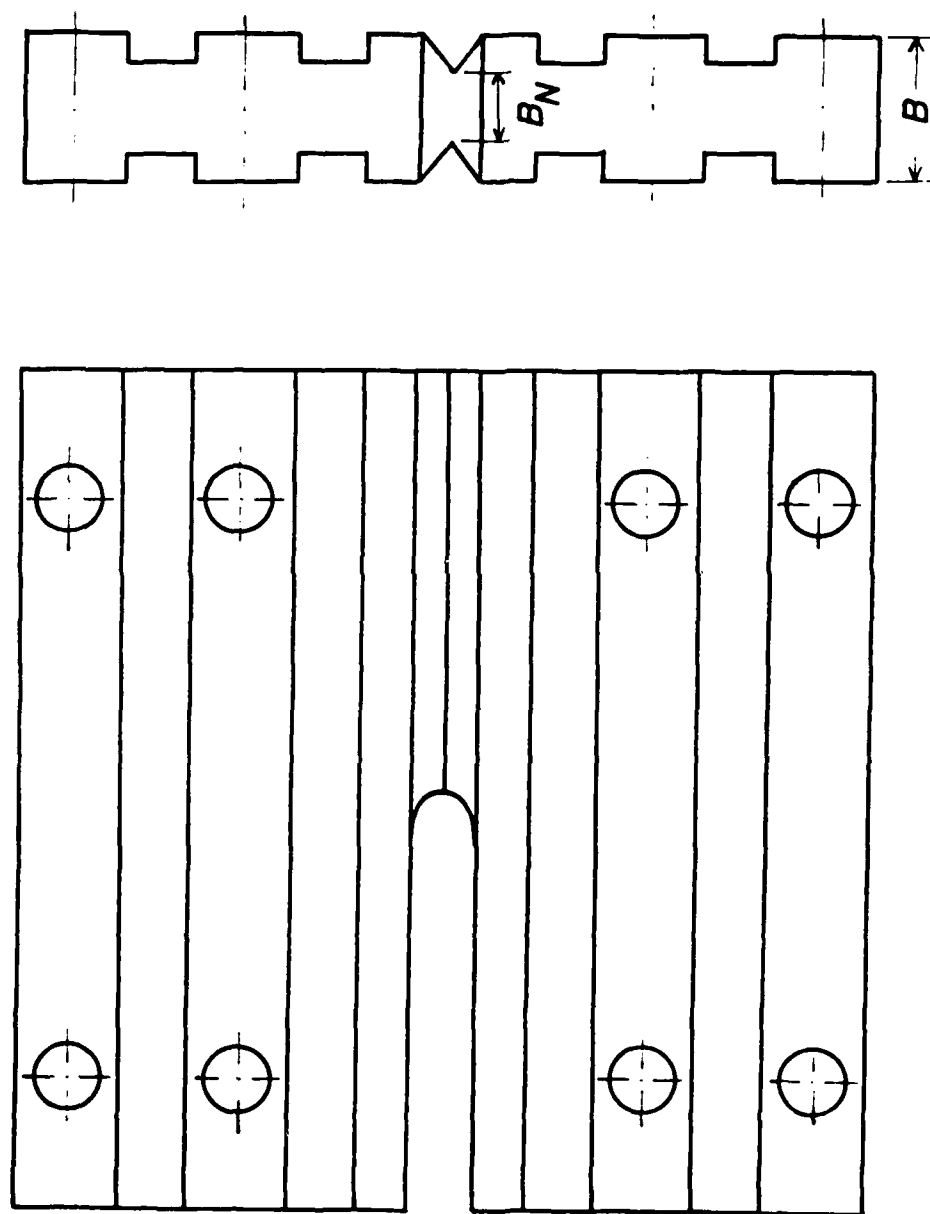FIGURE 2. J_{IC} and $J_a(2)$ variation with hardness for 7075-T165 aluminium.

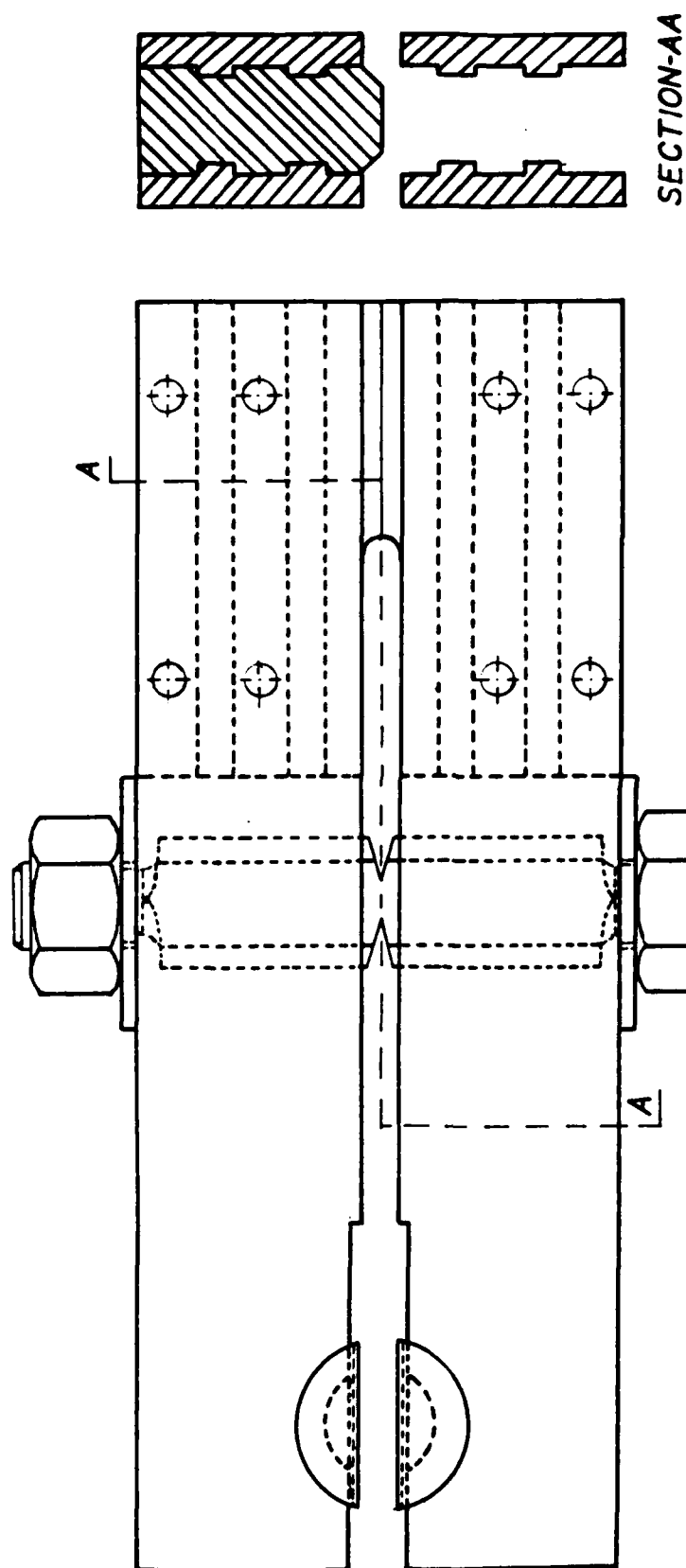FIGURE 3. Test specimen geometry (drawing is not to scale)

SECTION-AA

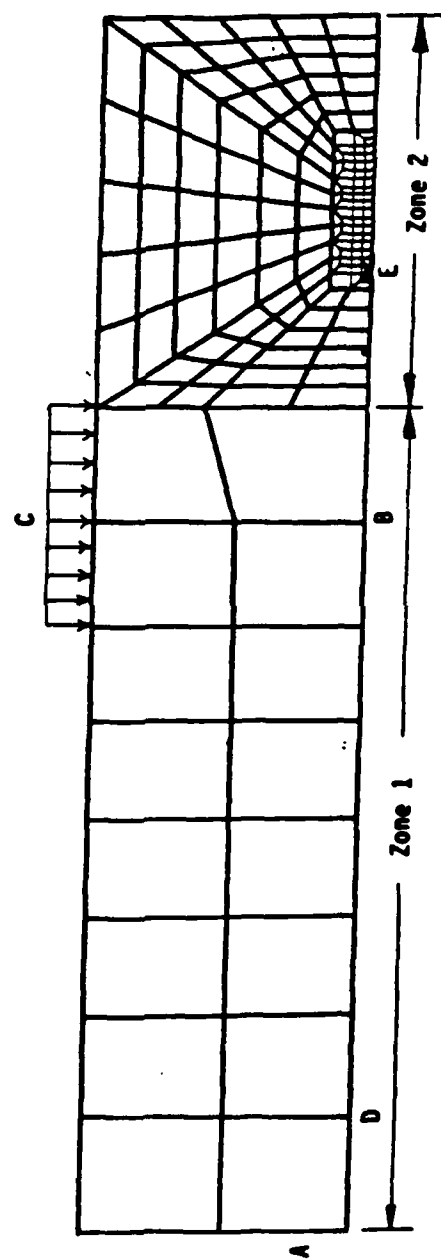FIGURE 4. Fast fracture loading device assembly (drawing is not to scale)

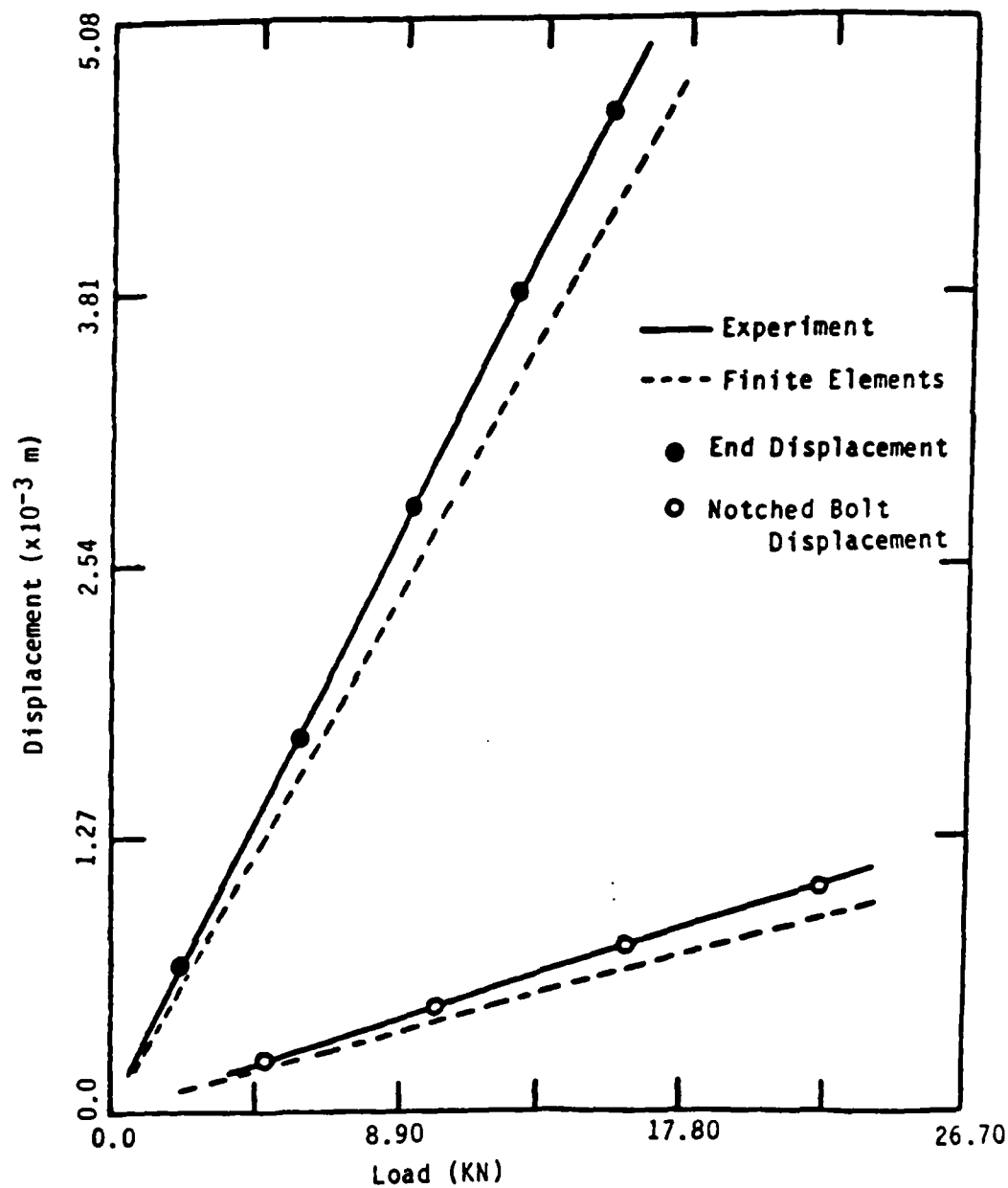FIGURE 5. Mesh geometry used in the finite element simulation of the device.

FIGURE 6. Comparison of compliance values measured without the bolt vs. the values obtained from finite element calculations.
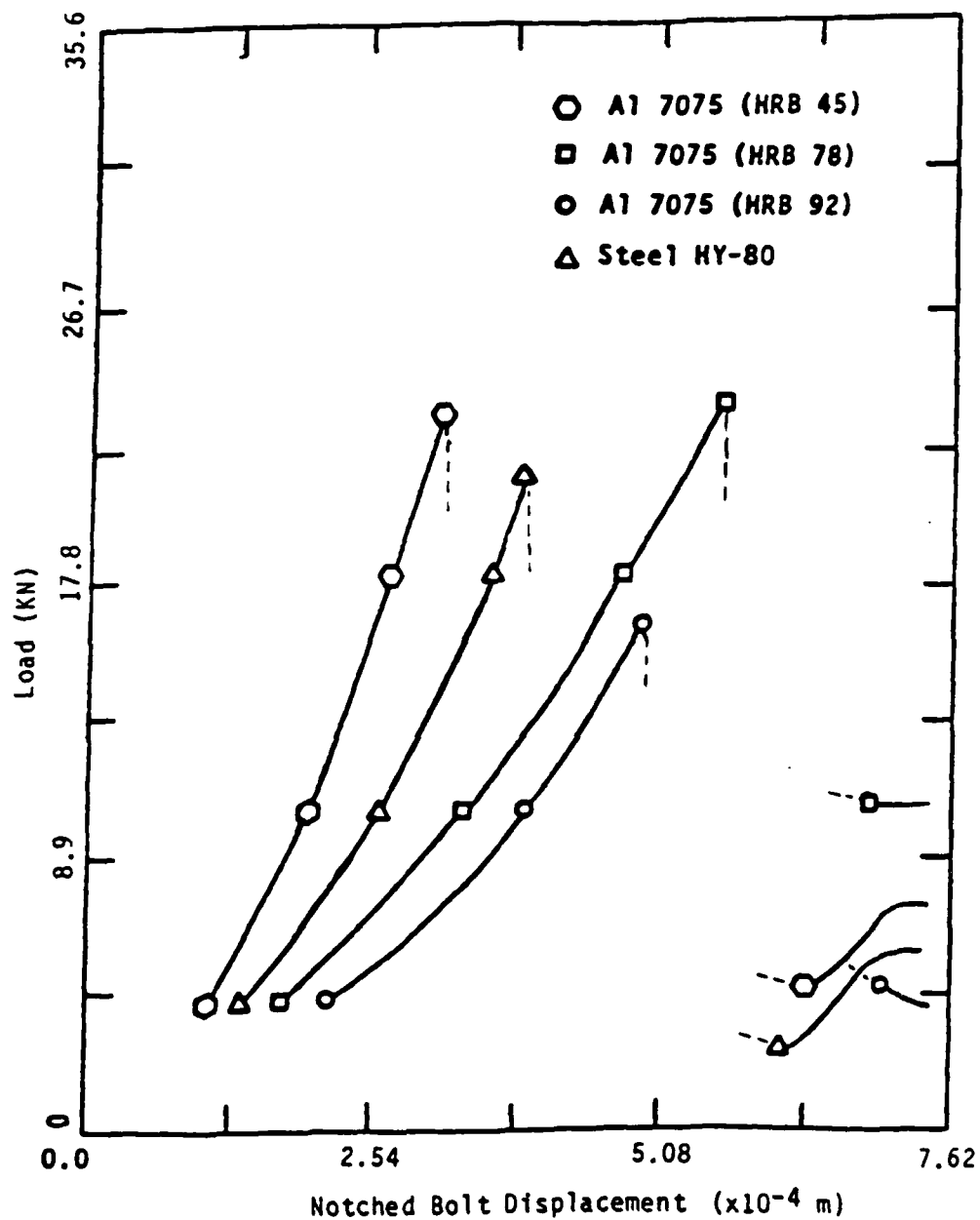
FIGURE 7. Load vs. notched bar displacement record for the four specimens.
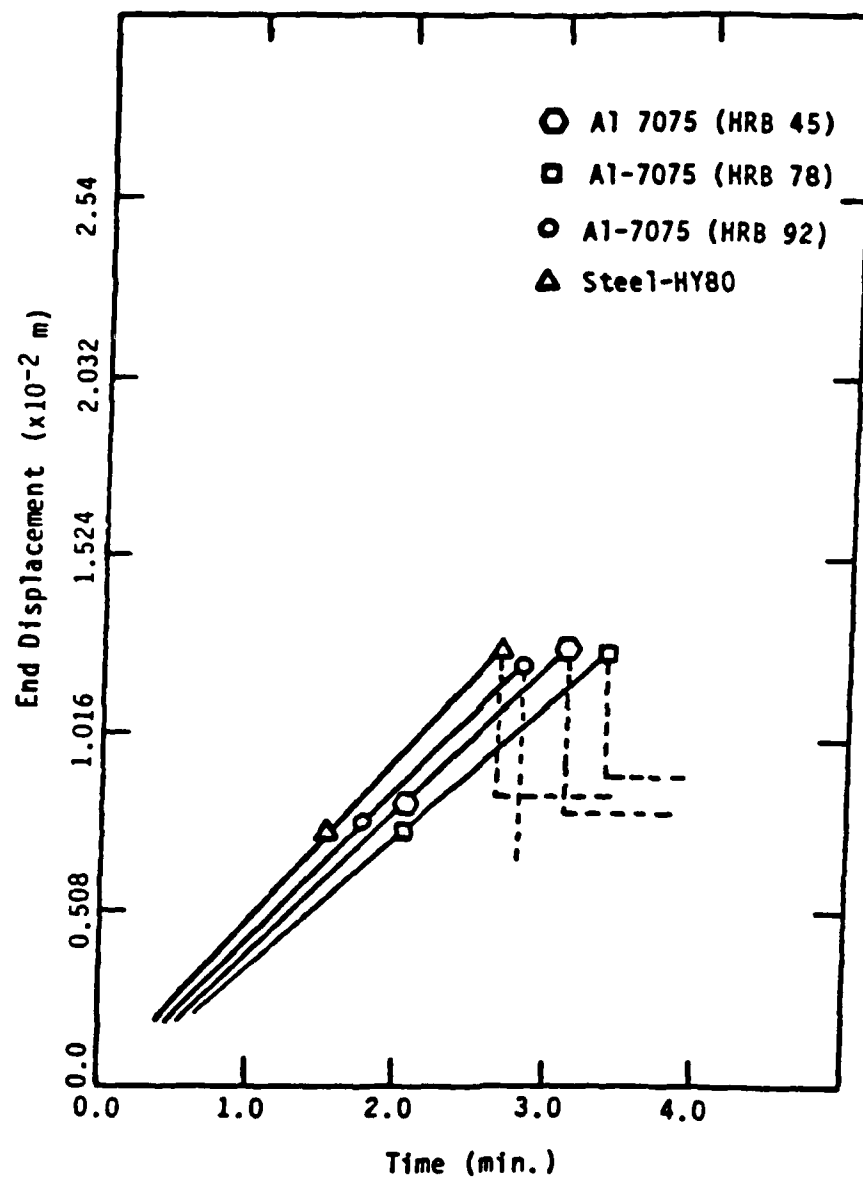
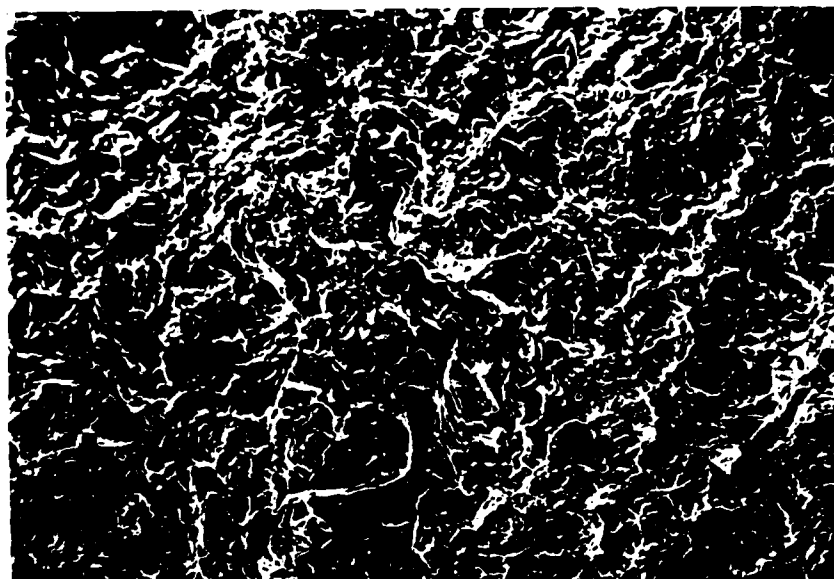FIGURE 8. End displacement vs. wedge travel time measurements.

FIGURE 9. Fast fracture surface of HY-80 steel specimen.
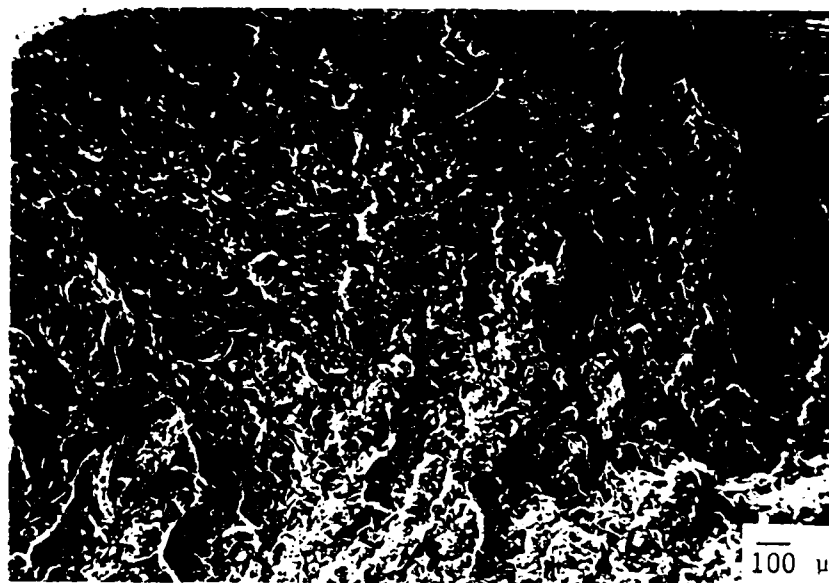
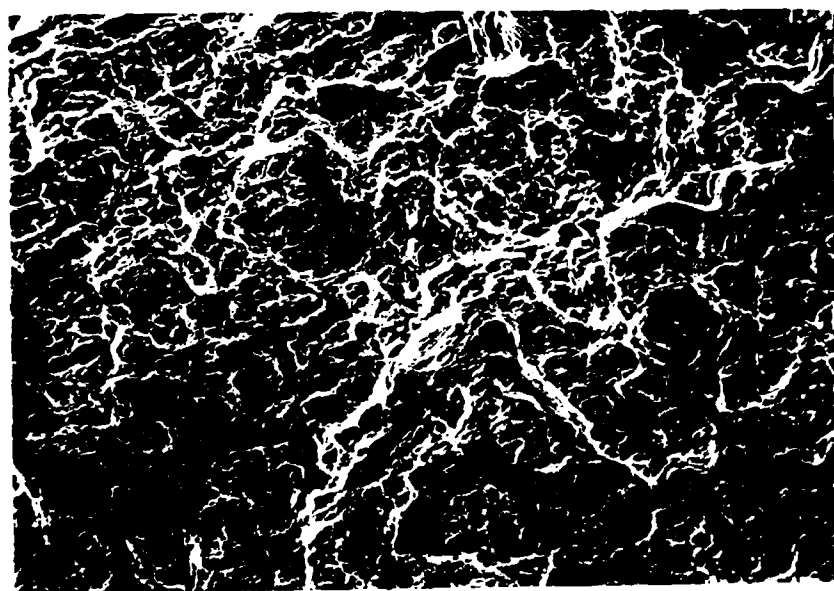FIGURE 10. Slow fracture surface of HY-80 steel
specimen.

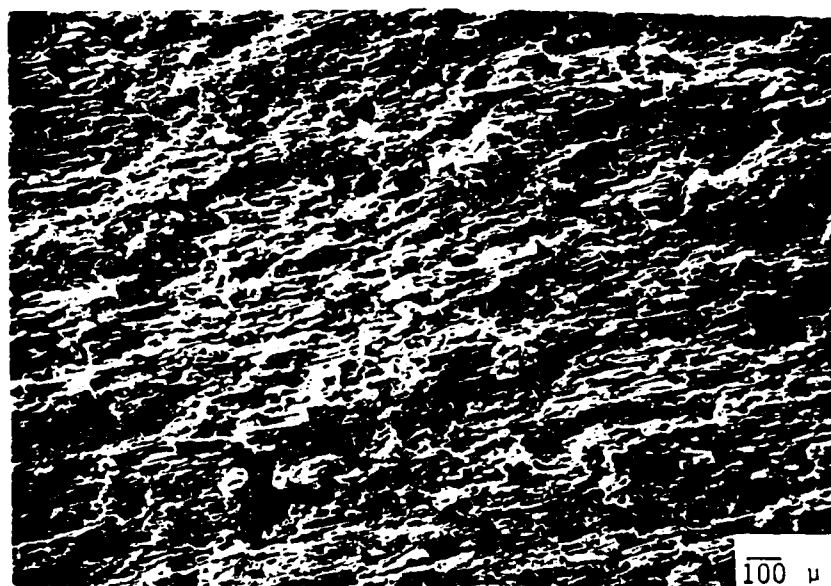FIGURE 11. Fast fracture surface of 7075 aluminium (HRB45).

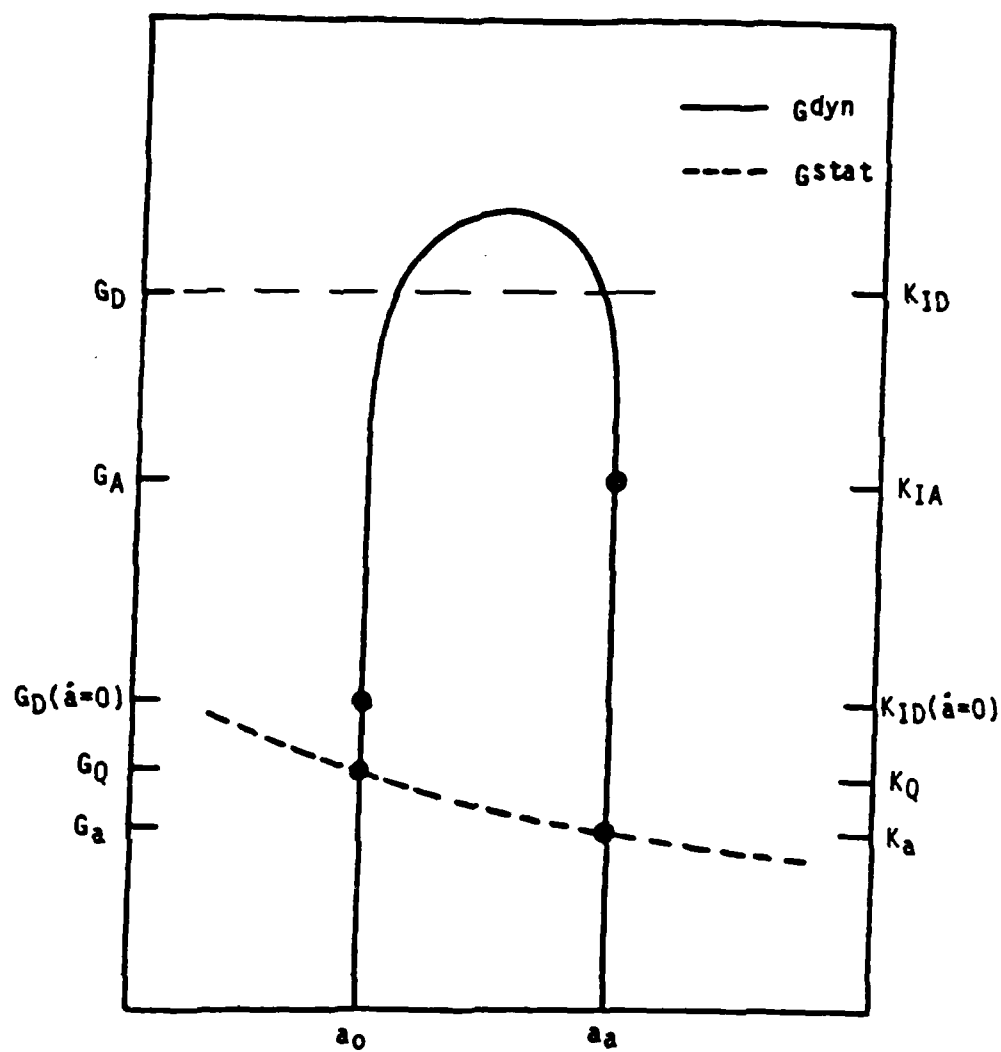FIGURE 12. Slow fracture surface of 7075 aluminium (HRB45).

FIGURE 13. Variation of G^{dyn} and G^{stat} with crack length.

TABLE 1

SUMMARY FOR FINITE ELEMENT ANALYSIS FOR STATIC CRACK GROWTH

$\Delta a\,(m)$	$C(mN^{-1})$	dC/da (N^{-1})	$G(Jm^{-2})$	$K(MPa\ m^{1/2})$
0.0	1.1395×10^{-7}	1.0664×10^{-6}	1.2279×10^{5}	164.3
0.39×10^{-3}	1.1437×10^{-7}	1.0690×10^{-6}	1.2219×10^{5}	163.9
0.71×10^{-3}	1.1471×10^{-7}	1.0712×10^{-6}	1.2171×10^{5}	163.5
1.42×10^{-3}	1.1547×10^{-7}	1.0759×10^{-6}	1.2064×10^{5}	162.8
2.85×10^{-3}	1.1712×10^{-7}	1.0855×10^{-6}	1.1852×10^{5}	161.4
5.67×10^{-3}	1.2010×10^{-7}	1.1045×10^{-6}	1.1449×10^{5}	158.6
8.48×10^{-3}	1.2323×10^{-7}	1.1236×10^{-6}	1.1062×10^{5}	155.9
11.3×10^{-3}	1.2643×10^{-7}	1.1430×10^{-6}	1.0691×10^{5}	153.3
14.12×10^{-3}	1.2968×10^{-7}	1.1625×10^{-6}	1.035×10^{5}	150.7
16.94×10^{-3}	1.2399×10^{-7}	1.1821×10^{-6}	9.9928×10^{4}	148.2
19.76×10^{-3}	1.3635×10^{-7}	1.2020×10^{-6}	9.6664×10^{4}	145.8

TABLE 2

SUMMARY OF PHOTOGRAMMETRIC MEASUREMENTS

| Specimen | Crack Speed | Point of Focus | Z-Coordinate Measurements | | | | Average Difference in Height | Ratio, r |
			1	2	3	Average		
7075 Al (HRB 45)	Slow	Peak	-0.69	-0.685	-0.71	-0.695	0.15	~2
		Valley	-0.85	-0.85	-0.825	-0.842		
	Fast	Peak	-0.505	-0.505	-0.51	-0.507	0.28	
		Valley	-0.78	-0.78	-0.80	-0.79		
HY-80 Steel	Slow	Peak	-0.35	-0.38	-0.365	-0.365	0.195	~3.5
		Valley	-0.51	-0.62	-0.56	-0.56		
	Fast	Peak	-0.41	-0.44	-0.45	-0.433	0.67	
		Valley	-0.98	-1.21	-1.12	-1.103		

TABLE 3

SUMMARY OF LOAD-DISPLACEMENT DATA

Material	Data Source	$v_{end}(m)$	$v_{load}(m)$	$v_{pin}(m)$	Vertical Load (kN) on wedge
HY80 Steel	Finite Element Calculations	0.0122	0.0099	3.81×10^{-4}	144
	Experiment	0.0122	---	3.74×10^{-4}	151
7075 Aluminum	Finite Element Calculations	0.0124	0.0101	3.05×10^{-4}	158
Specimen 1 (HRB 45)	Experiment 1	0.0124	---	3.03×10^{-4}	160
Specimen 2 (HRB 78)	Experiment 2	0.0125	---	3.62×10^{-4}	161
Specimen 3 (HRB 92)	Experiment 3	0.0125	---	3.73×10^{-4}	166

TABLE 4

SUMMARY OF ARREST MEASUREMENTS

Material	B_N/B	C_{p,a_0} (mN^{-1})	C_{u,a_1} (mN^{-1})	U_{a_0} (J)	U_{a_1} (J)	$\overline{G_D}$ (KJ/m^2)
Steel	80%	6.875×10^{-8}	1.18×10^{-7}	712.8	416.0	5499
Aluminum 7075 HRB 45	25%	6.32×10^{-8}	1.43×10^{-7}	808.0	357.0	2439
Aluminum 7075 HRB 78	25%	6.32×10^{-8}	2.29×10^{-7}	808.0	223	609.6
Aluminum 7075 HRB 92*	25%	6.32×10^{-8}	$>2.6 \times 10^{-7}$	808.0	<200	<446.5

*Crack did not arrest at this hardness level and therefore the figures calculated represent the upper limits.

TABLE 5

SUMMARY OF ARREST MEASUREMENTS AND CALCULATIONS

Specimen	B_N/B	Δa mm	K_Q MPa$\sqrt{m}$	K_{JC} MPa$\sqrt{m}$	K_{ID} MPa$\sqrt{m}$	$K_{Ja(2)}$ MPa$\sqrt{m}$	K_{Ia} MPa$\sqrt{m}$
HY-80 Steel	80%	9.0	402	214	1099.3	259	385
7075 Al (HRB 45)	25%	8.5	189	115	430	226	174
7075 Al (HRB 78)	25%	50.8	193	60	215	142	126
7075 Al (HRB 92)	25%	No Arrest	190	39	<184	101	<104

END

DATE

FILMED

6- 1988

DTIC